LUND UNIVERSITY

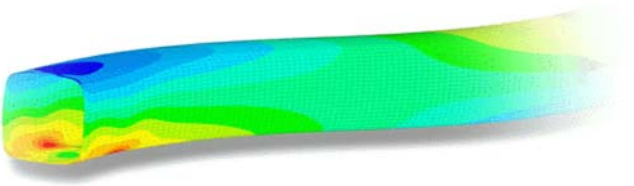

Proceedings of the 14TH NORDIC SEMINAR ON COMPUTATIONAL MECHANICS Lund, 19-20 October, 2001

L. Beldie, O. Dahlblom, A. Olsson,
N. S. Ottosen and G. Sandberg *(editors)*

Structural Mechanics
ISSN 0281-6679

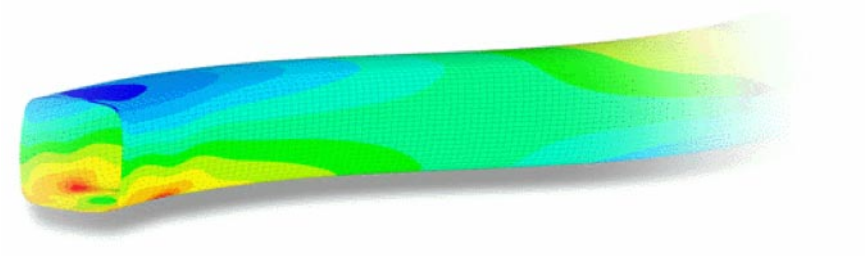

Proceedings of the 14TH NORDIC SEMINAR ON COMPUTATIONAL MECHANICS Lund, 19-20 October, 2001

L. Beldie, O. Dahlblom, A. Olsson,
N. S. Ottosen and G. Sandberg
(editors)

Printed by KFS I Lund AB, Lund, Sweden, October 2001.

For information, address:
Division of Structural Mechanics, LTH, Lund University, Box 118, SE-221 00 Lund, Sweden.
Homepage: http://www.byggmek.lth.se

Preface

These proceedings contain the papers presented at the Fourteenth Nordic Seminar on Computational Mechanics, held at Lund University, Lund, Sweden, 19-20 October 2001. The Nordic Seminars on Computational Mechanics represent a major activity of the Nordic Association for Computational Mechanics (NoACM). The NoACM was founded in 1988 with the objective to stimulate and promote research and practice in computational mechanics, to foster the interchange of ideas among the various fields contributing to computational mechanics, and to provide forums and meetings for dissemination of knowledge in computational mechanics. Younger researchers, including doctorate students etc., are especially encouraged to take part at these seminars. The member countries of NoACM are the Nordic countries (Denmark, Finland, Iceland, Norway and Sweden) and the Baltic countries (Estonia, Latvia and Lithuania). NoACM is a subchapter of the International Organization for Computational Mechanics (IACM) and the European Community on Computational Methods in Applied Sciences (ECCOMAS).

The responsibility for organizing this year's seminar was assigned by NoACM to the Division of Structural Mechanics, Lund University. This year's seminar contains five invited lectures and 59 contributed presentations divided into eleven sessions. In the present volume, all the invited lectures are placed first, followed by the contributed papers in the order of appearance.

On behalf of the organizers, sincere appreciations are extended to all contributors at the seminar, not least to the invited lecturers and to the other speakers for their efforts in preparing talks and papers (extended abstracts).

Lund, 3 October 2000

The editors

Organizing Committee

Eng lic Liliana Beldie
Docent Ola Dahlblom
Eng Lic Anders Olsson
Professor Niels Saabye Ottosen
Professor Göran Sandberg

Programme Committee

Kjell Magne Mathisen, Norway
Lars Damkilde, Denmark
Anders Eriksson, Sweden
Jaan Lellep, Estonia
Martti Mikkola, Finland
Göran Sandberg, Sweden
Nils-Erik Wiberg Sweden

NSCM14 secretariat

Division of Structural Mechanics
Lund University
PO Box 118
S-221 00 Lund
SWEDEN
Phone: +46 46 222 7370
Fax: +46 46 222 4420
strucmech@byggmek.lth.se

Session I-B

Session II-B

Session I-C

Session II-C

Session I-F

Interdisciplinary Analysis and Design Optimization of Systems with Fluid-Structure Interaction

E. Lund*, H. Møller and L.A. Jakobsen
Institute of Mechanical Engineering
Aalborg University, Denmark
e–mail: el@ime.auc.dk

ABSTRACT

Summary The objective of this work is to develop and implement efficient numerical procedures for gradient based design optimization of strongly coupled fluid–structure interaction problems. The solution for state is obtained using finite element residual formulations and the resulting nonlinear equations are solved using an approximate Newton method. Design sensitivity analysis is performed by the direct differentiation method, and the sensitivities form the basis for multidisciplinary gradient based design optimization.

Introduction

A challenging area in multidisciplinary analysis and design optimization is fluid-structure interaction problems due to the many nonlinearities involved. In this work gradient based shape design optimization of strongly coupled fluid-structure interaction problems between a viscous, incompressible fluid and an elastic solid undergoing large displacement is investigated. In this context strongly coupled means that the solid deformation is allowed to be large enough to significantly alter the flow of the fluid. Design problems where the dependence of the flow domain on the deforming interface must be taken into account are encountered when considering flexible structures under aerodynamic or hydrodynamic loads, e.g., flexible aerodynamic structures such as wind turbine wings, hydraulic valves, parts of turbomachinery, thermal process equipment, lightweight bridges, and elastic vessels in interaction with biofluids. The topic of analysis and design optimization of nonlinear fluid-structure interaction is therefore essential in both aerospace engineering, mechanical engineering, bioengineering, and civil engineering, and it has received much interest in recent years, see, e.g., [1, 2].

Analysis and Design Sensitivity Analysis

The viscous incompressible flow can be laminar or turbulent and is described using the Reynolds-Averaged Navier–Stokes equations (RANS) together with a turbulence model. The turbulence models used include both the algebraic Baldwin-Lomax turbulence model, the Spalart-Allmaras one-equation model and two-equation models such as the Wilcox 1988 and 1998 $k-\omega$ turbulence models and the shear stress transport (SST) $k-\omega$ turbulence model, see [3, 4]. The latter model is based on a blending of the $k-\omega$ model near walls with the standard $k-\epsilon$ model away from the interface. In the solid governing equations the Green–Lagrange strain tensor is used to facilitate large displacements and the constitutive law is for an elastic material. The two domains are coupled together by consistent interface conditions, this being continuity in tractions and velocities.

The solution for state of the 2D/3D stationary fluid-structure interaction problem is obtained using both Galerkin, Streamline-Upwind/Petrov-Galerkin and Pressure-Stabilized/Petrov-Galerkin FEM [5, 6], and due to the large displacements allowed, the finite element mesh of the fluid domain has to be updated as part of the solution algorithm. The mesh is updated by solving an

auxiliary elastic problem for the fluid mesh, considering the fluid as a linear elastic solid and imposing the calculated solid displacements found from the coupled problem as nodal displacements. The elements for solving the auxiliary problem are low order elements, and a direct factorization of the stiffness matrix is used. In this way the updating of the mesh is very cheap, amounting to one back substitution for every update.

However, if a direct elastic analogy for the fluid domain is employed, the elements close to the interface may become distorted or even degenerated. A simple strategy that reduces this problem is to scale the elastic properties of the associated elastic problem by a measure of the distance to the nearest fluid-solid interface. The stiffness matrix $\mathbf{K}$ of the mesh updating problem is scaled as

$$\mathbf{K} = \sum_{nElem} \frac{1}{d^p}\, \mathbf{k}_i \qquad \text{where} \begin{cases} d = d_i & \text{if } d_i \leq d_{transition} \\ d = d_{transition} & \text{if } d_i > d_{transition} \end{cases} \tag{1}$$

where $d_{transition}$ is the maximum distance from the interface for which scaling of the element stiffness $\mathbf{k}_i$ should be applied. The distance $d_{transition}$ must be provided by the user together with the power p. Further details and examples can be found in [7, 8].

The resulting nonlinear equations are solved using an approximate Newton method, i.e., a step $k+1$ in the solution procedure for the stationary strongly coupled fluid-structure interaction problem when an algebraic turbulence model is used can be described as

$$\frac{\partial \mathbf{R}(\mathbf{u}^k)}{\partial \mathbf{u}}\, \Delta\mathbf{u}^k \;=\; \mathbf{J}^k\, \Delta\mathbf{u}^k \;=\; \begin{bmatrix} \mathbf{J}^k_{FF} & \mathbf{0} & \mathbf{J}^k_{FI} \\ \mathbf{0} & \mathbf{J}^k_{SS} & \mathbf{J}^k_{SI} \\ \mathbf{J}^k_{IF} & \mathbf{J}^k_{IS} & \mathbf{J}^k_{II} \end{bmatrix} \begin{Bmatrix} \Delta\mathbf{u}^k_F \\ \Delta\mathbf{u}^k_S \\ \Delta\mathbf{u}^k_I \end{Bmatrix} \;=\; - \begin{Bmatrix} \mathbf{R}^k_F \\ \mathbf{R}^k_S \\ \mathbf{R}^k_I \end{Bmatrix} \tag{2}$$

where $\mathbf{u}^{k+1} = \mathbf{u}^k + \Delta\mathbf{u}^k$ and the total residual $\mathbf{R}$ has been decomposed into $\mathbf{R}_F$ containing fluid conservation of momentum residual, fluid conservation of mass residual, and interface conservation of mass residual, $\mathbf{R}_S$ containing residual of solid equilibrium equations, and $\mathbf{R}_I$ containing residual of continuity of interface traction equations.

If Eq. (2) is solved by a direct method, $\mathbf{J}$ is needed explicitly. The storage requirements for the system Jacobian $\mathbf{J}$ can be quite severe because of the interface. The worst part comes from the dependence of the fluid nodal coordinates on the interface displacements, i.e. $\mathbf{J}_{FI}$. Considering one interface displacement degree of freedom (d.o.f.), we observe that this one d.o.f. has the potential to move the fluid mesh everywhere. This means that the derivative of the fluid residual w.r.t. the interface displacements will be a dense matrix. If this submatrix were to be computed it would be dependent on the mesh updating strategy. With the approach used here every column will require state sensitivities of the fluid nodal displacements from the mesh update described by Eq. (1), and such storage requirements are, in general, impossible to fulfill. Furthermore, in case of turbulence models, the exact Jacobian is hard to compute. Therefore some approximation $\tilde{\mathbf{J}}$ to the exact Jacobian $\mathbf{J}$ is used

$$\mathbf{J} = \tilde{\mathbf{J}} + \mathbf{J}^d \tag{3}$$

where $\mathbf{J}^d$ is the error in the approximation to the Jacobian.

If an iterative solution method is used, $\mathbf{J}$ is not explicitly needed, but instead it's product with some vector. Here we can use the well known device of recognizing the product $\mathbf{Jz}$ as the directional derivative of the residual, a definition of which is

$$\mathbf{Jz} = \lim_{\alpha=0} \frac{\mathbf{R}(\mathbf{u} + \alpha\,\mathbf{z}) - \mathbf{R}(\mathbf{u})}{\alpha} \tag{4}$$

In this way the product of the system Jacobian with a vector can be approximated by a finite difference.

Design sensitivity analysis (DSA) is done by the direct differentiation method [9, 10]. Noting that at a solution $\mathbf{R}(\mathbf{u}) = \mathbf{0}$ the sensitivities of the state variables can be found by differentiation with respect to a shape design variable a_i

$$\frac{d\mathbf{R}}{da_i} = \frac{\partial \mathbf{R}}{\partial \mathbf{u}}\frac{d\mathbf{u}}{da_i} + \frac{\partial \mathbf{R}}{\partial a_i} = \mathbf{0} \qquad \text{i.e.,} \qquad \frac{\partial \mathbf{R}}{\partial \mathbf{u}}\frac{d\mathbf{u}}{da_i} = -\frac{\partial \mathbf{R}}{\partial a_i} \tag{5}$$

The right hand side of Eq. (5), $\frac{\partial \mathbf{R}}{\partial a_i}$, is sometimes called the pseudo load. It can easily be calculated analytically for material design variables, but for shape variables this requires some lengthy algebra. We evaluate the pseudo load by a central finite difference approximation on a perturbed mesh. If we had a factorization of the full system Jacobian the solution of Eq. (5) would be very efficient, requiring only one back substitution per design variable.

Since we do not have the exact Jacobian matrix available nor do we want to compute and store it, we have to solve Eq. (5) by an iterative method. Inserting Eq. (3) into Eq. (5), the sensitivity solve can be written as

$$(\tilde{\mathbf{J}} + \mathbf{J}^d)\frac{d\mathbf{u}}{da_i} = -\frac{\partial \mathbf{R}}{\partial a_i} \qquad \text{i.e.,} \qquad \tilde{\mathbf{J}}\frac{d\mathbf{u}}{da_i}^{k+1} = -\frac{\partial \mathbf{R}}{\partial a_i} - \mathbf{J}^d\frac{d\mathbf{u}}{da_i}^{k} \tag{6}$$

This can be rewritten to give the iterative solution method for DSA

$$\tilde{\mathbf{J}}\,\Delta\frac{d\mathbf{u}}{da_i}^{k} = -\frac{\partial \mathbf{R}}{\partial a_i} - \mathbf{J}\frac{d\mathbf{u}}{da_i}^{k} \qquad \text{with} \qquad \frac{d\mathbf{u}}{da_i}^{k+1} = \frac{d\mathbf{u}}{da_i}^{k} + \Delta\frac{d\mathbf{u}}{da_i}^{k} \tag{7}$$

In this way sensitivities can be calculated quite efficiently, reusing the factored matrix from the solution of the state variables. The iterations in Eq. (7) are performed until an acceptable small increment $\Delta\frac{d\mathbf{u}}{da_i}^{k}$ in sensitivities is obtained, see [11, 1, 8, 12].

In case of using one- and two-equation turbulence models, a segregated analysis and design sensitivity analysis scheme seems to be the most robust method and this will be presented.

Examples of Multidisciplinary Design Optimization

The implemented analysis and design sensitivity analysis facilities form the basis for gradient based optimization of structural, fluid flow, and fluid-structure interaction design problems. The optimization examples are solved by sequential linear programming (SLP) where the nonlinear optimization problem is transformed into a sequence of linearized subproblems. Several examples will illustrate the potential of the developed facilities for gradient based design optimization of strongly nonlinear multidisciplinary optimization problems.

Acknowledgments

This work was partly supported by the Danish Technical Research Council, project on “Interdisciplinary Analysis and Design Optimization of Systems with Fluid-Structure Interaction”.

REFERENCES

[1] O. Ghattas and X. Li Domain decomposition methods for sensitivity analysis of a nonlinear aeroelasticity problem. *Int. J. Comp. Fluid. Dyn.*, **11**, 113–130, (1998).

[2] K. Maute, M. Nikbay and C. Farhat. Analytically based sensitivity analysis and optimization of nonlinear aeroelastic systems. In *Proc. 8th AIAA/USAF/NASA/ISSMO Symposium on Multidisciplinary Analysis and Optimization, Long Beach, CA*, AIAA 2000-4825, 10 pages, (2000).

[3] D. C. Wilcox. *Turbulence modeling for CFD*, 2nd Ed. DCW Industries inc. (1998).

[4] F. R. Menter. Two-Equation Eddy-Viscosity Turbulence Models for Engineering Applications. *AIAA J.*, **32**:8, 1598–1605, (1994).

[5] A. N. Brooks and T. J. R. Hughes. Streamline Upwind/Petrov-Galerkin Formulations for Convecion Dominated Flows with Particular Emphasis on the Incompressible Navier-Stokes Equations. *Comp. Meth. Appl. Mech. Engng.*, **32**, 199–259, (1982).

[6] F. Ilinca, J.-F. Hétu and D. Pelletier. On Stabilized Finite Element Formulations for Incompressible Advective-Diffusive Transport and Fluid Flow Problems. *Comp. Meth. Appl. Mech. Engng.*, **188**, 235–255, (2000)

[7] H. Møller and E. Lund. Shape Sensitivity Analysis of Strongly Coupled Fluid-Structure Interaction Problems. In *Proc. 8th AIAA/USAF/NASA/ISSMO Symposium on Multidisciplinary Analysis and Optimization, Long Beach, CA*, AIAA 2000-4823, 11 pages, (2000).

[8] E. Lund, H. Møller and L. A. Jakobsen. Shape design optimization of steady fluid-structure interaction problems with large displacements. In *Proc. 42nd AIAA/ASME/ASCE/AHS/ASC SDM Conference, April 2001, Seattle, WA*, AIAA 2001-1624, 11 pages, (2001).

[9] J. Sobieszczanski-Sobieski. Sensitivity of Complex, Internally Coupled Systems. *AIAA J.*, **28**:1, 153–160, (1990).

[10] D. A. Tortorelli and P. Michaleris. Design Sensitivity Analysis: Overview and Review. *Inverse Problems in Engineering*, **1**, 71–105, (1994).

[11] V. M. Korivi, A. C. Taylor, P. A. Newman, G. W. Hou and H. E. Jones. An approximately factored incremental strategy for calculating consistent discrete aerodynamic sensitivity derivatives. *J. Comp. Physics*, **113**, 336–346, (1994).

[12] E. Lund, H. Møller and L. A. Jakobsen. Shape Design Optimization of Stationary Fluid-Structure Interaction Problems With Large Displacements and Turbulence. In *Proc. 4th World Congress on Structural and Multidisciplinary Optimization, June 2001, Dalian, China*, 6 pages, (to appear) (2001).

Optimization in Solid, Fluid and Bio-Mechanics

Thomas Borrvall, Anders Klarbring*, Joakim Petersson and Bo Torstenfelt
Department of Mechanical Engineering
Linköping University, Linköping, Sweden
e–mail: thobo@ikp.liu.se, andkl@ikp.liu.se, joape@ikp.liu.se, botor@ikp.liu.se

Matts Karlsson
Department of Biomedical Engineering and National Supercomputer Centre
Linköping University, Linköping, Sweden
e–mail: matka@imt.liu.se

ABSTRACT

Summary This document provides information on recent developments in topology optimization. Work in this area has almost exclusively been concerned with design of solids and structures. Here extensions to fluid mechanics, with applications in biomechanics, are given.

Optimization strategies are present everywhere in engineering and nature. When designing industrial products the designer tries out a sequence of designs in an attempt to gradually improve the product, i.e., even if not explicitly stated as such, an optimization is performed. In nature, evolution of biological systems follows paths that we can imagine are governed by an attempt to optimize some performance index. The mathematical paradigm that models optimization strategies in engineering as well as in nature is **Optimization with State Constraints (OSC)**.

The general form of an optimization problem with state constraints (a problem from OSC) is the following:

$$\begin{aligned} \min_{x,u} \quad & f(x,u) \\ \text{subject to} \quad & \begin{cases} \mathcal{S}(x,u) = 0 \\ g(x,u) \leq 0. \end{cases} \end{aligned}$$

Here f is the performance measure which is a function of two types of variables: the design variable x and the state variable u. The design variable is what can change when the industrial product or biological system is modified, and for each such design, the system will take on a certain state determined by the state variable. For a given design the state is defined by a mathematical system which we abstractly write $\mathcal{S}(x,u) = 0$ and call the analysis or state problem. This system will frequently be a partial or ordinary differential equation with its origin in continuum mechanics and is what is traditionally solved in computational engineering. The novelty of OSC is to surround this problem with an optimization goal. Finally, $g(x,u) \leq 0$ can represent any type of explicit constraints on the variables.

This talk will give several explicit examples of the above structure as well as discuss numerical procedures and present solutions. The most direct example of a problem from OSC, much studied within structural optimization, is the case of a truss structure, where u represents a displacement vector and x is a vector of cross-section areas of bars. The state problem, $\mathcal{S}(x,u) = 0$, takes the form

$$K(x)u = F, \tag{1}$$

where F is the prescribed load vector and $K(x)$ is the stiffness matrix, which will depend linearly on x. A frequently used performance measure is $f(x,u) = \frac{1}{2}F^T u$, which we interpret as the flexibility or the negative of the stiffness of the structure. One also easily concludes that this performance measure equals minus the equilibrium potential energy of the structure. Furthermore, it has the property that structures optimized by its use have uniformly distributed stress, implying that available material is used efficiently. This type of structural optimization is usually called topology optimization since trusses can be excluded from the optimal design by letting $x \approx 0$ and in this way an optimal connection or topology is found.

The continuum analogy of the truss topology optimization problem is when $\mathcal{S}(x,u) = 0$ represents the equations of linear elasticity. The problem then becomes substantially more complicated. In fact, a naive extension results in a non-well posed problem which lacks a solution. To remedy this, different types of regularisations are possible, as extensively discussed by Borrvall [1]. Furthermore, how to obtain a stable finite element discretization is not obvious and certain similarities with mixed finite elements in, for instance, Stokes flow exist. In Figure 1 a large-scale continuum topology optimization problem is shown.

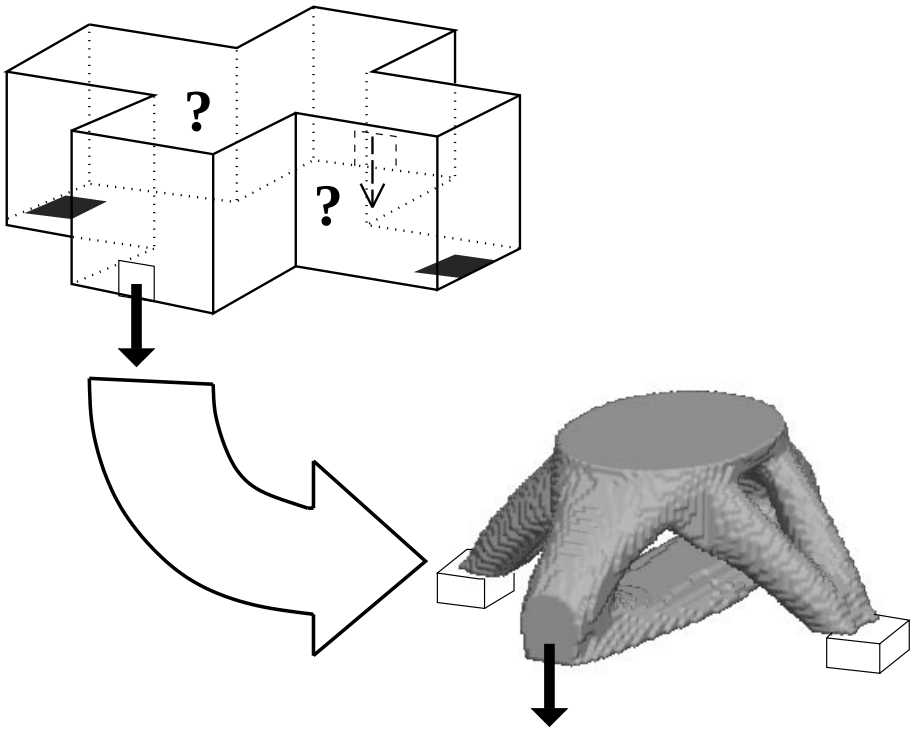

Figure 1: A continuum topology optimization problem. The cross-shaped domain should be partly filled by a prescribed amount of material to obtain an as stiff structure as possible.

Recently our attention was drawn to a series of papers (see, e.g. Karch et al. [2]) on modeling of arterial vascular trees, e.g. the corona artery in humans. Here a method based on optimality reasoning (but in our view, without formulating a clear overall goal in the sense of OSC) for constructing arterial trees is given. We almost immediately realized the possibility of transferring our

knowledge in truss topology optimization to this domain. Indeed, a very close analogy can be constructed: the stiffness objective becomes the objective of minimizing power losses for a prescribed flow; in the state problem, equation (1), u plays the role of pressure and F represents prescribed outflows of fluid. The stiffness matrix becomes a matrix representing fluid flow resistance, which if Hagen-Poiseuille flow is assumed will depend on the second power of cross-sectional areas, and, thus, not linearly as in the truss case. In Figure 2 an example of arterial tree optimization is shown.

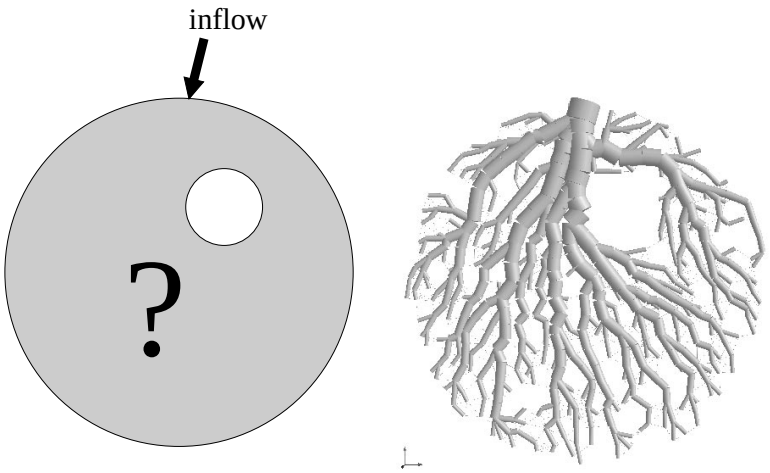

Figure 2: An optimal arterial tree problem: inflow and outflow is prescribed; the tree represents that of minimum pressure loss.

The next natural extension of this line of research is to do topology optimization in the fluid continuum case. The goal is to determine at what places of a predetermined design domain there should be fluid or not (i.e. solid) in order to extremize a power objective and subject to a given amount of fluid. Possible applications include design for minimum head loss in pipe bends, diffusers and valves, optimal conceptual design of air flow channels in aerial vehicles, as well as design of submerged bridge pillars for minimum environmental impact on watercourse flows. The state equation is in computations so far taken to be Stokes system governing very viscous flow. An example is shown in Figure 3.

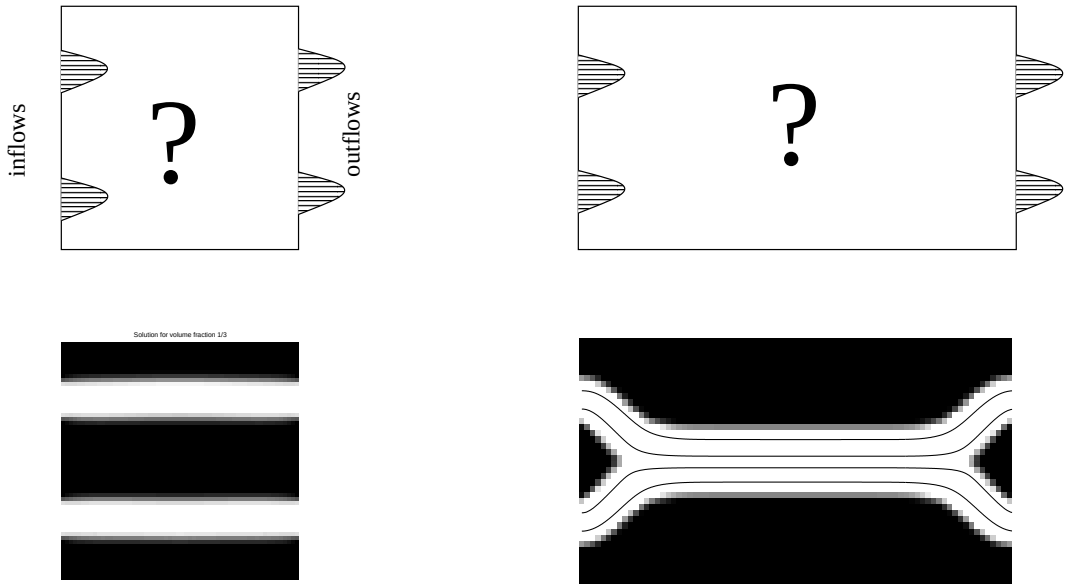

Figure 3: The system of channels giving minimum pressure loss for prescribed in- and out-flow is found. It is concluded that the length of the domain influences the topology.

REFERENCES

[1] T. Borrvall. *Computational Topology Optimization of Elastic Continua by Design Restriction.* Linköping Studies in Science and Technology. Thesis No. 848, (2000).

[2] R. Karch, F. Neumann, F. Neumann and W. Schreiner. A three-dimensional model for arterial tree representation, generated by constrained constructive optimization. *Computers in Biology and Medicine*, **29**, 19-38, (1999).

Adaptive FE-methods in Computational Mechanics Based on Variationally Consistent Postprocessing

Trond Kvamsdal*

Department of Computational Engineering
SINTEF Applied Mathematics, Trondheim, Norway
e–mail: Trond.Kvamsdal@math.sintef.no

Hallgeir Melbø

Department of Mathematical Sciences
Norwegian University of Science and Technology, Trondheim, Norway
e–mail: hallgeir@math.ntnu.no

ABSTRACT

Summary Mechanical work corresponds to an inner-product between (dual or) work conjugate quantities such as displacements and point-forces, displacements and surface tractions, strains and stresses. This can be utilized to recover stresses and stress resultants that obey the principle of virtual work, i.e. that are variationally consistent. Local pointwise error estimates of the recovered quantities and related refinement indicators are provided by solving a related (dual) adjoint problem.

1 Mathematical formulation

In many applications the primary aim of a finite element (FE) analysis is to obtain few design quantities with a prescribed accuracy. In computational mechanics quantities such as stresses, surface forces and surface force densities (surface tractions) are often important for design decisions. Thus special attention should be paid to how the FE model is adapted for computation of such quantities, and to which techniques that are used to extract these quantities from the primary FE results.

Herein, we present a general concept for adaptive postprocessing of FE results, developed by Kvamsdal [1, 2] for strucutral mechanics and futher explored for the Stokes problem in [3]. The presented concept fits into the very general postprocessing approach introduced by Babuška and Miller [4]. However, the specific choice of function space made herein for the extraction functions closely relates the postprocessing steps to the underlying FE method. This choice of extraction function space makes the presented approach unique.

Mechanical work or energy may be viewed as the product between a 'force' and its dual quantity of 'displacement type'. The 'force' can be point forces, $\boldsymbol{F}(\boldsymbol{x}_a)$, defined for a set of points Υ, a surface traction field, $\boldsymbol{t}(\boldsymbol{x}, \boldsymbol{n}_\Gamma)$, defined on a surface Γ, or a stress field, $\boldsymbol{\sigma}(\boldsymbol{x})$, defined in a body Ω. The dual quantities for these 'forces' are, respectively, $\boldsymbol{v}(\boldsymbol{x}_a)$, representing the displacement of the points $\boldsymbol{x}_a$, $a \in \Upsilon$, $\boldsymbol{v}(\boldsymbol{x})$, representing the displacement of the surface Γ, and $\boldsymbol{\varepsilon}(\boldsymbol{x}) = \mathbb{D}\boldsymbol{v}$, representing the strain field in the body Ω.

In a mathematical setting, mechanical work corresponds to an inner product between (dual or) work conjugate quantities $\boldsymbol{\nu} \in X$ and $\boldsymbol{\tau} \in Y$ defined on $D \subset \mathbb{R}^2$:

$$W(\boldsymbol{\nu}, \boldsymbol{\tau}; D) \;=\; (\boldsymbol{\nu}, \boldsymbol{\tau})_D \tag{1}$$

Hence, we may interpret the mechanical work functional, W, as a bilinear operator (or bilinear form), i.e. a mapping from $X \times Y$ into $\mathbb{R}$. On the other hand, for a given 'force' $\boldsymbol{\tau}$ we may interpret the same functional as a linear form mapping the 'displacement' space X into $\mathbb{R}$.

In Variationally Consistent Postprocessing (VCP) we relate linear work functionals corresponding to a given set of point forces, $\boldsymbol{F}$, surface tractions, $\boldsymbol{t}$, and stresses, $\boldsymbol{\sigma}$, to the relevant forms involved in the finite element problem. Let the quantity of interest be denoted $R(\boldsymbol{u})$, where $\boldsymbol{u} \in V(\Omega)$ is the unknown analytical solution of the underlying infinite dimensional variational problem. The VCP procedure may then be viewed upon as an extraction procedure of the following operator form:

$$R(\boldsymbol{u}) = a^h(\boldsymbol{w}, \boldsymbol{u}) - f_{\mathrm{R}}^h(\boldsymbol{w}) \tag{2}$$

Here, $V^h(\Omega) \subset V(\Omega) \subset H^1(\Omega))$, $\boldsymbol{w} \in X^h(\mathcal{M})$ is an extraction function for a quantity R, $X^h(\mathcal{M})$ the broken displacement space is defined through $X^h(\mathcal{M}) = \{v \in L_2(\Omega) : v|_{\Omega_e} \in X^h(\Omega_e)\}$, where the FE-displacement space $X^h(\Omega)$ is equal to $V^h(\Omega$ but with no boundary conditions taken into account, $a^h(\cdot,\cdot) : X^h(\mathcal{M}) \times X^h(\mathcal{M}) \to \mathbb{R}$ is the mesh dependent bilinear form (see definition in [2]) which for a given $\boldsymbol{w}$ becomes a linear form for $\boldsymbol{u}$, and $f_{\mathrm{R}}^h(\boldsymbol{w})$ is a mesh dependent linear form, assumed independent of $\boldsymbol{u}$. [1] Let $D \subset \Omega$ be a domain equal to a patch of elements, and assume that $\boldsymbol{w} \equiv \boldsymbol{0}$ on $\Omega \setminus \overline{D}$.

As $\boldsymbol{u} \in V(\Omega)$ is the unknown analytical solution we actually do the the VCP by inserting the FE approximation $\boldsymbol{u}^h$ to obtain the recovered quantity $R(\boldsymbol{u^h})$ (also denoted R^{VW}):

$$R(\boldsymbol{u^h}) = a^h(\boldsymbol{w}, \boldsymbol{u^h}) - f_{\mathrm{R}}^h(\boldsymbol{w}) \tag{3}$$

Taking the difference between the extraction formula using the exact solution $\boldsymbol{u}$, se Equation (2) and the the FE approximation $\boldsymbol{u}^h$ given in Equation (3) the error in the recovered quantity $R(\boldsymbol{u^h})$ reads:

$$e_{\mathrm{R}} \;=\; R(\boldsymbol{u}) - R(\boldsymbol{u}^h) \;=\; a^h(\boldsymbol{w}, \boldsymbol{u} - \boldsymbol{u}^h) \tag{4}$$

The expression in Equation (4) may be used to estimate the error in the recoverd quantity. Note that as $\boldsymbol{w}$ is known (i.e., given for each particular extraction functional) whereas $\boldsymbol{u}$ is unknown, $\boldsymbol{u} - \boldsymbol{u}^h$ have to be estimated.

To obtain an error norm with global support (which is needed for adaptive refinement) we introduce the following *dual problem:*
Given any $\boldsymbol{w} \in X^h(\mathcal{M})$ then find $\boldsymbol{z} \in V(\Omega)$ such that for all $\delta\boldsymbol{z} \in V(\Omega)$ we have:

$$a(\boldsymbol{z}, \delta\boldsymbol{z}) \;=\; a^h(\boldsymbol{w}, \delta\boldsymbol{z}) \tag{5}$$

The corresponding *dual FE problem* reads:
Given any $\boldsymbol{w} \in X^h(\mathcal{M})$ then find $\boldsymbol{z}^h \in V^h(\Omega)$ such that for all $\delta\boldsymbol{z}^h \in V^h(\Omega)$ we have:

$$a(\boldsymbol{z}^h, \delta\boldsymbol{z}^h) \;=\; a^h(\boldsymbol{w}, \delta\boldsymbol{z}^h) \tag{6}$$

Using Equation (5) and (6), the (Galerkin) energy orthogonality of the bilinear form $a(\cdot,\cdot)$ and the fact that $a^h(\cdot,\cdot) \equiv a(\cdot,\cdot)$ on $V(\Omega) \times V(\Omega)$ we obtain:

$$e_{\mathrm{R}} \;=\; a(\boldsymbol{z} - \boldsymbol{z}^h, \boldsymbol{u} - \boldsymbol{u}^h) \tag{7}$$

where $\boldsymbol{v}^h \in V^h(\Omega)$ is found by solving Equation (6).

[1] In some cases the FE boundary tractions, $\boldsymbol{t}^{\mathrm{el}}$, are present in $f_{\mathrm{R}}^h(\boldsymbol{w})$, i.e. $f_{\mathrm{R}}^h(\boldsymbol{w})$ is indeed dependent on $\boldsymbol{u}$.

2 Numerical example

Figure 1a) shows a L-shaped linear elastic domain subjected to a symmetric (Mode 1) loading. The analytical stress distribution for this plane strain problem may be found elsewhere.

Here we aim for computing the shear stress σ_{xy} at the point with coordinates $(25, 25)$. Origo is assumed to be located at the lower left corner. This problem has a singular point at the interior corner with strength $\lambda = 0.544$. Therefore, the rate of convergence when using uniform mesh refinement is not second order. However, by means of adaptive mesh refinement the pollution error may be controlled and second order accuracy may still be achieved.

The purpose of this numerical experiments is to verify that the developed adaptive recovery technique is actually capable to control the pollution error, Thus, we restrict ourselves to compute the element mean shear stress for the element with the point $(25, 25)$ in its interior, since by means of variationally consistent nodal patch recovery we may restrict the local interpolation error to be of the desired order.

Using VCP to recover element mean stress corresponds to solving a dual problem with loads equal to a weighted sum of the nodal forces along the boundary of the specified element. For any finite element size h the dual problem will be well posed.

We have performed an adaptive analysis using the (weighted) energy norm described above with a prescribed tolerance of $\overline{\eta} = 1.0\%$ for the error in the element mean shear stress. The error in the stresses $\boldsymbol{\sigma}^h$ is estimated by means of the Superconvergent Patch Recovery method, and the calculation of refinement indicators for mesh adaption (h-refinement) follows the procedure developed by Kvamsdal [2]. Now, the prescribed accuracy is reached after five adaptive mesh refinements and the resulting mesh sequence is presented in Figure 1c).

From the results presented in Figure 1b) we see that 'optimal' order of convergence, which for bilinear elements are $O(h^2)$, is obtained using the VCP procedure. Furthermore, the effectivity index for the estimated error is relative close to one.

REFERENCES

[1] T. Kvamsdal. Postprocessing of finite element results based on virtual work. In *Proceedings of Second ECCOMAS Conference on Numerical Methods in Engineering*, pages 284–290, Paris, France, September 9–13 1996.

[2] T. Kvamsdal. Variationally consistent postprocessing (VCP). In E. Oñate and S. R. Idelsohn, editors, *COMPUTATIONAL MECHANICS—New Trends and Applications*, pages CD–rom. CIMNE, Barcelona, Spain, 1998.

[3] H. Melbø and T. Kvamsdal. Goal oriented error estimators for Stokes equations based on Variationally Consistent Postprocessing. *Submitted to Computer Methods in Applied Mechanics and Engineering*, September 2001.

[4] I. Babuška and A. Miller. The post–processing approach in the finite element method—Part 1: Calculation of displacements, stresses and other higher derivatives of the displacements. *International Journal for Numerical Methods in Engineering*, 20:1085–1109, 1984.

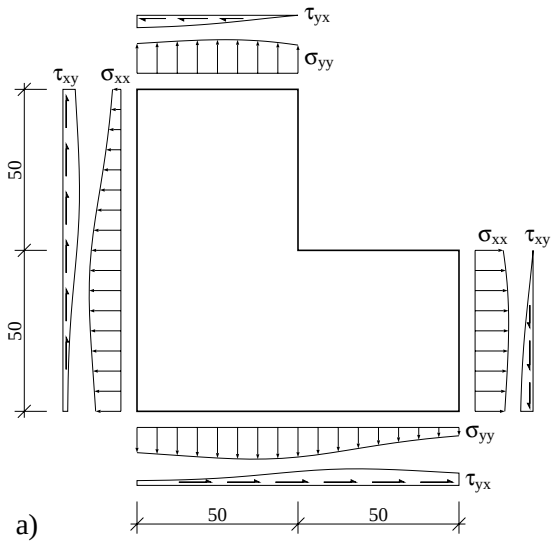

a)

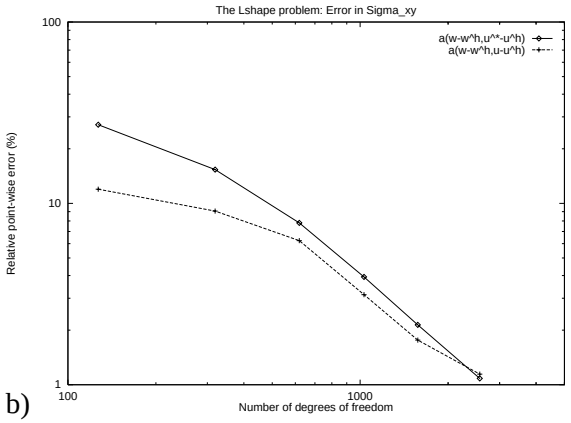

b)

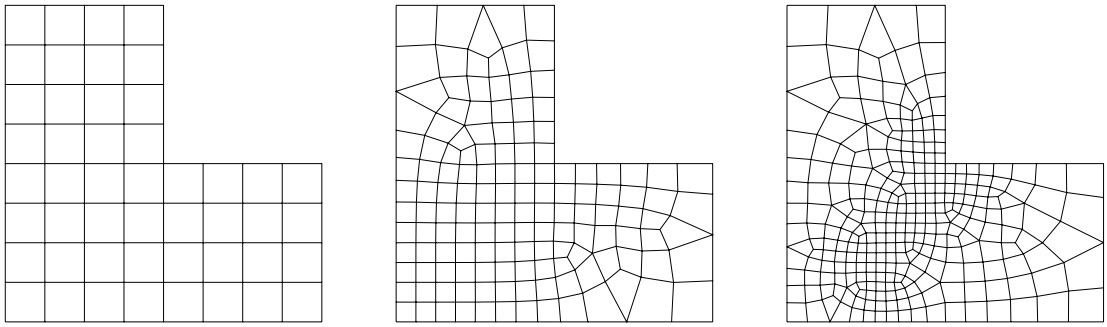

Mesh 0 : 48 elements
Error : 20.76%

Mesh 1 : 138 elements
Error : 15.25%

Mesh 2 : 284 elements
Error : 11.28%

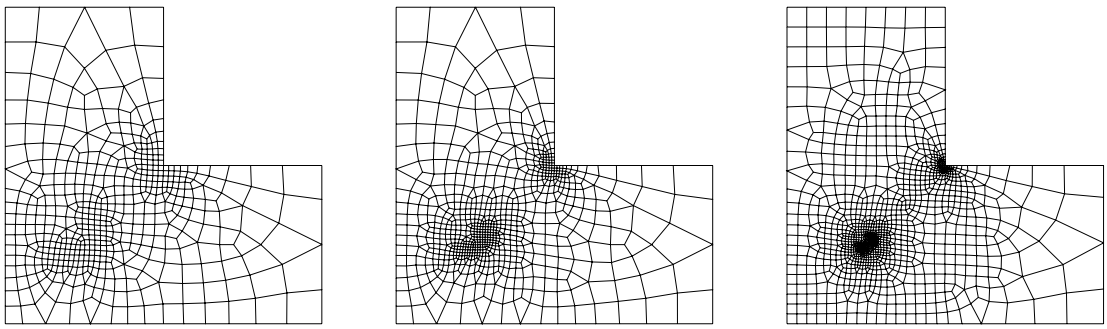

c)

Mesh 3 : 486 elements
Error : 8.70%

Mesh 4 : 756 elements
Error : 6.96%

Mesh 5 : 1241 elements
Error : 5.48%

Figure 1: The L-shape problem: a) Geometry and properties. b) Estimated and exact error in recovered element mean shear stress σ_{xy} for the element containing the point (25,25). c) Adapted finite element mesh sequence.

NUMERICAL SIMULATION OF ICE-INDUCED VIBRATIONS IN OFFSHORE STRUCTURES

Mauri Määttänen
Department of Mechanical Engineering
Helsinki University of Technology
mauri.maattanen@hut.fi

ABSTRACT

As moving ice fails against an offshore structure the resulting ice load is not constant. An evident reason for ice load fluctuations is the variation of oncoming ice properties. Transient loads are also caused by ice edge, floe or iceberg hitting the structure. Normally ice load fluctuations are resulting from a more or less random ice failure process. However the most severe dynamic ice load scenario can occur even though ice properties and ice velocity would be constant. Under certain conditions the ice failure becomes coupled with the dynamic response of the structure. Initially independent local ice failures at different locations at contact zone are likely to synchronise. The worst conditions are a resonance with one of the lowest natural modes. This paper gives a review of dynamic ice action scenarios, and methods to predict dynamic ice loads by numerical simulation. Such capabilities are dearly needed in near future while the projected offshore wind energy is being realised in Northern Europe.

1. INTRODUCTION

Adverse vibrations due to moving ice crushing against offshore structures were first reported in Cook Inlet oil drilling structures /2,25/. In Finland first experiences with single steel pile foundations for lighthouses in 1973 were disastrous. Severe resonant vibrations destroyed their superstructures during the first winter /16/. At Bohai Sea Chinese oil production platforms with jacket foundations were also damaged due to dynamic ice loads, /31,32/. Common to all these structures was that the construction included relatively narrow and flexible components that were directly under ice action. The opposite case was Molikpaq, an arctic caisson retained island, that is wide and very stiff structure. This drilling platform is a double walled steel ring, diameter 111 m, height 30 m, having the centre part filled with sand that enhances sliding resistance and damping capability. In 1986 while a multiyear ice floe was moving and crushing against the caisson, the whole structure vibrated continuously. Due to vibrations the pore pressure in the soil increased and the whole structure was close to be displaced /6/.

The problem of ice-induced vibrations in slender flexible structures that have to withstand the loads of moving ice fields has been under research over three decades but still a debate on the origin of vibrations continues. The main question is why the ice force is fluctuating periodically even though a constant thickness homogeneous ice field is moving at constant velocity and crushing against a vertical structure.

A number of approaches have been presented to predict dynamic ice loads during ice crushing /2,3,9,10,11,12,17,23,25,27,30,32/. If the loads are known then it is a straightforward process to numerically solve the dynamic equations of motion and to predict structural response. This kind of forced vibration analysis can readily be used to calculate transient response due to ice edge impacts or iceberg hits. Uncertainties come from assumptions on ice crushing pressure dependence on changing contact area and aspect ratio.

Theoretical explanations for dynamic ice structure interaction are based on forced or self-excited vibration models. In the former, ice is having a characteristic failure frequency, or ice is fractured into floes of certain size /25,23,11,13,28/. Hence ice force build-up and failure frequency is directly proportional to ice velocity. The interaction ice force depends only on the advancement of ice sheet. Ice force history is then known a priori when the ice velocity is known. If the dynamic response of the structure is insignificant there is no dynamic interaction, only dynamic reaction forces. A mechanical model for this kind of an interaction can be presented by breaking brittle cantilevers, Matlock /11/. In his model a moving chain of brittle elastic beams simulate ice contact. As a beam contacts the structure the load build-up is linear until the beam breaks and load returns to zero until a next beam makes the contact. “Ice” velocity controls the load build-up rate and the beam strength maximum load. The spacing of beams and ice velocity determine the load frequency. Matlock's model presents a predetermined forced vibration problem that well simulates the low ice velocity saw-tooth ice load history, and even the onset of a resonance condition but not the change into random response with further increasing ice velocity.

No physical reasoning exist to support characteristic ice failure length in crushing. Only in ice bending failure, the characteristic length of an elastic plate on Winkler foundation determines the size of broken floes. Indeed, at high ice velocities bending failures can excite a structure into resonance as has been witnessed in China, /33/.

In the self-excited ice-induced vibration model /2,17,22,30,32/, the interaction ice force is dependent on the dynamic response of the structure at the ice action point with no a priori known ice force time history. The model observes the dependence of ice strength on varying loading rate. Hence the feed-back - or coupling - variable is the dynamic response velocity. The system is autonomous and the only chance for vibrations to occur is then that the system is dynamically unstable, which yields to limit cycles in self-excited vibrations. An autonomous vibration system is one in which dynamic response and the interaction force originates from the system itself without need to know beforehand any loading history.

Scale model tests /18/ have indicated that the frequencies of natural modes of the structure control ice failure frequencies at a wide velocity range. Hence a lock-in to the natural mode frequency takes place. Thus in a multi-legged or wide structure independent ice failures at different locations are likely to synchronise. This is due to vibration velocity of a natural mode superimposing to the ice velocity, which promotes coherent ice failures at different locations.

A numerical model to simulate dynamic ice-structure interaction and ice-induced vibrations should be able to predict different velocity dependent ice failure patterns, saw tooth like at low ice velocities, frequency lock-in and synchronisation at increasing ice velocity, and random at high ice velocity. Both Sodhi /28/ and Määttänen /21/ give a review of different ice-structure interaction models. Thereafter further models have emerged that also observe multi-point ice load excitation /9,10,22/. Only the last represents results on predicted frequency lock-in and ice failure synchronisation.

This paper gives background information on such ice mechanics parameters that have significant effect on ice-structure interaction, and describes different approaches for numerical models. A brief description is given on ice impact loads. Vibrations that are caused by random variations of ice thickness, strength, etc. are not treated here. The presented self-excited model is based on ice crushing strength dependence on loading rate. The original model with single point ice action for beam structures has been used to predict ice-induced vibrations in Finnish steel lighthouses /20/, and later expanded for any three dimensional structure with multi-point ice excitation /22/. The theory behind the model is briefly described. Application examples are presented for both a multi-legged and a wide offshore structure to demonstrate the simulation

capabilities for varying ice thickness and velocity cases. Also ice-induced vibration analysis for offshore wind turbine foundations are discussed.

2. ICE MECHANICS BACKGROUND

Ice-structure interaction implies that both the ice and the structure are active partners. In the case of a rigid structure, the only contribution of the structure to ice failure process is the shape of the structure at the contact zone. Ice load fluctuations against rigid structures are caused by the properties of ice alone. Subsequent ice edge flaking failures is one explanation, tendency to fail into floes of certain size another, but also the dynamic response in the ice field together with the ice strength sensitivity to strain rate can contribute to resulting interaction ice force fluctuations. Instead of interaction a better expression in the case of a rigid structure would be ice action against a structure.

In the case of a flexible structure, the dynamic response of the structure plays an active role with the force originating from the ice failure process. Hence all structural properties, shape at the contact zone, stiffness, mass and damping will have their effect on the interactive forces between the ice and the structure. The distinction between a rigid or flexible structure is arbitrary, however. Even a solid rock undergoes elastic deformations when loaded by ice action. Also the ice field itself undergoes elastic deformations. From the practical point of view a structure can be considered flexible when its displacements are significant when compared to ice elastic deformations, e.g. of the same order as the ice grain diameter.

In dynamic ice structure interaction energy from the moving ice is being transferred and stored as elastic energy in the structure. After ice failure and at structural spring back phase stored energy is released. It is converted into breaking ice and into kinetic energy. Energy exchange implies also dynamic response to occur, either in the structure, in ice, or in both. As ice strength is strongly dependent on loading rate, dynamic response will alter the average loading rate, and hence interaction forces. Ice failure will occur at high loading rate with low ice strength, and load build up at low loading rate with high ice strength. This yields to the synchronisation of ice failure and structural response. It is more pronounced with flexible structures that exhibit significant displacements at the ice action point. Of course the stored kinetic and elastic energy in the ice cover itself can also activate and control ice crushing.

Ice velocity is the governing parameter in the character of ice load history. Velocity effects express themselves in stress or strain rate, which has a strong effect on the interaction ice force. Hence it is imperative to observe the relative velocity, which is a difference of ice edge and structure contact point velocities. At very low ice velocities, e.g. thermal expansion, ice behaviour is ductile and ice-structure interaction resembles viscous flow. Ice load is pseudo static. Ductile deformation may include cracking effects.

With increasing velocity cracking activity increases when interaction time becomes too short for ice stresses to be relaxed and bounded by creep. A damaged ice zone is forming. Ice load and stresses, as well as structural deflection build up until ice compressive strength level is reached. Ice starts to break into floes and small fragments. In certain conditions ice is practically being pulverised. The clearing mechanism of broken ice mass with ice floes or fragments are different to that of pulverised ice: the former pops out "explosively" while the latter is extruding. As ice major failure occurs the load level drops suddenly, and the deflection of the structure springs back. Often the spring-back stroke exceeds the zero state causing a gap between the ice edge and the structure. Thereafter the advancing ice edge makes contact to the structure and a new load cycle starts. This produces a saw tooth like ice force or displacement history.

At higher velocities the response history will gradually change. The frequency of ice failures increases with ice velocity until at a certain velocity range a natural mode of the structure may start to control the ice failure frequency: a lock-in resonant state occurs. At still higher ice velocities conditions for the resonance are lost. Ice failure turns into totally brittle and ice load fluctuations random. Stress or strain rate is directly proportional to relative velocity between ice and structure. It is at the transitional strain rate range from ductile to brittle, 10^{-3} - 10^{-2} 1/s, or stress rate around 0.2 - 0.6 MPa/s, where self-excited vibrations are most pronounced, Fig. 2.

Recent studies have found out how the actual ice failure is occurring at high loading rates. Studies by using high speed photographic techniques and transparent structure wall /7/, or tactile sensors /1,5/, indicate that there is only a narrow "contact line", in which high interaction pressure is acting and crushing the ice, while the rest of the contact zone is involved only in the clearing mechanism.

3. BASIC DYNAMIC ICE STRUCTURE INTERACTION MODEL

A schematic model of ice interaction with structures has three elements: structure, ice failure process, and ice sheet, Fig. 1. For the structure and ice there are well known governing differential equations, dynamic equations of equilibrium. The two interacting bodies are connected by the centre element, the ice failure process, which includes clearing mechanisms of broken ice mass. Also the conditions of continuity have to be taken care of in the centre element.

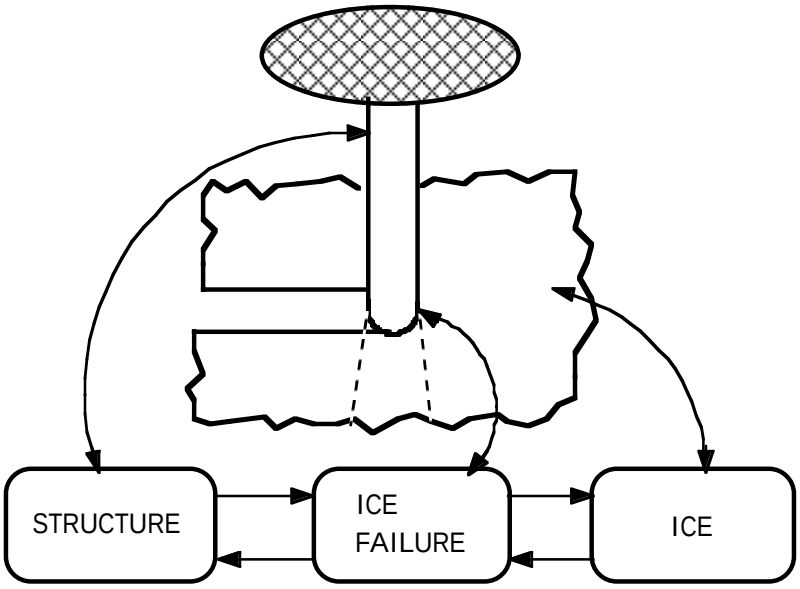

Figure 1. Elements in ice interaction with structures.

A schematic mathematical model of ice interaction with structures, Fig. 1, can be formulated with two coupled equations of equilibrium, Eq. 1 and 2,

$$[k]\{\delta\}+[d]\{\dot{\delta}\}+[m]\{\ddot{\delta}\}=\{f(\delta,\ \dot{\delta},\ \ddot{\delta},\ \Delta,\ \dot{\Delta},\ \ddot{\Delta},\ t,\ V)\} \quad (1)$$

$$[K]\{\Delta\}+[D]\{\dot{\Delta}\}+[M]\{\ddot{\Delta}\}=\{F(\delta,\ \dot{\delta},\ \ddot{\delta},\ \Delta,\ \dot{\Delta},\ \ddot{\Delta},\ t,\ V)\} \quad (2)$$

which represent the governing differential equations of the structure and ice in a discretized form. Symbols $\{\delta\}$ and $\{\Delta\}$ stand for the displacement vectors of the structure and ice, dot above means derivation in relation to time t giving velocities and accelerations, [k], [K], [d], [D], [m], and [M] are stiffness, damping and mass matrices respectively, V is the nominal ice velocity. The coupling is through non-linear functions {f} and {F} that describe interaction forces from the structure to ice failure process, and from ice failure process to the ice sheet.

Most problems could be analysed by means of computational mechanics if a mathematical model could correctly present all elements in Fig. 1. The main difficulty is in the ice constitutive model: elastic, viscous, and plastic behaviour including cracking should be modelled in three dimensions. Interaction forces in Eq. 1 and 2 are not known beforehand, they depend on the state of the system. The most common approach is to assume an interactive forcing function, which enables to separate the two systems. Physical interpretation of Eq. 1 is then ice with no response, and of Eq. 2, an infinitely rigid structure.

There are many simplifications in modelling ice behaviour and failure. The non-linear visco-elasto-plastic constitutive equations of ice are linearised and/or replaced by a simple constitutive law, which considers only one effect to be significant. This way it is possible to have a linear elastic material model for fast loading cases, reference stress method for slow loading cases, ideal plastic behaviour for limit load analysis, etc. Kärnä /9/ observes the ice behaviour at two scales: near field that observes ice damage, failure and extrusion during clearing, and far field that observe elastic only response including radiation damping.

Structural damping is important in suppressing ice-induced vibrations. In scale model, and full scale tests, it has been measured, that with a sufficiently high internal damping in the structure, resonant type self-excited vibrations can be totally avoided /20/.

Time is significant in two cases: if there is a characteristic failure frequency in the ice and if loading rate is so low that visco-plasticity becomes important. The latter can be considered insignificant if crushing frequency is higher than about 0.5 Hz, which is the normal case. When the ice failure occurs within a few seconds from the beginning of load build up, the ice failure is dominantly brittle with only an insignificant time dependent creep in the ice deformation response.

The effects of relative distance between the ice edge and the structure are also important. When there is a gap, the ice force is zero regardless of relative velocities. During crushing, normally more ice is crushed than the elastic rebound of the structure. During load build-up the uneven ice edge is being smoothened and there is some elastic indentation into the ice as well. All these displacement contributions have to be observed in the vibration model.

4. ICE IMPACT

The impact of ice against structure has different scenarios: transients during ice sheet edge hitting, splitting of floes, pushing aside floes, growler or iceberg impacts. These load cases are decisive in high arctic but of minor importance in the Baltic compared to resonant type crushing loads.

If a sufficiently large ice sheet is moving and its edge hitting a structure there will be a short duration transient after which continuous ice structure interaction will establish according to previous models. During the transient phase initial load build-up may induce higher dynamic response to the structure than in the continuous phase. If the laws for ice load build-up can be assumed, the calculation of dynamic response is straightforward. Typically dynamic amplification in the transient is less than twofold from that of the static loading. If a resonant

loading in dynamic ice structure interaction is possible, its dynamic amplification is much higher due to inherently low damping of structures.

Splitting of a small floe during an impact occurs easily. The interaction is just to initiate splitting. Theoretical models based on force equilibrium /13/ and on fracture mechanics /26/, explain the low load levels needed for splitting the ice. The latter model explains also the splitting of floes with a diameter of several kilometres.

The hit of an floe is rarely symmetric. Asymmetric contact causes the floe to rotate and then being pushed aside the structure. Interaction forces can be calculated according to laws of conserving energy and momentum /24/. The hit of a growler or iceberg can be treated like hit of an floe. However more emphasise is now in the load build-up history. It is dependent on the velocity, the size of contact area, and on aspect ratio. The velocity can be calculated from the energy balance and the rest from the geometry of impacting bodies /24/. An important factor is ice strength dependence on the contact area /26/.

5. SELF-EXCITED ICE-STRUCTURE INTERACTION MODEL

The first to propose self-excitation as the origin of ice-induced vibrations was Blenkarn /2/ who defined the dynamic stability condition for a single degree of freedom system. He used the concept of negative damping, which can be derived from the decreasing ice force versus loading rate.

Määttänen /17/ extended Blenkarn's model for a multi degree of freedom system and solved a stability condition for each natural mode of the structure. By using ice strength versus stress rate dependence as a starting point, limit cycles were also solved by numerical integration. Relative displacement effect was observed for gaps. Saw-tooth like ice force histories could be derived directly from the physical properties of ice and the structure without any a priori assumptions on time dependent ice forcing function. Ice force frequency lock-in with unstable natural modes is correctly predicted. A simple equation to predict the dynamic stability of a natural mode (sensitivity to ice-induced vibrations) and the frequency of saw tooth ice force frequency at low velocities was derived. Theoretical predictions were in good agreement with both scale model and full scale measurement data.

The structure is discretized by using Finite Element Method. Ice interaction is observed as a nodal load in those nodes that are under ice action. Ice load is simply ice crushing strength times the area that is controlled by the node in question. The crushing strength is dependent both on contact normal velocity and contact area.

$$\sigma_c = \sigma_c(v - \dot{u})\sqrt{\frac{A_0}{A}} \tag{3}$$

Ice crushing strength against a wide structure is reduced according to the area dependence as defined by Sanderson /26/. Relative velocity at a contact node is ice velocity v minus nodal displacement velocity du/dt. Crushing strength dependence on relative velocity is based on the stress rate as defined by Blenkarn

$$\dot{\sigma} = (v - \dot{u})\frac{8\sigma_0}{\pi d} \tag{4}$$

Here σ_0 is reference strength, now 2 MPa is used, and d the diameter of the structure. Equation 4 was originally intended for narrow structures and is not directly applicable for wide structures.

However, if non-simultaneous ice failure at different zones along the width of the structure is assumed a realistic value for d can be used. There is no definite answer for the width of an independent zone. E.g. a value of one or two times the ice thickness can be chosen. The effect of width d in the denominator is to scale velocity range. Thus ice velocity dependence comparisons can be made regardless of the correct width. In the following applications the real leg diameter is used for the multi-legged structure and d=1 m for the wide structure.

Based on the measurement data /25,2/, and combining Eq. 3, ice crushing strength vs. stress rate, is approximated by using a fourth degree polynomial,

$$\sigma_c = (2.00 + 7.80\dot{\sigma} - 18.57\dot{\sigma}^2 + 13.00\dot{\sigma}^3 - 2.91\dot{\sigma}^4)\sqrt{\frac{A_0}{A}}\ MPa \qquad (5)$$

in which $\dot{\sigma}$ is given in MPa/s and the reference area A_0=1 m^2. The polynomial part covers ice failure mode transition from ductile to brittle. At higher strain rates ice failure is brittle and strength is assumed to be constant, Fig. 2. At very low loading rate the ice behaves as a viscous fluid. However, as now the load build-up time is short, in order of a second or less, the viscous deformations in ice can be omitted. In reality there are always random variations in ice strength, now especially at the decreasing part. Hence the whole curve should be interpreted as a deterministic average presentation on ice crushing strength.

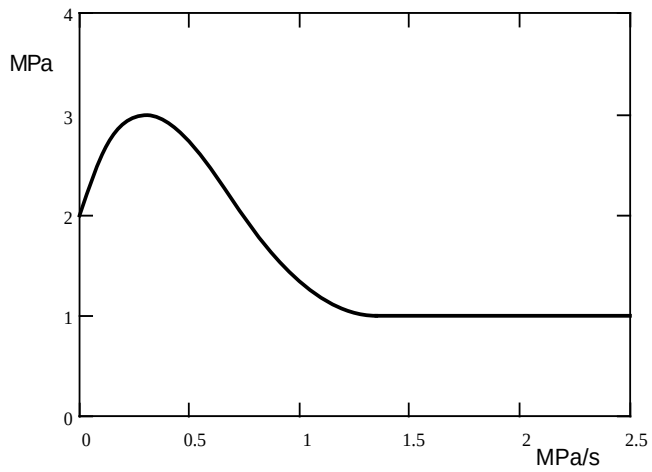

Figure 2. Ice crushing strength vs. stress rate.

Implementing ice crushing strength by Equation 4 and 5 into nodal loads in the dynamic equations of motion for the whole structure, Eq. 1 with δ replaced by u, yields

$$[k]\{u\} + [d]\{\dot{u}\} + [m]\{\ddot{u}\} = \{F(v,\{\dot{u}\})\} = \{F_0\} + [\phi]\{\dot{u}\} \qquad (6)$$

where [k], [d], and [m] are the stiffness, damping and mass matrices of the structure, $\{u\}$, $\{\dot{u}\}$, and $\{\ddot{u}\}$ are the nodal displacement, velocity and acceleration vectors. $\{F_0\}$ is the constant part of the load vector representing ice strength at the nominal stress rate corresponding to ice velocity v. Matrix [ϕ] has nonzero terms only at its diagonal corresponding to ice action nodes and resulting from the structural response velocity according to Equation 4 and 5. Each ice action node has its own ice load, which is independent from others. The coupling plays role only through the combined effect of all nodal loads to displacement and velocity response.

In initial state the structure is at rest with no vibrations. As both $\{\dot{u}\} = \{\ddot{u}\} = \{0\}$ only static displacements are caused by the loads $\{F_0\}$. In order to have vibrations the ice-structure system has to be dynamically unstable. Mathematically the autonomous system of equations 6 has then roots that have positive real part and make deviations from the equilibrium to grow with time.

This means that if there are any disturbances they tend to grow dynamically and develop into vibrations or into an aperiodic divergence. Considering the shape of the controlling curve, (Fig. 2), it is evident that disturbances will not grow without bounds but the vibrations have to develop into stable limit cycles. The reason is that energy is being pumped into the structure only at the decreasing part of Figure 2. Then with increasing vibration amplitudes increasing structural damping will eventually dissipate all the energy that is fed into system during each vibration cycle.

The Eq. 6 is highly non-linear both due to the shape of ice crushing strength curve and the possibility of contact loss between the ice edge and the structure. The response history of the structure can be solved by numerical integration. In order to get stable limit cycles as soon as possible, it is advantageous to use the static displacement of the average ice load as an initial condition. Another way to reduce CPU-time is to use principal mode presentation. Usually only a small number of the lowest modes are needed to model global structural vibration state. If ice velocity is such that the initial state will not fall into the decreasing part of the crushing strength curve, a sufficiently large disturbance is needed to make the structure to vibrate, allowing conditions for limit cycles either to develop or all vibrations to decay.

Any 3–D structure can be modelled by FEM. For ice-induced vibration analysis the needed output is natural modes and frequencies for the limit cycle program input. Number of ice action nodes are chosen according to the geometry of interaction, and nodal ice loads can have components to all co-ordinate directions. Each nodal load is calculated independently according to Equation 5.

6 APPLICATION STRUCTURES

Figure 3 presents the FEM-model of a generic three-legged jacket platform that is intended to operate in moderate first-year ice conditions. Water depth is 19 m and jacket legs go deep into sea bottom. Soil support is simply modelled by pinning the legs at -24 m depth. The diameter of jacket legs at waterline is 1.2 m. The structure is symmetric, each cross section forms an equilateral triangle. At the waterline the distance of legs is 10.2 m. The deck at +13 m level is hexagonal and has a mass of 300 Mg. The structural model includes only primary structures with the mass of secondary structures.

The first 16 natural modes are given in Table 1. Global modes that are most important in ice-structure interaction in global y-direction (from left to right) are presented in Figure 3. Due to structural symmetry many frequencies are repeated. The first and second bending modes are at 1.31 and 3.24 Hz, and twist modes at 1.44 and 3.70 Hz respectively. The structure is relatively flexible, especially in relation to ice load action at the waterline. The deck mass is a significant factor in the dynamic response of the structure.

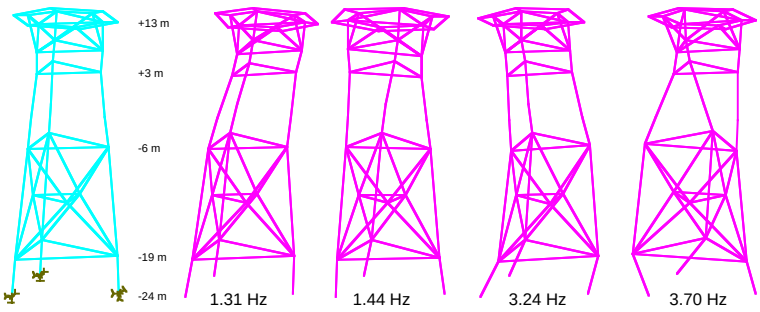

Figure 3. Three legged jacket platform and natural modes.

The wide application structure is a fictive caisson retained island (CRI) intended to withstand multi-year ice loads in 20 m water depth, Fig. 4. The retaining ring is made of steel. Wall height is 8 m above sea level. The deck rests freely on top of the ring. The planview is octagonal with longest sides 64 m at the waterline and total width 90 m. The base is 112 m wide and supported on soil. For vibration analysis soil stiffness including core sand is simply observed by linear spring elements at foundation nodes. Total horizontal spring coefficient is 29 GN/m. The total mass of the structure including core sand and added soil and water mass is 510 Gg. The foundation springs, ring cross section rigidity and total mass were adjusted to give natural frequencies roughly at the same range as what has been measured on an actual caisson retained islands /6/.

The first 16 natural frequencies are given in Table 1. The most important modes from the ice-structure interaction point of view are plotted in Figure 4. Even though the structure as a whole is very stiff against ice action, there are many low natural modes that contribute to deformations at ice action points. If the deck would have been fixed on the caisson ring to carry through loads, natural frequencies would have been higher, and many of the modes in Figure 4 totally different.

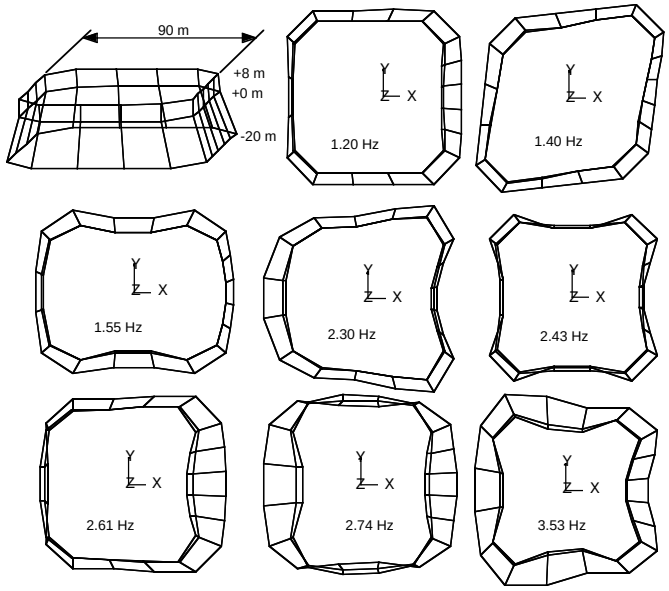

Figure 4. CRI natural modes.

Mode	CRI	3-leg
1	1.19	1.31
2	1.20	1.31
3	1.31	1.44
4	1.40	3.24
5	1.55	3.24
6	2.28	3.70
7	2.30	6.76
8	2.43	6.76
9	2.61	8.76
10	2.70	10.6
11	2.74	10.6
12	3.32	10.7
13	3.44	11.1
14	3.52	11.1
15	3.53	11.4
16	3.58	11.4

Table 1. Lowest natural frequencies (Hz)

Self-excited ice-structure interaction numerical simulation indicates that the 3-legged jacket platform in Figure 3 is highly sensitive for ice-induced vibrations. It would have needed over-critical structural damping to prevent ice-induced vibrations. Resonant lock-in type vibrations, synchronised at each leg, emerge at every practical ice thickness value. Limit cycles develop fast; at ice action point usually during the first cycle, (Fig. 5.a). On the other hand the deck mass takes several cycles before steady limit cycles are stabilised.

At very low ice velocities corresponding the nominal stress rate in the ductile range, left from the ice strength maximum in Figure 2, or at high velocities in the brittle range, no self-excited vibrations develop. If ice velocity makes the nominal stress rate just right from the ice strength maximum, the limit cycles predict saw tooth like structural response at the waterline, (Fig. 5.b). The frequency of repeating ice failures is well below the lowest natural frequency. With increasing velocity at certain point the first natural mode frequency starts to control the crushing frequency regardless of ice velocity, (Fig. 5.c). The lock-in can persist until a higher mode starts to control and makes a lock-in to another frequency, (Fig. 5.d). At velocity range in between,

there exist limit cycles that combine both natural modes, (Fig. 5.e). Partly this is a result of inertia loads from the deck mass.

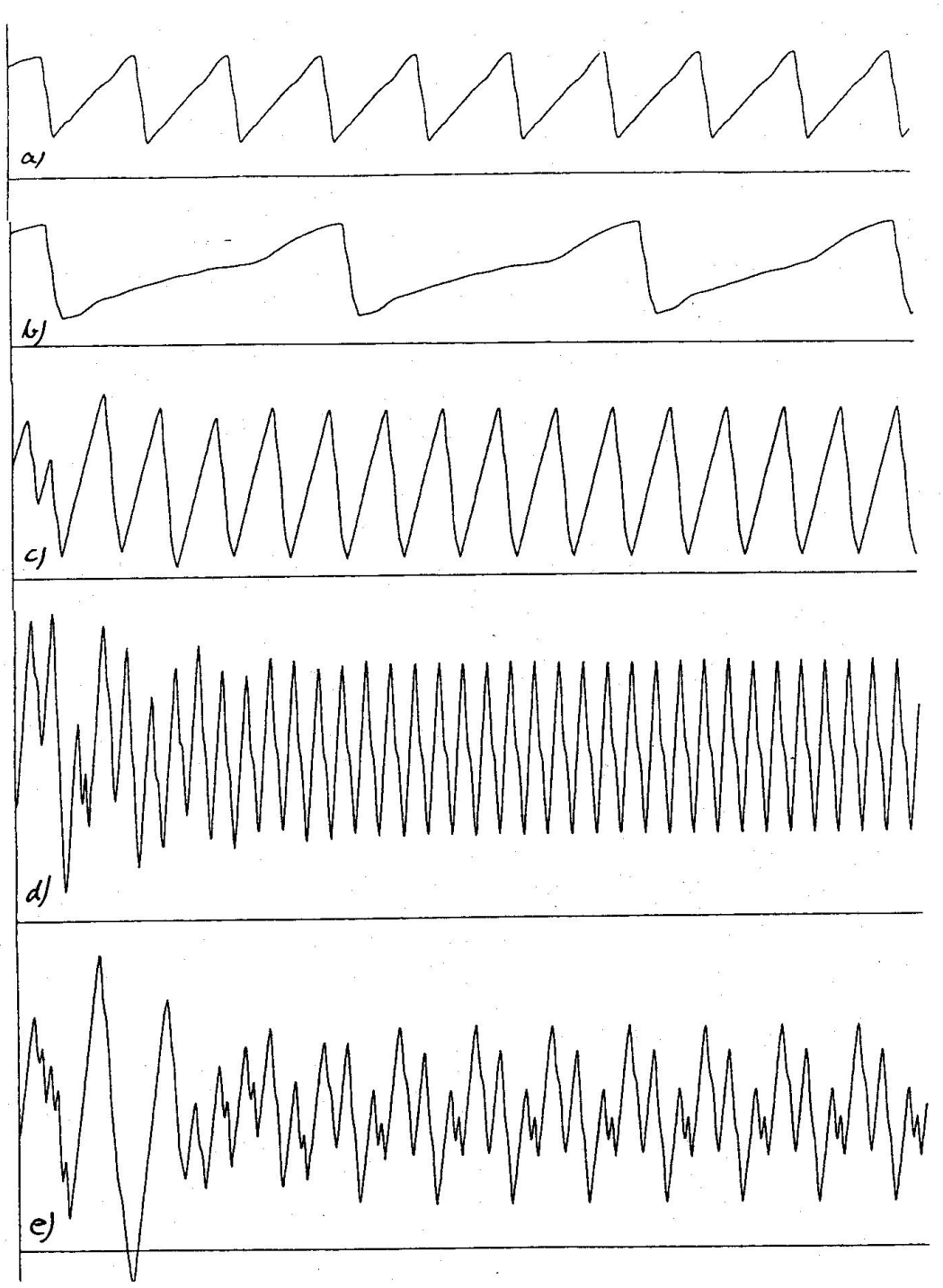

Figure 5. Jacket platform waterline node displacement history vs. time from 0 - 16 s at different ice velocity ratio r. f is limit cycle frequency and d is maximum displacement at ice action point.

a) h=1.0 m, r=0.5, f=0.78 Hz, d= 69 mm.
b) h=2.0 m, r=0.5, f=0.27 Hz, d=135 mm
c) h=1.0 m, r=1.0, f=1.32 Hz, d= 76 mm
d) h=1.0 m, r=1.7, f=3.06 Hz, d= 63 mm
e) h=1.0 m, r=1.4, f=-.-- Hz, d= 79 mm

If ice is thin, higher modes are likely to control the crushing frequency. E.g. in the case of a 0.1 – 0.2 m thick ice 11.1 Hz frequency is dominating and with 0.3 – 0.6 m thick ice 9.9 Hz respectively. With 0.7 m thick ice it is possible to have steady limit cycles at 6.84, 3.06 or 1.31 Hz frequency depending on ice velocity or whether all the three legs are under ice action. On contrary with thick ice, ice velocity directly controls the crushing frequency. Assuming an unrealistic high ice thickness of 2 m, steady saw tooth like limit cycles can be predicted from 0.27 Hz to about 1 Hz with increasing ice velocity. Thereafter the first mode at 1.31 Hz causes a lock-in to occur. Again at the brittle range no lock-in vibrations occur.

The displacement amplitudes of limit cycle vibrations were not simply related to ice velocity. The reason was the jump from one mode to another, and intermittent combination modes, that prevented distinct velocity dependence to show up.

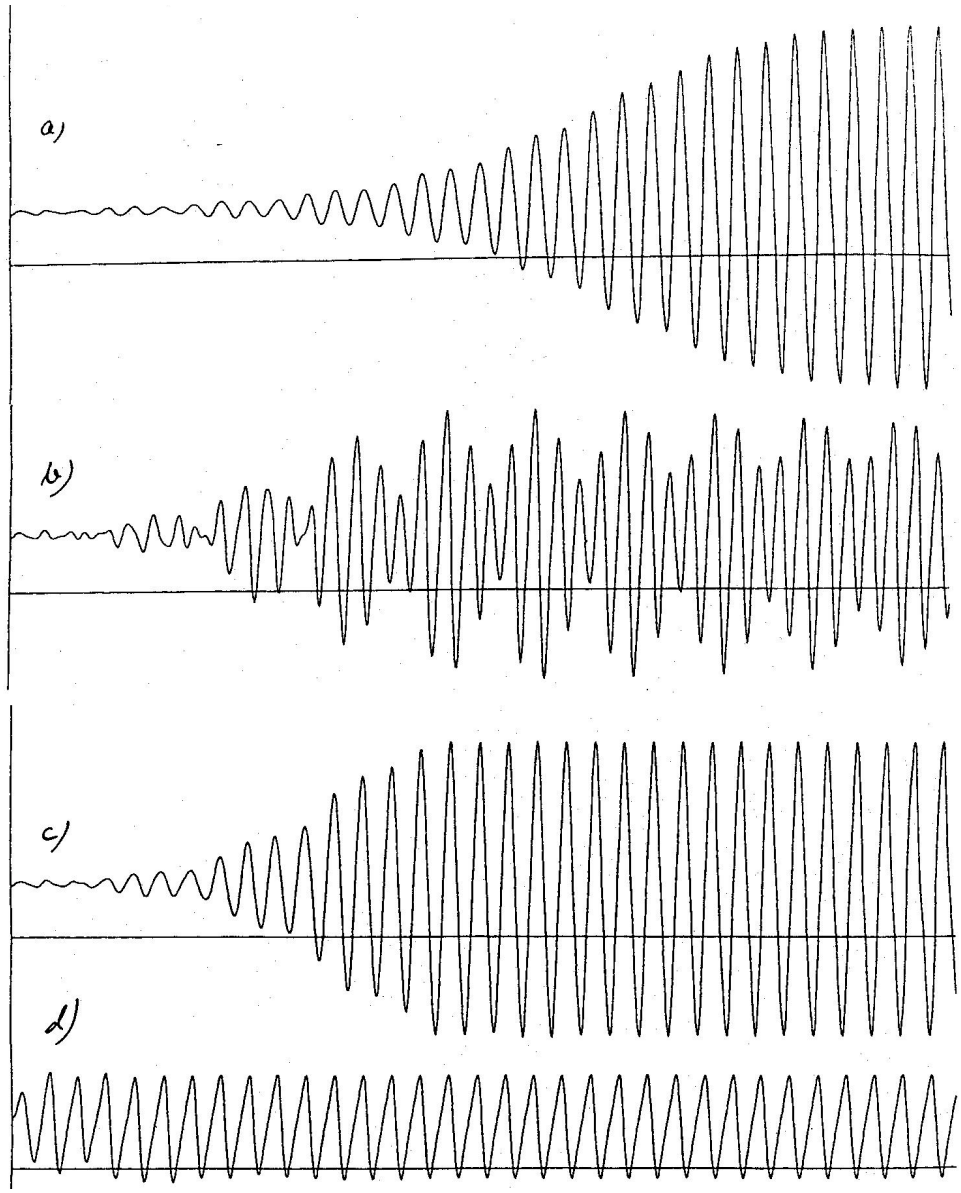

Figure 6. CRI centre node displacement history vs. time from 0 - 32.5 s at different ice thickness h. f is limit cycle frequency and d is maximum displacement at ice action point.

a) h=0.5 m, f=1.21 Hz, d=20 mm.
b) h=2.0 m, f=1.54 Hz, d=22 mm (ice action only at center 1/3-part)
c) h=1.0 m, f=1.18 Hz, d=26 mm
d) h=16. m, f=1.25 Hz, d=49 mm

It was not possible to predict the jacket structure in Figure 3 to exhibit asymmetric ice-induced vibrations, e.g. twisting along the vertical axis. Even if the initial state of deformation was that of a pure twist mode, and ice loads were acting only on two legs to allow 180 degree phase shift in excitation, the limit cycle lock-in response soon developed into a symmetric one controlled by the first mode. However, in another jacket platform with different mass and stiffness properties, persistent steady state lock-in twist mode limit cycles could be predicted

The wide caisson retained island was stiff and not very sensitive to exhibit ice-induced vibrations. By increasing structural damping it was possible to prevent resonant lock-in type ice-induced vibrations totally. In most cases it took many cycles before limit cycle amplitudes started to increase and a steady state to develop, (Fig. 6.a). Always the first mode at 1.2 Hz was the dominant one, and ice loads were synchronized at each ice action node. It was not possible to simulate such saw tooth like response history as was common with narrow structures. Also response, that would be a combination of different modes, Fig. 6.b, was unlikely. Steady state limit cycles were practically always controlled by the first natural mode frequency at 1.21 Hz regardless of ice thickness. Only small variations at 1.18 and 1.25 Hz appeared, Fig. 6.c – d.

With increasing velocity the crushing frequency was generally constant, close to the first natural frequency. The limit cycle displacement amplitude, on the other hand, has almost a linear dependence on velocity, Fig. 7. The non-dimensional velocity is scaled in relation to the center part of the decreasing range in Figure 1. Value r=0.5 corresponds to the peak value and r=1.5 the beginning of the brittle range.

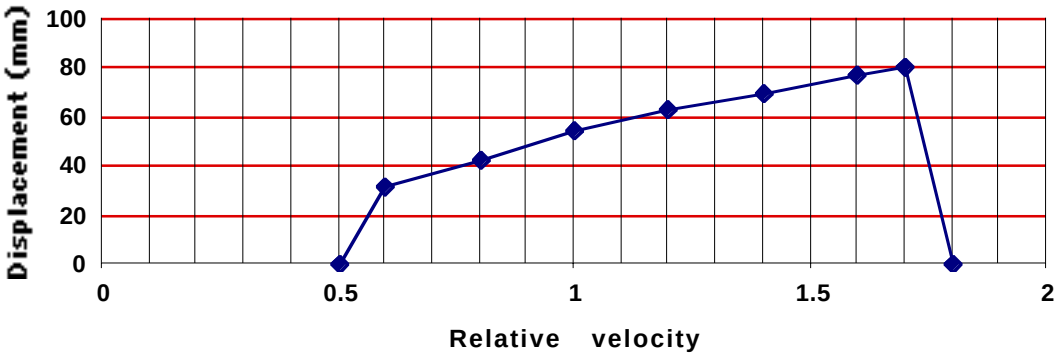

Figure 7. Limit cycle amplitude vs. velocity

It was not possible to achieve steady state limit cycles at asymmetric modes with the caisson-retained island. With symmetric modes it was easier to have lock-in vibrations if ice loads were only at the center part of the sidewall. This is to be expected when compared to the shape of natural modes. The nodes close to corner experience smaller displacement amplitudes and hence their interaction velocity differs from that of center part nodes. Thus corner nodes are in a sense out of phase of the center part and disturb the development of steady state limit cycles.

7. ICE LOADS ON WIND TURBINE FOUNDATIONS

European Commission has set a renewable energy goal to have 5 GW offshore wind energy by 2010 and 50 GW by 2020. Present wind turbine unit size is 2 MW and in design phase there are 3 to 5 MW units. Anyway the EC goal would require thousands of offshore foundations also in the Baltic at ice infested waters. Simultaneous wind and ice induced vibrations in tall structures is a combination with no in-field experience this far. Thus only computational mechanics simulations can give insight for proper design.

After the nature of ice-induced vibrations were learnt and vibration isolation for lighthouses were introduced, the steel foundation pile proved to be successful and replaced caisson foundations in Finland /20/. The same solution is not feasible for wind turbine foundations. Vibration isolation is intended to carry through high vertical and small horizontal loads between the tower and foundation. This function is hard to be combined with high horizontal wind loads.

Without vibration isolation there are two ways to mitigate the effects of dynamic ice forces. First the foundation can be made so stiff that foundation displacement response is insignificant. This requirement is likely to increase foundation cost even though with a caisson foundation the stiffness is naturally high. The second alternative is to use a conical section at the waterline that both changes ice failure from crushing to bending and reduces ice loads. Then the displacement response reduces as well. More important is that ice failure frequency is dependent on ice thickness. With thick ice the frequency falls well below the lowest natural frequencies of the complete structure. Thus the threat of resonant vibrations is avoided with thick ice. With thin ice resonance is possible but the resulting loads are small. The structure needs to be designed to withstand individual ice load pulses and random fluctuations.

In design the natural frequencies and modes of the complete structure has to solved first, and if needed, structural mass and stiffness changed in such a way that resonance due to propeller blade excitation is avoided. Load cases include transients due to ice edge hit or sudden ice load relaxation, random ice load level variations, and continuous repeating ice load failures. Transient or random loading response calculation is an ordinary practice if the loading function is known. Continuously repeating ice load fluctuation is dependent on the response of the structure itself. A self-excited vibration model has to be adopted /22/. A conservative estimate can be calculated by assuming a saw tooth like ice force function, Fig. 8, if level ice crushing force is used as a dynamic load, and the period T chosen to be identical to one of the lowest natural modes.

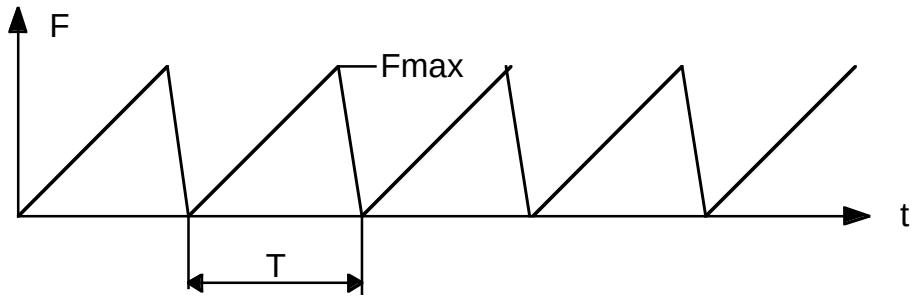

Figure 8. Assumed resonant ice force function

As an example forced dynamic response analysis results due to an assumed 1 MN saw tooth ice loading function are presented. The application pile foundation has a diameter of 4 m in 6 m water depth, it is driven down 16 m into bottom soil, the mass of 67 m high tower is 100 ton, and at the top is 78 ton nacelle and rotor. The first lowest natural frequencies are 0.38 and 2.5 Hz. The transient development of vibrations after the onset of resonance loading at the first natural frequency is given in Fig. 9 and 10. Nacelle displacement amplitude approaches 0.2 m, which is only about 20 % of maximum wind induced deflection. Acceleration levels at the nacelle also remain low at around 0.1 g. For a corresponding much stiffer caisson foundation displacement and acceleration response are only about one tenth of those of the pile foundation.

The application example indicates that dynamic ice loads do not become a restrictive factor for wind generators. With a conical section it is easy to reduce dynamic ice load fluctuations to the order of 1 MN. With cone the repetition rate of ice failures is dependent on ice thickness. Ice failure repeat after ice advances at least a distance of two times its thickness. In the Gulf of Bothnia thick ice velocity never gets over 0.3 m/s. Hence e.g. a 0.8 m thick ice will never fail

against a cone at higher frequency than 0.2 Hz. This is well below the wind generator lowest natural frequency, and hence resonant loading is possible only with thin ice and low ice forces.

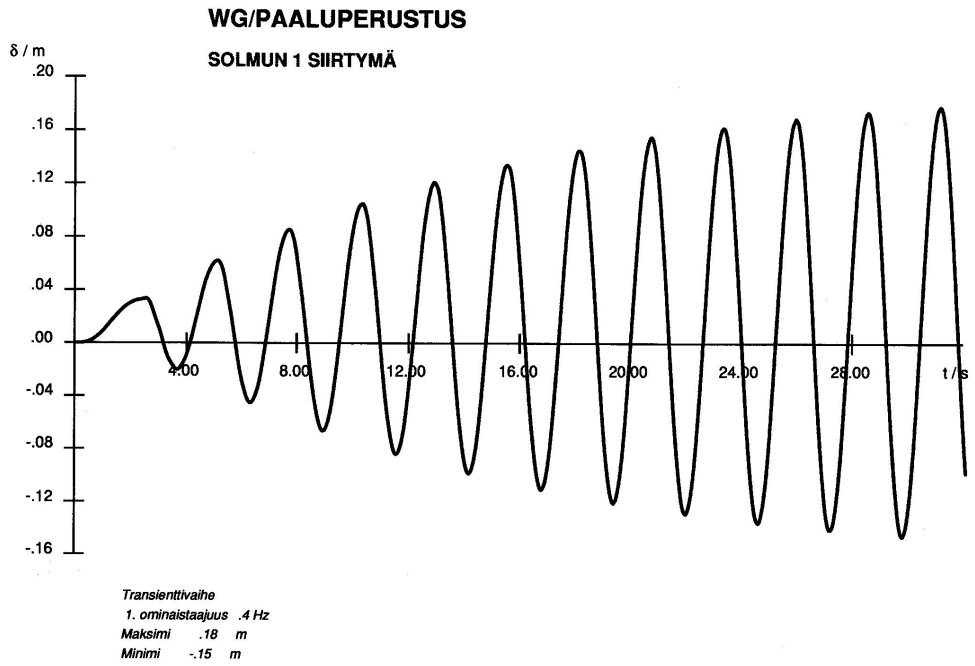

Figure 9. Transient displacement (m) vs. time (s) at the nacelle in resonant loading.

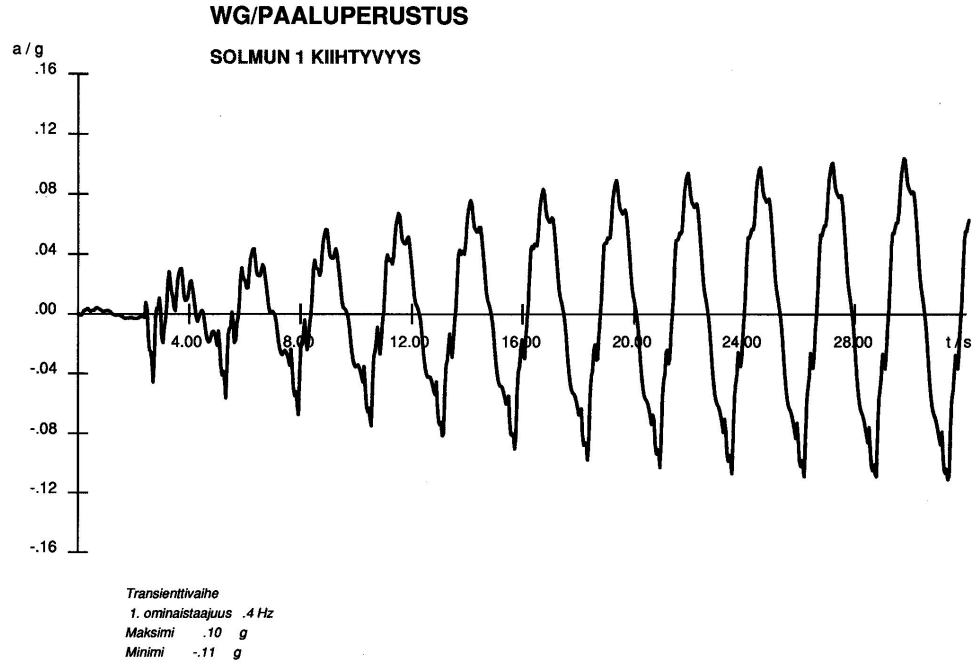

Figure 10. Transient acceleration (m/s^2) vs. time(s) at the nacelle in resonant loading.

CONCLUSIONS

Vibrations in offshore structures can be very severe while ice is moving driven by winds or current. Dynamic loading cases include transient impact loads and continuos ice failure loads. Measured dynamic load histories indicate saw tooth like functions, persistent close to harmonic

load repetition and random load variations. Most critical is the resonant type ice failure repetition.

Dynamic equations of motion of the structure are homogenous if a constant thickness level ice is moving and crushing against the structure. If the system of equations is dynamically unstable, ice-induced self-excited vibrations will emerge and tend to limit cycles.

Computational mechanics can be used efficiently to integrate numerically the dynamic response of an offshore structure to ice loads. Self-excited models predict similar response that has been observed and measured in-field.

Offshore wind energy applications need stringent dynamic analysis design both for wind- and ice-induced vibrations. Presented numerical analysis suggests that tall wind turbine towers can be designed to withstand also dynamic ice loads.

REFERENCES

1 Akagawa S., Saeki H., Takeuchi T., Sakai M., Matsushita H., Kamio Z., Terashima T. and Nakazawa N. (2001): Medium-scale field ice indentation test – Winter 1996-2000 test program. Proc. POAC ’01, Canadian Hydraulics Centre, Ottawa Canada, 2001. pp. 567-576

2 Blenkarn K. A. (1970): Measurement and analysis of ice forces on Cook Inlet structures. Proc. 2nd Offshore Technology Conference, Houston, TX, OTC 1261, Vol. II, pp. 365-378.

3 Daoud N. and Lee F. (1986): Ice-induced dynamic loads on offshore structures.OMAE 1986, Tokyo, Japan, Vol IV, pp. 212-218.

4 Engelbrektson A. (1983): Observations on a Resonance Vibrating Lighthouse Structure in Moving Ice. POAC 1983, Helsinki, Finland, Vol II, pp. 855-864.

5 Izumiyama K., Wako D., and Uto S.(1998): Ice Force distribution on a flat indentor. Proc. IAHR Symposium on Ice 1998, Potrsdam, USA. pp. 917- 922.

6 Jeffries M. G. and Wright W. H. (1988): Dynamic Response of "Molikpaq" to Ice-Structure Interaction. OMAE 1988, Houston, TX, USA, Vol IV, pp. 201-220.

7 Joensuu A. and Riska K. (1988): Jään ja rakenteen välinen kosketus. (Contact between Ice and Structure, in Finnish only,). Report M-88. Helsinki University of Technology, Laboratory of Naval Architecture and Marine Engineering, Espoo, Finland.

8 Jordaan I. J., Maes M.A., and Nadreau J-P. (1988): The Crushing and Clearing of Ice in Fast Spherical Indentation tests. OMAE 1988, Houston, TX, USA, Vol IV, pp. 111-116.

9 Kärnä T. (1992): A procedure for dynamic soil-structure-ice interaction. Proc. ISOPE 1992, Vol. II, pp 764-771. International Society of Offshore and Polar Engineers, San Francisco.

10 Kärnä T. (1997): A layered flaking model for ice load determination. Proc. 6th Finnish Mechanics Days, pp. 85-101. University of Oulu, Finland.

11 Matlock H., Dawkins W. and Panak J.(1969): A model for the prediction of ice structure interaction. Journal of Engineering Mechanics, ASCE, EM4:1083-1092.

12 Michel B. and Toussaint N. (1977): Mechanisms and theory of indentation of ice plates. Journal of Glaciology, 19(81):285-300.

13 Michel B. (1978): Mechanics of Ice. Universite Laval, Quebec, Canada.

14 Montgomery C.J, Gerard R. and Lipsett A.W (1980): Dynamic Response of Bridge Piers to Ice Forces. Canadian Journal of Civil Engineering, 7:345-356.

15 Muhonen A. (1996): Evaluation of three ice-interaction models. Helsinki University of Technology. Espoo, Finland. Licenciates's thesis. 90 p.

16 Määttänen M. (1975): Experiences of ice forces against a steel lighthouse mounted on the seabed, and proposed constructional refinements. Proc. POAC'75, Fairbanks, Alaska 1975.

17 Määttänen M. (1978): On conditions for the rise of self-excited ice-induced autonomous oscillations in slender marine structures. Finnish-Swedish Winter Navigation Board, Finland, Research Report 25, 98 p.

18 Määttänen M. (1983): Dynamic ice structure interaction during continuous crushing. U. S Army Cold Regions Research and Engineering Laboratory, Hanover, NH, USA 03755, CRREL Report 83-5, 53 p.

19 Määttänen M. (1984): The effect of structural properties on ice-induced self-excited vibrations, Proc. IAHR Symposium on Ice 1984, Hamburg, West Germany, Vol II, pp. 11-20.

20 Määttänen M . (1987): Ten years of ice-induced vibration isolation in lighthouses. OMAE 1987, Houston, TX, USA, Vol IV, pp. 261-266.

21 Määttänen M. (1988):Ice-induced Vibrations in Structures - Self-Excitation. Proc. IAHR Symposium on Ice 1988, University of Hokkaido, Sapporo, Japan, Vol 2. pp. 658-665.

22 Määttänen M. (1998): Numerical Model for Ice-Induced Vibration Load Lock-in and Synchronization. Proc. IAHR Symposium on Ice 1998, Potsdam, USA. Pp. 923-930.

23 Neill C. (1976): Dynamic ice forces on piers and piles: An assessment of design guidelines in the light of recent research. Canadian Journal of Civil Engineering, 3:305-341.

24 Nevel D. E. (1986):Iceberg Impact Forces. Proc. IAHR Symposium on Ice 1986, University of Iowa, Iowa City, IO, USA, Vol III, pp 345-369.

25 Peyton H. (1968): Sea ice forces. Ice pressure against structures, National Research Council of Canada, Ottawa, Canada, Technical Memorandum 92, pp. 117-123.

26 Sanderson T. (1988): Ice Mechanics – Risks to Offshore Structures. Graham and Trotman Ltd, London.

27 Sodhi D. and Morris C. (1986): Characteristic frequency of force variations in continuous crushing of sheet ice against rigid cylindrical structures. Cold Regions Science and Technology 12:1-12.

28 Sodhi D. (1988): Ice-induced vibration of structures. Proc. IAHR Symposium on Ice 1988, Sapporo, Japan, Vol 2. pp. 625-657.

29 Sodhi D. (1994): A theoretical model for ice-structure interaction. Proc. OMAE-94, Vol. IV, pp.29-34. ASME, New York.

30 Vershinin S, Kouzmitchev K. and Tazov D. (2001) Proc POAC'01, Canadian Hydraulics Centre, Ottawa. Vol. I, pp. 403-412.

31 Wang K., Wu H., Wang C. and Liu L. (2001): Modelling sea ice ride-up and pile-up against conical caisson in Bohai Bay. Proc. IAHR Symposium on Ice 1998, Potsdam, USA. pp. 939-945.

32 Xu J. and Lingyu W. (1988): Ice force oscillator model and its numerical solutions. OMAE 1988, Houston, TX, USA, Vol IV, pp. 171-176.

33 Yue Q., Bi X. and Yu X. (2000): Effect of ice-breaking cones for mitigating ice-induced vibrations. Proc. IAHR Symposium on Ice 2000, Gdansk, Poland. pp. 127-133.

Resilient modules in FE-simulations of unbound road material

Johan Olsson*
Department of Structural Mechanics
Chalmers University of Technology, Göteborg, Sweden
e–mail: johan.olsson@sm.chalmers.se

ABSTRACT

Summary In this abstract the development and implementation of a non-linear elastic material model for unbound pavement materials is described briefly. The material presented in the abstract is a part of a project in which a material model based on the resilient modulus technique is to be implemented into a FE-program with intention to investigate how it can be utilized in road design and analysis.

1 Introduction

A road is a multi-layered structure, which consists of a number of layers with materials that exhibits vastly different behavior when subjected to mechanical- and/or environmental loads, see figure 1. The top layers often consist of bitumen bound or bitumen stabilized materials. The bound materials can be modeled with e.g. an elastic or a visco-elastic material model described in [1]-[3]. Beneath the bitumen stabilized layers there are a number of layers consisting of unbound granular material. In several of the design codes that are used in road design today the standard linear-elastic (Hooke) model is used for reproducing the behavior of the unbound materials in the road structure. However tests performed have shown that the unbound materials exhibit a non-linear behavior when subjected to mechanical loads, [4]. In order to improve the accuracy of the design tools a number of material models, based on a non-linear elastic resilient modulus, have been suggested that would fit the test data and physical behavior of the unbound materials in a more accurate manner.

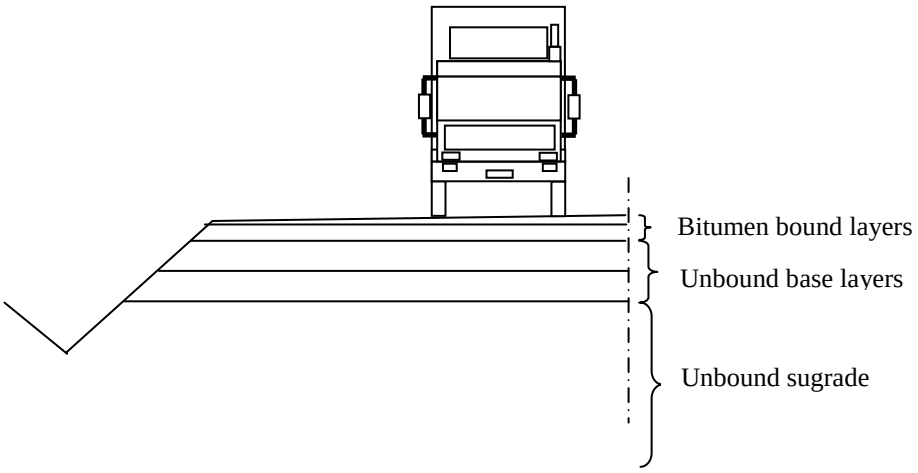

Figure 1. A multi-layer road structure.

2 Material Modeling

The mechanical behavior of unbound road materials, especially the base material, has been studied in vast number laboratory tests, see e.g. [4]. Cyclic triaxial testing apparatus are frequently used in order to find the physical behavior of the materials. After the initial load cycles a permanent strain is often detected. However the non-recoverable strain recorded is often referred to as strain from conditioning of the laboratory sample and are therefor often disregarded. They decreases with the number of load repetitions, see figure 2. After a large number of load cycles only or almost only non-linear elastic strains will occur.

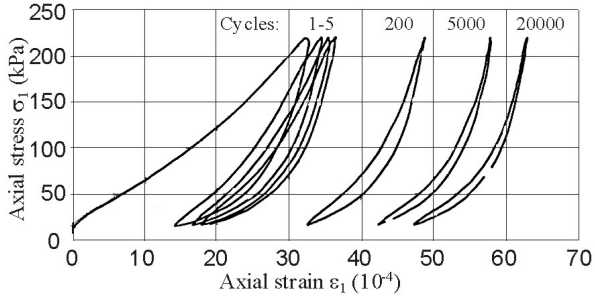

Figure 2. Example of a stress-strain relation curve, in the vertical direction, of a cyclic triaxial test [4].

Due to the non-linearity of the stress-strain response the ordinary assumption of using a linear elastic constitutive relation were questioned. In 1971 Hicks and Monismith, see [4], suggested the $K-\theta$ model (1), in which $\theta \equiv (\sigma_1 + 2\sigma_2)/3$, K and n are constants obtained from regression analysis from laboratory tests. The $K-\theta$ expression (1) yields an elastic property called the resilient modules M_r, which is a secant elastic stress dependent stiffness module.

$$M_r = K\theta^n \tag{1}$$

The expression (1) has been used in a number of applications during the 1970's. However expression (1) do not include any influence of shear stress. In order to take shear stresses into consideration a number of different material models have been suggested in the literature, see e.g. [2]. One of the more resent variants is the equation (2) which also is going to be an option in the new US 2002 Pavement Design Guide for road structures, [6].

$$M_r = k_1\left(\frac{\theta - 3k_6}{p_a}\right)^{k_2}\left(\frac{\tau_{oct}}{p_a} + k_7\right)^{k_3} \tag{2}$$

Expression (2) includes the influence of bulk stresses i.e. the part under exponent k_2 and the impact of shear stresses i.e. the part beneath the k_3 exponent. P_a is the atmospheric air pressure and is included in the formula in order to make the equation (2) dimensionless. The bulk stress is described by the first invariant of the stress tensor (3). Shear stresses are included in the expression through the introduction of the octahedral stress, which can be expressed like in equation (4). k_1-k_7 in equation (2) are constants gained through regression analysis and material testing.

$$\theta = \sigma_1 + \sigma_2 + \sigma_3 \tag{3}$$

The constant k_7 is inserted in order to avoid numerical problems that occurs in the case that the octahedral shear stress equals zero, which would yield a zero stiffness for the material.

$$\tau_{oct} = \frac{1}{3}\sqrt{\left(\sigma_x - \sigma_y\right)^2 + \left(\sigma_y - \sigma_z\right)^2 + \left(\sigma_z - \sigma_x\right)^2 + 6\tau_{xy}^2 + 6\tau_{yz}^2 + 6\tau_{xz}^2} \quad (4)$$

The material model described in equation (2) was selected for further studies and has been implemented in the general purpose FE-program ABAQUS [7] as a UMAT routine. Note that in this first version of the material model implemented into ABAQUS tensional strains is allowed to occur in the unbound material.

3 Numerical example

A numerical example was created in order to test the UMAT routine and investigate the impact of the non-linear stiffness modulus. The test road structure consists of 3 layers, see figure 3a. On the top there is a bitumen bound layer which is assumed to be linear-elastic. The second layer from the top i.e. the unbound base course is modeled with both the non-linear resilient module and the linear elastic material model e.g. used in the Swedish design guide [1]. Beneath the top two layers described above a subgrade is situated and modeled as linear-elastic material. The geometrical outline of the FE-model used in this case is based on axi-symmetry with infinite boundary elements in the horizontal direction. The elements used in the road structure itself are 8 node axi-symmetric elements. A vertical load P=550 kPa with a radius of 0.15 m was applied at the axi-sym. center of the FE-model of the road structure. The material properties used are presented below in Tab.1.

Calculation 1	E_{Bit}=6e9Mpa • $_{Bit}$=0.45	Ebase=5e4 MPa, • $_{Sub}$=0.35	Esub=5e7 MPa, • $_{Sub}$=0.4
Calculation 2	E_{Bit}=6e9Mpa • $_{Bit}$=0.45	k1=1252, k2=2.046 k3=1.610, k4= 1., k5= 1., k6=0 and k7=1	Esub=5e7 MPa, • $_{Sub}$=0.4

Tab. 1 Material properties assumed and used in the calculations.

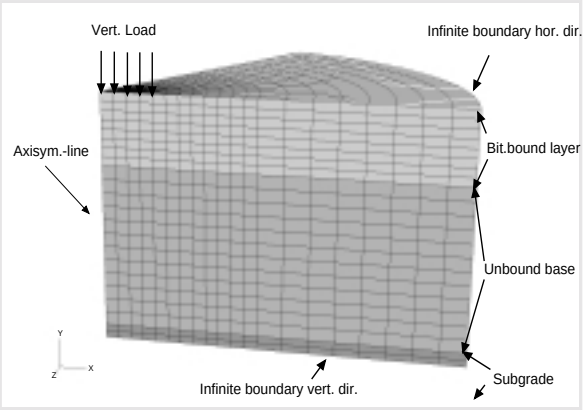

Figure 3a) FE-model

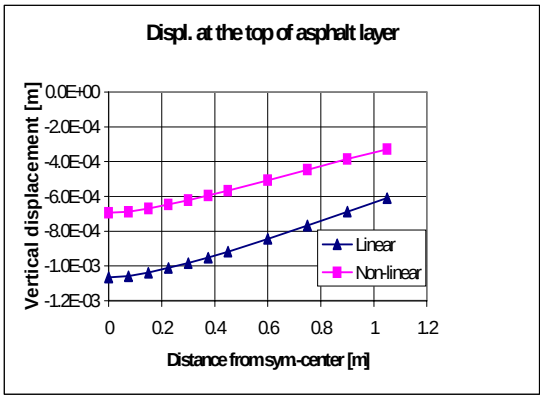

Figure 3b) Displacement at the road surfaces.

The results, from these first calculations performed with resilient modules stated in (2), indicates that the UMAT in which the material model is implemented appears to be giving reasonable results based on the magnitude of the displacements in the road surface, see figure 3b. A deviation between the linear elastic solution and the non-linear calculation is shown in figure 3b. The stiffer behavior can be explained with the circumstance that the magnitude of the resilient modulus increases rather fast when there is an increase in the stress levels and at a certain stress limit the resilient modulus becomes larger then the assumed elastic modulus.

4 Conclusions and future research

Including an expression for a non-linear stress dependent resilient (stiffness) modulus, equation (2), clearly has a significant impact on the calculated displacements in surface of the road structure. The non-linear resilient modules appears to make the unbound base layer stiffer in this case, but further studies have to be performed in order make any statements on the impact on road modeling in general.

Further development of the formulation of the materials model implemented in the UMAT in ABAQUS is necessary. The first object to target, in order to improve UMAT describing the material model, is to formulate and implement a tension-cut-off routine. This to avoid that tensional strain occurs in the unbound layers. Another important issue is how insitu stresses should be handled. This have do be considered due to the formulation of (2) in which the initial stresses gives the first resilient modules, which could lead to numerical problems if the initial stresses are zero or close to that value.

REFERENCES

[1] Swedish National Highway Administration. *General Specification for Highway Structures: ATB VÄG*. Borlänge, (2000).

[2] COST 333. *Development of New Bituminous Pavement Design Method: Final report of the action*. Belgium, (1999)

[3] J. Olsson. *Simulation of rutting phenomenon in road surfaces*. Licentiate thesis, Publ. 00:16, Dept. of Structural Mechanics, Chalmers University of Technology, (2000).

[4] F. Lekarp. *Resilient and permanent deformation behavior of unbound aggregates under repeated loading*. Royal Institute of Technology, Sweden, (1999).

[5] K. D. Hjelmstad and E. Taciroglu. Analysis and Implementation of Resilient Modules Models for Granular Solids. *J. of Eng. Mech.*, **126**, 821-830, (2000).

[6] C. W. Schwartz. *Effects of stress-dependent base layer on the superposition of flexible pavement solutions*. Proc. Of the second international symposium on 3D Finite Element for Pavement Analysis, Design and Reaserch, Charleston, West Virginia, (2000).

[7] Hibbit, Karlsson & Sorenson Inc. *ABAQUS/Standard User's Manual, Version 5.8*. Hibbit. Karlsson & Sorenson, Pawtucket Rhode Island, USA.

On the integration of inelastic constitutive models

Reijo Kouhia*
Laboratory of Structural Mechanics
Helsinki University of Technology, Finland
e–mail: reijo.kouhia@hut.fi

Pekka Marjamäki
Laboratory of Electronics Production Technology
Helsinki University of Technology, Finland
e–mail: pekka.marjamaki@hut.fi

ABSTRACT

Summary For the integration of inelastic constitutive models many different algorithms exist, however, the fully implicit backward Euler method has became the most popular one. In this study explanations why the backward Euler method seems to be the "most accurate" is sought and its limitations are discussed.

Motivation

Backward Euler scheme seems to be the most popular method for integrating inelastic constitutive models. A quotation from the book of SIMO & HUGHES, *Computational Inelasticity*, Remark 3.3.2.2 on page 125 states [1]: *"The overall superiority of the radial return method relative to other return schemes is conclusively established in Krieg and Krieg [1977]; Schreyer, Kulak and Kramer [1979] and Yoder and Whirley [1984]".* In these papers [2, 3, 4] comparisons has been performed numerically. However, explanation for the good performance is missing.

To start with, numerical integration of a simple scalar constant coefficient evolution equation

$$\dot{y} + \lambda y = 0, \qquad y(0) = \bar{y}_0 \tag{1}$$

is considered ($\lambda \geq 0$). The backward Euler scheme is the simplest implicit method for integrating such equation. However, it is asymptotically only first order accurate. On the other hand, second order accurate midpoint rule gives oscillating results when the amplification factor is negative, i.e. when $\Delta t > 2/\lambda$, which is also the stability limit for the explicit forward Euler method. Therefore none of the members of the single step one parameter generalized midpoint family seems to be ideal.

However, considering the behaviour of the integrators when large time steps are used, different conclusions can be drawn. In fig. 1 amplification factors of backward Euler (bE), midpoint rule (mpr)(equals to the (1,1) Padé approximation of $\exp(-\lambda\Delta t)$), continuous Petrov-Galerkin of degree 2 (= (2,2) Padé) and discontinuous Galerkin of degree 1 (= (1,2) Padé) methods are shown.[1] It is clearly seen that the backward Euler is the most accurate when large time steps are used, i.e. it has the smallest error measured by $|A_{\Delta t} - A_{\text{exact}}|$, where $A_{\Delta t}$ is the amplification factor of the numerical scheme in question.

[1] Here the name continuous Petrov-Galerkin (cPG) is used for a Galerkin method where the test functions are of one degree lower than the trial functions and are continuous in time. In the constant coefficient case the midpoint rule equals to the cPG method with piecewise linear trial functions.

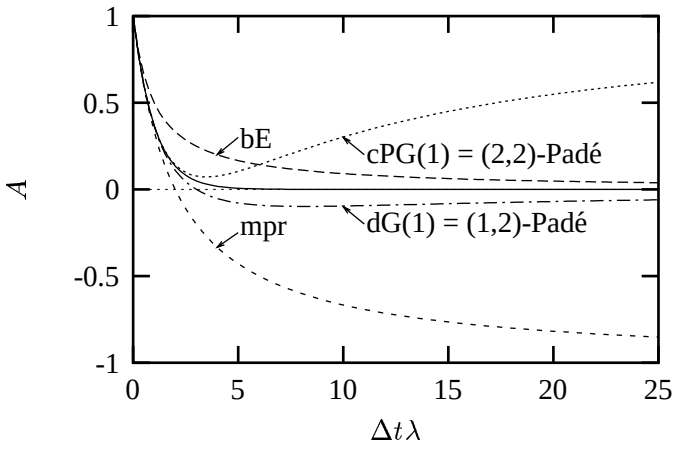

Figure 1: Amplification factors of different time integrators. Solid line represents the exact value.

However, the situation is different when the coefficient λ is time dependent. It is now assumed that

$$\lambda(t) = \lambda_0 \left[1 - \phi + \phi \exp(-\beta t)\right].$$

In this case the dG(0) method is different from the backward Euler scheme. Analytical expressions for the amplification factors are

$$\begin{aligned}
A_{\text{exact}} &= \exp\left[-\lambda_0 \left[(1-\phi)t + \phi(1-\exp(-\beta t))\right]\right], \\
A_{\text{bE}} &= \frac{1}{1 + \lambda_0 \left[1 - \phi + \phi \exp(-\beta \Delta t)\right] \Delta t}, \\
A_{\text{dG(0)}} &= \frac{1}{1 + \left[\lambda_0 (1-\phi)\Delta t + \phi(1 - \exp(-\beta \Delta t))/\beta\right]}, \\
A_{\text{dG(0)-mpq}} &= \frac{1}{1 + \lambda_0 \left[1 - \phi + \phi \exp(-\frac{1}{2}\beta \Delta t)\right] \Delta t},
\end{aligned}$$

where $A_{\text{dG(0)-mpq}}$ denotes the amplification factor of the dG(0) method where the integrals are evaluated by the midpoint quadrature.

When the diffusivity coefficient is monotonously growing, then the difference between the bE and dG(0) methods is insignificant. However, in the opposite case, especially in the extreme cases, the dG(0) method is considerably better than the bE integrator if the necessary integrations are carried out accurately. This is shown in fig. 2 where the amplification factors are shown for a case $\phi = 0.9, \beta = 0.5$, which means that $\lambda \longrightarrow 0.1\lambda_0$ when $t \longrightarrow \infty$.

Inelastic material model

A material model developed in refs. [5, 6] will be used in the following discussion. In this model the inelastic strain rate, $\dot{\epsilon}_{\text{in}}$, is described in the uniaxial case by expression

$$\dot{\epsilon}_{\text{in}} = f \exp\left(\frac{-Q}{R\theta}\right) \left(\frac{\lambda_0}{\lambda}\right)^p \sinh^m\left(\frac{\sigma}{\sigma_y}\right), \tag{2}$$

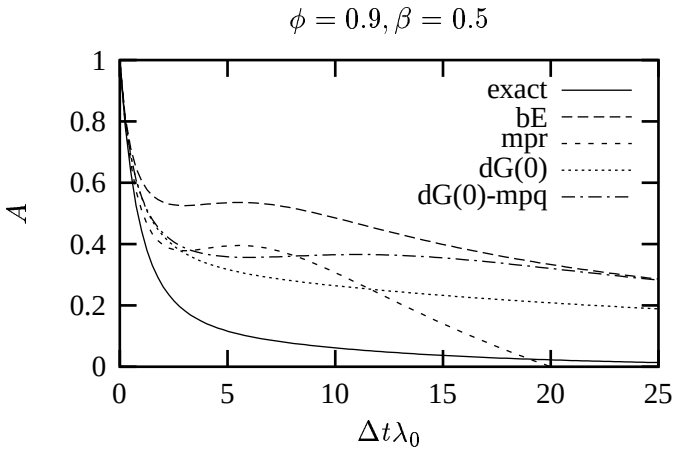

Figure 2: Aplification factor in the time dependent coefficient case.

E	=	33 GPa	Q	=	12 kcal/mol
ν	=	0.3	R	=	$2{\cdot}10^{-3}$ kcal/mol·K
σ_y	=	20 MPa	f	=	10^5 s^{-1}
m	=	3.5	p	=	2
λ_0	=	30 μm			

Table 1: Material parameters of the binary near eutectic Sn40Pb solder.

where f, p, m and Q are material parameters, R is the gas constant, θ the absolute temperature, λ, λ_0 are the current and initial grain sizes (average diameters) and σ_y is the "flow stress".

Assuming linear elasticity, the material behaviour in the uniaxial case is described by a scalar equation

$$\dot{\sigma} + E\tilde{f} \sinh^m \left(\frac{\sigma}{\sigma_y} \right) = E\dot{\epsilon}, \tag{3}$$

where E is the Young's modulus and $\tilde{f} = f \exp(-Q/R\theta)(\lambda_0/\lambda)^p$. The critical time step for the explicit Euler scheme of the linearized form of the equation (3) is

$$\Delta t_{\mathrm{cr}} = \frac{2}{m\tilde{f}} \left(\frac{\sigma_y}{E} \right) \frac{1}{\sinh^{m-1}(\sigma/\sigma_y) \cosh(\sigma/\sigma_y)} = \frac{2}{m\tilde{f}} \left(\frac{\sigma_y}{E} \right) \mathcal{F}(\sigma/\sigma_y).$$

For the material parameters shown in Table 1, the value of $2\sigma_y/(m\tilde{f}E) \approx 2.7$ s. The material data is taken from ref. [6], which represents mechanical properties of the binary near eutectic Sn40Pb solder. The critical times step for explicit schemes can thus vary several orders of magnitude (for the above mentioned material $\Delta t_{\mathrm{cr}} \sim 10^{-2} - 10^2$ s), depending on the state, as also pointed out in ref. [7].

Concluding remarks

For standard elasto-plastic models the backward Euler method seems to be the best integration scheme. However, when the material parameters are time dependent, e.g. due to temperature changes etc., or there are non-diffusive components in the material model, e.g. damage, other integration schemes will be more appropriate, for time independent case see ref. [8]. For time dependent models the discontinuous Galerkin could be a competitive alternative to the backward Euler scheme.

REFERENCES

[1] J. Simo and T.J.R. Hughes. *Computational Inelasticity*. Springer, New York, (1998).

[2] R.D. Krieg and D.B. Krieg. Accuracies of numerical solution methods for the elastic-perfectly plastic model *J. Pressure Vessel Technology*, **101**, 510–515, (1977).

[3] H.L. Schreyer, R.F. Kulak and J.M. Kramer. Accurate numerical solutions for elastic-plastic models. *J. Pressure Vessel Technology*, **101**, 226–234, (1979).

[4] P.J. Yoder and R.L. Whirley. On the numerical implementation of elastoplastic models. *J. Appl. Mech.*, **51**, 283–287, (1984).

[5] D.R. Frear, S.N. Burchett, M.K. Neilsen, and J.J. Stephens. Microstructurally based finite element simulation of solder joint behaviour. *Soldering & Surface Mount Technology*,**1** (25), 39–42, (1997).

[6] S.N. Burchett, M.K. Neilsen, D.R. Frear, and J.J. Stephens. Computational continuum modelling of solder interconnects. In R.K. Mahidhara et al., editors, *Design and Reliability of Solders and Solder Interconnects*, pages 171–178, The Minerals, Metals & Materials Society, (1997).

[7] H.L. Schreyer. Unconditionally stable time integration of creep constitutive equations. Eccomas 2000, Barcelona 11-14 September 2000, CD-ROM Proceedings.

[8] M. Wallin and M. Ristinmaa. Accurate stress updating algorithm based on constant strain rate assumption. *Comp. Meth. Appl. Mech. Engng.*, **190**, 5583–5601, (2001).

A Fitting Procedure for a Viscoelastic-Elastoplastic Material Model

Anders K. Olsson* **and Per-Erik Austrell**
Division of Structural Mechanics
Lund University, Lund, Sweden
e–mail: bmako@byggmek.lth.se

ABSTRACT

Summary A fitting procedure for a viscoelastic-elastoplastic material model capable of representing amplitude and frequency dependent properties of filled elastomers is presented. This model can be implemented into three dimensions using allready available constutive models in standard non-linear FE-software. In the one-dimensional case the model can be represented using a simple mechanical analogy. A model like this contains a lot of material parameters that have to be fitted to experimental data.

1 Introduction

Filled rubber is a two-phase material consisting of long polymer chains in a structure of microscopical carbon-black particles. Reorganization of the rubber network during dynamic loading gives rise to a viscous damping. When subjected to a dynamic load, breaking and reforming of the carbon-black structure results in a frictional damping. Experimental results show that the viscoelastic behaviour is independent of the elastoplastic behaviour [7].

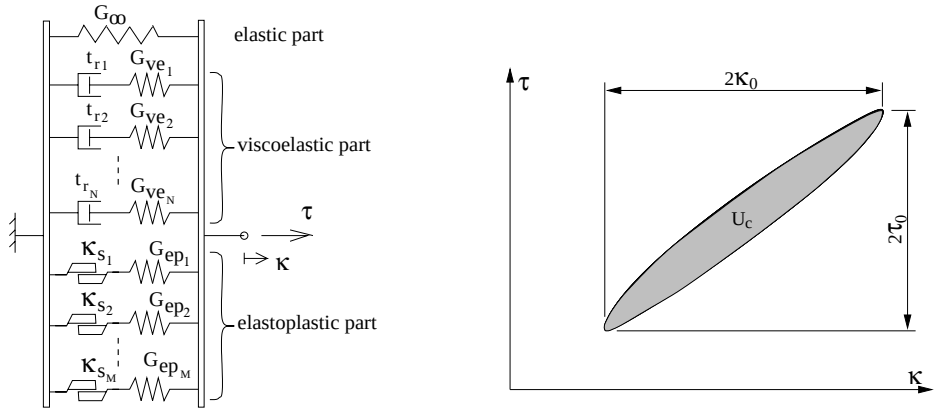

Figure 1: Left: The generalized one-dimensional material model. Right: Typical hysteretic loop for a filled rubber.

This observation of independence between the viscoelastic and elastoplastic behaviour has lead to a constitutive model, suitable for finite element analysis. The one-dimensional representation of this model is shown in figure 1a. In simple shear the elastic properties of rubber is rather linear. This makes it possible represent the material model as a one-dimensional model, where the elastoplastic elements are coupled in parallel with the viscoelastic elements and all springs are linear. The reason for having more than one viscoelastic or elastoplastic element is to get a better fit to a wider range of experimental data.

In [1] it is shown how this model can be generalized into three dimensions by an overlay principle, where one viscoelastic and one elastoplastic FE-mesh are merged. The advantage of this approach is that it does not require any implementation of new constitutive laws, since it only uses already implemented finite elements models. Another advantage of this approach is the ability to use the parameters already obtained for the one-dimensional model in figure 1a. Hence, it is sufficient to fit the one-dimensional model to the experimental data.

2 Material testing

A test batch of 13 different elastomers has been evaluated, using a simple shear test. Experiments were carried out at the Marcus Wallenberg Laboratory in Stockholm [5].

The test specimens have been subjected to a sinusoidal load, for a wide range of different frequencies and amplitudes, with shear strain amplitudes up to 12% and frequencies up to 180 Hz. To prevent hysteretic heat build-up from ruining the result, the measurement was performed during a very brief time period, but still long enough to obtain a stationary reading and to avoid Mullin's effect.

The dynamic behaviour of a rubber component is mainly attributed to the dynamic stiffness and the hysteretic damping. I.e. the aim of the fitting procedure is a material model with the same damping and stiffness properties as the tested rubber material. For this purpose the dynamic shear modulus G_{dyn} and the hysteretic damping d, have been derived from the experimental data according to

$$G_{dyn} = \frac{\tau_0}{\kappa_0}, \qquad d = \frac{U_c}{\pi \kappa_0 \tau_0} \tag{1}$$

with variables $U_c,\ \tau_0$ and κ_0 defined in figure 1b. The hysteretic work per unit volume U_c is obtained through numeric integration of the experimentally recorded time history data.

3 Fitting procedure

Although the one-dimensional material model is rather simple in its appearance, the number of material parameters to be determined, makes the fitting procedure difficult. The dynamic behaviour of rubber components is mainly attributed the dynamic stiffness and the damping properties. Thus the aim is to obtain a material model which exhibits the same stiffness and damping as the rubber material, for a given range of frequencies and strain amplitudes.

3.1 *An optimization approach*

The fitting procedure can be viewed as an minimization of the relative error of the material model compared to the experimental data. For this purpose an error function is proposed.

$$err = \sum_{i=1}^{m} \left(\frac{d_i - d_{exper,\,i}}{d_{exper,\,i}} \right)^2 + k \sum_{i=1}^{m} \left(\frac{G_i - G_{exper,\,i}}{G_{exper,\,i}} \right)^2 \tag{2}$$

By choosing the scale factor k, it is possible to decide whether to emphasize a correct modeling of the dynamic modulus or a correct modeling of the damping. The damping d_i and shear modulus G_i

are calculated from the material model at the specified frequencies and amplitudes. Thus the error function is a function of the material parameters (see fig. 1a).

3.2 *Implementation*

Evaluation of damping and dynamic stiffness can be done in two different ways. The most correct way is to simulate the material model using a time-stepping algorithm. This is, however, a time-consuming procedure, especially if the optimization algorithm is such that the error function needs to be evaluated repeatedly. For an increasing number of experimental data and material parameters this approach will be very slow. A more efficient approach is to use an analytical approximation. However, the poor accuracy of this approach yields a model with poor fit to experimental data. The solution to this problem is to use the analytical approach for repeated evaluations and to use the time stepping algorithm to calibrate the analytical expression with certain intervals. Based on this basic idea a fitting procedure has been developed.

Since the material model may contain a large number of parameters it is sometimes difficult to find a true global optimum. To stabilize the optimization algorithm it is important to use a structured approach. At first the elastic and the elastoplastic elements are fitted to only the lowest frequency for which the influence of the viscoelastic elements may be neglected. The second step is to keep the elastoplastic parameters constant and to fit the elastic and viscoelastic parameters to all experimental data. At this stage the model is rather close to its best fit. This viscoelastic fitting process could be accelerated using a complex calculation approach as done by (Tervonen 1995).

The final step is then to fit all material parameters to all experimental data, resulting in a minor adjustment of the material model.

4 Results

In this section the material model is fitted to experimental data from a hydrogeneted nitrile rubber (HNBR). The dynamic modulus and damping of HNBR is equaly dependent on both frequency and amplitude.

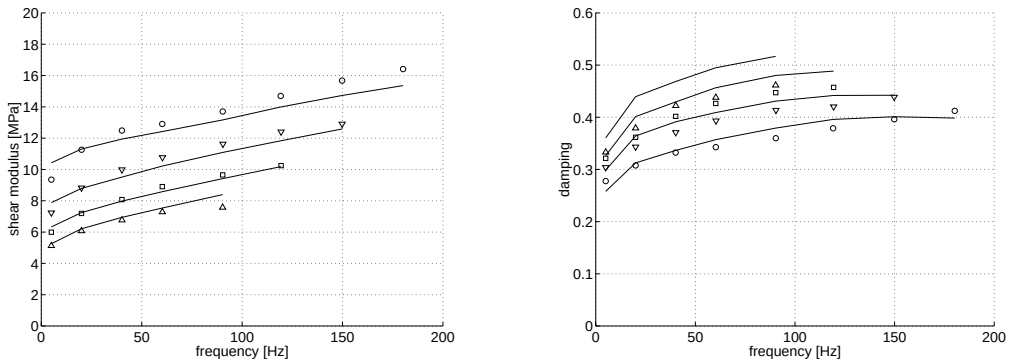

Figure 2: Left: Dynamic shear modulus of HNBR. Right: Damping properties of HNBR. Solid line: material model. Symbols: experimental data. $\bigcirc$: $\kappa_0 = 1\%$; $\bigtriangledown$: $\kappa_0 = 3\%$; $\square$: $\kappa_0 = 7\%$; $\bigtriangleup$: $\kappa_0 = 12\%$.

As seen in figure 2 the assumption of independence between amplitude and frequency behaviour is not entirely true. Thus, it is impossible to get a perfect fit to the dynamic shear modulus. In order to get a good fit to dynamic modulus a large k according to equation 2 was used. This results in a more moderate fit to the damping behaviour.

5 Conclusion

The material model has two basic limitations. Firstly, it assumes independence between frequency and amplitude. Secondary, it does not include any damage effects.

As earlier discussed, the assumption of independence between rate and amplitude behaviour is not entirely true. However, the error introduced in the model seems to be relatively small.

The second limitation means that the main use of the model is restricted to modeling conditioned rubber or rubber with neglectable damage properties. Out of the 13 tested rubber materials, only two filled natural rubber materials exhibited damage behaviour.

It can be concluded that the viscoelastic-elastoplastic material model is a good model for conditioned rubber or rubber with little or no damage effects.

REFERENCES

[1] P-E. Austrell, A.K. Olsson. *A Method to Analyze the Non-Linear Dynamic Behaviour of Carbon-Black-Filled Rubber Components Using Standard FE-codes.* Second European Conference on Constitutive Models for Rubber, Germany, (2001).

[2] P-E. Austrell. *Modeling of Elasticity and Damping for Filled Elastomers.* Lund University, Division of Structural Mechanics, Report TVSM-1009, Sweden, (1997).

[3] A.R. Johnson, T. Chen. *Modeling Step-Strain Relaxation and Cyclic Deformation of Elastomers.* NASA Langley Research Center Hampton, USA, (2000).

[4] M. Kaliske, H. Rothert. *Int. J. Solids Structures*, Vol. 35, No. 17, pp. 2057-2071, (1998).

[5] L. Kari, K. Lindgren. *Personal communications conserning tests.* MWL, KTH, Sweden, (2001).

[6] M. Tervonen. *From Measured Complex Modulus to Creep Compliance-Theory and Matlab Implementation.* Matlab Conference, University of Oulu, Finland, (1995).

[7] G.E. Warnaka. *Effects of Dynamic Strain Amplitude on the Dynamic Mechanical Properties of Polymers.* ASME Rubber and Plastics Div., Paper 62-WA-323, New York, (1962).

Damage induced Anisotropi in a Hyperelasto-Viscoplastic model with Mixed Hardening

Edin Omerspahic

Department of Structural Mechanics
Chalmers University of Technology, Göteborg, Sweden
e–mail: edin@sm.chalmers.se

Volvo Cars Corporation
Safety Centre, Crash Simulations, Göteborg, Sweden
e–mail: eomerspa@volvocars.com

ABSTRACT

Summary Hyperelasto-Viscoplastic Damage theoretical model with mixed hardening is developed for finite deformations. Damage (**D**) is given as an anisotropic damage by means of a fourth order transformation tensor (**M(D)**). The effective stress concept and the energy equivalence hypothesis provide the evolution of the mechanical properties of the continuum through the elastic stiffness degradation ($\mathbf{C}=\mathbf{M}^T\mathbf{C}_0\mathbf{M}$). The constitutive and evolution equations are derived from the Helmholtz free energy and the potential of dissipation, respectively.

Crash simulations by means of explicit FE codes are frequently used today in the automotive industry in order to guarantee crash safety of the cars. High strength steel and aluminium are materials, which become more and more used in the car structures. Materials like these are less ductile than the materials normally used today, and it is likely that rupture and separation in the material will occur in crash situations. Considering the materials in the automobile body as the virgin ones, the significance of continuum damage mechanics in order to discover initial flows of future cracks is very important.

The development of anisotropic damage can occur even if the virgin material is assumed to be isotropic. This is accomplished with the fourth order damage transformation tensor, **M**(**D**), where **D** is the second order damage tensor. In principal coordinates it is given by

$$\mathbf{D} = diag\left[d_{11} \quad d_{22} \quad d_{33}\right] \tag{1}$$

Chow and Wang [2] introduced the fourth order rank symmetric damage transformation tensor.

$$\mathbf{M} = diag\left[1-d_{11} \quad 1-d_{22} \quad 1-d_{33} \quad \sqrt{1-d_{22}}\sqrt{1-d_{33}} \quad \sqrt{1-d_{11}}\sqrt{1-d_{33}} \quad \sqrt{1-d_{11}}\sqrt{1-d_{22}}\right] \tag{2}$$

In index notation, this equation can be seen as

$$M_{ijkl} = \left(d_{ik} - d_{ik}\right)^{\frac{1}{2}}\left(d_{jl} - d_{jl}\right)^{\frac{1}{2}} \tag{3}$$

In order to facilitate easier derivation of constitutive and evolution equations, an approximation to this equation is introduced.

$$M_{ijkl} \approx \frac{1}{2}\left(d_{ik}d_{jl} + d_{il}d_{jk} - d_{ik}d_{jl} - d_{jl}d_{ik}\right) \tag{4}$$

The formulation of the damage transformation tensor presumes the acquaintance of the concept of the effective stress (Chaboche [1]), which states that the real stresses in damaged material are influenced by the damage, i.e.

$$\bar{\mathbf{s}} = \mathbf{M}^{-1}\mathbf{s} \tag{5}$$

The energy equivalence hypothesis (postulate by Cordebois and Sidoroff [3]), which states that the elastic energy for a damaged material is the same as the one in a fictitious undamaged material in which the stress is replaced by the effective stress ($w_e(\mathbf{s}, \mathbf{C}(\mathbf{D})) = w_e(\bar{\mathbf{s}}, \mathbf{C}_0)$), leads to an expression for the damaged stiffness tensor.

$$\mathbf{C}(\mathbf{D}) = \mathbf{M}(\mathbf{D})^{\mathrm{T}}\mathbf{C}_0\mathbf{M}(\mathbf{D}) \tag{6}$$

Making use of the index notation, performing multiplication and taking into consideration only first order damage dependence give us the "dynamic" expression for the stiffness tensor. The stiffness degradation is obvious during the damage propagation.

$$C_{ijkl} = \frac{1}{2}m\left(d_{ik}d_{jl} + d_{il}d_{jk}\right) + l\,d_{ij}d_{kl} - m\left(d_{ik}d_{jl} + d_{jl}d_{ik} + d_{il}d_{jk} + d_{jk}d_{il}\right) - l\left(d_{ij}d_{kl} + d_{kl}d_{ij}\right) \tag{7}$$

A physically transparent formulation of the finite viscoplasticity with mixed hardening can be defined on the stress free intermediate configuration, by means of the well-known multiplicative split of the deformation gradient, $\mathbf{F} = \mathbf{F}^{e}\mathbf{F}^{vp}$. The strain tensor on the intermediate configuration ($\bar{\mathbf{E}}$) is given by a push-forward of the Lagrangian strain tensor. This tensor can be additively decomposed into an elastic and a viscoplastic strain tensor ($\bar{\mathbf{E}} = \bar{\mathbf{E}}^{e} + \bar{\mathbf{E}}^{vp}$). The dual stress tensor corresponding to $\bar{\mathbf{E}}$ is the second Piola-Kirrchhoff tensor defined on the intermediate configuration ($\bar{\mathbf{S}}_2$), obtained by a push-forward of the same tensor given on the reference configuration.

The Helmholtz free energy is an energy potential function from which we derive the constitutive equations. For a hyperelasto-viscoplastic process with mixed hardening and damage it is a function of four variables: the elastic strain tensor, the damage tensor, the accumulated plastic strain scalar (k) and the back strain tensor ($\bar{\mathbf{z}}$). This energy function can be decomposed into three energy potentials: the elastic strain energy and the free energies due to isotropic and kinematic hardening, respectively.

$$y\left(\bar{\mathbf{E}}^{e}, \mathbf{D}, k, \bar{\mathbf{z}}\right) = w_e\left(\bar{\mathbf{E}}^{e}, \mathbf{D}\right) + y_{p}^{iso}\left(k\right) + y_{p}^{kin}\left(\bar{\mathbf{z}}\right) \tag{8}$$

The constitutive equations give the conjugated variables to them on which the energy potential depends: the second Piola-Kirrchhoff stress tensor, the damage energy release rate tensor ($\bar{\mathbf{Y}}$), the isotropic strain hardening scalar stress (R) and the back stress tensor ($\bar{\mathbf{X}}$).

$$\bar{\mathbf{S}}_2 = \frac{\partial w_e}{\partial \bar{\mathbf{E}}^{e}} = \mathbf{C}(\mathbf{D})\bar{\mathbf{E}}^{e} \tag{9}$$

$$\bar{\mathbf{Y}} = \frac{\partial w_e}{\partial \mathbf{D}} = \frac{1}{2}\bar{\mathbf{E}}^{e}\frac{\partial \mathbf{C}(\mathbf{D})}{\partial \mathbf{D}}\bar{\mathbf{E}}^{e} \tag{10}$$

$$R = \frac{\partial y_p^{iso}}{\partial k} = R_\infty \left(1 - e^{-dk}\right) \tag{11}$$

$$\bar{\mathbf{X}} = \frac{\partial y_p^{kin}}{\partial \bar{\mathbf{z}}} = k\bar{\mathbf{z}} \tag{12}$$

where R_∞, d and k are material parameters.

The evolution equations are derived from the potential of dissipation. The assumption is that the dissipated energy in plastic flow and damage process is uncoupled. In accordance with that, the dissipation potential consists of a plastic dissipation potential and a damage dissipation potential. Associated laws are suggested, i.e. both the plastic yield function (the von Mises yield criterion) and the damage yield function are taken for the plastic and damage dissipation potential, respectively.

$$f_p = \sqrt{\frac{3}{2}\left(\bar{\mathbf{P}}^D - \bar{\mathbf{X}}^D\right)\left(\bar{\mathbf{P}}^D - \bar{\mathbf{X}}^D\right)} - R - s_y \tag{13}$$

$$f_d = Y_{ekv} - Y_0 = \left[\frac{1}{2}\bar{\mathbf{Y}}^T \mathbf{J} \bar{\mathbf{Y}}\right]^{\frac{1}{2}} - Y_0 \tag{14}$$

where superscript ^{D} stands for deviatoric part of the tensors, $\bar{\mathbf{P}}$ is the Mandel stress tensor, s_y is the yield stress (material parameter), Y_0 is an energy release rate threshold (which must be overcome in order to accomplish the damage propagation), Y_{ekv} is the equivalent damage energy release rate and **J** is a suitable damage characteristic tensor. Hayakawa and alt. [4] define it as the fourth order tensor function, which describes the damage induced change of the damage surface. By noting that the damage dissipation potential is a symmetric function of each component of damage conjugated forces they defined it as

$$J_{ijkl} = \frac{1}{2}\left(d_{ik}d_{jl} + d_{il}d_{jk}\right) \tag{15}$$

Finally the evolution equations can be obtained. One should notice that the evolution equation for the back stress tensor is not derived from the dissipation potential, because the case of Armstrong-Fredrick kinematic hardening includes non-associated evolution law.

$$\overset{\Delta}{\bar{\mathbf{E}}}^{vp} = \dot{\lambda}_p \frac{\partial f_p}{\partial \bar{\mathbf{P}}} = \frac{1}{h_p}\left\langle f_p \right\rangle^m \sqrt{\frac{3}{2}} \frac{\bar{\mathbf{P}}^D - \bar{\mathbf{X}}^D}{\left\| \bar{\mathbf{P}}^D - \bar{\mathbf{X}}^D \right\|} \tag{16}$$

$$\dot{k} = -\dot{\lambda}_p \frac{\partial f_p}{\partial R} = \frac{1}{h_p}\left\langle f_p \right\rangle^m \tag{17}$$

$$\dot{\mathbf{D}} = -\dot{\lambda}_d \frac{\partial f_d}{\partial \bar{\mathbf{Y}}} = \frac{1}{2h_d}\left\langle f_d \right\rangle^p \frac{\mathbf{J}\bar{\mathbf{Y}}}{Y_{ekv}} \tag{18}$$

$$\overset{\nabla}{\bar{\mathbf{X}}} = c\,\overset{\Delta}{\bar{\mathbf{E}}}^{vp} - b\dot{\lambda}_p \bar{\mathbf{X}} \tag{19}$$

h_p, h_d, m, p, c and b are material parameters, $\kappa = \left[\frac{2}{3}\overset{\Delta}{\mathbf{E}}^{vp}\overset{\Delta}{\mathbf{E}}^{vp}\right]^{1/2}$ is the accumulated strain while $\overset{\nabla}{\mathbf{X}} = \overset{\circledast}{\mathbf{X}} - \overline{\mathbf{L}}^{vp}\overline{\mathbf{X}} - \overline{\mathbf{X}}\overline{\mathbf{L}}^{vpT}$ and $\overset{\Delta}{\mathbf{E}}^{vp} = \overset{\circledast}{\mathbf{E}}^{vp} + \overline{\mathbf{L}}^{vpT}\overline{\mathbf{E}}^{vp} + \overline{\mathbf{E}}^{vp}\overline{\mathbf{L}}^{vp}$ are contravariant and covariant Oldroyd rates of the stress and strain tensor, respectively.

The numerical model of the presented theoretical model is under construction.

REFERENCES

[1] Chaboche, J.-L.: Sur l'utilisation des variables d'etat interne pour la description du comportement viscoplastique et de la rupture par endommagement, *In Symposium Franco-Polonais Problemes Non-Lineaires de Mecanique,* Cracow, Poland, *Pages* 137-159, (1977)

[2] Chow, C.L. and Wang, J.: An anisotropic theory of elasticity for continuum damage mechanics, *International Journal of Fracture, Volume* **33**, *Pages* 3-16, (1987)

[3] Cordebois, J-P. and Sidoroff, F.: Damage induced elastic anisotropy, *Proceedings of the Euromech Colloquimum 115, Mechanical behaviour of Anisotropic Solids (edited by J.-P. Boehler), Colloques Internationaux du Centre National de la Recherche Scientifique, Netherlands, No* **295**, *Pages* 761-774, (1982)

[4] Hayakawa, K., Murakami, S. and Liu, Y. Irreversible thermodynamics theory for elastic-plastic-damage materials, *European Journal of Mechanics, A/Solids, Volume* **17**, *Issue* **1**, *Pages* 13-32, (1998)

[5] Lämmer, H. and Tsakmakis Ch.: Discussion of coupled elastoplasticity and damage constitutive equations for small and finite deformations, *International Journal of Plasticity, Volume* **16**, *Pages* 495-523, (2000)

[6] Simo, J.C. and Ju J.W. On continuum damage-elastoplasticity at finite strains, *Computational Mechanics, Volume* **5**, *Pages* 375-400, (1989)

[7] Zhu, Y. Y. and Cescotto S. A fully coupled elasto-visco-plastic damage theory for anisotropic materials, *International Journal of Solids and Structures, Volume* **32**, *Issue* **11**, *Pages* 1607-1641, (1995)

[8] Lemaitre Jean: *A Course on Damage Mechanics*, Springer-Verlag Berlin Heidelberg New York, ISBN 3-540-53609-4, Germany, (1992)

[9] Haupt Peter: *Continuum Mechanics and Theory of Materials*, Springer-Verlag Berlin Heidelberg New York, ISBN 3-540-66114-x, Germany, (2000)

[10] Simo J. C. and Hughes T. J. R.: *Computational Inelasticity, Interdisciplinary Applied Mathematics, Volume 7*, Springer-Verlag New York, Inc. ISBN 0-387-97520-9, USA, (1998)

Computational model for composites with anisotropic reinforcement

Janis Brauns
Department of Structural Engineering
Latvia University of Agriculture, Jelgava, Latvia
e-mail: braun@latnet.lv

ABSTRACT

Summary In designing of structural composite materials, numerical modelling is used as an approach to determine mechanical properties. Here structural wooden board was modelled as a multilayer system consisting of thin layers. To determine elastic and viscoelastic characteristics of the layer a method for estimation and analysis of the stressed state during deformation of structural element consisting of flat orthotropic viscoelastic platelet (fibre) and binder is developed.

Products of widespread and growing popularity are structural wooden boards and oriented strand boards (OSB). These are engineered products made by processing trees into strands or wafers, which are bonded together under heat and pressure with waterproof resin. To determine elastic and viscoelastic characteristics of structural element a method for determination and analysis of the stress state during deformation in calculation element with flat orthotropic fibres taking into account rheological characteristics of the fibre and binder (matrix), the content of components and the degree of anisotropy of fibres is developed.

The primary calculation element consists of an orthotropic fibre (reinforcement) with rectangular cross-section A_f , the dimensions of which are $b_f \times h_f$, the thickness of binder is h_m. Here and bellow, the index *f* refers to the fibre and index *m* to matrix. In the case of spraying the binder does not completely fill the space between the reinforcing elements. The complexity of the problem is magnified by the necessity of predicting the workability of the material with the time factor being taken into account [1].

In order to determine the strain characteristics of a structural element, i.e., the compliance tensor S_{ijkl} and its variations with the passage of time t at a given load, certain assumptions must be made. The calculation element is a macroscopically homogeneous orthotropic body, and there is a good coalescence at the sites of the fibre and sprayed binder. Additional stresses in the lateral directions x_2 and x_3, if stresses along the fibre (direction x_1) are applied, are small. During loading of the element in a lateral direction, the strains are proportional to the volume of the corresponding component of the material:

$$\varepsilon_{ij}(t) = \mu_f \varepsilon_{f\,ij}(t) + (1-\mu_f)\varepsilon_{m\,ij}(t) \quad (i, j = 2,3)\,, \tag{1}$$

where μ_f is volume fraction of reinforcement.

As the physical dependences for matrix and fibre we use the dependence of the linear heredity theory of creep (the Bolzmann-Volterra theory), which, using the integral operators, are written in the form

$$\varepsilon_{m\,ij}(t) = S_{m\,ijkl}\sigma_{m\,kl}(t) + \tilde{K}_{m\,ijkl}\sigma_{m\,kl}; \tag{2}$$

$$\varepsilon_{f\,ij}(t) = S_{f\,ijkl}\sigma_{f\,kl}(t) + \tilde{K}_{f\,ijkl}\sigma_{f\,kl} \quad (i, j, k, l = 1,2,3). \tag{3}$$

In the dependencies (2) and (3), the value of S_{ijkl} is determined by using technical constants of the densified wooden flakes and binder. The influence of the particle length l_f and discrete bonding is taken into account in finding the calculated value of the longitudinal modulus and the corresponding coefficients of the lateral strain $\nu_{f\,i1}$ (i= 2, 3). Here the reduction factor ψ is used, which is obtained from the dependence

$$\psi = \frac{\int_{l_{f\min}}^{l_{f\max}} \left[\frac{\tilde{\sigma}_{f1\max}}{\sigma_{f1\max}}(l_f) - \frac{\mathrm{th}(Dl_f/4)}{Dl_f/2} \right] Z(l_f)\,dl_f}{\int_{l_{f\min}}^{l_{f\max}} Z(l_f)\,dl_f}. \tag{4}$$

The factor ψ takes into account variable length of fibres l_f, statistical distribution of fibres with respect to length $Z(l_f)$ and incomplete bonding between fibres. The fibre stresses $\tilde{\sigma}_{f1}$ arise in the case of alternating regions with and without an ideal bond, σ_{f1} – in the case of an ideal bond. The value of coefficient D is found according to [2]. The effective values of modules in transversal directions E_{f2} and E_{f3} as well as Poisson's ratio ν_{f32} was determined according to the assumption of uniformity of the field of stresses and taking into account the binder volume.

The compliance tensor components $S_{iijj}(t)$ and stresses in material constituents are determined by solving a system of three linear equations, which in matrix form is written as

$$\mathbf{AX}(t) = \mathbf{B}(t). \tag{5}$$

The unknown vector components are the compliances and stresses, i.e.,

$$\mathbf{X}(t) = \left[S_{iijj}(t), \sigma_{m11}(t), \sigma_{f11}(t)\right]^{\mathrm{T}} \quad (i, j = 1,2,3). \tag{6}$$

The index "T" denotes transposition.

For the compliance S_{1111}(t) the matrix of the system **A** and vector **B**(t) are determined on the basis of physical equations and equilibrium equation during the action of σ_{11} = 1. They have the following form

$$\mathbf{A} = \begin{bmatrix} 1 & -1/E_m & 0 \\ 1 & 0 & -1/E_{f1} \\ 0 & 1-\mu_f & \mu_f \end{bmatrix}; \tag{7}$$

$$\mathbf{B}(t) = \left[\tilde{K}_{m1111}\sigma_{m11}, \tilde{K}_{f1111}\sigma_{f11}, 1\right]^{\mathrm{T}}. \tag{8}$$

During determination of the compliance $S_{1122}(t)$ we shall consider the deformation of a structural element by the action of stresses $\sigma_{22} = 1$. In this case, the matrices **A** and **B**(t) are determined by using physical equations for the main strains, main lateral strains, and the additional lateral strains of the binder and fibre, the equations for the simultaneity of strains for complete lateral strains, and equation for equilibrium for additional stresses. The form of matrix **A** coincides with (7), while vector **B**(t) is written as

$$\mathbf{B}(t) = \begin{bmatrix} -\dfrac{\nu_m(t)}{E_m} - \nu_m(t)\tilde{K}_{m2222}\cdot 1 + \tilde{K}_{m1111}\sigma_{m11} \\ -\dfrac{\nu_{f12}(t)}{E_{f2}} - \nu_{f12}(t)\tilde{K}_{f2222}\cdot 1 + \tilde{K}_{f1111}\sigma_{f11} \\ 0 \end{bmatrix}. \tag{9}$$

In the case of the action of stresses $\sigma_{22} = 1$, the component $S_{2222}(t)$ is also found. The matrices **A** and **B**(t) are formed using the dependence (1) for the main strains of the components of the material, the physical equations for the main strains, the complete main strains and lateral strains of the composite, and also the equation for simultaneity of strains in the lateral direction. The vector of the free terms has the form

$$\mathbf{B}(t) = \begin{bmatrix} \dfrac{\mu_f}{E_{f2}} + \dfrac{1-\mu_f}{E_m} + \mu_f\tilde{K}_{f2222}\cdot 1 + (1-\mu_f)\tilde{K}_{m2222}\cdot 1 - \\ -\nu_m(t)(1-\mu_f)\tilde{K}_{m1111}\sigma_{m11} - \nu_{f21}(t)\mu_f\tilde{K}_{f1111}\sigma_{f11} \\ -\dfrac{\nu_{f12}(t)}{E_{f2}} + \dfrac{\nu_m(t)}{E_m} - \nu_{f12}(t)\tilde{K}_{f2222}\cdot 1 + \nu_m(t)\tilde{K}_{m2222}\cdot 1 - \\ -\tilde{K}_{m1111}\sigma_{m11} + \tilde{K}_{f1111}\sigma_{f11} \\ 0 \end{bmatrix}, \tag{10}$$

but the system matrix can be given as

$$\mathbf{A} = \begin{bmatrix} 1 & (1-\mu_f)\dfrac{\nu_m}{E_m} & \mu_f\dfrac{\nu_{f21}}{E_{f1}} \\ 0 & 1/E_m & -1/E_{f1} \\ 0 & 1-\mu_f & \mu_f \end{bmatrix}. \tag{11}$$

The remaining compliances of this group are determined in a similar way, and because of their size are not given here.

The compliance in shear is estimated from the dependence of the change in the longitudinal force $F(x_1)$ in the fibre of finite length during shear loading. By numerical differentiation of function $F(x_1)$, the dependence of the change in the shear stresses for discrete bonding $\tau_m(x_1)$ and the length-averaged value of these stresses is found. In the case of short fibers and incomplete bonding the reduction factor χ for shear compliance is determined by the dependence

$$\chi = \frac{1}{\langle \tau_m \rangle^*} \frac{\int_{l_{f\min}}^{l_{f\max}} \langle \tau_m \rangle (l_f) Z(l_f) dl_f}{\int_{l_{f\min}}^{l_{f\max}} Z(l_f) dl_f}. \tag{12}$$

Here the value $<\tau_m>^*$ expresses the conditional level of the mean shear stress, if the fibre length is large and the bonding is ideal. During the action of shearing stresses $\sigma_{ij} = 1$ ($i \neq j$; $i, j = 1,2,3$), the components of the compliance tensor can be written as

$$S_{ijij}(t) = \mu_f S_{f\,ijij}(t) + (1-\mu_f) S_{m\,ijij}(t) \chi . \tag{13}$$

The averaging of the strain characteristics according to Foigt and Reuss [3, 4] in effect makes it possible to determine the lower and upper bonds of elastic and viscoelastic characteristics of composite material with anisotropic reinforcement.

REFERENCES

[1] A.M. Skudra, F.J. Bulavs und K.A. Rocens. *Kriechen und Zeitstandverhalten verstarkter Plasten*. VEB Dt. Verlag, Leipzig, (1975).

[2] J.A. Brauns and K.A. Rocens. Applied Model of a Composite with Incomplete Bonding and Finite Length of the Reinforcing Elements. *Mechanics of Composite Materials*, No 5, 868-875, (1991).

[3] R. M. Christensen. *Introduction to the Mechanics of Composites*. John Wiley & Sons, New York, (1979).

[4] A. Z. Lagzdins, V. P. Tamuzs, G. A. Teters and A. F. Kregers. *Method of Orientational Averaging in the Mechanics of Materials*. Longman Group VK, London, (1992).

Micro mechanics modelling of fibre composite materials

Kristian Stålne* **and Per Johan Gustafsson**
Division of Structural Mechanics
Lund University, Lund, Sweden
e–mail: kristian.stalne@byggmek.lth.se

ABSTRACT

Summary The mechanical performance of a wood fibre composite material is simulated using finite element analysis and a 3D micro-mechanics model. The fibre network geometry is created by an own developed preprocessor taking in account how the shape of a fibre is affected by the shape and location of the neighbouring fibres.

Predicting the mechanical properties of composite materials is a problem that has been subject to a great interest the past fifty years and it has renderd in number of analytical models [1]. With the development of the finite element analysis it has been made possible to perform more accurate analysis and to simulate more complex materials like wood fibre composites containing orthotropic cellulose fibres. Many finite element models for composite stiffness are using finite element analysis on a representative volume, most often containing a single fibre covered by a matrix material phase [2, 3]. These models are well motivated when dealing with short fibre composites with a low fibre volume fraction. For other fibre composites there is a significant influence on the shape of a fibre from the shape and location of the neighbouring fibres. The possibility of making large numerical models of composite materials is increasing with the performance of computers, making it possible to create advanced morphology-based fibre network composite models containing several fibres. Still, so far only simple, regular fibre geometries have previously been analysed using 3 dimensional FE analysis [4]. The present study relates to composite materials with random fibre networks with geometrical fibre-to-fibre interactions [5].

The present model uses an advanced fibre network preprocessor in order to simulate composites with long orthotropic fibres such as high pressure laminates, HPL, which are made up of layers of impregnated paper. The purpose of the model is to estimate all stiffness and hygroexpansion components of the composite material. The model is a 3D model and uses a square unit cell with a number of fibres modelled as orthotropic solid elements in a surrounding of an isotropic matrix material. The response of the unit cell is simulated while exposed to an increase in moisture content and to loading in the x-, y- and z-directions respectively. The hygroexpansion analysis is in direct analogy with thermal analysis and can as well be used for that purpose. The model parameters are the constituents mechanical properties and fibre geometry including fibre dimensions, fibre orientation distribution, volume fractions and how the fibres form when being placed on top of each other and then pressed together. The geometry of the fibre network is created in a preprocessor where the user can decide the location of every single fibre. This enables a good representation of the micro geometry of a fibre composite material.

Some assumptions are needed to simplify the problem. The composite is built up of discrete fibre-matrix plates, storeys, with equal height which means that all fibres are of equal thickness. There

is full adhesion between the fibres and the matrix material, and matrix material occupies all fibre-free space, i.e. there are no voids. The fibres are considered as long, i.e. no fibre ends in the middle of the unit cell, and the cross section has a rectangular shape since the HPL material is made of collapsed craft paper fibres. Constitutive relations for the fibres and matrix material are orthotropy and isotropy respectively and they are linear elastic with no time or rate effects.

The fibre network geometry preprocessor is written in Matlab-code. It generates Patran pcl-code for creation of fibre and matrix geometry in Patran. Placing of the fibres are made by mouse-clicking in a diagram. The first fibre will then cross the square in the lowest composite storey, the next fibre will in general cross the first fibre, climbing over it to the second storey according to a smooth third-degree polynomial spline. When a new fibre is added the preprocessor calculates all areas and points where it intersects with the previously placed fibres, giving the information of its form in the z-direction.

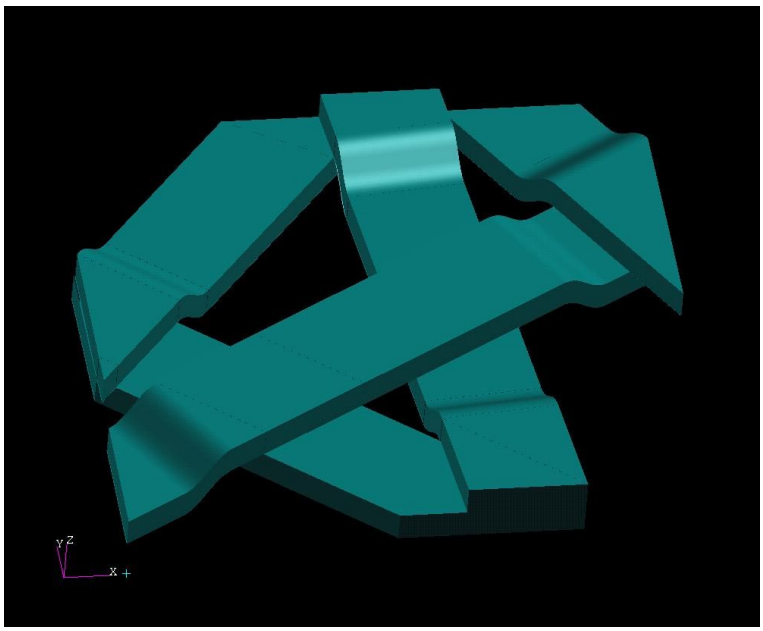

Figure 1: Five fibres in a network

As more fibres are added the geometry will typically be as shown in Figure 1. Figure 2 shows the corresponding shape of the matrix material, which together with the fibre geometry will form the unit cell.

The indata to the preprocessor is fibre dimensions, orientation, slope distance and number of fibres. This will control the maximum fibre density, i.e. the degree of fibre packing. Maximal hard packing of fibres is achieved by using large fibres with short slope distance and, most important, smartly placed. Each fibre added to the model makes it harder to pack to a high density. With five fibres a fibre volume ratio of 40 per cent is possible.

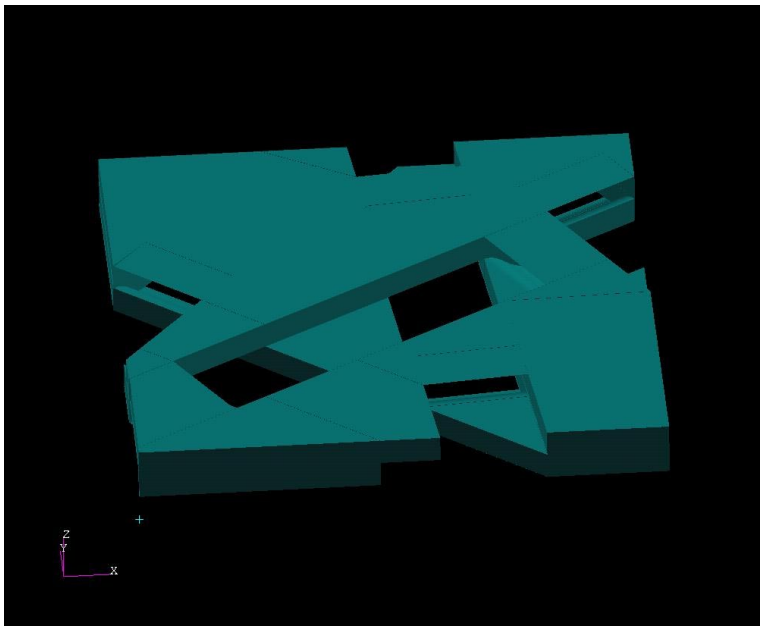

Figure 2: Corresponding matrix material geometry

The finite element mesh is generated by Patran, a finite element preprocessing software. The mesh is first generated to make surface elements which are extruded to the next storey to make them solid elements. The most difficult part is making the elements between two storeys compatible. This is achieved by dividing the matrix material areas into smaller sections. A more convenient way of creating the finite element model from the geometrical data would be by using a solid modeller instead of Patran.

The models results shows good agreement with experimental results from measurements of stiffness and hygroexpansion properties of HPL. Some comparisons are also made with a recent developed analytical model [6].

The fibre network preprocessor can be used in order to simulate larger composite network models with complicated geometries. The model can also be used to simulate fibre materials without any matrix material, like paper. Further development will enable use of nonlinear constitutive models like viscoplasticity and mechanosorption.

This work is financed by the Swedish Wood Technology Research Colleague.

REFERENCES

[1] J. Aboudi. *Mechanics of Composite Materials*, Elsevier, NY, USA.

[2] J.G. Bennett, K.S. Haberman. An alternative unified approach to the micromechanical analysis of composite materials. *J. Composite Mat.*, **16**, 1732–1747, (1996)

[3] D.S. Li, M.R. Wisnom. Michromechanical modelling of SCS-6 fibre reinforced Ti-6Al-4V under transvers tension - Effect on fibre coating. *J. Composite Mat.*, **5**, 561–588, (1996)

[4] A. Dasgupta, R.K. Agarwal, S.M. Bhandarkar. Three-dimensional modeling of wowen-fabric composites for effective thermo-mechanical and thermal properties. *Composites Sci. Techn.*, **56**, 209–223, (1996).

[5] K. Stålne, P.J. Gustafsson. A Three Dimensional Finite Element Fibre Network Model for Composite Material Stiffness and Hygroexpansion Analysis. *Proceedings to the 2nd European Conference on Computational Mechanics*, Cracow, Poland, June 26–29, (2001).

[6] K. Stålne, P.J. Gustafsson. A 3D Model for Analysis of Stiffness and Hygroexpansion Properties of Fibre Composite Materials. *Accepted for publication in the Journal of Engineering Mechanics, ASCE*, (2001).

Optimal Topology Design of Microstructures with a Constraint on Local Buckling Behaviour

Miguel M. Neves
IDMEC, Instituto Superior Técnico,Av. Rovisco Pais, 1, 1049-001 Lisboa, Portugal
e-mail: maneves@dem.ist.utl.pt

Ole Sigmund, Martin P. Bendsøe*
Technical University of Denmark, Building 404, DK-2800 Lyngby, Denmark
e-mail: sigmund@mek.dtu.dk , M.P.Bendsoe@mat.dtu.dk

ABSTRACT

Summary: The goal of the present work is to introduce a buckling performance criterion into the design of optimal topologies for periodic structures – assumed to be of infinite extent and linearly elastic. This is based on a linearized elastic buckling formulation for perfectly periodic microstructured materials. Some finite element results illustrate the idea and the influence on optimal microstrucures.

Introduction

Spatially periodic microstructures can be obtained by a periodic repetition of a base cell (also termed unit cell). The "averaged", homogenized or effective elastic properties can be found by the mathematical theory of homogenization (see, e.g., [1]). These elastic properties can be optimized by varying the size, the shape or the topology of the base cell using the techniques of structural topology optimization. Such an "inverse homogenization" can be found for example in [2-4]. A typical feature of a broad range of the optimal periodic microstructures obtained is that they are extreme in the sense of linear elasticity but will fail by local buckling at a microscale level. It is also characteristic for the "inverse homogenization" problem that it is possible to find several distinct periodic materials that represent equally optimal elastic properties. Thus, the material design process should allow for an improvement of the buckling performance of the base cell while maintaining the optimal elastic properties of the homogenized material.

The wavelengths of the buckling modes of structures built from materials with periodic microstructure can have several different length scales depending on the geometry, dimensions and loading of the medium. In the present paper we employ a simplified analysis problem covering only the case of highly localized modes. The linearized elastic buckling model is based on an Euler (eigenvalue) type of elastic buckling where the displacements prior to the first critical load at both macro- and microscale are assumed to be small and in the linear elastic range. This simple model captures the essence of the local instability phenomenon and results in a tractable topology optimization problem. The asymptotic model is based on the limit of infinitely small scale, i.e. the cell characteristic size is assumed to be much smaller than the characteristic size of the structure. Finally, it is assumed that the modes are Y-periodic, i.e. with the same periodicity as that of the base cell. This is related to our main concern of selecting an elastic buckling measure that characterizes if a cell is more or less prone to highly localized buckling modes. This buckling measure is subsequently used to introduce a local buckling load control as a constraint in the topology optimization of the base cell of periodic materials.

Linearized Stability Problem

In general terms, homogenization theory applied to linear problems establishes macroscopic

properties without any quantifiable size scale parameter. Here we briefly state a stability condition that is a local condition for an infinite medium that has stress-stiffening as the only non-linear effect. The problem of finding the first local (microscale) and Y-periodic eigenmode at the length scale of the base cell reduces to:

$$\int_Y E_{ijkm}(\mathbf{y})\frac{\partial u_i^{10}}{\partial y_j}\frac{\partial w_k}{\partial y_m}dY + P^Y\int_Y\left(E_{ijkm}(\mathbf{y}) - E_{ijpq}(\mathbf{y})\frac{\partial \chi_p^{km}}{\partial y_q}\right)\frac{\partial u_i^{00}}{\partial x_j}\frac{\partial u_c^{10}}{\partial y_k}\frac{\partial w_c}{\partial y_m}dY = 0,\ \forall w \in V_Y,$$

where P^Y is a *local scalar critical load factor* (stability parameter), $\mathbf{u}^{10}(y)$ is the correspondent *local Y-periodic eigenmode,* and $\mathbf{u}^{00}(\mathbf{x})$ and $\boldsymbol{\chi}^{km}$ (prebuckling displacements and corresponding local cell displacements) are the solutions of the standard linear homogenization problem. These fields describe the level and distribution of stress stiffening in the cell.

In the computations we use finite elements to solve this eigenvalue problem that takes the form:

$$(\mathbf{K}_Y - P^Y_r\,\mathbf{KG}_Y)\boldsymbol{\phi}^r = \mathbf{0},$$

where $\mathbf{K}_Y$ and $\mathbf{KG}_Y$ are the stiffness and geometric stiffness matrices, respectively, for the Y-periodic base cell and where Y-periodic eigenmodes are denoted $\boldsymbol{\phi}^r$.

Topology Design of Materials with a Local Stability Constraint

The topology design problem is stated as the search for an optimal distribution of a limited amount of material in the base cell domain, which maximizes a given linear combination of the homogenized elastic properties. To assure a reasonable local buckling performance, we introduce a lower bound on the local critical load value and assume that all buckling load factors are positive. Thus, the design problem is stated as:

$$\min_{\boldsymbol{\mu}} \quad -\beta_{ijkm}E^H_{ijkm} + \alpha\int_Y \boldsymbol{\mu}(\mathbf{y})(1-\boldsymbol{\mu}(\mathbf{y}))dY$$

$$\text{subject to: } P^Y \geq P_{min},\ \int_Y \mu(\mathbf{y})dY = V_0,\ 0 < \boldsymbol{\mu}_{min} \leq \boldsymbol{\mu} \leq \boldsymbol{\mu}_{max} = 1$$

where the constant tensor $\boldsymbol{\beta}$ defines the weighting of the material properties to be optimized and P_{min} is a lower bound on the local critical load value. The design variables are the local material densities represented by the vector $\boldsymbol{\mu}$ in the base cell and the total amount of material is V_0. The term $\alpha\int_Y \boldsymbol{\mu}(1-\boldsymbol{\mu})dY$ represents a penalization of intermediate densities imposed to obtain material distributions that are nearly black and white designs, i.e., designs with no intermediate density at the microlevel. Finally, the local material properties $E_{ijkm}(\boldsymbol{\mu}, \mathbf{y})$ in the base cell are expressed as $E_{ijkm}(\boldsymbol{\mu}, \mathbf{y}) = \left[\boldsymbol{\mu}(\mathbf{y})\right]^p E^o_{ijkm}$ (with p>1).

Computational Model and Examples

For the optimization result presented here we use the sequentially convex approximation method MMA (Method of Moving Asymptotes [5]). This has proven itself as an extremely efficient and reliable mathematical programming method for topology optimization in general.

For the buckling analysis of the base cell, the appearance of low-density regions may result in non-physical *localized modes in the low-density regions*, which are an artifact of the inclusion of these low-density regions that represent void in the analysis. In order to deal with this, a *stress filtering* is required to identify the physically relevant modes. This can be accomplished by reducing the stress level to an insignificant stress value in low density areas (see figure 1).

Finally, in order to control the geometric complexity in the optimized base cell, a *mesh independent filter* (cf. e.g. [2]) has been applied for some examples.
In figure 2 we show a comparison of the local buckling performance of different distributions of the same amount of material in the same base cell size. Of special interest are the cases 2 and 3 that include "chains of one-point connections".
The remaining examples consider the maximization of the homogenized in-plane bulk modulus k^H of a composite material. For the first results no mesh independent filter was used as it allows to clearly illustrate how the constraint on the minimum buckling performance results in a penalization of 'chains of one point connections' as well as checkerboard patterns. This should be expected on the basis of figure 2.
We note that here, and in the results below, the buckling constraint is not necessarily active at the computed (locally) optimal design. This is the case for small values of P_{min}, while higher values of P_{min} does imply that the buckling constraint is active. Even when not active at the optimum, the constraint does influence the result; it is active at the initial steps of the iterative optimization procedure and thus "steers" the computational procedure to a local optimum with buckling performance better than specified.
The geometric complexity or the mesh-dependency of the resulting designs can be controlled through the use of a mesh independent algorithm (filter), as mentioned above. Using this algorithm, small scale variations in the cell can be removed and figure 4-b) to 4-e) show examples of base cells obtained with this strategy.

Conclusions

In this work we have used an eigenvalue buckling criteria at the microscale level to characterize if a certain base cell of a periodic medium is more or less prone to highly localized buckling modes. When applied as a minimal local buckling performance requirement in design of microstructures, it improves the original model for optimizing linear elastic material properties because the stress stiffening effect penalizes the presence of slender members, checkerboard pattern regions and 'chains of one-point connections'.
Important issues remain to be analyzed. For future work, one can consider other macroscopic loading cases and a different parameterization of design in terms of structural elements, e.g. frame element models. Moreover, one should investigate the effect of evaluating the local critical load P^Y using more cells of the periodic medium. The use of Bloch waves and the analysis of solids of finite extent [6] are also of interest. However, these approaches do require a much more complex modelling and their use in an optimization context will be a challenge.

Acknowledgments

The authors are grateful to Prof. Krister Svanberg from the Royal Institute of Technology, Stockholm, for having supplied his MMA code, and to Alejandro Díaz from Michigan State University, Michigan, and the topology optimization groups at the Technical University of Denmark (DTU) and at Instituto Superior Técnico (IST), Lisbon, for fruitful discussions. This work has been sponsored by the Danish Research Academy, and by the European Research Training Network, "Homogenization and Multiple Scales" (HMS2000), Project RTMI-1999-00040.

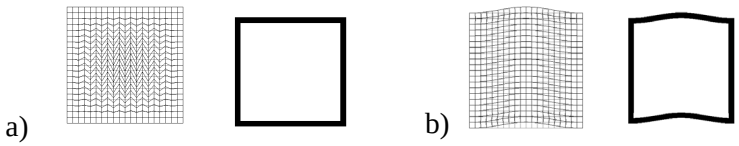

Figure 1. Instability modes for a macroscopic strain $\{-1 \quad 0 \quad 0\}$: (a) without and (b) with stress filtering.

Distribution case		1st mode	ρ	P^Y/E
Uniform			0.52	0.118
1			0.52	0.208
2			0.52	0.000
3	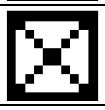	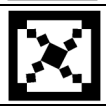	0.52	0.000

Figure 2: Comparison of different cells (Y-periodic mode, E is the Young modulus of the base material) for a macroscopic strain field given by $\{-1 \quad 0 \quad 0\}$.

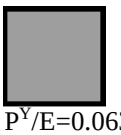
a) $P^Y/E=0.063$ $k^H=0.053$


b) $P^Y/E=0.04$ $k^H=0.149$

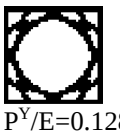
c) $P^Y/E=0.128$ $k^H=0.143$

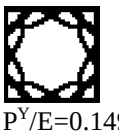
d) $P^Y/E=0.149$ $k^H=0.128$


e) $P^Y/E=0.199$ $k^H=0.136$

Figure 3 - a) Initial design, b) solution obtained without local buckling constraint, and solutions obtained with buckling constraint of: c) $P_{min}=0.10$, d) $P_{min}=0.15$ and e) $P_{min}=0.20$.


a) $P^Y/E=0.200$ $k^H=0.152$


b) $P^Y/E=0.176$ $k^H=0.152$


c) $P^Y/E=0.192$ $k^H=0.155$


d) $P^Y/E=0.203$ $k^H=0.155$


e) $P^Y/E=0.223$ $k^H=0.153$

Figure 4 - Solutions obtained with both mesh independent algorithm and buckling constraint for: a) $P_{min}=0.00$, b) $P_{min}=0.10$, c) $P_{min}=0.15$, d) $P_{min}=0.20$ and e) $P_{min}=0.225$.

References

[1] E. Sanchez-Palencia. *Non-homogeneous Media and Vibration Theory*. Lec. Notes Physics, 127, Springer, Berlin, (1980).

[2] O. Sigmund. Materials with Prescribed Constitutive Parameters: An Inverse Homogenization Problem. *Int. J. Solids Struct.* 31 (17), 2313-2329, (1994).

[3] O. Sigmund. Tailoring Materials with Prescribed Elastic Properties. *Mech. of Mat.* 20 (4), 351-368, (1995).

[4] E. Silva, S. Nishiwaki, J. Fonseca and N. Kikuchi. Optimization methods applied to material and flextensional actuator design using the homogenization method. *Comput. Methods Appl. Mech. Engrg*. 172, 241-271, (1999).

[5] K. Svanberg. The method of Moving Asymptotes – A new method for structural optimization. *Int. J. Num. Meth. Engrg.*, 24, pp. 359-373, (1987).

[6] N. Triantafyllidis and S. Bardenhagen. The influence of scale size on the stability of periodic solids and the role of associated higher order gradient continuum models. *J.Mech.Phys. Solids*, Vol.44, 11, pp.1891-1928, (1996).

Reliability and Collapse of Layered Shells; Numerical Procedure

U. Nyman* **and P. J. Gustafsson**
Division of Structural Mechanics
Lund University, Lund, Sweden
e–mail: ulf.nyman@byggmek.lth.se

ABSTRACT

Summary This paper is a merging of two categories of established methods, one for the analysis of stability and collapse of geometrically non-linear shells and one for the reliability analysis of structures using FORM. The formulation and implementation of a finite element procedure is described as well as the finite difference method in order to find the gradients of the limit state function. Numerical examples are performed on an in-plane loaded corrugated board panel involving uncertainties in geometrical imperfection, material properties and load.

Thin structures such as laminated shells has been extensively investigated by the use of the finite element method during the last decades. Numerous work is presented, where the aim is to formulate a shell element which can be used for response analysis of general shell structures. Since the degenerated shell element was presented [1], this type of formulation has formed a basis for the development of procedures for as well small as finite shell deformations. Its popularity is due to the straightforward representation of geometry and kinematics, nevertheless including the effect of transverse shear deformations. However, the simple assumption of kinematics leads to deteroriating performance when the thickness decreases, which is known as shear locking. To overcome this shortcoming work has been done in order to reduce the locking effect, e.g. reduced integration techniques, [2, 3], and formulations based on assumed strain, [4, 5].

In many applications it is from a lifetime and economic perspective important that a structure under consideration possesses a suitable degree of safety, i.e. the structure should withstand loads under normal conditions, but nevertheless, it must not be exceedable dimensioned in order keep house with resources. One example, which is the focus of this work, is corrugated board packages as, for example, used for the distribution of consumer goods. Corrugated board is a material which to a large extent incorporates uncertainties, manifested as well in material properties, geometrical properties and load conditions under handling. In a reliability analysis, the variables affecting the performance of the structure, called basic variables, are depicted probabilistic measures, i.e. mean and variance. The outcome of the analysis is the share of structures that will fail encountering certain load conditions. The purpose of this paper is to merge two categories of established methods, one for the analysis of stability and collapse of geometrically non-linear shells and one for the reliability analysis of structures using FORM.

The different techniques excisting for reliability analysis can be categorized as either exact or approximate, where in the latter case, some error is inferred from a simplified representation of variation of stochastic variables. Among the exact methods are multifold integration and Monte Carlo simulation techniques. Examples of approximate techniques are methods involving response surface fitting and FORM/SORM (First/Second Order Reliability Methods. The exact methods are numerically intensive and in the analysis of structures, e.g. by the finite element method, the computational cost may be prohibitively large. This is certainly expressed for problems which are numerically intensive in the deterministic case, for example as in non-linear finite element analysis.

In this work, FORM is used together with a geometrically non-linear finite element procedure for the collapse analysis of in-plane loaded shells.

In using FORM, a limit state function is expressed in terms of the structural resistance and the load. This limit state function represents a n-dimensional surface in the basic variable space. The limit surface can then be mapped into the standard uncorrelated normal space of the basic variables, as proposed in [6]. The idea in FORM is to approximate the limit state surface by a tangent hyper-plane at the design point, which is the point at the limit surface closest to the origin. At this point the frequency function of the standard normal variables is most dense, i.e. it provides the largest contribution to the probability content. The design point can be found by an iterative minimization procedure, e.g. as described in [7], and the distance from the origin to the design point is referred to as the reliability index, which provides a first order measure of the probability of failure. Typically, the convergence of the iterative procedure is very fast, even though the basic problem involve strong non-linear properties. In the figure below an example of the convergence of the limit state function is shown, where g is the difference between the failure stress and evaluated stress. The failure probability level for the postbuckling problem is in this case 4×10^{-4}. The application of reliability methods to the finite element method is currently subject for intensive research activities and examples of work done in this area [8, 9, 10, 11, 12].

The iterative procedure for finding the design point involves finding the gradient of the limit state function. The gradient can be found either analytically, as was done in [10] for the case of truss elements and four node plane elements, or numerically. The advantage of an analytically derived gradient is of course the computational fastness, nevertheless, at the expense of the generality in the code. Herein, a finite difference technique is used in order to find the gradient. A Newton Raphson procedure is used for calculation of the response at the current values of the stochastic variables. This point is subsequently used as a start point for the new values of variables and equilibrium iterations are anew performed. It can be noted that all the variables in the non-linear finite element equation are functions of the stochastic variables. For example, the strain-displacement matrix varies as a function of the geometrical imperfections.

The structure analyzed in this work is an in-plane loaded corrugated board panel. The analysis is part of a larger project devoted to reliability design of corrugated board packages. Failure is assumed to take place in either of the facings due to material failure or local buckling and the failure criterion presented in [13] is used for the analysis. The stability behaviour of the panel is analyzed by several numerical examples. The variable uncertainties studied are for example the magnitude of the geometrical imperfection of the panel, material properties such as strength and stiffness, and load magnitude.

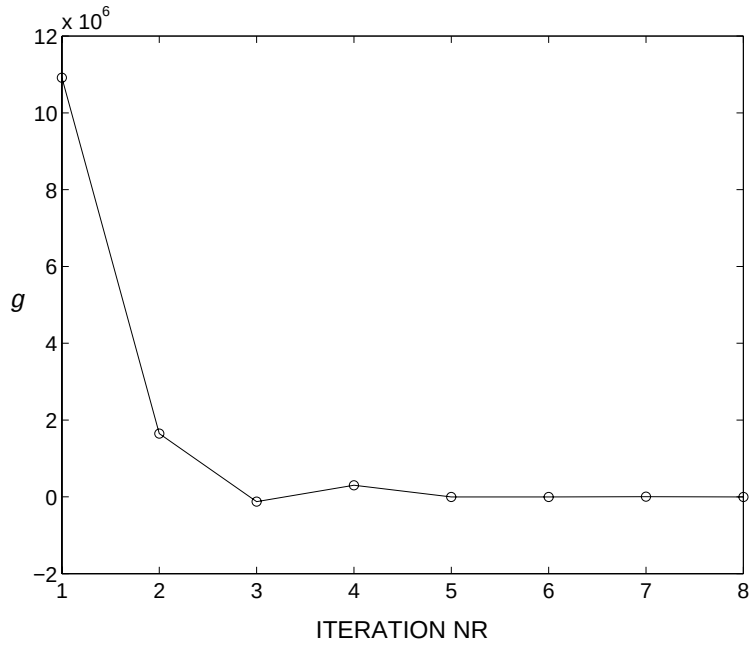

Figure 1: Convergence of the limit state function.

REFERENCES

[1] S. Ahmad et. al. Analysis of thick and thin shell structures by curved finite elements, *Int. J. Numer. Meths. Eng.*, 2, 419-451, (1970).

[2] O. Zienkiewicz et. al. Reduced integration technique in general analysis of plates and shells, *Int. J. Numer. Meths. Eng.*, 3, 275-290, (1971).

[3] H. Parish. A critical survey of the 9-node degenerated shell element with special emphasis on thin shell application and reduced integration, *Comput. Meth. appl. Mech. Eng.*, 20, 323-350, (1979).

[4] E. N. Dvorkin and K. J. Bathe. A continuum based four-node shell element for general non-linear analysis, *Engineering Computation*, 1, 77-88, (1984).

[5] H. C. Huang and E. Hinton. A new nine node degenerated shell element with enhanced membrane and shear interpolation, *Int. J. Numer. Meths. Eng.*, 22, 73-92, (1986).

[6] A. M. Hasofer and N. C. Lind. An Exact and Invariant First Order Reliability Format, Proc. ASCE, *J. Eng. Mech. Div.*, pp 111-121, (1974).

[7] H. O. Madsen, S. Krenk and N. C. Lind. *Methods of Structural Safety*, Prentice-Hall, New Jersey, (1986).

[8] D. M. Frangopol, Y-H. Lee and K. J. Williams. Nonlinear Finite Element Reliability Analysis of Concrete, *J. Eng. Mech.*, Vol. 122, No. 12., (1996).

[9] P-L. Liu and K-G. Liu. Selection of Random Field Mesh in Finite Element Reliability Analysis, *J. Eng. Mech.*, Vol. 119, No. 4., (1993).

[10] P-L. Liu and A. Der Kiureghian. Finite Element Reliability of Geometrically Nonlinear Uncertain Structures, *J. Eng. Mech.*, Vol. 117, No. 8., (1991).

[11] X. L. Guan and R. E. Melchers. A Load Space Formulation for Probabilistic Finite Element Analysis of Structural Reliability, *Probabilistic Engineering Mechanics*, 14, pp 73-81., (1999).

[12] F. Viadero, J. I. Bueno, L. N. Lopez de Lacalle and R. Sancibrian. Reliability Computation on Stiffened Plates, *Advances in Engineering Software*, **20**, pp 43-48., (1994).

[13] U. Nyman and P. J. Gustafsson. Material and Structural Failure Criterion of Corrugated Board Facings, *Composite Structures*, **50**(1), (2000).

Sensitivity gradients computations for the homogenized elastic properties of fiber-reinforced composites

Marcin Kamiński
Division of Mechanics of Materials, Technical University of Łódź
Al. Politechniki 6, 93-590 Łódź, Poland, tel/fax 48-42-6313551
e–mail: marcinka@ck-sg.p.lodz.pl, webpage: http://kmm.p.lodz.pl/Marcin_Kaminski

ABSTRACT

Summary The paper is devoted to the computational studies on the sensitivity coefficients of the homogenized elasticity tensor of the fiber-reinforced periodic composites. The general methodology is based on the Central Difference Method (CDM) implemented in the Finite Element Method (FEM) homogenization-oriented MCCEFF computer system. The sensitivity functional is proposed as the elastic strain energy stored in the homogenized system to approximate the sensitivity of the entire composite structure in various elasticity problems.

As it is known, the sensitivity analysis in engineering systems is employed to verify how input design parameters of a specific engineering problem influence the analyzed state functions. The sensitivity coefficients (or gradients) [1,2], being the purpose of such an analysis, are computed using partial derivatives of the considered state function with respect to the particular input parameter. The main goal is in our case to carry out the general computational sensitivity studies of the homogenized elasticity tensor for the fiber-reinforced composites with linear elastic and transversely isotropic constituents. The composite is first homogenized - the effective material tensor components are computed using the FEM-based additional computer program. Then, material parameters of the composite most decisive for its effective material properties are determined numerically using special algorithm based on the Finite Difference approach. The sensitivity analysis introduces a new aspect of the homogenization technique – it can be verified if the homogenized and original structures have the same or even analogous (in terms of their signs) sensitivity gradients. Therefore, if for instance the sensitivity analysis show that most of the sensitivity coefficients with respect to composite material parameters are negative, then the homogenization theory should be essentially corrected.

The effective (homogenized) tensor $C_{ijkl}^{(eff)}$ is determined from the following equation:

$$C_{ijpq}^{(eff)} = \frac{1}{|\Omega|}\int_{\Omega} C_{ijpq}\,d\Omega + \frac{1}{|\Omega|}\int_{\Omega} C_{ijkl}\varepsilon_{kl}\left(\chi^{(pq)}\right)d\Omega, \tag{1}$$

where $\chi^{(11)}$, $\chi^{(12)}$ and $\chi^{(22)}$ denote some specific homogenization displacement fields. Next, the sensitivity gradients of effective elasticity tensor components with respect to the design parameters vector represented by $\mathbf{h}$ are computed as

$$\frac{dC_{ijpq}^{(eff)}}{d\mathbf{h}} = \frac{\partial}{\partial \mathbf{h}}\left\{\frac{1}{|\Omega|}\int_{\Omega} C_{ijpq}\,d\Omega\right\} + \frac{\partial}{\partial \mathbf{h}}\left\{\frac{1}{|\Omega|}\int_{\Omega} C_{ijkl}\varepsilon_{kl}\left(\chi^{(pq)}\right)d\Omega\right\}, \tag{2}$$

The most interesting problem however is not to determine the sensitivity coefficients of the effective tensor with respect to particular composite parameters but to approximate the sensitivity of the entire structure to these parameters. So that, let us define the sensitivity functional as the strain energy of the homogenized composite under combination of the uniform constant strains in x and y directions as well as under the transverse strain ε_{xy}. It can be shown that therefore, the partial derivatives of G with respect to the design parameter 'h' can be calculated as

$$G^{.h} = \frac{\partial G}{\partial h} = \frac{\partial l^2}{\partial h}\left\{C_{1111}^{(eff)} + C_{1122}^{(eff)} + 2C_{1212}^{(eff)}\right\} + l^2\left\{\frac{\partial C_{1111}^{(eff)}}{\partial h} + \frac{\partial C_{1122}^{(eff)}}{\partial h} + 2\frac{\partial C_{1212}^{(eff)}}{\partial h}\right\}. \qquad (3)$$

Using this formula the most decisive design parameter for the homogenized composite for the uniform plane strain can be determined from the computed effective elasticity tensor gradients. This definition is tested for the fiber-reinforced composite with the fiber having round cross-section, while the entire cell is rectangular (reinforcement ratio is equal to 50%, e_1=84.0 GPa, e_2=4.0 GPa, ν_1=0.34 and ν_2=0.22). All computational tests are done by the use of the specially tailored computer program MCCEFF, designed and implemented for deterministic and stochastic homogenization-based computational studies.

Tab. no 1. Averaged sensitivity gradients

h	$\frac{\partial C_{1111}^{(eff)}}{\partial h}$	$\frac{\partial C_{1122}^{(eff)}}{\partial h}$	$\frac{\partial C_{1212}^{(eff)}}{\partial h}$	$G^{.h}$
$\mathbf{e_1}$	0.141	0.072	0.958	**2.129**
$\boldsymbol{\nu_1}$	0.056	0.180	-0.173	**-0.090**
$\mathbf{e_2}$	0.867	0.926	0.044	**1.881**
$\boldsymbol{\nu_2}$	1.205	2.814	-0.011	**3.987**

Finally, the approximation of the gradients by some specific numbers is done by the arithmetic average of the values corresponding to 1% and 10% increments of the design parameters in Finite Difference computations. These values are used to approximate the value of $G^{.h}$ what follows the unstable behavior of these gradients [1,2]. Using such an approximation, the Poisson's ratio of a matrix and next Young's modulus of the fiber are detected as the most decisive design material parameters of this composite in the view of its homogenized elastic parameters.

REFERENCES

[1] M. Kamiński. On sensitivity of effective elastic moduli for fibre-reinforced composites. *Comm. Num. Meth. Engrg.*, **17(2)**, 127–135, (2001).

[2] M. Kamiński. Material sensitivity analysis in homogenization of the linear elastic composites. *Archive of Applied Mechanics*, (in press).

The Minimization of Stretches in Diode-Pumped Solid-State Laser

F. Ivanauskas*
Department of Mathematics and Informatics
Vilnius University, 2600 Vilnius, Lithuania
Institute of Mathematics and Informatics
E-mail: Feliksas.Ivanauskas@maf.vu.lt

J. Dabulytė
Department of Mathematics and Informatics
Vilnius University, 2600 Vilnius, Lithuania
Kaunas Technology University
E-mail: jurdabu@one.lt

L. Giniūnas
Laser Research Centre
Vilnius University, 2040 Vilnius, Lithuania
E-mail: Linas.Giniunas@ff.vu.lt

ABSTRACT

Summary: In this report we present a mathematical model of the diode-pumped solid- state laser cooling system for minimization of the thermal gradients in the laser material. Particular attention was drawn to the compensation of the thermal expansion and the thermal stretches.

Due to the specific nature of some laser materials, e.g. ytterbium doped YAG crystal high intensity pump beams are required to achieve sufficient inversion in the laser material. However part of the pump power is transformed into heat in a small volume of the active media. Thermal effects caused by the heat are limiting the efficiency of the laser. Recently, optimal design of a diode-pumped laser was theoretically and experimentally investigated [1-5], where the pump and laser mode sizes relation and the deformation of laser was considered. Particular attention was drawn to the design of the laser cavity and pressure compensation of the thermal expansion.

In this report we present a mathematical model of the diode-pumped solid-state laser cooling system for minimization of the thermal gradients in the laser material. The schematic view of the laser is presented in Figure 1.

In this work, we analyze the model in which the additional cooling is taken into account (thermal effects in the laser may cause the laser deformation or even laser decomposition). Namely if the thermal stretches $\Delta l_{li} = l_i C_i (t - t_0) > \Delta_{0i}$, $i = 1,2,3$, then we can observe the laser deformation (this is a limiting factor for the efficiency of the laser). On the other hand, if the thermal stretches $\Delta l_{li} > \Delta_{1i}$, $i = 1,2,3$, it may cause the laser decomposition. Here C_i are the thermal expansion coefficients, t temperature in the crystal, t_0 initial temperature, l_i measures of the crystal, Δ_{0i} and Δ_{1i} are limit values of stretches. The minimization problem of

stretches in a diode-pumped solid-state laser is transformed to the minimization problem of the cooling in laser crystal.

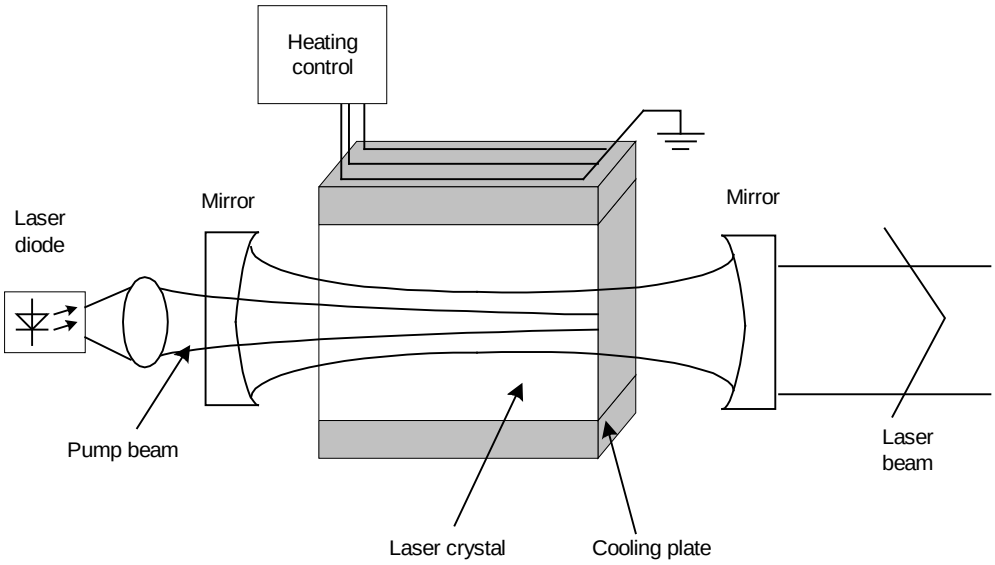

Figure 1. Schematic view of the end pumped laser with cooling system

The mathematical model of the temperature regime in the crystal is based on heating equation with mixed boundary conditions. The model can be written as differential equation

$$\frac{\partial u}{\partial t} = D_1 \frac{\partial^2 u}{\partial x^2} + D_2 \frac{\partial^2 u}{\partial y^2} + D_3 \frac{\partial^2 u}{\partial z^2} + \frac{f(x,y,z)}{Q \cdot \rho},$$

where u is temperature, t is time, $f(x,y,z)$ is the light source, D_1, D_2 and D_3 are the diffusion coefficients, Q is the specific heat and ρ is the crystal density.
Below, we describe initial and boundary conditions.

Initial condition $(t = 0)$:

$$u\big|_{\Omega} = u(0,x,y,z) = u_0,$$

where u_0 is the chosen or room temperature and $\Omega = \{0 \le x \le a,\ 0 \le y \le b,\ 0 \le z \le c\}$ is the whole investigated area.

Boundary conditions *(t>0)*:

$$\left.\frac{\partial u}{\partial x}\right|_{x=0;x=a} = 0, \quad \left.\frac{\partial u}{\partial z}\right|_{z=0;z=c} = 0, \quad u\big|_{y=0;y=b} = \varphi(x,y).$$

Here a is crystal width, b crystal height and c crystal length.

The first two boundary conditions mean full isolation and the third means cooling. The temperature in the crystal increases when the laser beam shoots to the crystal. Because of the increasing temperature, the crystal can be deformed or simply decomposed. In order to avoid this we have to place over and under the crystal refrigeration plates. The function $\varphi(x, y)$ describes refrigeration process in the laser crystal. Since the biggest temperature is in the middle of the crystal, i.e., $x = \frac{a}{2}$, so the functions $\varphi(x, y)$ will also attain its minimum value there. The function $\varphi(x, y)$ has to minimize temperature gradients.

For simplicity we investigate the optimization problem in two dimensions. When the crystal is lightened by the lighting source, it is important that the temperature gradients

$$\max_{[0,a]}\left|\frac{\partial u}{\partial x}\right|, \qquad \max_{[0,b]}\left|\frac{\partial u}{\partial y}\right|$$

would not be too big.

For us, the most important temperature gradient is $\max_{[0,a]}\left|\frac{\partial u}{\partial x}\right|$. So the minimization problem was to find

$$\min_{\varphi(x)} \max_{[0,a]}\left|\frac{\partial u}{\partial x}\right|.$$

Some problems arise when we solve analytically the differential equation with such boundary conditions. Therefore, we solved our mathematical model numerically. The finite – difference technique [6] was used for the discretization of the model. This technique allows us to solve effectively the differential equation with mixed boundary conditions.

The numerical analysis was made with the following values: crystal width $a = 3\,mm$, crystal height $b = 0.5\,mm$, specific heat $Q = 0.5\,J/(gK)$, crystal density $\rho = 0.00717\,g/mm^3$, initial temperature $u_0 = 20\,K$, thermal conductivity coefficients $k_1 = k_2 = k_3 = 0.003\,W/(mmK)$, power $P = 2.4\,W$, quantum defect $K = 7\,\%$, $\alpha = 0.8\,mm$, $\beta = 0.1\,mm$, $\gamma = 1.7\,mm$.

The minimization process was performed as follows: the function $\varphi(x)$, which means cooling, was chosen for the temperature gradient in the x direction, to satisfy the inequality $\max_{[0,a]}\left|\frac{\partial u}{\partial x}\right| \le 5\frac{K}{mm}$. First of all the function $\varphi(x)$ was chosen to be a constant: $\varphi(x) = u_0 = 20K$. That means that the top and the bottom of the crystal are evenly cooled (from the physical point of view, it is the simplest system of cooling). Our calculations show

that the maximum temperature gradient in the crystal was $\max_{[0,a]}\left|\frac{\partial u}{\partial x}\right| = 8.90\,K/mm$. Then the constant value $\varphi(x) = 20K$ was replaced by the parabola

$$\varphi(x) = -4\frac{u_0 - u_1}{a^2}x^2 + 4\frac{u_0 - u_1}{a}x + u_1.$$

The minimal temperature gradient was obtained for $u_1 = 27\,K$ and the parabola was $u = \frac{28}{9}x^2 - \frac{28}{3}x + 27$. Then we used this parabola in the minimization process by changing parabola values in some net points. The gradients were calculated for $y = \frac{b}{2}$ in the places, where they were big, we corrected the values of the function $\varphi(x)$. This process allowed us to reduce the previous value of $8.90\,K/mm$ to a lower level of $2.08\,K/mm$ (see Fig. 2).

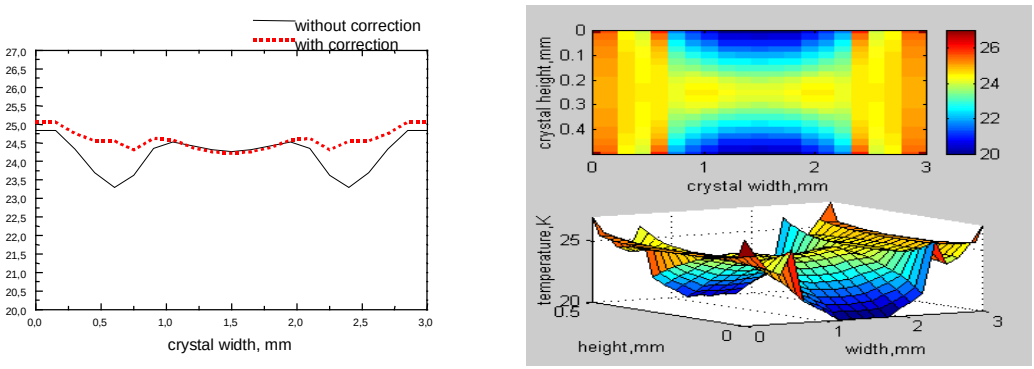

Figure 2. The temperature distributions in the crystal

REFERENCES

[1] T. Y. Fan. Heat generation Nd:YAG. *IEEE J of Quantum Electronics*, **29**, 1457-1459, (1993).

[2] W. Koechner. *Solid State Laser Engineering*, 4th ed. Springer-Verlag, Berlin, p.396 (1996).

[3] Yung-Fu Chen. Pump-to mode size ratio dependence of thermal loading in diode–end-pumped solid–state–lasers. *J. Opt. Soc. Am. B 17*, 1835-1840, (2000).

[4] K.-M. Du, N. Wu, J. Xu, J. Giesekus, P. Loosen, R. Poprawe. Partially end pumped Nd:YAG slab laser with a hybrid resonator. *Opt. Lett.*, 23, 370-372 (1998).

[5] Y. Liao, R. J. D. Miller, M. R. Armstrong. Pressure tuning of thermal lensing for high - power scaling. *Opt.Lett.*, ***24***, 1343-1345 (1999).

[6] A. A. Samarskii. *The Theory of Difference Schemes*, Nauka, Moscow, (1989) (in Russian).

Optimization of stepped conical shells of von Mises material

J. Lellep* and E. Puman
Institute of Applied Mathematics
Tartu University, Tartu, Estonia
e–mail: lellep@math.ut.ee

ABSTRACT

Conical shells of piece wise constant thickness are considered. The shells are simply supported at the outer edge and subjected to the uniform lateral pressure loading. Optimal designs are established assuming that the material of shells obeys von Mises yield condition.

1. Introduction

Limit analysis of rigid-plastic conical shells was studied by Hodge [2] in the case of the Tresca's yield condition. Much less light has been shed on the load carrying capacity of shells made of von Mises material. Bryant, Lee and Mura [1] suggested a variational method for lower bound analysis of plastic conical shells. In the earlier works by the authors [3, 4] optimal designs have been established for conical shells in the case of a Tresca material. In the present sudy the optimization technique used in [5] for optimization of plastic spherical shells is accomodated for conical shells subjected to the lateral pressure.

2. Formulation of the problem and basic equations

Consider a conical shell (Fig.1) subjected to the uniformly distributed lateral pressure. Assume that the thickness is piece wise constant, e.g.

$$h = h_j$$

for $r \in (a_j, a_{j+1}); \quad j = 0,...,n.$

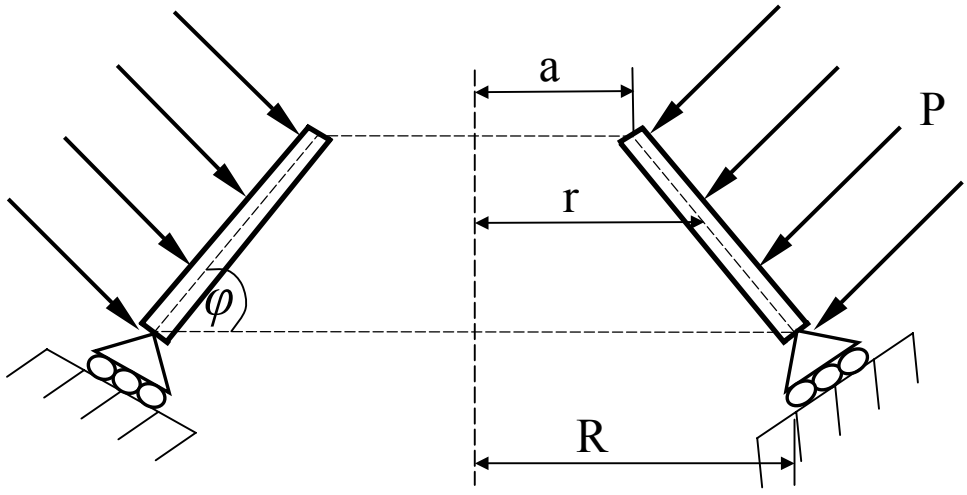

Fig. 1 Conical shell subjected the uniformly distributed lateral pressure

We are looking for the design of the shell corresponding to the maximum load carrying capacity for given weight of the structure. Thus the material volume

$$V_0 = \sum_{j=0}^{n} h_j \left(a_{j+1}^2 - a_j^2\right) \cdot \frac{\pi}{\cos\varphi} \tag{1}$$

is assumed to be given.

Due to symmetry the stress state of the shell is defined by membrane forces N_1, N_2 and moments M_1, M_2. Equilibrium equations of a shell element may be presented as

$$\begin{cases} \dfrac{d}{dr}\left(rN_1\right) - N_2 = 0, \\ \dfrac{d}{dr}\left[\dfrac{d}{dr}\left(rM_1\right) - M_2\right] + N_2 \dfrac{\sin\varphi}{\cos^2\varphi} + \dfrac{\mathrm{Pr}}{\cos^2\varphi} = 0. \end{cases} \tag{2}$$

The corresponding strain rate components are

$$\begin{aligned} \dot{\varepsilon}_1 &= \frac{d\dot{U}}{dr}\cos\varphi, \qquad \dot{\varepsilon}_2 = \frac{1}{r}\left(\dot{U}\cos\varphi + \dot{W}\sin\varphi\right), \\ \dot{\kappa}_1 &= -\frac{M_0}{N_0}\frac{d^2\dot{W}}{dr^2}\cos^2\varphi, \qquad \dot{\kappa}_2 = -\frac{M_0}{N_0}\cdot\frac{d\dot{W}}{dr}\cos^2\varphi. \end{aligned} \tag{3}$$

In (2) $\dot{U}$ and $\dot{W}$ stand for displacement rates in the normal and circumferential directions, respectively, whereas $M_0 = \sigma_0 h^2/4, N_0 = \sigma_0 h, \sigma_0$ being the yield stress of the material.

In the case of a distributed loading it is reasonable to introduce the following nondimensional quantites:

$$\begin{aligned} &\rho = \frac{r}{R}, \qquad \alpha_j = \frac{a_j}{R}, \qquad \gamma_j = \frac{h_j}{h_*}, \\ &\mathrm{v} = \frac{h}{h_*}, \quad k = \frac{M_* \cos^2\varphi}{RN_* \sin\varphi}, \qquad \mathrm{w} = \frac{W}{R}, \\ &u = \frac{U}{R}, \qquad n_{1,2} = \frac{N_{1,2}}{N_*}, \qquad m_{1,2} = \frac{M_{1,2}}{M_*}, \quad p = \frac{PR}{N_* \sin\varphi}. \end{aligned} \tag{4}$$

In (4) M_* and N_* stand for the limit moment and limit load for the reference shell of constant thickness h_*. Thus $M_* = M_0\big|_{h=h_*}$, $N_* = N_0\big|_{h=h_*}$. In variables (4) the equilibrium equations (2) take the form

$$\begin{cases} \left(\rho n_1\right)' - n_2 = 0, \\ k\left[\left(\rho m_1\right)' - m_2\right]' + n_2 + p\rho = 0. \end{cases} \tag{5}$$

where the primes denote differentiation with respect to ρ. Making use of (4) the strain rate components may be presented as

$$\begin{aligned} \dot{\varepsilon}_1 &= \dot{u}\cos\varphi, \qquad \dot{\varepsilon}_2 = \frac{1}{\rho}\left(\dot{u}\cos\varphi + \dot{w}\sin\varphi\right), \\ \dot{\kappa}_1 &= -k_0\,\dot{w}''\sin\varphi, \qquad \dot{\kappa}_2 = -\frac{k_0}{\rho}\dot{w}'\sin\varphi, \end{aligned} \tag{6}$$

where

$$k_0 = \frac{M_0 \cos^2 \varphi}{RN_0 \sin \varphi}. \tag{7}$$

Boundary conditions for stress components are following

$$n_1(\alpha_0) = 0, \quad m_1(\alpha_0) = 0, \quad s(\alpha_0) = 0. \tag{8}$$

3. Stepped shell of von Mises material

The problem posed above consists in the maximization of the limit load so that the conditions (2) – (8) are satisfied.

The problem is treated as a variational problem and the solution can be obtained as the solution of the boundary value problem with equations

$$\begin{cases} n_1' = -\dfrac{n_1}{\rho} + \dfrac{n_2}{\rho}, \\ m_1' = -\dfrac{m_1}{2\rho} \pm \dfrac{\sqrt{1 - \dfrac{3}{4}m_1^2 - n_1^2 - n_2^2 + n_1 n_2}}{\rho} - \dfrac{n_1}{k} + \dfrac{p}{2k\rho}\left(\alpha_0^2 - \rho^2\right), \\ p' = 0, \\ \psi_1' = \dfrac{\psi_1}{\rho} \mathrm{m} \dfrac{\psi_2}{2\rho\sqrt{1 - \dfrac{3}{4}m_1^2 - n_1^2 - n_2^2 + n_1 n_2}}\left(n_2 - 2n_1\right) + \dfrac{\psi_2}{k}, \\ \psi_2' = \dfrac{\psi_2}{2\rho} \mathrm{m} \dfrac{\psi_2}{2\rho\sqrt{1 - \dfrac{3}{4}m_1^2 - n_1^2 - n_2^2 + n_1 n_2}}\left(-\dfrac{3}{2}m_1\right), \\ \psi_3' = -\dfrac{\psi_2}{2k\rho}\left(\alpha_0^2 - \rho^2\right), \end{cases}$$

where $n_2 = \dfrac{n_1}{2} \pm \dfrac{1}{2}\dfrac{\sqrt{\psi_1^2\left(4\left(\psi_2^2 + 1\right) - 3\left(n_1^2 + m_1^2\right)\left(\psi_1^2 + \psi_2^2\right)\right)}}{\psi_1^2 + \psi_2^2}$.

The set is integrated by the use of the method adjoint operators.

In Fig. 2 the curves labeled with 1, 2 and 3 correspond to $k = 0.9$, $k = 0.3$ and $k = 0.1$ respectively.

Acknowledgement

The support of the Estonian Science Foundation through the Grant No 4377 is gratefully acknowledged.

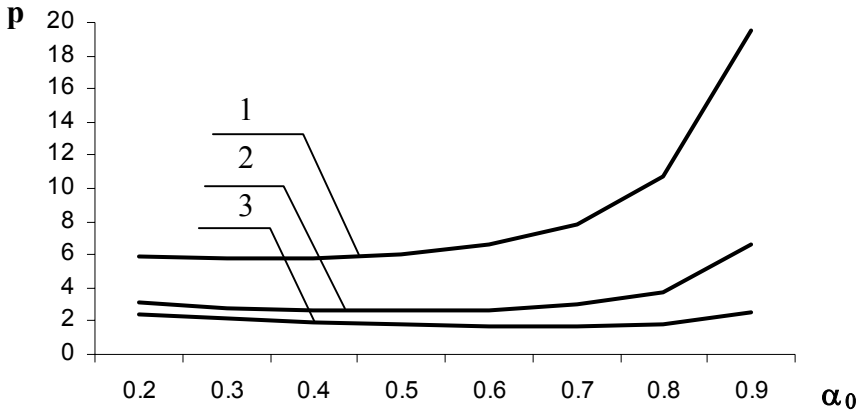

Fig. 2. Load carrying capacity vs. internal radius for von Mises yield condition.

REFERENCES

[1] R.H. Bryant, S.L. Lee and T. Mura. Mises limit load for simply supported conical sandwich shells. *Ing.-Arch.*, **37**, 281–287, (1969).

[2] P.H. Hodge. Limit analysis of Rotationally Symmetric Plates and Shells. Prentice-Hall, New York, (1963).

[3] J. Lellep and E. Puman. Optimization of plastic conical shells of piece wise constant thickness. *Struct. Optimiz.*, **18**, 74–79, (1999).

[4] J. Lellep and E. Puman. Optimization of plastic conical shells loaded by a rigid central boss. *Int. J .Solids and Struct.*, **37**, 2695–2708, (2000).

[5] J. Lellep and E. Tungel. Optimization of plastic spherical shells of von Mises material. (in press).

Using Surrogate Models and Response Surfaces in Structural Optimization

Marcus Redhe*, Tomas Jansson and Larsgunnar Nilsson
Division of Solid Mechanics
Linköping University, Linköping, Sweden
e–mail: marre@ikp.liu.se

ABSTRACT

Summary The aim of this work is to determine if space mapping technique using surrogate models together with response surfaces can be used for structural optimization of crashworthiness problems. Further, the efficiency of optimization using space mapping will be compared to traditional structural optimization using the Response Surface Methodology.

Structural optimization often uses gradients for the objective and constraints in order to find the optimum solution. For nonlinear transient problems traditional structural optimization methods, e.g. Svanberg [1], do not work due to noise in the response.

To be able to determine the optimum the Response Surface Methodology (RSM) is often used. Surfaces based on polynomial expressions are created for the objective and constraint functions. These surfaces smoothen out the noisy response and the gradients can easily be calculated from the surface approximation. For further reading about RSM, see Myers and Montgomery [2].

If the number of design variables is not too large, RSM only needs a few number of evaluations to calculate the surface approximation. Still the simulation time for each design can be rather long. There is therefor a need for methods where simplified models can be used for the functional evaluation instead of using the full simulation models. The simplified models can be developed using less number of elements, other solvers, simple approximations with analytic solutions etc.

One method which makes this possible is called space mapping where a surrogate model is used together with the full model. The surrogate model (coarse model) determines in what direction the optimization will continue and the full model (fine model) will determine the design point for the next iteration. The use of the coarse model makes it possible to reduce the total simulation time and the fine model is used to get an accurate solution.

The first space mapping paper was written by Bandler et al. [3] where the basic theory was stated. In Bandler et al. [4] the problem was formulated for using Broydens method for non-linear equations and Bakr et al. [5] introduced a trust-region methodology. A mathematical viewpoint of space mapping can be found in Madsen and Sondergaard [6] .

The space mapping method has until now mainly been used in electromagnetics and circuit optimization applications, see e.g. Bandler et al. [3] and Bakr et al. [7]. Leary et al. [8] used it in structural optimization on a simple cantilever beam.

The aim of this work is to study if the space mapping technique can be used on nonlinear transient dynamic problems, e.g. crashworthiness problems.

Table 1: Results from optimization of the beam for RSM and space mapping optimization. $\sigma_1 \leq 250$, $\sigma_2 \leq 0.55$, cost in minutes (SM space mapping).

	x^*	f^*	σ^*	iter	fine	coar	cost
RSM-L	21.83;25.0	0.8510	250.4;0.482	4	20	0	40
SM	21.63;25.0	0.8435	250.9;0.487	5	5	45	10

Optimization methods

The response surface methodology is a method for constructing global approximations of the objective and constraint functions based on functional evaluations at various points in the design space. The strength of the method is in applications where gradient based methods fails, i.e. when design sensitivities are difficult or impossible to evaluate. The selection of approximation functions to represent the actual behavior is essential. These functions can be polynomials of any order or be the sum of different basis functions, e.g. sine and cosine functions. To determine the unknown coefficients a least square approach is used. This approximation is applicable for all types of objectives and constraints in the optimization problem.

The idea of space mapping is to use two models for optimization. One coarse model, the surrogate model, that is fast to solve but not accurate enough, and one fine model that takes long time to solve but is more accurate. With these two models the optimization algorithm using space mapping takes advantage of the coarse model short solution time and the accuracy of the fine model. Therefore the vast amount of function evaluations are performed on the coarse model and corrections are made with the fine model. The theory for space mapping can be found in Leary et al. [8].

Examples and results

Three examples are used to study the algorithm where all examples are constrained structural optimization problems with one or two design variables. The problems are: one optimization of a beam and two crashworthiness problems. The crashworthiness problems are one square tube and one symmetric model of a vehicle front from Saab Automobile AB which both impacting onto a stone wall. All models are Finite Elements (FE) models.

One coarse model is developed for each system, used as surrogate model in the optimization using space mapping. For the beam problem the analytic solution to the problem is used as a coarse model and the fine model is solved with the nonlinear FE program LS-DYNA Hallquist [9] with a nonlinear material model. For the square tube both the fine and coarse models are solved in LS-DYNA, but the mass of the coarse model is increased in order to lower the total CPU-time. Finally, in the coarse model of the vehicle model only the most important parts are included in the model. The two vehicle FE models are shown in Figure 1.

The optimum solution and the total CPU time used for the optimization using space mapping and RSM with linear (RMS-L) and quadratic (RMS-Q) surface approximations are given below for all examples. The vehicle model is only optimized using space mapping due to the excessive solution time.

Table 2: Results of square tube for RSM and space mapping optimization. $\sigma_1 \leq 110$, cost in hours (SM space mapping).

	x^*	f^*	σ^*	iter	fine	coar	cost
RSM-Q	1.347;55	0.7771	110.0	3	28	0	32.6
RSM-L	1.349;55	0.7781	109.7	3	16	0	18.7
SM	1.395;55	0.775	110.4	4	4	36	8.87

Table 3: Design variable, objective and constraint history for the vehicle reanalysis using space mapping, $42000 \leq \sigma_1$.

iter	0	1	2	3	4	5
x_k	1.650	1.568	1.490	1.475	1.436	1.450
f_k	—-	2.995	2.846	2.819	2.742	2.751
σ_k	—-	44508	43425	43578	42318	42702

Conclusions

The algorithm converged to the optimum solution for all problems. The total CPU time for convergence was reduced with up to 53% using space mapping compared to RSM. The conclusions are that optimization using space mapping can be used for optimization of crashworthiness problems with a significant reduction in CPU time. The drawback of the algorithm using space mapping is that it seems to be more unstable compared to RSM, e.g. if a bad starting point is chosen space mapping might not converge due to a too large derivation between the models. The starting point must be 'intelligently' chosen based on knowledge of how the space mapping technique works and how the model behaves for parameter changes.

This work is founded by Saab Automobile AB, Volvo Car Corporation, the research programmes:

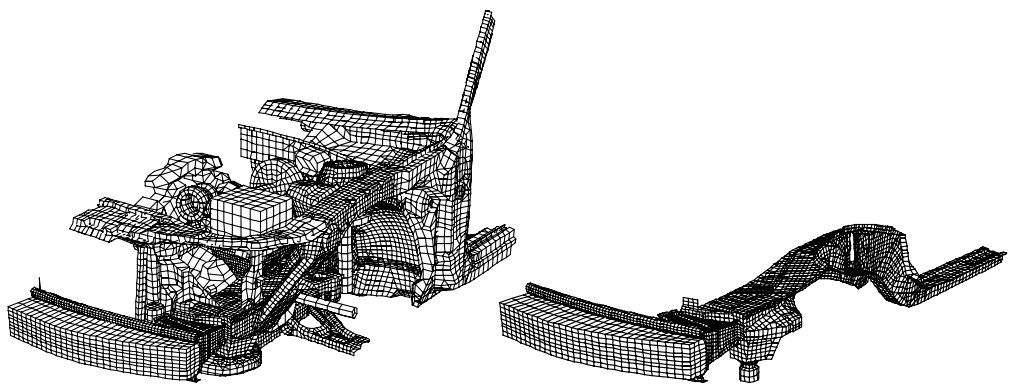

Figure 1: The fine and coarse model for the vehicle reanalysis

ENDREA and PROPER through the Swedish Foundation for Strategic Research. Saab Automobile AB has provided geometry and material data for the vehicle model application. We acknowledge Nielen Stander at LSTC for allowing us to use the optimization package LS-OPT.

REFERENCES

[1] Svanberg, K. The Method of Moving Asymptotes – a new method for structural optimization *International Journal for Numerical Methods in Engineering* **24**, 359–373, (1987).

[2] Myers , R.H. and Montgomery, D.C. *Response Surface Methodology* John Wiley & sons Inc, New York, (1995).

[3] Bandler, J.W, Biernacki, R.M., Chen, S.H., Grobelny, R.H. and Hemmers, R.H. Space Mapping Technique for Elecromagnetic Optimization *IEEE Trans. Microwave Theory. Tech.*, **42** 2536-2544, (1994).

[4] Bandler, J.W., Biernacki, R.M., Chen, S.H., Hemmers, R.H. and Madsen, K. Electromagnetic Optimization Exploition Aggrasive Space Mapping *IEEE Trans. Microwave Theory. Tech.*, **43** 2874-2882 (1995).

[5] Bakr, M.H, Bandler, J.W, Biernacki, R.M., Chen, S.H. and Madsen, K. A Trust Region Aggressive Space Mapping Algorithm for EM Optimization *IEEE Trans. Microwave Theory. Tech.*, **46** 2412-2425 (1998).

[6] Madsen, K. and Sondergaard, J. Space Mapping From a Mathematical Viewpoint *Conference on Surrogate Modelling and Space Mapping for Engineering Optimization*, Lyngby (2000).

[7] Bakr, M.H., Bandler, J.W., Madsen, K., Rayas-Snchez, J.E. and Sondergaard, J. Space Mapping Optimization of Microwave Circuits Exploiting Surrogate Models *IEEE Trans. Microwave Theory. Tech.*, **48** (2000).

[8] Leary, S., Bhasker, A. and Keane, A. A Constraint Mapping Approach to the Structural Optimization of an Expensive Model using Surrogates *Conference on Surrogate Modelling and Space Mapping for Engineering Optimization*, Lyngby (2000).

[9] Hallquist, J.O. LS-DYNA User's Manual v. 950 *Livermore Software Technology Company*, Livermore (1999)

Digital data processing using the orthogonal polynomials and its applications in mechanics

Gregory M. Slugocki

Warsaw Technical University, Poland
E-mail: gms@poland.com

ABSTRACT

Summary: The present paper is devoted to the orthogonal polynomials and their application to numerical local approximation and higher order differentiation algorithms used to the data, which can be either equally or randomly sampled. The Gram polynomials norms spectra will be compared to the respective spectra associated with the Chebyshev polynomials in view to the Runge phenomenon. The applications of such algorithms in flight dynamics and biomechanics will be shown in the separate paper.

INTRODUCTION

The numerical methods of local approximation and higher order differentiation, which are based on the use of orthogonal Gram polynomials [1,2,6,10-14], still attest their performances facing to other methods, polynomial [3,4,7,8,16,19,21] or other, e.g. spline method [5,15,17]. Nevertheless, they are limited to the case of strictly equidistant samples and then it is necessary to generalize the set of orthogonal polynomials to the fall of randomly but orderly distributed nodes in the standard interval. Contrary to the Gram polynomials, which once developed for the desired odd number of local nodes are valid for all positions of the local grid on the global set of nodes, the generalized orthogonal polynomials must be designed on each local set of nodes. Such procedure was adapted for the wavelet networks (called wavenets) [20] by Espiau et al. [18].
The author has developed the generalized orthogonal polynomial method and designed the associated software as the programs THOR and TOR (1999) computing the derivatives up to the 2nd, and the program TORFL (2000) which can compute all allowed arbitrary order derivatives.

GENERALIZED LOCAL ORTHOGONAL POLYNOMIALS

Let consider the GN randomly distributed nodes being a dense set in the closed interval

$$z \in [a,b]$$

such that:

$$z_0 = a \wedge z_{GN-1} = b \qquad z_{j+1} - z_j > 0 \underset{0 \le j \le GN-1}{\forall}$$

and the N (odd) nodes local subset of the global nodes dense in the standard interval:

$$x \in [-1,1]$$

such that N≤GN and:

$$x_0 = -1 \wedge x_{N-1} = 1$$

Then it can exist M=GN-N+1 possible local subsets of nodes denoted by the index ls satisfying the inequalities 0≤ls ≤M-1.
The generalized orthogonal polynomials set with the discrete type of orthogonality is defined as follows:

$$\phi_r(x) = \sum_{j=0}^{r} A_{r,j} x^j, \quad r = 0,1,..., N-1$$

where their scalar products and norms in the Hilbert space $l^2[-1,1]$ are commonly defined below:

$$(\phi_k, \phi_l) = \delta_{k,l} \|\phi_k\|^2 = \delta_{k,l} \sum_{i=0}^{N-1} \left(\sum_{j=0}^{k} A_{k,j} x_i^j \right)^2$$

where $\delta_{k,l}$ denotes the Kronecker symbol.

To develop the sets of generalized orthogonal polynomials for each ls, we use the recurrent formula:

$$\phi_r(x) = \alpha_{r-1}(x - \beta_{r-1})\phi_{r-1}(x) - \gamma_{r-1}\phi_{r-2}(x)$$

where:

$$\alpha_{r-1} = \frac{\|\phi_r\|^2}{(x\phi_{r-1}, \phi_r)} = \frac{A_{r,r}}{A_{r-1,r-1}} \qquad A_{0,0} = 1$$

$$\beta_{r-1} = \frac{(x\phi_{r-1}, \phi_{r-1})}{\|\phi_{r-1}\|^2} \qquad \gamma_{r-1} = \frac{\alpha_{r-1}\|\phi_{r-1}\|^2}{\alpha_{r-2}\|\phi_{r-2}\|^2} = \frac{A_{r,r}A_{r-2,r-2}\|\phi_{r-1}\|^2}{A_{r-1,r-1}^2\|\phi_{r-2}\|^2}$$

and the symbol $A_{r,r}$ denotes the leading coefficient of the polynomial φ_r of r-th order.

The length of each subinterval of the interval [a,b] is determined (for given ls) as below:

$$z_{ls+N-1} - z_{ls} = DN_{ls} \neq 2$$

then the scaling of the given subinterval is defined by the following formula:

$$SK_{ls} = \frac{2}{DN_{ls}}$$

which will be further useful.

Let now consider the function f(z) for $a \le z \le b$ and sampled in the knots (nodes) defined earlier. Then the approximating polynomial y(z) can be defined for each subinterval ls comprising a respective set of local nodes as follows:

$$y_{ls}(z) = \sum_{j=0}^{r} a_{j,ls}\phi_{j,ls}(x) = \sum_{j=0}^{r} a_{j,ls}\phi_{j,ls}(z - z_{ls})$$

where $r \le N-1$ and:

$$a_{j,ls} = \frac{(f, \phi_{j,ls})}{\|\phi_{j,ls}\|^2}$$

The sets:

$$\Omega_{ls} = \mathrm{Span}\left\| \|\phi_{0,ls}\|^2, \|\phi_{1,ls}\|^2, ..., \|\phi_{N-1,ls}\|^2 \right\|_{\forall 0 \le ls \le M-1}$$

are the spectra of norms defined for all local subintervals (containing N knots) of the global interval, and when the knots are equidistant then for the all subintervals then one spectrum of norms exists. The Chebyshev polynomials [1,2,6] have the interesting properties concerning their spectra of norms L^2 and l^2 respetively:

$$\|T_j\|^2_{L^2[-1,1]} = \begin{cases} \pi & j = 0 \\ 0.5\pi & j \neq 0 \end{cases} \qquad \|T_j\|^2_{l^2[-1,1]} = \begin{cases} N & j = 0 \\ 0.5N & 1 \le j \le N-1 \end{cases}$$

In the case of discrete type norm the nodes are zeros of the $T_N(x)$ which are a dense set in the [-1,1] standard interval, also:

$$T_N(x) = 0 \Leftrightarrow x_k = \cos\left[\frac{(2k+1)\pi}{2N} \right]_{\forall 0 \le k \le N-1}$$

The central point of the each local set has the label ls+0.5(N-1) and generally does not lie at the midpoint of the respective subinterval i.e $z_{ls+0.5(N-1)} \neq 0.5(z_{ls}+z_{ls+N-1})$, this means that referring to the standard interval $x_{0.5(N-1)} \neq 0$. One can prove that at the midpoint of the local set of knots the derivatives of the function f(z) are the most precise and least sensitive to data disturbances, when the grid is equidistant such proof is mathematically easy to do [12-14].
The differentiating polynomials for all subintervals assume the following form:
where the inequality n≤r denotes the capacity of the differentiation order, and the polynomial order r

$$y_{ls}^{(n)}(z)=\sum_{j=0}^{r} a_{j,ls}\phi_{j,ls}^{(n)}(z-z_{ls})=\left(\frac{2}{z_{ls+N-1}-z_{ls}}\right)^{n}\sum_{j=0}^{r} a_{j,ls}\phi_{j,ls}^{(n)}(x)=(SK_{ls})^{n}\sum_{j=0}^{r} a_{j,ls}\phi_{j,ls}^{(n)}(x)$$

can not exceed $r \leq 2(N-1)^{0.5}$ when the nodes are equally distributed, i.e. for Gram polynomials.

RESULTS

Due to the large amount of data files we can not include all them in the paper even as plots. However, some examples will be given.
The list of files concerning the norms spectra is following: GRAMNO5, GRAMNO7, GRAMNO9, GRAMNO11, GRAMNO13, GRAMNO15, GRAMNO17, GRAMNO19, GRAMNO21, GRAMNO23, GRAMNO25, GRAMNO27, GRAMNO29, GRAMNO31, GRAMNO33, GRAMNO35, GRAMNO37, GRAMNO39, GRAMNO41, GRAMNO43, GRAMNO45, GRAMNO47, GRAMNO49, GRAMNO51, GRAMNO53, GRAMNO55. Here, the numbers are the amounts of nodes N of the local grids.
The list of files concerning the norms spectra of the modified Chebyshev polynomials is following: TJEBNO5, TJEBNO7, TJEBNO9, TJEBNO11, TJEBNO13, TJEBNO15, TJEBNO17, TJEBNO19, TJEBNO21, TJEBNO23, TJEBNO25, TJEBNO27, TJEBNO29, TJEBNO31, TJEBNO33, TJEBNO35, TJEBNO37, TJEBNO39, TJEBNO41, TJEBNO43, TJEBNO45, TJEBNO47, TJEBNO49, TJEBNO51, TJEBNO53, TJEBNO55.
The modified set of Chebyshev polynomials is: $T_0(x)$, $2T_1(x)$, $2T_2(x)$, ..., $2T_{N-1}(x)$, and they have the identical leading coefficients as the orthogonal Gram polynomials described above.
The example of comparison of the norm spectra either for Gram and Chebyshev polynomials (modified) for N=11 is shown in the Tab.1.

J	$\|p_j\|^2$	$\|mT_j\|^2$
0	11	11
1	17.6	22
2	21.9648	22
3	25.3034496	22
4	26.99034624	22
5	26.17245695999999	22
6	22.40215896436364	22
7	16.21227011821029	22
8	9.277233159408746	22
9	3.722382097397441	22
10	.7836593889257 84	22

Tab.1. Spectra of norms for Gram polynomials (file GRAMNO11) and modified Chebyshev polynomials (file TJEBNO11) where: m=1 for j=0, m=2 for j≠0. The Runge phenomenon limit is $2(N-1)^{0.5}=6.324555320336759$.

CONCLUSIONS

1. The numerical development of the orthogonal polynomials set must be done using the double precision numbers regardless the data numbers type.
2. Such procedure is valid for N≤39 if the interpolation is required and N≤55 is nowadays the absolute limit.

3. The use of randomly distributed nodes makes more realistic the computations of data derivatives when the sampling sway occurs.
4. The limit $r \leq 2(N-1)^{0.5}$ can not be overtaken for practical computations

REFERENCES:

[1]. Björck Å. (1996) Numerical methods for least square problems, *SIAM,* Philadelphia.
[2]. Björck Å., Dahlquist G. (1969) Numeriska Metoder, Liber Grafiska AB, Stockholm
[3]. Carlsson B. (1989) Digital differentiating filters and model based fault detection, Doctoral Thesis, Uppsala Dissertations from the Faculty of Science No.28.
[4]. Carlsson B.(1991) Maximum flat digital differentiation. *Electronic Letters,* Vol.27, No.8, pp.675-676.
[5]. Dierckx P. (1975) An algorithm for smoothing, differentiation and integration of experimental data using spline functions. *J. Comp. Appl. Math.*, Vol. 1, pp. 165-184.
[6]. Hildebrand F. B. (1956) Introduction to numerical analysis, J. Wiley & Sons, New York
[7]. Lanshammar H. (1982) On practical evaluation of differentiation techniques for human gait analysis. *J. Biomechanics.* Vol. 15, No. 2, pp. 99-105
[8]. Lanshammar H. (1982) On precision limits for derivatives numerically calculated from noisy data. Technical Note. *J. Biomechanics.* Vol.15, No. 6, pp. 459-470
[9]. Pezzack J., Norman R. W., Winter D. A. (1977) An assessment of derivative determining techniques used for motion analysis, *J. Biomechanics,* Vol. 10 pp. 377-382
[10]. Slugocki G. M. (1994) Verification of the kinematic and dynamic parameters on the airplane board (in Polish, with English summary), *Theoretical and Applied Mechanics,* Proc. of the 6th Conf. "Mechanics in Aeronautics", Warsaw, pp. 487-499
[11]. Slugocki G. M. (1994) Filtration and differentiation of measured data (linear and angular displacements) (in Polish, with English summary), *Coll. papers of the 12th School of Biomechanics,*Wroclaw, pp. 274-277
[12]. Slugocki G. M. (1994), Numerical smoothing and differentiation as a development of the classical smoothing calculus and their applications (in Polish, with English summary). *Proc. of 14th Polish TMM Conference,* Gdansk, pp. 345-350
[13]. Slugocki G. M. (1997) White noise in the input data, effects on the results and techniques of its elimination, *Biology of Sport*, Vol. 14, Suppl. 7, pp. 260-265
[14]. Slugocki G. M., Jaworek K. (1999) Digital processing of biomechanical data, *Proc. of the 12-th International Biomechanics Seminar,* Göteborg 1999.09.10-11, pp. 35-58
[15]. Soudan K., Dierckx. P. (1979), Calculations of derivatives and Fourier coefficients of human motion data, while using spline functions, *J. Biomechanics.* Vol.12, No.1, pp.12-26
[16]. Söderström T., Stoica. P. (1989) System Identification, Prentice Hall International
[17]. Wood G., Jennings L. (1979) On the use of spline functions for data smoothing. *J. Biomechanics,* Vol.12, pp. 477-479
[18]. Espiau F. X., Cordier E., Espiau B. (1998), Wavelet networks: an efficient tool for handling gait kinematic data, *Computer Methods in Biomechanics & Biomedical Engineering*, Vol. 2, Edited by J. Middleton et al. Gordon and Breach Science Publishers, pp. 807-814
[19]. Anderssen R. S., Bloomfield P. (1974) Numerical procedures for non exact data, *Numerische Math.*, Vol. 34, pp. 157-182
[20]. Resnikoff H. L., Wells R. O. (1998) Wavelets Analysis –The Scalable Structure of Information, Springer Verlag, Berlin, Heidelberg, New York
[21]. Larsson E. M., Söderström T. (2000), Identifiering av tidskontinuerliga sytemer vid ojämna sampling, *Reglermöte 2000,* Uppsala 2000.06.07

Application of Semi-Analytical Finite Elements for Thin-Walled Beams with Distortion

Michail Samofalov* and Rimantas Kačianauskas

Department of Strength of Materials
Vilnius Gediminas Technical University, Vilnius, Lithuania
e–mail: ms@fm.vtu.lt

ABSTRACT

Summary The semi-analytical finite elements (SAFE) for approximation of three-dimensional state variables into cross-sectional direction of thin-walled beams are proposed. The method is able to describe distortion of cross-section by additional DOF. Attention is focussed on simulation of buckling. The versatility of the SAFE approach is demonstrated by the solution of practical examples for *U*-section beam.

1. Introduction

The engineering theory of thin-walled beams describes bending, non-uniform torsion and out-of-plane warping, but restricts in-plane distortion of the cross-section. It is based on an analytical approximation of displacements and stresses within cross-section. As an alternative to the existing classical models the semi-analytical finite element approximation [1] of cross-sectional distribution of state variables is further developed in this report. The proposed approach, extended here to distortion, considers a thin-walled section as an assemblage of finite elements, where linear warping is described by membrane deformations of individual elements, while linear distortion of cross-section by bending of elements.

2. Conception of Semi-Analytical Finite Elements

Generally, three-dimensional distribution of the displacement field of the beam $\boldsymbol{u}(x, y, z)$ is reduced to one-dimensional one by an approximation in the form of

$$\boldsymbol{u}(x, y, z) = [\, \boldsymbol{f}(y, z)]\boldsymbol{U}(x) \,, \tag{1}$$

where $[\, \boldsymbol{f}(y, z) \,]$ is the cross-sectional approximation matrix and $\boldsymbol{U}(x)$ is the vector of generalised displacements. The stresses may be approximated independently in the same manner.

Let us consider the beam as a thin-walled cylinder. The contour of the cylinder build up of straight segments and shaping cross-section is considered as domain of one-dimensional finite elements. These elements are termed here as *semi-analytical finite elements*. The flat segment of cross-section, which is defined by single SAFE, is termed here as *subelement*. Actually, the construction of global displacement approximation (1) for the entire cross-section focuses on local approximation within a single semi-analytical element *se* along perimetric co-ordinate p:

$$\boldsymbol{u}^{se}(x, p) = \left[\boldsymbol{f}^{se}(p)\right] \boldsymbol{U}^{se}(x) \,. \tag{2}$$

The second task – derivation of conventional finite elements – follows a standard well-defined path. Longitudinal distribution of generalised displacements $\boldsymbol{U}^{se}(x)$ within subelement *se* may be expressed in a standard manner, while three-dimensional approximation of displacement is

$$\boldsymbol{u}^{se}(x, y, z) = \left[\boldsymbol{f}^{se}(y, z) \right] \left[\boldsymbol{N}^{se}(x) \right] \boldsymbol{U}^{se} . \tag{3}$$

Here, $\boldsymbol{U}^{se}$ is the vector of nodal displacements, $[\, \boldsymbol{N}^{se}(x) \,]$ is the longitudinal displacement approximation matrix.

Now, the global approximations (1) is element-wise approximations, which may be constructed by assembling local approximations (2-3). Indeed, once semi-analytical elements *se* and corresponding shape $[\boldsymbol{f}^{se}(p)\,]$ and $[\, \boldsymbol{N}^{se}(x) \,]$ functions are determined, they will be used to establish alternative energy expressions or governing equations of the beam in terms of new generalised variables.

3. Finite Element Discretisation

As stated above thin-walled subelement couples membrane behaviour and distortion. The membrane behaviour is described by simplified two-dimensional membrane element (Fig. 1). Here, the displacement field contains two components $\boldsymbol{u}(x, p) = \{\, u_x(x, p),\ u_p(x, p) \,\}^{\mathrm{T}}$. Finally, after semi-analytical discretisation, displacements are defined by three independent nodal variables $\boldsymbol{U}^{se}(x) = \{U^{se}_{xk}(x),\ U^{se}_{xl}(x),\ U^{se}_{p}(x)\}^{\mathrm{T}}$. The longitudinal components $U^{se}_{xk}(x)$ and $U^{se}_{xl}(x)$ attached to lines *l* and *k* are usually approximated by the simplest Lagrangian polynomials. For the transversal component $U^{se}_{p}(x)$ the higher-order interpolation polynomials providing a link between longitudinal and transverse variables are required.

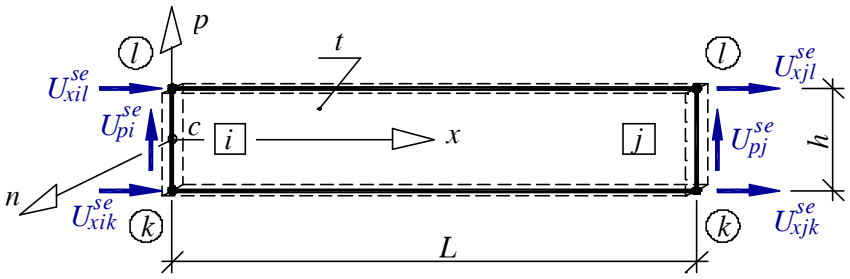

Fig. 1. Membrane subelement with shear

Distortion as local out-of-plane bending is illustrated in Fig. 2. The cubic distribution of transverse displacement $u_n(x, p)$ along co-ordinate *p* is assumed for the distortion model. The vector of generalised distortion displacements $\boldsymbol{U}^{se}_{d}(x) = \{U^{se}_{nk}(x),\ \varphi^{se}_{xk}(x),\ U^{se}_{nl}(x),\ \varphi^{se}_{xl}(x)\}^{\mathrm{T}}$ in approximation contains two translations $U^{se}_{nk}(x)$ and $U^{se}_{nl}(x)$ and two rotations $\varphi^{se}_{xk}(x)$ and $\varphi^{se}_{xl}(x)$, while approximation matrix $[\, \boldsymbol{f}^{se}_{n}(p) \,]$ contains Hermitian polynomials. The same polynomials are used for construction of $[\, \boldsymbol{N}^{se}(x) \,]$.

The membrane and distortion DOF of subelement are stuck together by selection of complex thin-walled elements. The example of *U*-section beam element composed of three subelements is presented in Fig. 3.

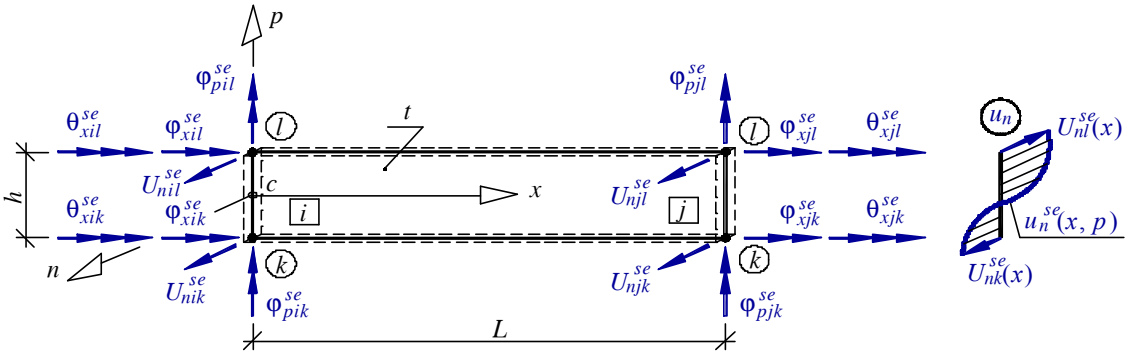

Fig. 2. Distortion DOF of subelement and transversal displacement distribution

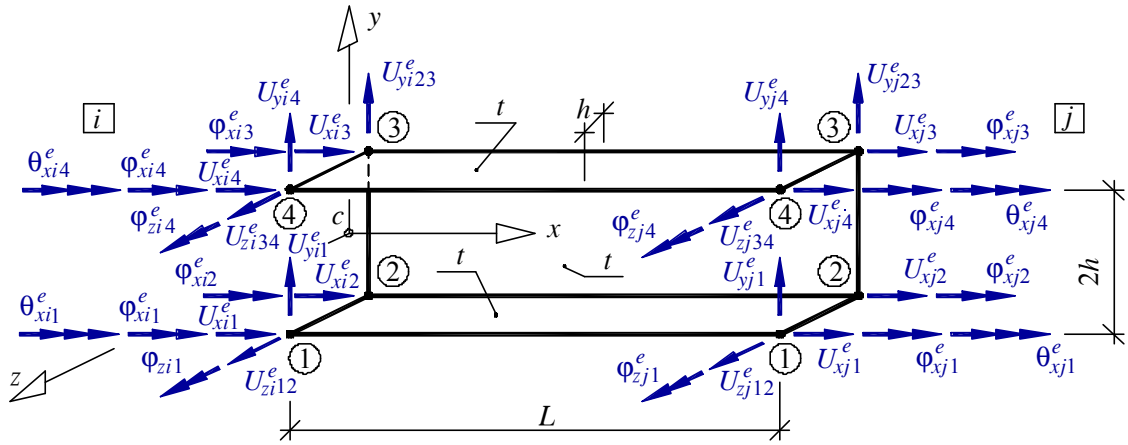

Fig. 3. Finite element of *U*-section beam and its global DOF

4. Distortion in Buckling Problem

Buckling and especially local buckling is chosen here to illustrate distortion phenomenon of a thin-walled beam. A critical condition, at which buckling of a structure impends, is obtained considering the second variation of the total potential energy of a continuum, expressed in terms the internal strain energy E_{int} stored in the volume V of a continuum and the external work W_{ext} done. This condition provides buckling problem as a linear eigenvalue problem. By separating membrane and distortion behaviour the strain energy may be expressed in terms of linear and non-linear membrane energies $E_{lin\,m}$ and $E_{non\,m}$ as well as distortion energy $E_{lin\,d}$, where subscript *m* indicates *membrane* and *d* indicates *distortion* variables.

Linear membrane energy $E_{lin\,m}$ produces membrane stiffness matrix $[\,\boldsymbol{K}_{lin\,m}\,]$ the general expression for which is obtained using mixed approach [1]. The distortion part of strain energy $E_{lin\,d}$ may be presented in terms of curvatures $\kappa_x(x, p)$ and $\kappa_p(x, p)$ and bending moments $M_x(x, p)$ and $M_p(x, p)$ using simplified model of bending plate. It produces distortion stiffness matrix $[\,\boldsymbol{K}_{lin\,d}\,]$.

The non-linear strain energy $E_{non\,m}$ expressed in terms of non-linear strain $\varepsilon_{non\,x}(x, p)$ produces geometric stiffness matrix. Generally, the non-linear strain associated with transverse displacements $\boldsymbol{U}_m$ produces membrane geometric stiffness matrix $[\,\boldsymbol{K}_{g\,mm}\,]$ while strain

associated with distortion displacement $\boldsymbol{U}_d$ produces distortion geometric stiffness matrix $[\boldsymbol{K}_{g\,md}]$. Finally, the buckling problem now may be presented as eigenvalue problem

$$\left(\begin{bmatrix} \boldsymbol{K}_{lin\,m} & \boldsymbol{O} \\ \boldsymbol{O} & \boldsymbol{K}_{lin\,d} \end{bmatrix} + \lambda_{cr} \begin{bmatrix} \boldsymbol{K}_{g\,mm} & \boldsymbol{O} \\ \boldsymbol{O} & \boldsymbol{K}_{g\,md} \end{bmatrix} \right) \begin{Bmatrix} \boldsymbol{U}_m \\ \boldsymbol{U}_d \end{Bmatrix} = \begin{Bmatrix} \boldsymbol{0} \\ \boldsymbol{0} \end{Bmatrix} . \tag{4}$$

Usually, by solution of buckling problem of beams or plates, matrix $[\boldsymbol{K}_{g\,mm}]$ is neglected but in thin-walled beams its role is significant.

5. Numerical Example and Conclusions

Various different examples of *U*-section beams under longitudinal loading have been tested to verify the proposed SAFE distortion approach. The example of compression loads $F_1 > F_2$ is presented for illustration (Fig. 4).

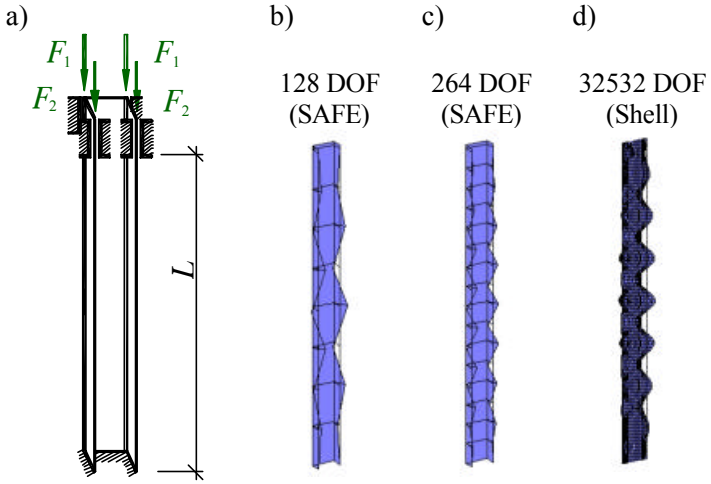

Fig. 4. Beam and local buckling mode obtained by different discretisation of DOF occurs

As expected by variation of relative wall thickness, the change of buckling modes occurs. In the range of thin section local instability occur (Fig. 4b-c). The results show a rather good agreement between semi-analytical and 'exact' shell approaches (Fig. 4d). In the range of moderate thickness global buckling is observed. This may be explained as predominating of shear effects, which is insufficiently incorporate into our model.

The SAFE has some advantages in comparison to the classical thin-walled beam theory: a) the proposed on-dimensional semi-analytical model of thin-walled beam is much more simple comparing it with expensive shell finite element model; b) higher-order deformations as well as buckling modes may be described by introducing additional DOF; c) new types of local loads and supports my be introduced;

REFERENCES

[1] J. Argyris and R. Kačianauskas. Semi-analytical finite elements in the higher-order theory of beams. *Comp. Meth. Appl. Mech. Eng.*, **138**, 19-72, (1996).

Shell Element for Geometrically Non-linear Analysis of Composite Laminates and Sandwich Structures

J. Stegmann*, J. C. Rauhe, L. Rosgaard and E. Lund
Institute of Mechanical Engineering
Aalborg University, Denmark
e–mail: js@ime.auc.dk

ABSTRACT

Summary This paper deals with a finite element formulation of a 4-node element for geometrically non-linear (GNL) analysis of layered shell structures. The element employs the MITC approach proposed by Dvorkin & Bathe [1] in order to eliminate the problem of shear locking. It uses full numerical integration both in-plane and through the thickness. The formulation passes all patch tests and shows good results in all tested configurations.

Introduction

The quest for robust finite elements for shell analysis has since the introduction of shell elements been a major goal. The goal seems to be almost reached with the introduction of the Assumed Natural Strain methods, which include the MITC (Mixed Interpolation of Tensorial Components) approach applied in the present work. A natural next step is to generalize these robust elements to allow the analysis of structures ranging from conventional metal structures, over composite laminates to sandwich structures. Furthermore, the use of these enhanced elements in other fields such as design optimization seems an obvious development. Such work has already begun and the present work is to a great extend related to the work of e.g. [2, 3, 4] but further introduces robust shell finite elements into the field of topology optimization. These robust shell element are essential for future design and optimization of advanced structures such as wind-mill wings.

Element formulation

Considering some of the typical applications of laminated shells, such as ship hulls, wind-mill wings, aeroplanes and other large structures it seems reasonable to limit the element modelling capabilities to gross response of structures. Consequently, an equivalent single layer model for describing the laminate behavior seems adequate. Furthermore, considering the material properties and layer stacking of such large structures, it is noted that these often change rapidly over the structural surface. Consequently, the mesh of finite elements in such a model must be relatively fine to model the changing material properties, and in such situations the benefit of a coarse mesh of higher order elements is lost. Thus, it seems a sound startegy to choose a linear element which is also less expensive in computational cost. However, the purely displacement-based 4-node shell element suffers heavily from shear locking and consequently, the MITC method is incorporated in the formulation thus eliminating these problems.

The current element formulation is based on the degenerated solid approach and the kinematic assumptions enforced classifies the formulation as a Mindlin-type element with the following kinematic interpolation:

$$u_i = \sum_{a=1}^{4} N_a u_i^a + \sum_{a=1}^{4} \frac{t}{2} h_a N_a (-\alpha_{a\ 0} V_{2i}^a + \beta_{a\ 0} V_{1i}^a) \tag{1}$$

in which a is the a'th node, u_i are the displacements, N_a is the interpolation, t is the thickness coordinate and h_a is the element thickness at node a. The first term of (1) represents the in-plane contribution and the second term the out-of-plane contribution. The latter is described by the displacement of the reference surface normal ${}_0V_{3i}^a$ but this can be expressed through the rotation about the two in-plane *node directors* ${}_0V_{1i}^a$ and ${}_0V_{2i}^a$ which are defined as shown in Fig. 1.

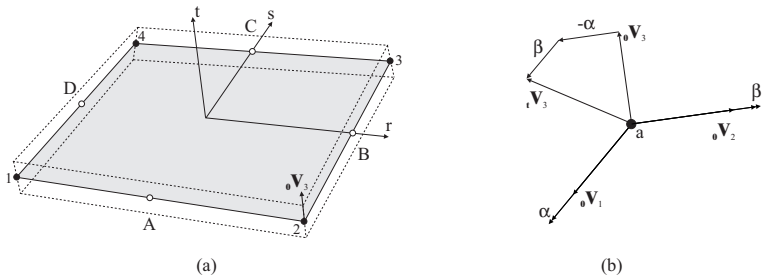

Figure 1: The 4-node shell element (a) and definition of unit node director ${}_0\mathbf{V}_3^a$ in node a (b). The rotations α and β about ${}_0V_{2i}^a$ and ${}_0V_{1i}^a$ respectively express the displacement of the surface normal.

From the kinematic interpolation the element strain-displacement matrix, $\mathbf{B}$, may be formulated directly, but to eliminate shear locking (emanating from spurious transverse shear energies) rows 5 and 6 are corrected according to the MITC method. The MITC method is founded in the observation that the transverse shearing strains are computed correctly at the mid-sides of the 4-node element. The idea is to correct the B-matrix so that transverse shearing strains are computed in these four mid-side points $A-D$ (called *tying points*) in stead of in the Gauss-points. These correct values are then interpolated across the element through a new set of interpolation functions:

$$\tilde{\epsilon}_{ij}^{AS} = \sum_{k=1}^{4} N_k^{ij}(r,s)\tilde{\epsilon}_{ij}^{DI}(r_p,s_p,t) \tag{2}$$

where N_k^{ij} are the new interpolation functions in r and s corresponding to the ij'th strain and the k'th tying point. From the expression in (2) the assumed strains (AS) are expressed from the directly interpolated (DI) strains at the mid-side points. The new interpolations must naturally fulfill the relation:

$$N_k^{ij}|^l \equiv N_k^{ij}(r_l,s_l) = \delta_{kl} \tag{3}$$

so that the k'th interpolation function assumes the value 1 in the k'th tying point and the value 0 in all other tying points. The new interpolations are of the same order as the standard isoparametric interpolation functions used in the element. This leads to a corrected strain-displacement matrix and in turn to an element stiffness matrix, $\mathbf{K}$, by expressing the constitutive matrix, $\mathbf{C}$, with the following coefficients in the material coordinate system:

$$\begin{aligned} C_{11} &= \frac{E_1}{1-\nu_{12}\nu_{21}} & C_{22} &= \frac{E_2}{1-\nu_{12}\nu_{21}} & C_{12} &= \frac{\nu_{21}E_1}{1-\nu_{12}\nu_{21}} \\ C_{44} &= G_{12} & C_{55} &= G_{23} & C_{66} &= G_{13} \end{aligned} \tag{4}$$

Note that the constitutive matrix resulting from the coefficients in (4) will have zero-values in the third row and column. This is done to enforce the Mindlin-assumption of negligible transverse effects. As shear correction factor we use $5/6$ for all but sandwich structures.

The global system of equations is then assembled using the equilibrium of work, expressed for any element of volume V and area A:

$$\int_V \mathbf{u}_a^T \mathbf{B}^T \mathbf{S}\, dV = \int_V \mathbf{u}_a^T \mathbf{N}^T \mathbf{r}^b\, dV + \int_A \mathbf{u}_a^T \mathbf{N}^T \mathbf{r}^s\, dA + \sum_{k=1}^{n_a} \mathbf{u}_k^T \mathbf{r}_k^c - \int_V \mathbf{u}_a^T \mathbf{N}^T \rho \mathbf{N} \ddot{\mathbf{u}}_a\, dV \quad (5)$$

where $\mathbf{r}$ denotes a load vector and the superscripts b, c and s denote body-, concentrated and surface loads respectively. The stress is expressed as the Second Piola-Kirchhoff stress tensor to ensure work conjugacy with the Green-Lagrange strain tensor for finite strain. The global governing equations are obtained as the sum of (5) over all elements in the discretized domain. The element integration is carried out by a full numerical Gauss integration. The in-plane integration is carried out as usual but the thickness-direction integration is carried out as piecewise integration over all layers in the element. Consequently, the thickness-direction coordinate, t, is corrected using the transformation in (6) so that $t_l \in [-1, 1]$ in each layer:

$$t = -1 + \frac{1}{h}\left(2\sum_{i=1}^{l} h_i - h_l(1 - t_l)\right) \quad (6)$$

where h_l is the thickness of the l'th layer and the sum of the first term of the parenthesis constitutes the total thickness of the preceding layers. Inserting the modified coordinate in the Gauss integration represents an integration by substitution and consequently, the derivative of the coordinate transformation in (6) must be found and multiplied to the integrand.

Numerical examples

The element passes all patch tests performed in constant curvature, shear, twist and membrane as also noted by [1]. As benchmark examples we use the laminated cylindrical shell shown in Fig. 2. The geometry appears in various articles but the current example was adopted from [5] who developed an enhanced full layerwise 3-node triangular element for geometrically non-linear analysis.

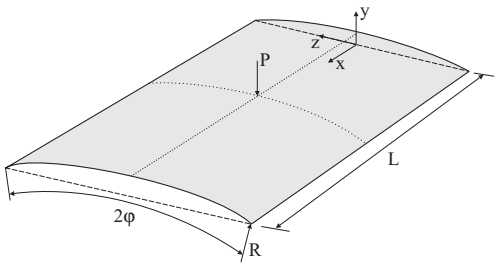

Figure 2: Cylindrical laminated shell used as numerical example.

The cylindrical shell is hinged at the straight sides and free at the two curved ends. The entire geometry is modelled with side length $L = 508$ mm, radius of curvature $R = 2540$ mm and angle $2\varphi = 0.2$ rad. The lay-up is a +45/-45 (measured from the global x-axis) laminate of equal thickness layers and a total thickness of $h = 12.4$ mm. The material properties are stated in the material coordinate system (1-axis aligned with the global x-axis) as: $E_1 = 3.2993 \cdot 10^6$ MPa, $E_2 = E_3 = 1.0998 \cdot 10^6$ MPa, $G_{12} = G_{13} = 6.5985 \cdot 10^5$ MPa, $G_{23} = 4.4128 \cdot 10^5$ MPa and $\nu = 0.25$. The results from the current element formulation are presented in Fig. 3 and compared

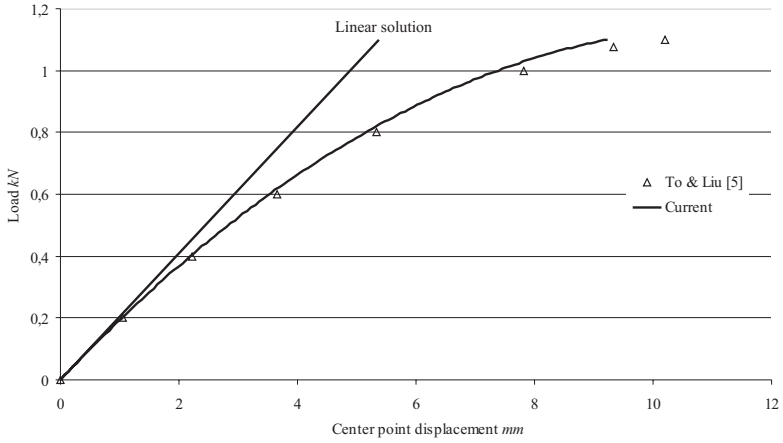

Figure 3: Results of linear and non-linear analysis of the cylindrical laminated shell in Fig. 2.

to the results obtained with a 8×8 mesh of triangular elements by [5].
As can be seen the results correlate very well although the current formulation exhibits slightly stiffer behavior. The current formulation also performs very well in linear analysis and numerous other non-linear examples.

Topology optimization of laminated shell structures has recently been implemented using the present element formulation and preliminary results show good correlation with those obtained by e.g. [6]. The development of optimization capabilities will continue in the near future, both for topology and shape design optimization.

REFERENCES

[1] Eduardo N. Dvorkin & Klaus-Jürgen Bathe. A continuum mechanics based four-node shell element for general non-linear analysis. *J. Eng. Comp.*, **1**, 77–88, (1984).

[2] G. Alfano, F. Auricchio, L. Rosati & E. Sacco. MITC finite elements for laminated composite plates. *Int. J. Num. Met. Eng.*, **50**, 707–738, (2001).

[3] S. Klinkel, F. Gruttmann & W. Wagner. A continuum based three-dimensional shell element for laminated structures. *Computers & Structures*, **71**, 43–62, (1999).

[4] B. Brank & E. Carrera. Multilayered shell finite element with interlaminar continuous shear stresses: a refinement of the Mindlin-Reissner formulation. *Int. J. Num. Met. Eng.*, **48**, 843–874, (2000).

[5] C. W. S. To & M. L. Liu. Geometrically nonlinear analysis of layerwise anisotropic shell structures by hybrid strain based lower order elements. *Finite Elements in Analysis and Design*, **37**, 1–34, (2001).

[6] S. J. Lee, J. E. Bae & E. Hinton. Shell topology optimization using the layered artificial material model. *Int. J. Num. Met. Eng.*, **47**, 848–867, (2000).

Scanning – A New Approach to Numerical Modelling of Structures

Karl Vincent Høiseth
Division of Structural Engineering
MARINTEK/SINTEF Group, Trondheim, Norway
e–mail: kalle.hoiseth@marintek.sintef.no

ABSTRACT

Summary Improvements in laser scanning and visualisation techniques makes 3-dimesional digital models of typical civil engineering structures attractive for FEM-meshing. A FEM-mesh based on the scanned geometry of an existing structure is beneficial because it represents true, in situ shapes and measures. Two demonstration studies are being performed in order to evaluate the efficiency of such procedures. While scanned models are easily achieved, the conversion to mesh-generators needs considerable data-reduction.

INTRODUCTION

Laser scanning has become a versatile technique for a number of applications. In the construction world, lasers has been used for surveying purposes for a many years. Scanning of structures, however, has just recently been introduced to the civil engineering community, and the perspectives are most promising. Laser scanning provides a new mean for making digital models of existing structures. Digital models can henceforth be converted to true geometrical models applicable for FEM-meshing. In the CMC-project[1], two demonstration cases, based on the Cyrax[2] system, are being performed in order to study the feasibility of such a procedure for numerical modelling [1]. One of the studies concerns a complex part of the Nidaros Cathedral. In the second demonstration study, the regular shape of a hydroelectric arch dam is being modelled.

THE CYRAX SYSTEM

Cyrax is a portable, 3D laser scanning system for capturing, visualisation and modelling of complex structures and sites. The scanner unit operates in a 40° vertical by 40° horizontal sector in space, for each scan. When the scanning starts, a laser beam is sent out, pointing towards the left, uppermost corner of the chosen spacious segment. The distance from the scanner to the target is measured by the laser-lights "time of flight". Next, the same action is repeated, however the direction of the emitted laser beam is rotated downwards by a set angle. This procedure continuous until the left, lowermost corner of the chosen segment is reached, and a complete column of points have been measured. Subsequently, a new column of points, with a set horizontal angle to the right, is measured. The scan is completed when the lowermost, right angle of the chosen segment is reached. The result is a regular cloud of points on the surface of the scanned object, with known relative co-ordinates.

The scanner also records the intensity of the reflected pulse, from all the measured points. This enables the associated software [2] to visualise the object through various graphical techniques. By combining separate scans, complete 3-dimensional models of structures, including exterior as well as interior surfaces are readily available. The software supports the .dxf file format, which implies that the models

[1] CMC- Computational Mechanics in Civil Eng (www.sintef.no/units/civil/projects/cmc/index.htm)
[2] www.cyrax.com

can be imported to popular CAD-programs like AutoCad and Microstation. From there, the necessary geometric entities can be transferred to mesh-generators like Femgen, which is being used in the current study. This way, a geometric model with true, in-situ measures, for FEM-purposes should easily be achieved.

MODELLING THE NIDAROS CATHEDRAL

Nidaros Cathedral dates back to the Middle Ages or last period of the Viking era, 1070 AD. The church is the largest and most impressive cathedral in the Nordic countries. Since 1869, the cathedral has been subjected to extensive rebuilding and renovation by NDR, the *Nidaros Cathedral Restoration Works*.

Currently, NDR are working out a detailed restoration plan, where one of the issues concerns the loadcarrying capacity of specific parts of the cathedral. An area of special interest is the King's entrance, which is located at the south wall, as illustrated in Figure 1.

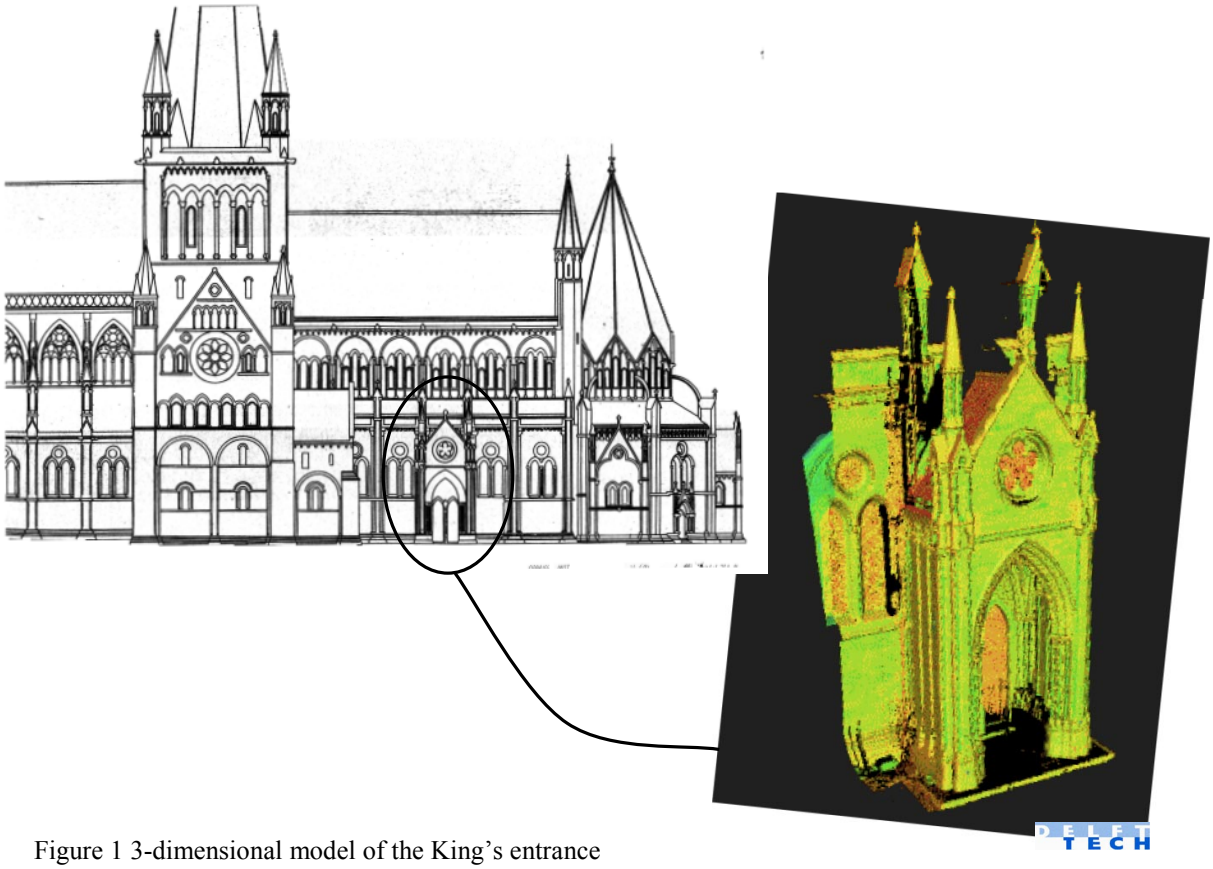

Figure 1 3-dimensional model of the King's entrance

The purpose of the study is to determine the tilting of the tower and assess the belonging stress distribution by the following approach:

- Modelling the geometry of the tower as a separate unit by means of scanning and perform a stability analysis.
- Carry out a global analysis. This can be achieved by scanning and a pragmatic modelling of the connections between tower, church walls, column and inner ceiling vaults.

THE MYKSTUFOSS HYDROELECTRIC ARCH DAM

In Norway, more than 99% of the electricity is being produced by hydropower. This is achieved by a large number of water reservoirs with a vast number of dam structures. Due to the severe implications of failure, the design basis are strict, and the owners are obliged to monitor the structural conditions continuously. Reassessment of the load-carrying capacity and safety conditions of hydroelectric dam structures is frequently necessary. The purpose of the study is to demonstrate the capabilities of scanning with respect to efficient modelling for structural analysis.

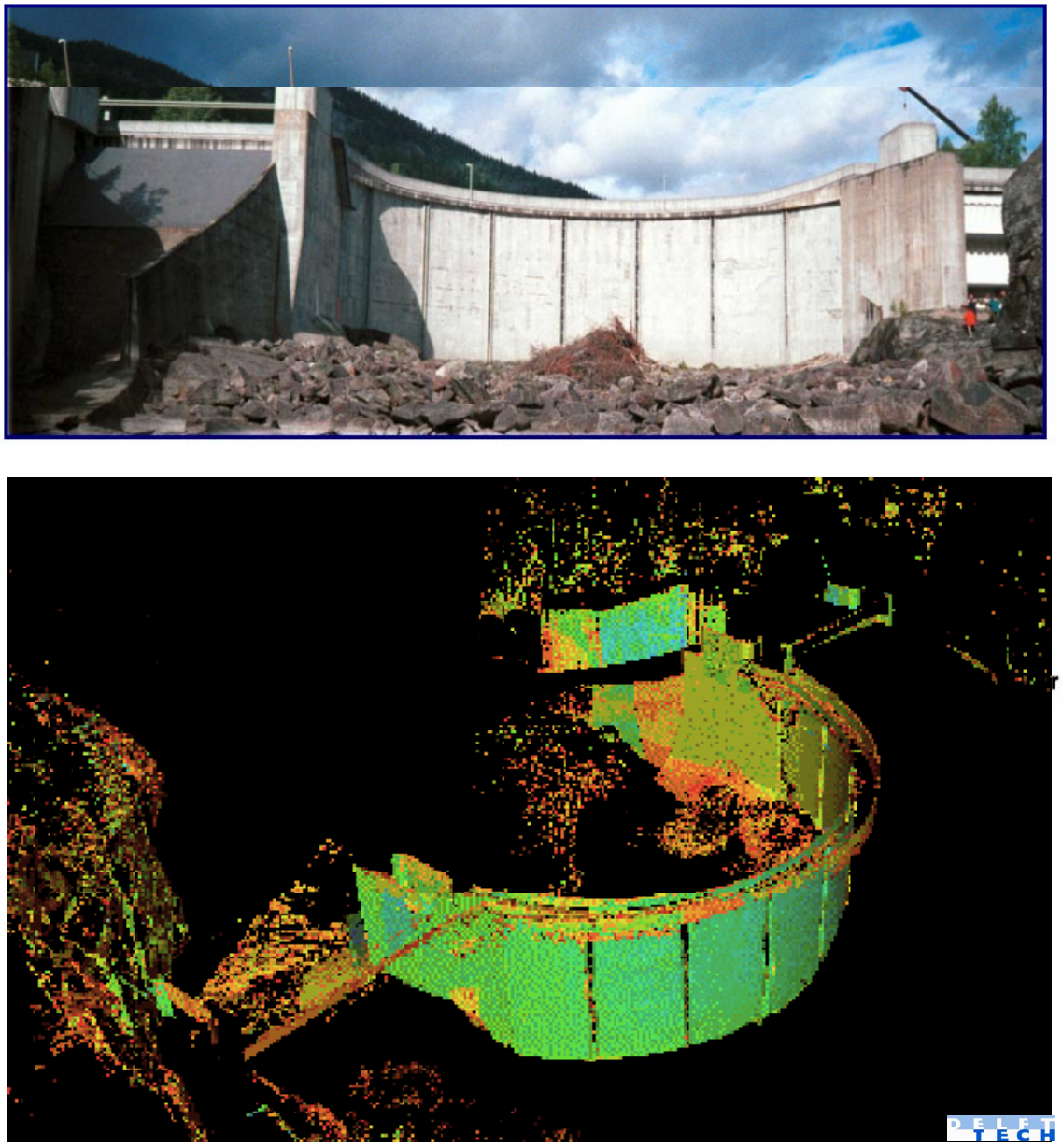

Figure 2 Picture and digital model of the arch dam

CONCLUSIONS

Both structures, the King's entrance and the Mykstufoss dam, were scanned during a three-days working period. The number of separate scans, 8 and 10, for the cathedral and the dam, respectively, were combined partly at the spot, and complete models where available the day after.

The models are currently being used as basis for FEM-modelling and structural analysis. This is a straight forward process, however data reduction is necessary, and this is an issue which needs to be addressed.

Scanning as basis for numerical modelling of existing structures will be a common approach, be it for reassessment purposes, for determination of load-carrying capacity of structures subjected to accidental events, or for structural documentation in general.

ACKNOWLEDGEMENTS

The scanning, modelling and visualisation was performed by the company DelfTech bv in the Netherlands. The skilful work of Willem van Spanje and Erwin Beernink is highly appreciated.

The demonstration studies were made possible thanks to the practical support and enthusiasm of Kristin Bjørlykke at NDR and Henrik Grosch in Statkraft Grøner.

REFERENCES

[1] K. V. Høiseth. Three-Dimensional Structural Scanning. SINTEF Report MT70 F01-252.

[2] Computer Graphics Perception (CGP) Software Manuals, Cyra Technologies Inc.

On the $Q_2 - P_1$ Stokes element

Daniele Boffi[*]
Dipartimento di Matematica "F. Casorati"
Università di Pavia, Pavia, Italy
e–mail: boffi@dimat.unipv.it

Lucia Gastaldi
Dipartimento di Matematica
Università di Brescia, Brescia, Italy
e–mail: gastaldi@ing.unibs.it

ABSTRACT

Summary In this talk we comment on the popular $Q_2 - P_1$ Stokes element. In particular, we recall that on meshes of general quadrilaterals two different definitions of the scheme are possible: a *global* pressure approach or a *local* one. The inf-sup condition for the former method is known to hold; we have proved that the same is true also for the latter one. However, the global approach is to be preferred because of a lack in the approximation properties for the local one. Numerical experiments confirms the theory.

We consider the standard mixed formulation for the Stokes problem

$$\begin{array}{l}\text{find } (\mathrm{u}, p) \in V \times Q \text{ such that} \\ \begin{cases} a(\mathrm{u}, \mathrm{v}) + b(\mathrm{v}, p) = F(\mathrm{v}) & \forall \mathrm{v} \in V \\ b(\mathrm{u}, q) = 0 & \forall q \in Q, \end{cases}\end{array}$$

where Ω is a polygon, $V = H_0^1(\Omega)^2$, $Q = \operatorname{div} V$, the bilinear form $a(\cdot,\cdot) : V \times V \to \mathbb{R}$ is a weak form for the vector Laplace operator and $b(\cdot,\cdot) : V \times Q \to \mathbb{R}$ is the Stokes bilinear form $b(\mathrm{u}, p) = -\int_\Omega p \operatorname{div} \mathrm{u}\, dx$.

Given a sequence of quadrilateral meshes $\{\mathcal{T}_h\}$ of Ω, we consider, as usual, the bilinear map F_K from the reference square $\hat{K}$ which defines a generic quadrilateral $K \in \mathcal{T}_h$. The widely used $Q_2 - P_1$ finite element method for approximating the Stokes problem consists in choosing $V_h \subset V$ and $Q_h \subset Q$ as follows. Starting from the space of bilinear vectorfields on $\hat{K}$ denoted by $\hat{V}$, we can define $V(K)$ as the compositions of functions in $\hat{V}$ with F_K^{-1}. Then the definition of V_h is the following

$$V_h = \{\mathrm{v} \in V : \mathrm{v}|_K \in V(K),\ \forall K \in \mathcal{T}_h\}.$$

The pressure spaces Q_h can be defined in two different ways. Since no continuity is required, there is no need for composing reference functions with the inverse of F_K; this observation gives rise to the so called *global* approach: functions in $Q_h^{(g)}$ are "true" piecewise linears, namely

$$Q_h^{(g)} = \{q \in Q : q|_K \text{ is affine},\ \forall K \in \mathcal{T}_h\}.$$

The *local* approach consists in defining Q_h in a similar way as it has been done for V_h. Let $\hat{Q}$ be the space of affine functions on $\hat{K}$ and denote by $Q(K)$ the space of compositions of functions in $\hat{Q}$ with F_K^{-1}. Then $Q_h^{(l)}$ is given by

$$Q_h^{(l)} = \{q \in Q : q|_K \in Q(K),\ \forall K \in \mathcal{T}_h\}.$$

We make clear that $Q_h^{(g)} = Q_h^{(l)}$ whenever F_K is affine for any $K \in \mathcal{T}_h$ (i.e., when the elements of $\mathcal{T}_h$ are parallelograms); however, if K is a general quadrilateral (for which F_K is not affine) then $Q(K)$ contains functions which are not affine, since F_K^{-1} is not a polynomial.

The $Q_2 - P_1$ Stokes approximation then reads

$$\begin{array}{l} \text{find } (\mathrm{u}_h, p_h) \in V_h \times Q_h \text{ such that} \\ \left\{ \begin{array}{ll} a(\mathrm{u}_h, \mathrm{v}) + b(\mathrm{v}, p_h) = F(\mathrm{v}) & \forall \mathrm{v} \in V_h \\ b(\mathrm{u}_h, q) = 0 & \forall q \in Q_h, \end{array} \right. \end{array} \tag{1}$$

with either $Q_h = Q_h^{(g)}$ or $Q_h = Q_h^{(l)}$.

Both approaches have been widely used in the engineering literature. The global approach has been analyzed in [3, 4].

In [1] it has been shown that particular care has to be taken into account when dealing with quadrilateral elements. It follows that the spaces $Q_h^{(g)}$ and $Q_h^{(l)}$ achive different approximation properties, namely

$$\inf_{q_h \in Q_h^{(g)}} ||q - q_h||_{L^2} = O(h^2) \qquad \inf_{q_h \in Q_h^{(l)}} ||q - q_h||_{L^2} = O(h) \tag{2}$$

for a smooth function q (the lack of approximation properties for the space $Q_h^{(l)}$ cannot be avoided, even for q polynomial).

When $Q_h = Q_h^{(g)}$ it is known that problem (1) is stable. In [2] it has been proved that this is the case also when $Q_h = Q_h^{(l)}$. Hence the standard quasi-optimal error estimate for mixed methods holds true

$$||\mathrm{u} - \mathrm{u}_h||_V + ||p - p_h||_Q \leq C \inf_{\mathrm{v} \in V_h,\ q \in Q_h} \big(||\mathrm{u} - \mathrm{v}||_V + ||p - q||_Q \big). \tag{3}$$

Combining (3) with (2), together with standard approximation properties for the space V_h (for the space V_h optimal second order approximation holds true) we get, for a smooth solution (u, p),

$$\begin{array}{ll} ||\mathrm{u} - \mathrm{u}_h||_V + ||p - p_h||_Q = O(h^2) & \text{for the global approach,} \\ ||\mathrm{u} - \mathrm{u}_h||_V + ||p - p_h||_Q = O(h) & \text{for the local approach.} \end{array}$$

Numerical results confirm the suboptimal rate of convergence for the local approach. Even though the suboptimality arises from the bad choice of the pressure space, the loss of one order of convergence involves also the computed velocities. This result is in good agreement with the general phylosophy of mixed methods.

REFERENCES

[1] D. N. Arnold, D. Boffi, and R. S. Falk. Approximation by quadrilateral finite elements. *Math. Comp.*, to appear. (1999)

[2] D. Boffi and L. Gastaldi. On the quadrilateral $Q_2 - P_1$ element for the Stokes problem. *Pubblicazione IAN-CNR, Pavia (Italy)*, **1194/00**, (2000).

[3] V. Girault and P.-A. Raviart *Finite element methods for Navier–Stokes equations*. Springer–Verlag, Berlin, (1986).

[4] R. Stenberg. Analysis of mixed finite element methods for the Stokes problem: a unified approach. *Math. Comp.*, **42(165)** 9–23, (1984).

Airbag inflation simulations using coupled fluid-structure analysis

Per-Olof Marklund and Larsgunnar Nilsson
Department of Mechanical Engineering, Division of Solid Mechanics
Linköping University, Linköping, Sweden
e–mail: perma@ikp.liu.se

ABSTRACT

Summary This presentation concerns the problem of simulating airbag inflation. Traditionally this has been done using uniform pressure models, where the whole airbag is considered to be one single control volume. This is not sufficient for Out of Position problems, where the pressure distribution both in space and in time is needed. Here some results for airbag inflation problems using fully coupled fluid-structure analysis will be presented.

The issue of passive safety in cars has become more and more important for the car manufacturers. Today there are not only one or two airbags in a car, certain models have ten times more then that. With the increasing usage of airbags, the number of accidents where the airbag causes the main injury also increases. Especially in one type of situation this is apparent; the "Out Of Position" (OOP) crash. Several types of OOP crashes can be categorized, but they all have one thing in common, which is that the occupant is situated very close to the airbag as it inflates, possibly giving rise to severe injuries.

Computer simulations based mainly on the Finite Element (FE) method has for a long period of time been used for parametric studies of airbag inflation problems. Most of these simulations are based on uniform pressure models which originates from the work of Wang and Nefske [1]. Although these models work well for situations where the airbag is fully inflated before it is hit by an occupant, they cannot predict injury criteria in OOP crashes, as the pressure is not constant in space in this situation.

In this study an airbag inflation problem is solved by the use of coupled fluid-structure analysis, where the fluid is modeled using a Multi-Material Arbitrary Lagrangian Eulerian (MMALE) description. The Euler equations

$$\frac{\partial \rho}{\partial t} + \nabla \cdot (\rho \boldsymbol{v}) = 0 \tag{1}$$

$$\frac{\partial \rho \boldsymbol{v}}{\partial t} + \nabla \cdot (\rho \boldsymbol{v} \otimes \boldsymbol{v}) = \nabla \cdot \boldsymbol{\sigma} + \rho \boldsymbol{g} \tag{2}$$

$$\frac{\partial \rho e}{\partial t} + \nabla \cdot (\rho e \boldsymbol{v}) = \boldsymbol{\sigma} : \boldsymbol{D} + \rho \boldsymbol{g} \cdot \boldsymbol{v} \tag{3}$$

are solved using an operator split technique in the commercial FE-code LS-DYNA, see Hallquist [2], and the fluid and the structure are connected together with a penalty based coupling algorithm based on the work of Olovsson [3]. The structure is modeled using membrane shell elements with orthotropic properties. A figure of an airbag inflation simulations is provided in Fig. 1.

Experiments have been carried out in cooperation with Autoliv Research where an airbag is inflated using pressurized gas from a tank. In the tank, pressure and temperature are measured as functions of time. Also the pressure just inside the airbag is measured. From this data the inflow

boundary conditions of the airbag can be calculated assuming isentropic flow from the gas tank to the interconnecting hose and Fanno frictional flow inside the hose, techniques which are described in Anderson [4].

The results show good comparison between the head accelerations in the test and the simulations, see Fig. 2, results which cannot be produced using uniform pressure models.

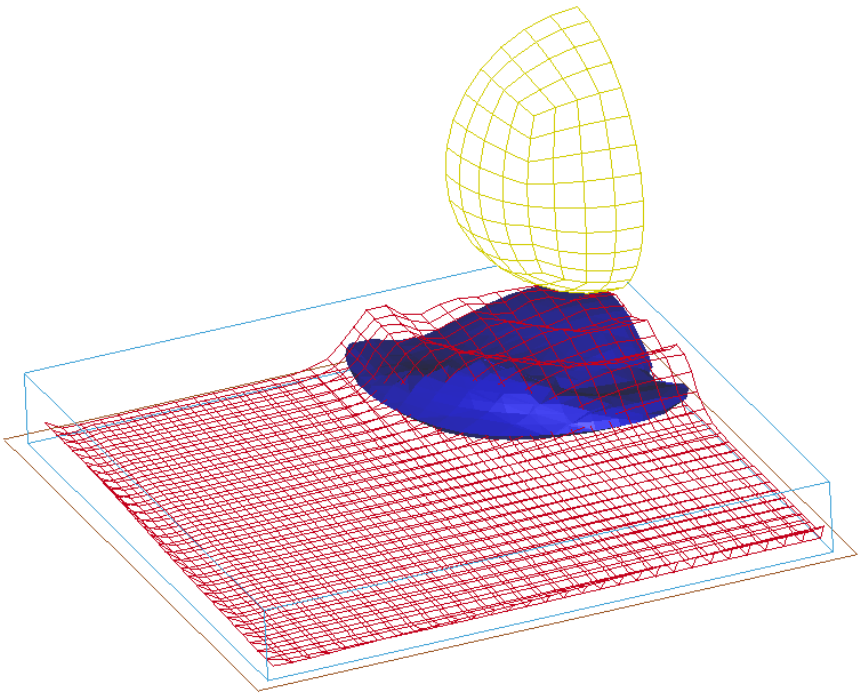

Figure 1: Iso surface for fluid volume fractions

REFERENCES

[1] J.T. Wang and D.J. Nefske. A New CAL3D Airbag Inflation Model. Int'l Cong. Expo., SAE 880654, Detroit, (1988).

[2] J.O. Hallquist. *LS-DYNA Users Manual*. Livermore, Livermore Software Technology Corp., (2001).

[3] L. Olovsson. *On the Arbitrary Lagrangian-Eulerian Finite Element Method*. Ph.D thesis, Linköping University, (2000).

[4] J. Anderson. *Modern Compressible Flow*. New York, McGraw-Hill, (1982).

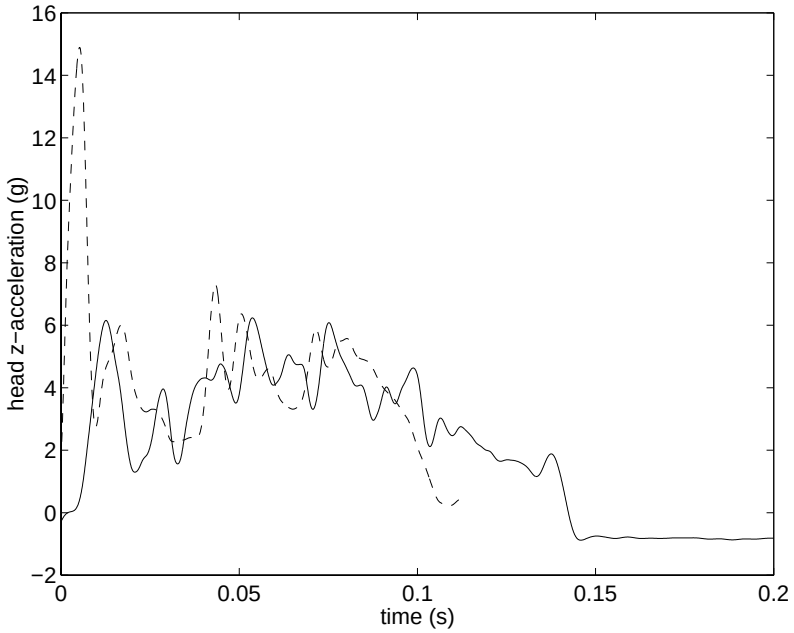

Figure 2: Head acceleration comparison

Reducing of Dimensionality in Modelling of Moisture Diffusion Process in Porous Solid

Feliksas Ivanauskas* **and Romas Baronas**
Faculty of Mathematics and Informatics
Vilnius University, Vilnius, Lithuania
Institute of Mathematics and Informatics, Vilnius, Lithuania
e–mail: feliksas.ivanauskas@maf.vu.lt

ABSTRACT

Summary A model of the moisture movement in porous solid under isothermal conditions taking into consideration coating of the surface of a specimen is presented in a 2-D-in-space formulation. The conditions of usage of the 2-D model in contrast to the corresponding 1-D one for accurate predicting of the drying process are investigated. A measure of reliability of the 1-D model is introduced.

1. Introduction

In the literature on moisture movement in porous solids, one-dimensional-in-space (1-D) models have been usually used. The 1-D-in-space model of moisture movement describes the process accurately only for extremely long and wide specimens. It is reasonable to assume 2-D moisture transfer according to the domain geometry is typical for sawn timber. However, 1-D analysis can be successfully used to predict the process for a relatively short and narrow specimen if four of six surfaces are heavily coated. The advantage of 1-D model is an efficiency of the problem solution [1]. Because of this it is important to estimate a level (degree) of surface coating, making 1-D model as admissible to predict the process accurately. A measure of reliability of 1-D model was introduced.

Moisture movement models have been used to solve the inverse coefficient problem when the diffusion and surface emission coefficients need to be recovered by certain known information on the solutions of the problem. The inverse solutions are known to be sensitive to changes in input data resulting from measurement and modelling errors. Nevertheless, the determination of the diffusion as well as surface emission coefficients for various species of wood is the problem of today [2, 3]. Since the multidimensional inverse methods are especially complex, it is important to determine properties of a specimen to be used in physical and numerical experiments, allowing us to apply 1-D in the analysis.

2. Moisture movement problem

In a two-dimensional-in-space formulation, the moisture movement, under isothermal conditions, in a symmetric piece of a porous medium (sawn board) of thickness $2a$ and width

$2b$ can be expressed through the following diffusion equation:

$$\frac{\partial u}{\partial t} = \frac{\partial}{\partial x}\left(D_1(u)\frac{\partial u}{\partial x}\right) + \frac{\partial}{\partial y}\left(D_2(u)\frac{\partial u}{\partial y}\right), \quad x \in (0,a), y \in (0,b), t \in (0,T], \tag{1}$$

here $u = u(x,y,t)$ is concentration of moisture, t is time, x, y are space coordinates measured from the surface of the specimen to the center, and $D_1(u)$, $D_2(u)$ are the moisture concentration-dependent diffusion coefficients in the space directions x, y, respectively.

The initial condition ($t = 0$) is

$$u(x,y,0) = u_0, \quad x \in [0,a], y \in [0,b]. \tag{2}$$

Let us assume, that edges of the sawn board may be coated, e.g. painted. The boundary conditions that describe symmetry and surface evaporation ($t > 0$) are

$$\left.\frac{\partial u}{\partial x}\right|_{x=a} = \left.\frac{\partial u}{\partial y}\right|_{y=b} = 0, \tag{3}$$

$$\begin{aligned} -D_1(u)\frac{\partial u}{\partial x} &= Su_e - u, \quad x = 0, \\ -D_2(u)\frac{\partial u}{\partial y} &= (1-\alpha)(Su_e - u), \quad y = 0, \end{aligned} \tag{4}$$

where S is the surface emission coefficient, u_e is the equilibrium moisture content (EMC) with the ambient air climate, and α is the dimensionless degree of coating of edges ($0 \leq \alpha \leq 1$). Let us notice, if an edge of a board is extremely coated, then corresponding surface coating degree is 1, and it equals to 0 if the surface is not coated at all.

The moisture transfer model (1)-(4) was used to simulate the drying of specimens from northern red oak (*Quercus rubra*). It was assumed that the diffusion coefficient is constant above fiber saturation point (fsp, 0.3 for red oak) and it is equal to the coefficient at the fsp value. Though the radial and tangential diffusion coefficient may be different, the transverse (in the x and y directions) diffusion below fsp for red oak was represented as

$$D_1(u) = D_2(u) = D(u) = Ae^{B/T+Cu}, \tag{5}$$

where T is the temperature, A, B and C are experimentally determined coefficients [3].

Analytical solutions of problems, described by partial differential equations of diffusion type, do not usually exist in cases of variable diffusion coefficients and complex boundary conditions. Therefore, the model (1)-(4) was solved numerically. The finite-difference technique has been used for the discretization of the model. We introduced a non-uniform discrete grid to increase the efficiency of calculations. Since moisture evaporates from the surface of a piece of wet wood, a bilinear step of the grid was used in the space directions x and y from the surface to the center, while a constant step was used in t direction.

3. Reliability of 1-D-in-space moisture transfer model

The average moisture content is usually measured at various times to predict the dynamics of sorption as well as desorption in a real experiment. The calculated average moisture content $\overline{u}(t)$ values at any time t can be determined by numerical integration of the finite difference solutions. The relative amount of the remaining moisture content $E(t)$ in wood during drying at time t is usually called as the fraction of total moisture content [2]:

$$E(t) = (\overline{u}(t) - u_e)/(u_0 - u_e). \tag{6}$$

Let k be a dimensionless ratio of the width to the thickness of a specimen, $k = b/a$, and $t_{0.5}(\alpha, k)$ be a function of α and k as the time when the drying process reaches medium, called halfdrying time, i.e., $E(t_{0.5}(\alpha, k)) = 0.5$ [2]. Let $t^*_{0.5}$ be a limitting value of halfdrying time, extremely increasing the width of the specimen.

A model of drying in a 1-D-in-space formulation can be successfully used to predict drying time for an extremely wide plate as well as for a board with heavily coated edges. In the case of use of 1-D model, the calculated halfdrying time equals to $t^*_{0.5}$. Because of this the use of 1-D model can be called as admissible for a board if the halfdrying time, calculated by using corresponding 2-D model, equals approximately also to $t^*_{0.5}$. Let us define a function p of α and k as follows:

$$p(\alpha, k) = (t^*_{0.5} - t_{0.5}(\alpha, k))/t^*_{0.5}, \quad t^*_{0.5} = \lim_{k \to \infty} t_{0.5}(\alpha, k), \tag{7}$$

where $t_{0.5}(\alpha, k)$ is the halfdrying time of the specimen calculated by using 2-D model, assuming the specimen as an extremely long sawn board. Since $t^*_{0.5}$ can be also calculated by using an appropriate 1-D model, $p(\alpha, k)$ can be called as a relative error of the use of 1-D model for a specimen having the width k times greater than the thickness at degree α of edges coating. $p(\alpha, k)$ may also be called as a level of 1-D model reliability to predict a drying process of a sawn board. Let us notice that $0 \leq p(\alpha, k) \leq 1$.

We have investigated the relative error $p(\alpha, k)$. The transverse section of a specimen was modelled as a rectangle having various width keeping the thickness equal to $2a = 29$mm. The model (1)-(4) was solved numerically for various values of the ratio $k (1 \leq k \leq 100)$ and coating degree $\alpha (0 \leq \alpha \leq 1)$. In each board geometry and edges coating degree case, the drying until the halfdrying time was simulated at different drying conditions [3].

It was found, that the relative thickness of the lumber appears to be important for the drying dynamics for different values of the degree α of coating of edges. This importance decreases with increase of α. In the case of uncoated edges ($\alpha = 0$), the halfdrying time notable increases with increase of the ratio k up to $k \approx 10$ (see also [4]). Very similar situation appears in the case where $\alpha = 0.5$. The increase of the halfdrying time versus k is rather slight only for values of α greater than 0.9. The function $p(\alpha, k)$ is a monotonous decreasing function of k ($k \geq 1$) as well as of α ($0 \leq \alpha \leq 1$).

Using a computer simulator based on 2-D model and the definition of the relative error of the usage of 1-D model, it is possible to adjust value of k as well as α ensuring the error not greater than the required one in case of use of the 1-D model. Let us define an inverse

function $k_\alpha(p)$ to the function $p(\alpha, k)$ as the minimal value of the ratio k for which $p(\alpha, k)$ does not exceed p at given α, i.e.

$$k_\alpha(p) = \min\{k : p(\alpha, k) \leq p\}. \tag{8}$$

In other words, if k is the ratio of the width to the thickness of a specimen, $k \geq k_\alpha(p)$, and α is the degree of edges coating of the specimen then the relative error of the halfdrying time, calculated by using 1-D model, does not exceed p due to the use of the 1-D model.

We have calculated $k_\alpha(p)$ for several values of α and p. It was noticed that the accurate result of the halfdrying time can be achieved by using 1-D model if a specimen is relatively wide, irrespective of the level of edges coating. However, the accurate result can be achieved also by increasing the degree of the edges coating. For example, if 1-D model is used for a specimen having $k \geq 4$ and $\alpha \geq 0.95$, then the relative error p of the result will not exceed 0.05 because of use of 1-D model, i.e. relative difference between halfdrying time calculated by using 2-D model and another one calculated by using appropriate 1-D model does not exceed 0.05. The values of $k_\alpha(p)$ depend on the drying conditions slightly.

4. Conclusions

The 2-D-in-space moisture transfer model (1)-(4) can be successfully used to investigate the influence of the surface coating degree as well as geometrical shape of the specimen of northern red oak on the drying dynamics under isothermal conditions.

The proposed error estimation procedure can be used to adjust the width of the specimen (long sawn board) as well as degree of edges coating to ensure required relative error resulting from the reducing the model from 2-D to 1-D-in-space.

The 2-D model guarantees better prediction than the corresponding 1-D one of the drying process of a sawn board if the ratio of the width to the thickness of the specimen is rather small (< 10) or the degree of coating of edges is not very high ($< 0.95 - 0.99$).

REFERENCES

[1] S. Svensson and A.Martensson. Stress-strain Relationship of Drying Wood - Part 2: Verification of a One-dimensional Model and Development of a Two-dimensional Model. *Holzforschung*, **51(6)**, 565–570, (1997).

[2] O. Söderström and M.-G. Salin. On Determination of Surface Emission Factors in Wood Drying. *Holzforschung*, **47**, 391–397, (1993).

[3] W.T. Simpson and J.Y. Liu. An Optimization Technique to Determine Red Oak Surface and Internal Moisture Transfer Coefficients During Drying. *Wood Fiber Sci.*, **29(4)**, 312–318, (1997).

[4] R. Baronas, F. Ivanauskas and M. Sapagovas. The Influence of Wood Specimen Geometry on Moisture Movement During Drying. *Wood Fiber Sci.*, **33(2)**, 166–172, (2001).

On Computation of Unsteady Motion of Two-Fluid Interfaces in Porous Media Flow

N. H. Sharif* and N.-E. Wiberg *

*****Department of Structural Mechanics
Chalmers University of Technology, Gothenburg, Sweden
e−mail: nahidh@sm.chalmers.se

key words: Free Surfaces, Navier-Stokes equations, The Finite Element Method, The Interface Capturing Technique, The Level Set Method, The characteristic-based split methods, The Transient Analysis, The stabilization Technique

ABSTRACT

Summary: We present a numerical model for motion of unsteady two-fluid interfaces in porous media flow. The model is based on the tracking of the interface on a fixed mesh domain. The zero level set of a pseudo-concentration function, which defines the interface between the two fluids, is advected by a time dependent advection equation. The time dependent Navier-Stokes equation and the advection equation are spatially discretized by the finite element method with local mesh refinements in the vicinity of the viscous incompressible interface. The characteristic-based split (**CBS**) algorithm is used for the velocity-pressure segregation of the equations. The explicit forward Eulerian scheme for the time integration is used for the transient analysis. The non-linear flow equation of the Forchheimer form is adopted in the Navier-Stokes equation for the simulation of the flow in porous media. The finite element discretization is stabilized by the **SUPG** and **PSPG** formulations that added to the standard Galerkin formulation. The stabilization formulations provide stability and permit the usage of the same linear interpolation function overall the unknowns. Numerical examples of unsteady non-linear flow of two-fluid interfaces in an earth dam are investigated.

1. Introduction:

Recently the level set method has recognized as a versatile method in solving problems of multiphase flow that encountered in many engineering and medical applications [1,2,3,4,11,12]. The authors in a series of publication has presented an Interface Capturing Technique (**ICT**) for solving problems that involves propagation of fluid-gas or fluid-fluid interfaces in porous media flow [5,6,7,8]. In these articles the interfaces are simulated using the advection equation that derived from the level set method. The level set method represent an initial value problem (**IVP**) of the Hamiltonian-Jacobi PDE type [13], which can be solved using any hyperbolic numerical scheme. Steady flow analyses are presented in recent publications with different artificial time integration methods for the initial value problems. Accordingly the formulations can be used for real time applications. In this paper we intend to couple the time integration technique for the **IVP** with the characteristic-based split method [9,14,15] in order to solve a transient flow in porous media that associated with propagation of two-fluid interfaces. The formulation is performed on a fixed mesh domain where the Eulerian perceptive consist the main framework.

2. Governing equations

The governing equations are the time-dependent Navier-Stokes equations of incompressible flows in porous media, which briefly reviewed here. The space and time domain are denoted by W and $(0,T)$ respectively, and G denotes the boundary of W. The velocity, $\boldsymbol{u}(x,t)$ and the pressure $p(x,t)$ are governed by the momentum and mass balance equations:

$$\begin{aligned} &\frac{\rho}{n_e}\frac{\partial \boldsymbol{u}}{\partial t} + \left(\boldsymbol{A} + \boldsymbol{B}\|\boldsymbol{u}\|^{m}\right)\boldsymbol{u} - \rho \boldsymbol{f} - \nabla \cdot s = 0 \qquad \text{on } W. \quad \forall t \in (0,T) \\ &\nabla \cdot \boldsymbol{u} = 0 \qquad\qquad \text{on } W. \quad \forall t \in (0,T) \end{aligned} \tag{1}$$

The body force due to gravity is denoted by $\boldsymbol{f}$. and the porosity of the porous medium is denoted by n_e. Whereas $\boldsymbol{A} = \mu / k_i$ and $\boldsymbol{B} = \rho \hat{c} / \sqrt{k_i}$ are the Forchheimer parameters, while the power m has the limitation of $1.0 < m < 2.0$. The symbols k_i, $\hat{c}$, represent the intrinsic permeability of porous medium and the constant of the inertial effect, respectively. The divergent of the stress is obtained with the linear constitutive equation relating the stress s to velocity and pressure fields. In the linear constitutive equation for a Newton fluid, the deviatoric stress is assumed to be proportional to fluid rate of strain tensor, which is defined as

$$e(\boldsymbol{u}) = \frac{1}{2}(\nabla \boldsymbol{u} + (\nabla \boldsymbol{u})^{T}) \tag{2}$$

Hence, the stress tensor for a fluid with dynamic viscosity μ is defined as follows:

$$s = -p\boldsymbol{I} + \boldsymbol{T}, \qquad \boldsymbol{T} = 2\mu e(\boldsymbol{u}) \tag{3}$$

To model fluid-gas interfaces, we consider two immiscible fluids, l and g, with densities ρ_l and ρ_g, viscosities μ_l and μ_g. An interface function f serves as a marker identifying the fluid-gas domain by the following simple definition $f = \{1 \text{ for fluid and } 0 \text{ for gas}\}$. The interface between the two fluids is approximated to be at $f = 0.5$, and accordingly the phase dependent variables defined as

$$x(f) = \begin{cases} x_l & f = 1 \\ 0.5 \cdot (x_l + x_g) & f = 0.5, \\ x_g & f = 0 \end{cases} \qquad x = \rho, \mu, n_e \tag{4}$$

The evolution of the interface function is governed by the regularized time dependent advection equation

$$\left.\frac{\partial f^{e}}{\partial t}\right|_{e \to 0} + \boldsymbol{u} \cdot \nabla f - e\Delta f^{e} = 0. \qquad \text{on } W. \quad \forall t \in (0,T) \tag{5}$$

A set of boundary condition and a divergent free initial condition for the velocity field and an initial profile of the interface function is provided to the solution of above equations.

3. Explicit Time Integration and CBS method

An explicit time integrator based on the forward Euler scheme is used to solve the time dependent problem. This scheme has potential ability to reduce the time of the computation and especially for large-scale problems and for higher dimension. For the purpose of describing the explicit time integration scheme and the operator splitting of the CBS method the obtained discretized and stabilized system of equation can be written as

$$
\begin{aligned}
&(\mathbf{M}+\mathbf{M}_{\mathbf{d}})\dot{\mathbf{U}}+\mathbf{A}(\mathbf{U})+\mathbf{B}(\mathbf{U})\mathbf{U}+(\mathbf{C}+\mathbf{C}_{?})\mathbf{P}+\mathbf{D}\mathbf{U}=\mathbf{F}+\mathbf{F}_{?} \\
&\mathbf{C}^{T}\mathbf{U}=\mathbf{0} \\
&(\mathbf{M}_{\Phi}+\mathbf{M}_{\mathbf{d}})\dot{\mathbf{F}}+\mathbf{K}_{\Phi}(\mathbf{U})\mathbf{F}+\mathbf{K}_{\mathbf{d}}(\mathbf{U})\mathbf{F}+\mathbf{K}\mathbf{F}^{\mathbf{e}}=\mathbf{F}_{\Phi}
\end{aligned}
\tag{6}
$$

Where **U**, **P** and F are the vectors of unknowns of the (nodal values) velocities, pressures and the advection functions respectively. The construction of the matrices **M**, **K**, **C**, **A**, **B**, $\mathbf{M}_{\mathbf{T}}$, $\mathbf{M}_{\mathrm{d}}$, $\mathbf{K}_{T}$, $\mathbf{K}_{\mathrm{d}}$, $\mathbf{C}_{\mathrm{g}}$ and the vectors **F,** $\mathbf{F}_{\mathrm{g}}$ are reviewed briefly in [5,6,7,8]. The forward Euler method of time integration, applied to equation (6) gives

$$
\mathbf{U}_{n+1}=\mathbf{U}_{n}+dt(\mathbf{M}+\mathbf{M}_{\mathrm{d}})^{-1}[\mathbf{F}+\mathbf{F}_{\mathrm{g}}-\mathbf{A}(\mathbf{U}_{n})-\mathbf{B}(\mathbf{U}_{n})\mathbf{U}_{n}-(\mathbf{C}+\mathbf{C}_{\mathrm{g}})\mathbf{P}_{n}] \tag{7}
$$

In order to use equation (7) to advance the velocity, the pressure at time t_n has to be computed; this is done by the CBS method, by combining the momentum equation with the time differentiated version of compressibility constraint in (6), ($\mathbf{C}^{T}\dot{\mathbf{U}}=\mathbf{0}$ since $\mathbf{C}^{T}\mathbf{U}=\mathbf{0}$ for all time) to generate the consistent discretized Poisson equation for the pressure, evaluated at time t_n,

$$
(\mathbf{C}^{T}\mathbf{M}_{L}^{-1}\mathbf{C})\mathbf{P}_{n}=\mathbf{C}^{T}\mathbf{M}_{L}^{-1}[\mathbf{F}+\mathbf{F}_{\mathrm{g}}-\mathbf{A}(\mathbf{U}_{n})-\mathbf{B}(\mathbf{U}_{n})\mathbf{U}_{n}-\mathbf{D}\mathbf{U}] \tag{8}
$$

With $\mathbf{U}_n$ that satisfies $\mathbf{C}^{T}\mathbf{U}=\mathbf{0}$ The sequence of steps of advancing the velocity and pressure from t_n to t_{n+1} is thus

$$
\mathbf{G}_{n}=\mathbf{M}_{L}^{-1}[\mathbf{F}+\mathbf{F}_{\mathrm{g}}-\mathbf{A}(\mathbf{U}_{n})-\mathbf{B}(\mathbf{U}_{n})\mathbf{U}_{n}-\mathbf{D}\mathbf{U}] \tag{9}
$$

$$
(\mathbf{C}^{\mathbf{T}}\mathbf{M}_{\mathbf{L}}^{-1}\mathbf{C})\mathbf{P}_{n}=\mathbf{C}^{T}\mathbf{G}_{n} \tag{10}
$$

$$
\mathbf{U}_{n+1}=\mathbf{U}_{n}+dt[\mathbf{G}_{n}-\mathbf{M}_{L}^{-1}(\mathbf{C}+\mathbf{C}_{\mathrm{g}})\mathbf{P}_{n}] \tag{11}
$$

$$
\mathbf{F}_{n+1}=\mathbf{F}_{n}+dt(\mathbf{M}_{\Phi}+\mathbf{M}_{\mathrm{d}})^{-1}[\mathbf{F}_{\Phi}-\mathbf{K}_{n}(\mathbf{U})\mathbf{F}+\mathbf{K}_{\mathrm{d}}(\mathbf{U})\mathbf{F}+\mathbf{K}\mathbf{F}^{\mathrm{e}}] \tag{12}
$$

The presence of the $\mathbf{M}_{L}^{-1}$ in above equation required the use of a lumped mass matrix.

4. Conclusion

The computation of the problem is very intensive, hence an efficient implementation is required in order to produce the desired accuracy and to minimize the computation effort. An object oriented programming using the C++ package of PETSC [10] is under processing. Furthermore we intend to improve the technique by combining the formulation with FE-adaptivity in the

vicinity of the interface. The formulation is more flexible in handling fixed mesh domain in order to track two-fluid interfaces.

REFERENCES

[1] J. A. Sethian, Level Set Methods, Evolving Interface in Geometry, Fluid Mechanics, Computer Vision, and Material Science, Cambridge University Press (1996).

[2] J. A. Sethian, Level Set Methods and Fast Marching Methods, Cambridge, Cambridge University Press (1999).

[3] M. Sussman, P. Smareka and S. Osher, "A Level Set Approach for Computing Incompressible Two-Phase Flows", *J. Comp. Phys.*, **114**, 146-168, (1994).

[4] M. Sussman, E. Fatemi, P. Smareka and S. Osher, "A Improved Level Set Method for Incompressible Two-Phase Flows", *J. Computers and Fluids*, Vol. **4**, 212-223 (1996).¨

[5] N. H. Sharif and N.-E. Wiberg, "Free-Surface Flow Predictions by an Interface Capturing FE-Technique" International Journal for Computational Civil and Structural Engineering (*IJCCSE*), Vol. **1**, Issue **2**, 98-106, (2000).

[6] N. H. Sharif and N.-E. Wiberg, "Free Surface Flow through Rock-Fill Dams Analyzed by FEM with Level Set Approach", to appear in Journal of Computer Modeling and Simulation in Engineering (*C.M.S.E*), Vol. **3**, (2001).

[7] N. H. Sharif and N.-E. Wiberg, "Adaptive ICT-Procedure for Nonlinear Seepage Flows with Free Surface in Porous Media", accepted for publication in Communications in Numerical Methods in Engineering (*CNME*), June (2001).

[8] N. H. Sharif and N.-E. Wiberg, "Computing Steady Motion of Incompressible Fluid Interface in Porous Media Flow", on CD in the European Congress on Computational Methods in Applied Sciences and Engineering, ECCOMAS Computational Fluid Dynamics Conference 2001, Swansea, Wales, UK, 4-7 September (2001).

[9] O.C. Zienkiewicz and R.L. Taylor, " The Finite Element Method" Volume 3, Fluid Dynamics, Fifth Edition. BH, (2001).

[10] PETSC WWW home page: http://www-fp.mcs.anl.gov/petsc/, 2000.

[11] S. Osher, and J. A., Sethian, "Fronts Propagating with Curvature Dependent Speed: Algorithm Based on Hamilton-Jacobi Formulations", *J. Comput. Phys.* **79**, 12-49 (1988)

[12] S. Osher and R. P. Fedkiw, "Level Set Method: An overview and some Recent Results" Recent UCLA Computational and Applied Mathematics Reports, Department of Mathematics, University of California, Los Angeles, California, February 2000

[13] T. J. Barth and J. A. Sethian, "Numerical Schemes for the Hamilton-Jacobi and Level Set Equations on Triangulated Domains", *J. Comp. Phys.*, **145**, 1-40, (1998)

[14] T. Tezduyar, S. Aliabadi, M. Behr, "Enhanced-Discretization Interface-Capturing Technique (EDICT) for Computation of Unsteady Flows with Interfaces", *Comp. Methods Appl. Mech. Eng.*, **155**, pp. 235-248, (1998).

[15] Y. Saad and M. H. Schultz, "GMRES: A Generalized Minimal Residual Algorithm for Solving Non-symmetric Linear Systems", *J. Soc. Idust. Appl. Math.* Vol. **7**, No. 3, July (1986).

Interactive Finite Element Analysis by Java3D API

Ling Lu, Odd Tullberg

Department of Structural Mechanics
Chalmers University of Technology, Gothenburg, Sweden
ling@sm.chalmers.se, odd@sm.chalmers.se

Summary the paper presents a framework for performing interactive Finite Element Analysis (FEA) in Virtual reality (VR). The Java3d API has been chosen as the software tool to develop our system and perform interactive FEA in VR. A 3D world for interactive FEM by Java 3D API is set up where the 3D models for analysis are loaded from other CAD packages, such as 3DS and DXF.

1. INTRODUCTION

In recent years, there has been much excitement about Virtual Reality (VR). From its beginning in the field of scientific simulation, VR has gradually grown into a new phase and become a distinct field in the world of computing. The utility of VR have already been researched and used in car design, robot, medicine, chemistry, biology and education, as well as in building design and construction.

The Finite Element Method (FEM) and Finite Element Analysis (FEA) were created in the late 1940's as a structural analysis tool that was to assist aerospace engineers design better aircraft structures [1]. Since then, aided by the rapid growth of computer power, the method has continually developed until it has become a sophisticated generic tool for accomplishing a wide array of engineering tasks. It has been used in civil, mechanical, geotechnique,, and environment engineering, as well as in many other areas. The software techniques for FEA are already very developed and mature.

The traditional way to express a design before the construction is finished is to use 2D or 3D drawings, which are drawn on 2D paper; Current Computer Aided Design (CAD) software, like AutoCAD or SolidWorks, can do semi-real-time visualisation and rendering of the 3D data on the computer display system. It is usually very difficult to imagine a complex building before it is constructed. VR systems present a new method to show the ideas in a realistic 3D world. In this world, the architects and final users can discuss how the building will look before it is constructed and reach agreement on design decisions in a more intuitive and efficient way. Engineers can see abstract data, such as deformation, stress or strain, which needed to be visualised in a "concrete and real" way. Constructors can choose a better way to finish construction of the building.

To perform interactive FEA in VR leads to a comprehensive understand of the analysis and the design in a 3D world. The basic ideas have already been around for some time. Interactive FEA in VR, as one useful application of VR is taking off and being actively developed [2].

By using virtual pointers (like 3D mouse) and sharing virtual workspaces, remote collaboration and accurate information sharing can be achieved. Apart from using VR in interactive FEA in the building and construction industry, it can also be used in the education of engineering students, to give students an intuitive understanding of the FEA technique.

2. FRAMEWORK OF INTERACTIVE FEM AND AIM OF THE RESEARCH

Most FEA package, such as ABAQUS and ANSYS, support importing geometry from other CAD packages, and have an interactive pre/post processor, which include modelling, managing, monitoring analysis jobs, and result animations. The aim of the research is to set up an interactive FEA system in VR. It will integrate CAD, FEA and VR to perform real time interactive FEA. The system consists of five components:

- Approximation module: Software to provide fast feedback and results to the user even at the expense of accuracy.
- FEA module: FEA code to perform analysis.
- VR module: Software to interact with the VR world.
- Visualisation module: Software to visualise the numerical results from the FEA module.
- Database module: Software to handle the input output and storage of results.

The "Glue" code is needed to make all the modules work together. The Layout of an interactive FEA framework is as Figure 1.

The commercial FEA package available will be explored for FEA module, and FEA in Java has been studied. This research will be concentrated on VR and Visualization modules.

The main aims of the research are:

- Set up a 3D world for interactive FEA in VR.
- Interactively modify input within VR.
- Interactively view of the results in VR.
- Implement FEA in view of the specific requirements of conducting FEA in VR (primary latency reduction)

Within this project, the main task will be setting up a 3D world and modifying the input to show some interesting results in VR.

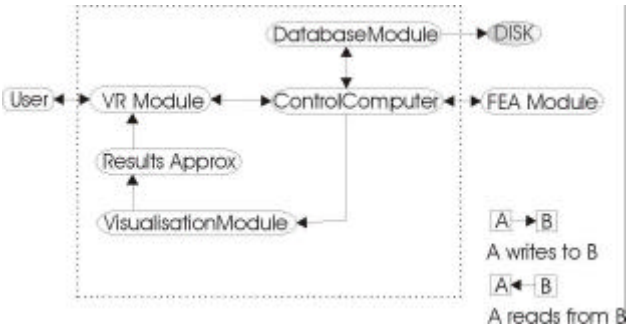

Figure 1 Interactive FEA Framework

3. SET UP AN INTERACTIVE FEA 3D WORLD USING THE JAVA 3D API

3.1. Why Java and Java 3D API is chosen as the developing tool?

A language called "Oak" was created at Sun Microsystems, Inc. in 1991, but was renamed "Java" in 1995. It is created with the initial motivation for the need of a platform-independent language. It can be used to create two types of programs: applications and applets. It has many properties, such as: simple, portable, secure, robust, multithreaded, distributed, high performance, Object-oriented. As an object oriented programming language, Java also has the three principles of OOP: Encapsulation, Inheritance, and Polymorphism.

The Java 3D API is an interface for writing programs to display and interact with 3D graphics. 3D geometric objects are created and manipulated reside in a virtual universe, which is then rendered. The Java 3D renderer is capable of rendering in parallel. The instances of Java 3D objects are put into a scene graph data structure. The scene graph is an arrangement of 3D objects in a tree structure that completely specifies the contents of the virtual universe, and how it should

be rendered. The virtual universe is referenced to Locale objects, and Locale objects serves as the root of multiple subgraphs of the scene graph. A BranchGroup (BG) object is the root of a subgraph, which has two categories: the view branch graph and the content branch graph. A content branch graph is assembled from objects to define the geometry, behaviours, sound, lights, location, appearance, etc. A view branch graph specifies viewing parameter. A TransformGroup (TG) is often used in the creation of scene graphics, which hold geometry and its transformation [3]. Figure 2 shows a simple scene graph.

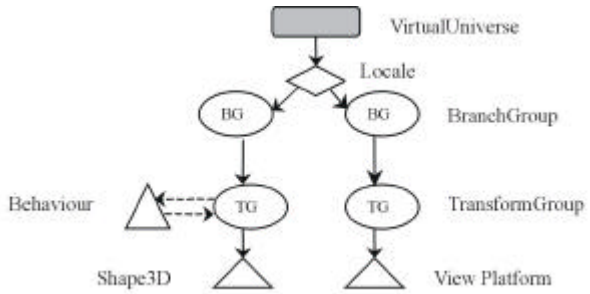

Figure 2 A Simple Scene Graph

The objects in the Java 3D can be created either by code to specify the geometry or by loader classes, which are provided by Java 3D utility package. Loaders can create Java 3D visual objects from files created with 3D modelling software. Loaders today exist for VRML files, AutoCAD DXF files, 3D studio 3DS files, Solid Works SLD, Visual Toolkit VTK, and a variety of other 3D file formats.

To implement interaction, Behaviour objects can be defined in a Java 3D scene graph. It is used to change the scene graph or objects in scene graph, in respond to stimulus. Changes include adding objects, detaching objects, change attributes of the objects, or a combination of these behaviours.

3.2. Framework of the interactive FEA in Java 3D world

To implement interactive FEA in VR, The Java 3D API is used to set up a 3D world for the VR module. The scene graph is produced as figure 3.

BranchGroup BG1, BG2, BG3 are the main components for the 3D world. BG2 is mainly used for setting up the static scene by reading the model from 3DS files or from direct coding of geometry, and is usually used to set up the environment. BG1 is mainly used for dynamic reading in the model from the code of the geometry, which can be changed during the interactive procedure.

BG3 is used for setting up the view platform in the VR world. The interactive behaviour is mainly performed in BG1. BGN can be added if more components are needed in the scene graph.

4. CONCLUSIONS AND FUTURE WORK

Using VR in FEA gives a more comprehensive and intuitive way to understand the work. The overview of the available VR system and graphic APIs, and the study of the related work show the feasibility of using VR in FEA.

A framework of performing interactive FEA has been set up. A 3D world for interactive FEM by Java 3D API has been set up where the 3D models for analysis are loaded from other CAD packages, such as 3DStudio.

The basic 3D world for interactive FEA has been set up; next we will further develop the interface, which include modelling the environment and the user, modelling interface for interactive FEM and FEA, connecting with the FEA software to implement interactive finite element analysis in VR.

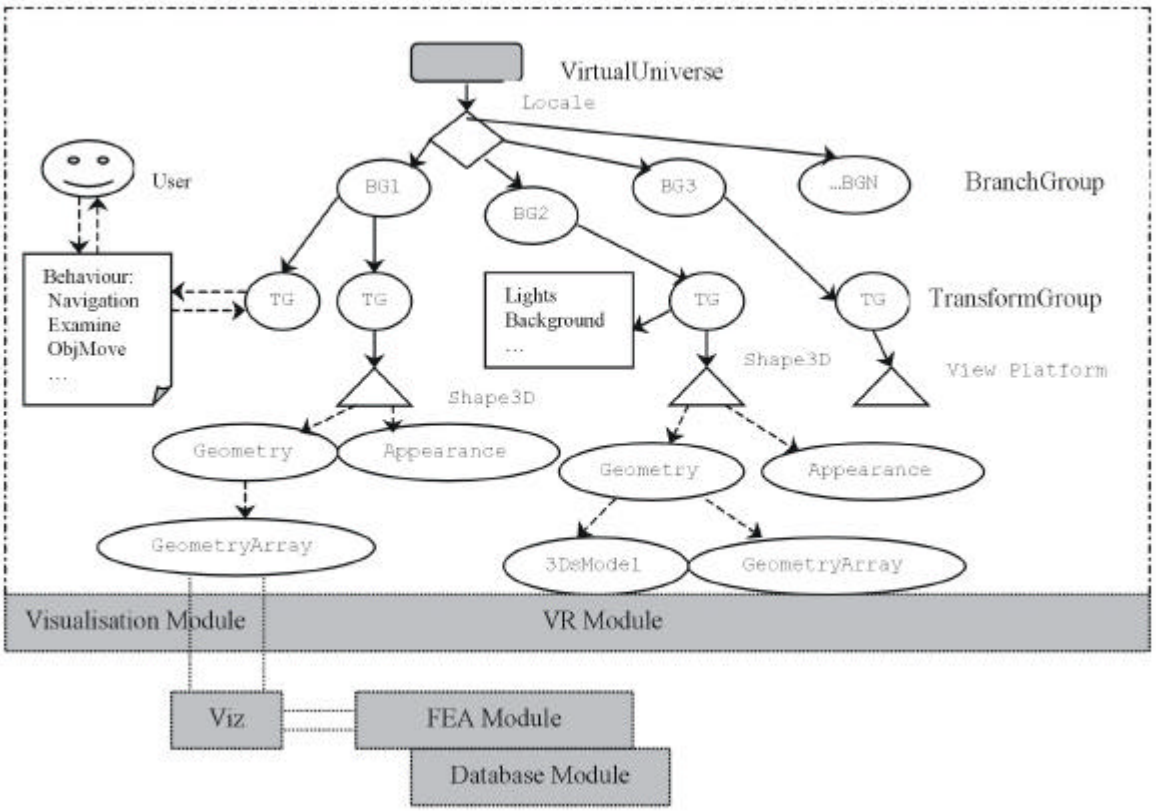

Figure 3 Interactive FEA in Java 3D World

REFERENCE

[1] Zienkiewicz, O.C., *The Finite Element Method*, 4th edition, McGraw-Hill, London, 1994.

[2] Connell, M., Kettil, P., Tägnfors, H., Tullberg, O., Wibeerg, N., (2000, Greece) *Integrating modelling, simulation and visualisation in immersive VR environments- A Tool in bridge design*, computational methods for shell and spatial structures, IASS-IACM 2000, Athens, Greece.

[3] Java3d Homepage, accessed July 28, 2000, http://java.sun.com/products/java-media/3D/collateral/, *Getting started with the Java 3D API*, tutorial v1.5.1.

CORBA in distributed finite element applications

J. Lindemann*, O. Dahlblom and G. Sandberg
Division of Structural Mechanics
Lund University, Lund, Sweden
e–mail: struchmech@byggmek.lth.se

ABSTRACT

Summary A sample structural mechanics code is encapsulated using CORBA components implemented in C++. The different components of the code can be transparently placed, either locally or remotely without changing the client application.

1 Introduction

A complex hardware product often consists of many exchangeable components. As long as a component fits into the product, the internal implementation can differ. Software components are analogous to hardware components. Components in programs can be exchanged without the need for recompilation, as long as the component interface is unchanged. The use of components in software development has increased during the last few years. The reason for this is the need to reduce the size of the client programs. When the first client/server systems appeared, the client software were often large programs. Most of the processing was done in the client program and the database server was used as data storage. The problem with these systems was the cost of installing and maintaining the client software. New systems developed today often use a thin client with little or no data processing capabilities. Instead of calling the database servers directly, they use a set of components placed on central servers for data processing. These components then access the database servers. The advantage of this approach is that the components can be placed on powerful systems, reducing the amount of processing needed at the client. This approach has been successfully applied to database applications. It is of interest to apply this technique to analysis software as well. Using the technique of distributed computing, clients can use components as if they were located on the same machine, making it possible to create integrated programs with transparent access to computational resources, such as available workstations on the network or resources at High Performance Computing (HPC) centres. This would make high performance computing more available to a wider user group.

2 Client/server architecture

Three-tier and n-tier applications emerged from the need to shield the client program from changes at the server side by placing a layer between the client and the server. A detailed history of the client/server architecture is described by Schussel [3]. For a more detailed description, see Orfali and Harkey [2]. The logical three-tier or n-tier model divides an application into three or more logical components. Each component is responsible for a well-defined task. In a database application

there would be a presentation layer for displaying data and modifying data, a logic and rules layer and a database layer responsible for storing the data.

The components of the logical model can be grouped together in different configurations to form a physical model. One of the most interesting combination of the logical model is when the three logical services are placed as separate applications on different computers, forming a physical three-tier application. This implementation enables developers to have a greater flexibility in the choice between different hardware and software configurations.

3 CORBA

CORBA is the Object Management Group's [1] specification for interoperability and interaction between objects and applications. Objects and applications can be placed on any platform and accessed from any platform. CORBA is a specification, and therefore platform-independent. To use the CORBA specification there has to be an ORB (Object Request Broker) for the specified platform. There are ORB:s for almost all existing platforms today.

CORBA is a client/server architecture. Client make request on objects, located locally or remotely. The requests are dispatched by the client ORB to the server ORB. The server ORB then directs the request the object implementations.

To invoke an operation on an object, the client must know the interface it supports. The interface is composed of methods the objects support. The interfaces are described using the interface definition language (IDL). The purpose of the interface definition language is to define the object interfaces in a way that is independent of any programming language.

4 Finite element CORBA implementation

To illustrate the method for distribution of resources, a three-dimensional beam analysis program was chosen as a sample implementation. The application was divided into three logical components, see Figure 1. By dividing the application into components, the application becomes easier to maintain during and after development. The middlelayer was implemented as one server compo-

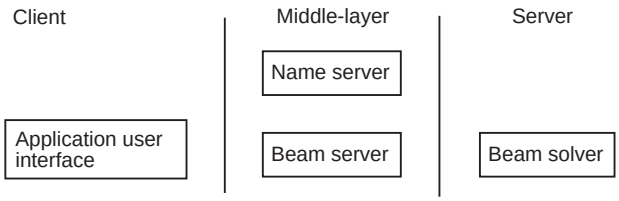

Figure 1: Application components

nent using the ORBacus [6] ORB. ORBacus is a commercial ORB, which is available with source code for non-commercial use. It is also portable across a wide range of platforms including Windows and many Unix dialects. The implementation layer is written in C++ using the newmat09 library [7].

The interfaces used in the beam server should be general enough to handle any static finite element model. By using a general interface it can be reused at later date without needing any changes to its definition.

5 Configuration of a CORBA finite element system

One of the biggest benefits of CORBA is location transparency. Information about server location is often not included in the client application. This makes it easy to configure a client server setup. A client only needs an object reference to connect to an object. Object references are unique identifiers, which also include information about the location of objects. To connect to objects the client needs a way of retrieving an object reference. This is done using a special name server introduced in CORBA 2.3. The name server stores object references in a human readable form. The client queries the server by name to receive the object reference.

The easiest configuration of the finite element system is to install the client application together with the beam server and the finite element solver on a single computer, see Figure 2. This configuration is typically used to do calculations that fit into the memory of the local machine.

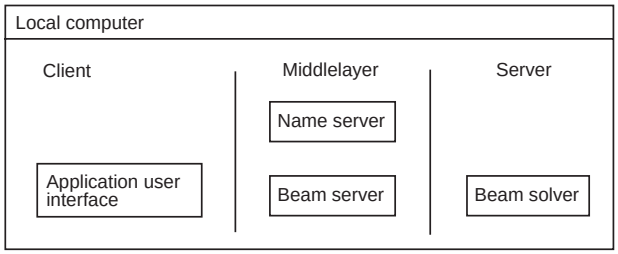

Figure 2: Local configuration

In the first distributed configuration, the middlelayer and implementation are moved to a separate computer. This configuration requires the server to be able to run a CORBA ORB. If the server running the finite element solver does not support running an ORB, the middlelayer can be placed on a separate computer. Figures 3 and 4 show two of the possible configurations. Many more configurations are possible.

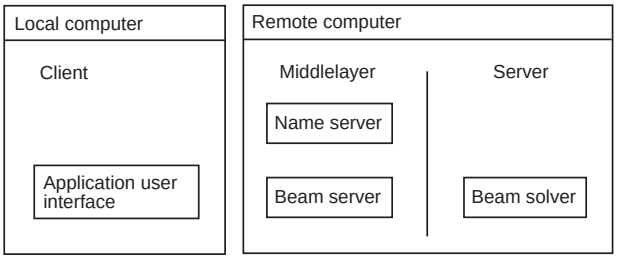

Figure 3: Remote configuration 1

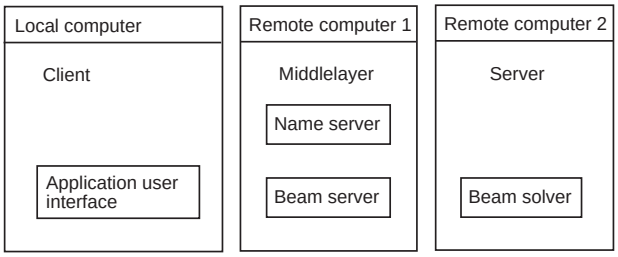

Figure 4: Remote configuration 2

6 Conclusion

Using a three-tier implementation with interfaces and components, creates a very flexible finite element application. The three-tier implementation protects the client applications from changes in configuration and solver design. Components are easily configurable and maintainable, reducing the need for further development. By using interfaces when communicating with components, the need to recompile client software when a new functionality is introduced in the solver components is reduced. Interfaces can also be published enabling other software to use the finite element application in an effective way. The CORBA specifications also enable new ways of using software. Client software can easily distribute calculations over available workstations. High Performance Computing (HPC) centres would be able to host a set of applications as CORBA objects. From a web site, users can register themselves as users and download client applications that connect to the objects. This would make high performance computing more available to a wider user group.

REFERENCES

[1] Object Management Group, Inc., http://www.omg.org, 2000

[2] R. Orfali and D. Harkey, Client/server programming with Java and CORBA. - 2nd ed., John Wiley and Sons Inc., 1998

[3] G. Schussel, Client/Server: Past, Present and Future, http://www.dciexpo.com/geos/dbsejava.htm, 1996

[4] The Open Group, http://www.opengroup.org/dce, 2000

[5] M. Henning and S. Vinoski, Advanced CORBA Programming with C++, Addison Wesley Longman Inc., 1999

[6] Object Oriented Concepts Inc., ORBacus 4.0, http://www.ooc.com/ob, 2000

[7] R. Davies, newmat09, a matrix library in C++, http://webnz.com/robert/cpp_lib.htm#newmat09, 200

An adaptive strategy based on gradient of strain energy density with application in meshless methods

Yunhua Luo
Concrete Division, Institute of Concrete Structures and Building Materials
University of Karlsruhe, 76128 Karlsruhe, Germany
e–mail: gd92@rz.uni-karlsruhe.de

ABSTRACT

Summary A gradient-based adaptive procedure is proposed in this paper. The relative error in strain energy from two adjacent adaptation stages is used as a stop-criterion. The refinement criterion is based on the gradient of strain energy density. The strategy was implemented in the Element-Free Galerkin method. Numerical investigation was conducted to study the performance of the proposed procedure.

General idea In numerical methods such as finite element methods, meshless methods and so on, mesh refinement based on an adaptivity mechanism is becoming a standard procedure, in order to achieve a prescribed accuracy with a minimal number of nodes or to capture a local structural behavior. Most conventional adaptive methods [1, 2] were developed aiming at the finite element methods and it is for this reason, some of them have limitations or are inconvenient in application to meshless methods.

In this paper, a gradient-based adaptive procedure is suggested and implemented in the Element-Free Galerkin method. The two main ingredients in an adaptive procedure are: when to stop and how to refine. For a given structure under a set of given loads with a given load path, at an equilibrium point the total strain energy stored in the structure is definite. As a basic requirement on an adaptive procedure, approximate strain energy must converge to its real value. Therefore the relative variation in strain energy can be used as a stop-criterion. The other ingredient is how to refine meshes. The aim of refinement is to give a better approximation to unkown fields such as displacements, strains, stresses and so on, and thus give a better approximation to strain energy. Based on this reasoning, the gradient of strain energy density can be used as a guide to refine meshes.

Stop-criterion The principle of minimum potential energy is used here as a starting point. The total potential energy in a load-bearing structure can be written as

$$\Pi = \Pi^s + \Pi^e = \frac{1}{2}\int_\Omega \boldsymbol{\sigma}^T \boldsymbol{\varepsilon} d\Omega - \int_\Omega \boldsymbol{p}^T \boldsymbol{u} d\Omega - \int_S \boldsymbol{q}^T \boldsymbol{u}\, ds \tag{1}$$

where $\boldsymbol{\sigma}$ and $\boldsymbol{\varepsilon}$ are stress and strain vectors. $\boldsymbol{u}$ is the displacement vector. $\boldsymbol{p}$ and $\boldsymbol{q}$ are respectively body force and surface traction. Ω is the domain occupied by the structure and S the surface where traction is exerted. Π^s and Π^e represent strain energy and external potential energy. For a given structure under a set of given loads with a given load path, at an equilibrium point the total strain energy stored in the structure is definite, although it is unknown in most cases, except an analytical solution to the problem is available.

In pursuing a better approximate solution, an adaptive procedure produces a series of approximate strain energy, $\tilde{\Pi}_i^s$ (i=1, 2, $\cdots$), corresponding to a series of meshes M_i ($i = 1, 2, \cdots$). As a basic requirement on an adaptive procedure, the above series $\tilde{\Pi}_i^s$ must converge to Π^s. That is, for a given δ ($\delta > 0$), $\exists$ an integer K ($K > 0$), so that $\forall\, k > K$,

$$|\tilde{\Pi}_k^s - \Pi^s| \leq \delta\, |\Pi^s|, \qquad |\tilde{\Pi}_{k+1}^s - \Pi^s| \leq \delta\, |\Pi^s|$$

This leads to the following equivalent relation

$$|\tilde{\Pi}_{k+1} - \tilde{\Pi}_k| \leq \eta\, |\tilde{\Pi}_{k+1}| \qquad (0 < \eta \leq \delta) \tag{2}$$

Equation (2) provides a criterion to stop an adaptation loop, which is similar to a conventional global error estimator defined by the energy-norm of errors from strains or stresses [2], except that the more exact solution is from a subsequent (better) mesh rather than from the same mesh by a recovery or a projection procedure.

Refinement-criterion The general idea for mesh-refienment in a gradient-based method can be briefly stated as: A larger gradient needs a richer mesh and *vice versa*. A coarse mesh may not be able to produce accurate solutions to displacements or stresses, but might give adequate information about how these fields vary in the problem domain. As regard to variation from which field should be considered, there are quite several choices, displacement, strain or stress and so on. But strain energy density is a reasonable choice for the following reasons: strain energy density is scalar and independent of coordinate system; information about other fields such as displacement, strain, stress, load distribution and so on are comprehensively embodied in the strain energy density.

To measure the the richness of mesh with respect to the variation of strain energy density, mesh intensity r_d is introduced and defined as the ratio of the variation (gradient) of strain energy density to mesh density.

$$r_d = \frac{G^{SED}}{D^M} \tag{3}$$

where G^{SED} is the gradient of strain energy density. D^M is mesh density defined as the number of nodes in a unit area or volume. The maximum and minimum of r_d are, respectively, denoted as R_{max} and R_{min}. The criterion for mesh-refinement is set up as

$$R_{min} \leq R_c \leq R_{max}$$

$$\begin{cases} r_d > R_c & \text{refine} \\ r_d < R_c & \text{coarsen} \end{cases} \tag{4}$$

Numerical results The above adaptive procedure was implemented in the Element-Free Galerkin method [3, 4] and is obviously applicable to finite element methods in principle. Numerical investigation was conducted to study the performance of the proposed procedure. Results from one example, among many others, are presented here. The cantilever beam shown in Fig. 1 was simulated as a plane strain problem. The beam has a length $L = 10$ and a width $2b = 2$. The material of the beam is elastic, with Young's modulus $E = 1000$ and Poisson's ratio $\nu = 0.3$. The beam is constrained at its left end and loaded at right end by a distributed shear force with a resultant Q.

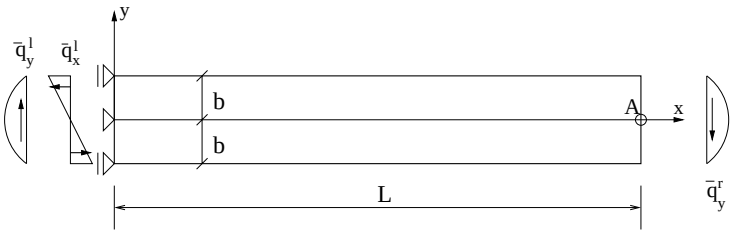

Figure 1: A cantilever beam simulated as a plane stress model

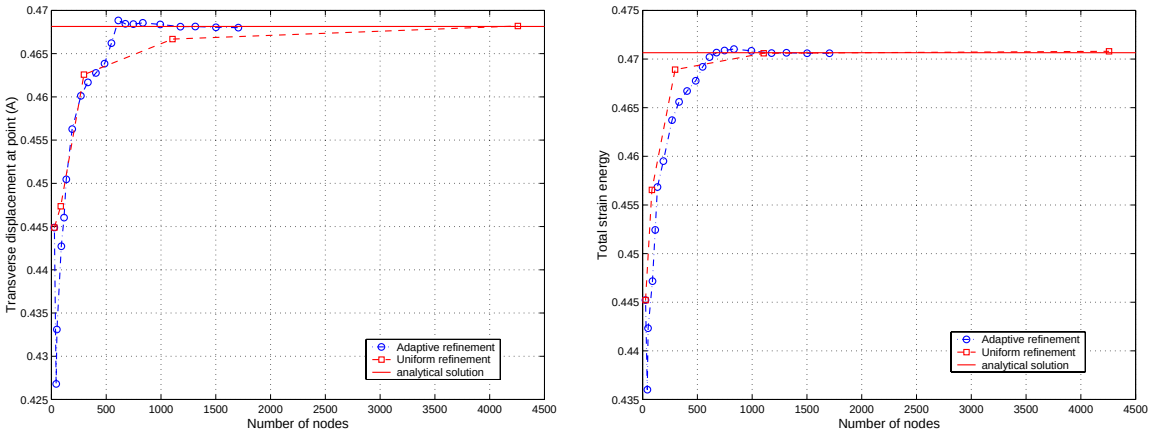

Figure 2: Convergence in displacement at point A and in total strain energy

To avoid singularity distributed loads are also applied at left end. The convergences in transverse displacement at point A, cf Fig. 1, and in strain energy are shown in Fig. 2, and compared with analytical solutions. Fig. 3 displays mesh configurations from different stages.

Conclusions A gradient-based adaptive procedure is proposed in this paper. The relative error in total strain energy from two adjacent adaptation stages is used as a stop-criterion. Mesh refinement is guided by the gradient of strain energy density. The procedure was implemented in the Element-Free Galerkin method. Numerical investigations show that the approximate strain energy, $\tilde{\Pi}_i^s$, steadily converges to its 'real' value, Π^s, with the increase of node number, or more exactly with the decrease of maximal mesh intensity; Approximate fields such as displacements and stresses converge to their corresponding 'real' fields with the decrease of error in total strain energy. The gradient of strain energy density is very effective as a guide for mesh refinement; For problems free of singularity the accuracy of approximate fields can always be improved by reducing the maximal mesh intensity; For problems with singularity, convergence in strain energy can

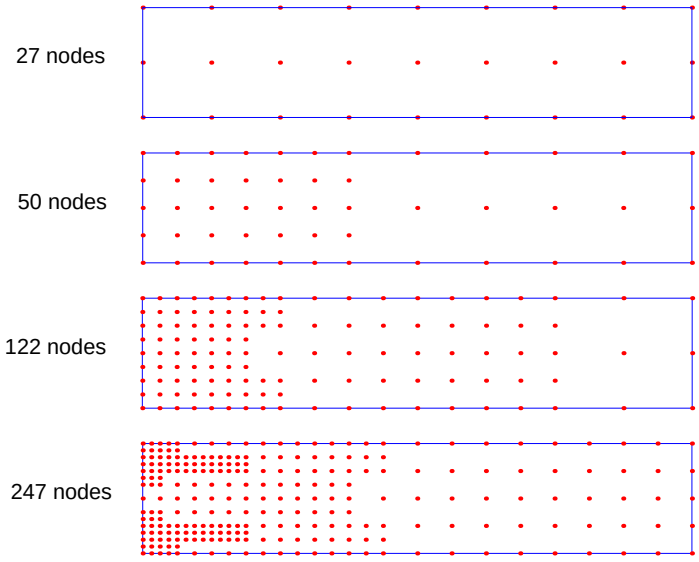

Figure 3: Node configurations from different adaptation stages

be guaranteed by suitably controlling the minimal nodal distance.

REFERENCES

[1] I. Babuška and W. C. Rheinboldt. Error estimates for adaptive finite element computations. *SIAM J. Numer. Anal.* 1978; **15**:736-754.

[2] O. C. Zienkiewicz and J. Z. Zhu. A simple error estimator and adaptive procedure for practical engineering analysis. *Int. J. Numer. Meth. Engng.* 1987; **24**:337-357.

[3] Y. H. Luo and U. Häussler-Combe. An adaptivity procedure based on gradient of energy density and its application in meshless methods. *International Workshop on Meshfree Methods for PDEs*, Bonn, Sept. 11-14, 2001.

[4] Y. H. Luo and U. Häussler-Combe. A gradient-based adaptation procedure and its implementation in Element-Free Galerkin method. Manuscript submitted to *Int. J. Numer. Meth. Engng.*, 2001.

Boundary knot method for Laplace and biharmonic problems

W. Chen
Department of Informatics, University of Oslo, P.O.Box 1080, Blindern, 0316 Oslo, Norway
E-mail: wenc@ifi.uio.no

ABSTRACT

Summary The boundary knot method (BKM) [1] is a meshless boundary-type radial basis function (RBF) collocation scheme, where the nonsingular general solution is used instead of fundamental solution to evaluate the homogeneous solution, while the dual reciprocity method (DRM) is employed to approximation of particular solution. Despite the fact that there are not nonsingular RBF general solutions available for Laplace and biharmonic problems, this study shows that the method can be successfully applied to these problems. The high-order general and fundamental solutions of Burger and Winkler equations are also first presented here.

Introduction: As a boundary-type RBF scheme, the method of fundamental solution (MFS), also known as regular boundary elements, attains refresh attentions in recent years [2]. Because of the use of singular fundamental solution, the MFS requires a controversial fictitious boundary outside physical domain, which effectively blocks its practical use for complex geometry problems. Chen and Tanaka [1] recently developed a boundary knot method (BKM), where the perplexing artificial boundary is eliminated via the nonsingular general solution. Just like the MFS and dual reciprocity BEM (DR-BEM) [3], the BKM also applies the DRM to approximate the particular solution. The method is symmetric, spectral convergence, integration-free, meshfree and easy to learn and implement, and successfully applied to Helmholtz, convection-diffusion, and Winkler plate problems. Unfortunately, the nonsingular RBF general solutions of Laplace and biharmonic operators are a constant rather than the RBF. Based on some physical investigations, this paper presented a few simple strategies to apply the BKM to these problems without losing its merits.

BKM for Laplacian: For a complete description of the BKM see ref. 2. Here we begin with a Laplace problem

$$\nabla^2 u = f(x), \qquad x \in \Omega, \tag{1}$$

$$u(x) = R(x), \qquad x \subset S_u, \qquad \frac{\partial u(x)}{\partial n} = N(x), \qquad x \subset S_T, \tag{2a,b}$$

where x means multi-dimensional independent variable, and n is the unit outward normal. The governing equation (1) can be restated as

$$\nabla^2 u + \delta^2 u = f(x) + \delta u \quad \text{or} \quad \nabla^2 u - \delta^2 u = f(x) - \delta u, \tag{3a,b}$$

where δ is an artificial parameter. Eqs. (3a,b) are respectively Helmholtz and diffusion-reaction equations. Their zero and high order general solutions [3] are

$$u_m^{\#}(r) = Q_m(\gamma r)^{-n/2+1+m} J_{n/2-1+m}(\gamma r), \quad \text{and} \quad u_m^{\#}(r) = Q_m(\pi r)^{-n/2+1+m} I_{n/2-1+m}(\pi r), \ n \geq 2, \tag{4}$$

where n is the dimension of the problem; $Q_m = Q_{m-1}/(2*m*\gamma^2)$, $Q_0 = 1$; m denotes the order of general solution; J and I represent the Bessel and modified Bessel function of the first kind. The solution of the problem can be split as the homogeneous and particular solutions

$$u = u_h + u_p, \tag{5}$$

The latter satisfies the governing equation but not boundary conditions. To evaluate the particular solution, the inhomogeneous term is approximated by

$$f(x) \cong \sum_{j=1}^{N+L} \beta_j \varphi(r_j), \tag{6}$$

where β_j are the unknown coefficients. N and L are respectively the numbers of knots on the domain and boundary. The use of interior points is usually necessary to guarantee the accuracy and convergence of the BKM solution. $r_j = \|x - x_j\|$ represents the Euclidean distance norm, and φ is the radial basis function.

By forcing approximation representation (5) to exactly satisfy governing equations at all nodes, we can uniquely determine

$$\beta = A_\varphi^{-1}\{f(x_i)\}, \tag{7}$$

where A_φ is nonsingular RBF interpolation matrix. Then we have

$$u_p = \sum_{j=1}^{N+L} \beta_j \phi(\|x - x_j\|), \tag{8}$$

where the RBF ϕ is related to the RBF φ through governing equations. In this study, we chose the first and second order general solutions as the RBFs ϕ and φ.

On the other hand, the homogeneous solution u_h has to satisfy both governing equation and boundary conditions. By means of nonsingular general solution, the unsymmetric and symmetric BKM expressions are given respectively by

$$u_h(x) = \sum_{k=1}^{L} \alpha_k u_0^{\#}(r_k), \qquad u_h(x) = \sum_{s=1}^{L_d} a_s u_0^{\#}(r_s) - \sum_{s=L_d+1}^{L_d+L_N} a_s \frac{\partial u_0^{\#}(r_s)}{\partial n}, \tag{9a,b}$$

where k is the index of source points on boundary, α_k are the desired coefficients; n is the unit outward normal as in boundary condition (2b), and L_d and L_N are respectively the numbers of knots on the Dirichlet and Neumann boundary surfaces. The minus sign associated with the second term is due to the fact that the Neumann condition of the first order derivative is not self-adjoint. Hereafter we only consider the symmetric BKM for the brevity. In terms of representation (9b), the collocation analogue equations (3a) (or (3b)) and (2a,b) are written as

$$\sum_{s=1}^{L_d} a_s u_0^{\#}(r_{is}) - \sum_{s=L_d+1}^{L_s+L_N} a_s \frac{\partial u_0^{\#}(r_{is})}{\partial n} = R(x_i) - u_p(x_i), \tag{10}$$

$$\sum_{s=1}^{L_d} a_s \frac{\partial u_0^{\#}(r_{js})}{\partial n} - \sum_{s=L_d+1}^{L_d+L_N} a_s \frac{\partial^2 u_0^{\#}(r_{js})}{\partial n^2} = N(x_j) - \frac{\partial u_p(x_j)}{\partial n}, \tag{11}$$

$$\sum_{s=1}^{L_d} a_s u_0^{\#}(r_{ls}) - \sum_{s=L_d+1}^{L_d+L_N} a_s \frac{\partial u_0^{\#}(r_{ls})}{\partial n} = u_l - u_p(x_l). \tag{12}$$

Note that i, s and j are reciprocal indices of Dirichlet (S_u) and Neumann boundary (S_Γ) nodes. l indicates response knots inside domain Ω. Then we can employ the obtained expansion coefficients α and inner knot solutions u_l to calculate the BKM solution at any other knots.

If the inhomogeneous solution u_p is simply ignored (i.e., let $u=u_h$) when δ is reasonably small, the above procedure for particular solution is omitted. We only need to solve analog equations

$$\sum_{s=1}^{L_d} a_s u_0^{\#}(r_{is}) - \sum_{s=L_d+1}^{L_s+L_N} a_s \frac{\partial u_0^{\#}(r_{is})}{\partial n} = R(x_i), \tag{13}$$

$$\sum_{s=1}^{L_d} a_s \frac{\partial u_0^{\#}(r_{js})}{\partial n} - \sum_{s=L_d+1}^{L_d+L_N} a_s \frac{\partial^2 u_0^{\#}(r_{js})}{\partial n^2} = N(x_j), \tag{14}$$

This strategy is called simplified BKM hereafter which can be understood that the use of nonsingular general solutions of Helmholtz-like operators with small characteristic parameter approximates the constant general solution of the Laplace and harmonic operators. I found that the simplified BKM is not stable for irregular geometry since the poor accuracy appears at very few nodes. However, it is noted that the strategy can produce very accurate solutions for regular geometry. For instance, the L_2 relative error norm at 495 nodes of an ellipse for the following 2D Laplace problem (15) by the simplified BKM using 9 nodes is 5.3e-3.

Numerical results and discussions: Figs. 1 and 2 show the tested 2D and 3D irregular geometries, where the 3D ellipsoid cavity locates at the center of the cube with the characteristic lengths 3/8, 1/8 and 1/8. Except Neumann boundary conditions on x=0 surface of 3D case, the otherwise boundary are all Dirichlet type. The tested 2D and 3D examples have accurate solutions

$$u = x^3 y - x y^3 + 10x + 10, \qquad u = x^3 yz - 2xy^3 z + xyz^3 + 10x + 10. \tag{15a,b}$$

The BKM L_2 norms of relative errors are displayed in Table 1. Note that the BKM only uses 9 boundary knots (δ=0.1) for 2D case and 66 ones (δ=0.2) for 3D case. The corresponding L_2 norms of relative errors are calculated at 492 sample nodes for 2D and 1000 sample nodes for 3D. The absolute error is taken as the relative error if the absolute value of the solution is less than 0.001. One can find that the present BKM methodology is very simple, accurate and efficient compared with other methods, especially for complicated geometry domain.

Although we do not use inner knots in the present test, a few inner nodes are usually necessary in practical use to significantly improve the solution accuracy and stability (i.e., insensitive to artificial parameter δ).

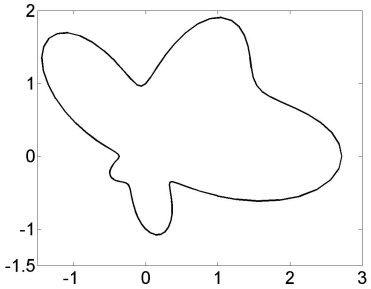

Fig. 1. A 2D irregular geometry

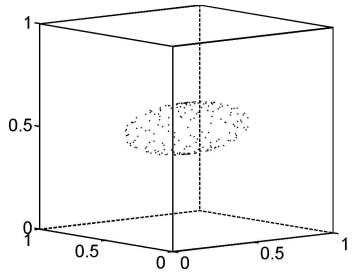

Fig. 2. A cube with an ellipsoid cavity

Table 1. L_2 norm of relative errors for 2D and 3D Laplace problems with the general solution of Helmholtz (H) and modified Helmholtz (MH) operators.

BKM (H)	BKM (MH)	BKM (H)	BKM (MH)
1.1e-3 (2D)	1.5e-3 (2D)	5.2e-3 (3D)	1.3e-3 (3D)

Biharmonic problems and high order general solutions of Berger and Winkler equations: We can use the general solutions of vibration plate, Winkler plate and Burger equation of finite deflection of plate to approximate the constant general solution of the biharmonic operator. We list these general solutions in Table 2, where ber and bei respectively represent the Kelvin and modified Kelvin functions of the first kind. Among them, it is believed that those of Winkler plate and Burger plate are first presented here.

Table 2. M-order general solutions of vibration plate, Winkler equation and Burger equation, where n=2,3 denotes dimensionality.

	Operators	General solutions (m=0,1,2…)
Vibration plate	$L\{u\} = \nabla^4 u - \lambda^2 u$	$u_m^{\#}(r) = \left(r\sqrt{\lambda}\right)^{-n/2+1+m}\left(A_m J_{n/2-1+m}\left(\sqrt{\lambda} r\right) + B_m I_{n/2-1+m}\left(\sqrt{\lambda} r\right)\right)$
Winkler plate	$L\{u\} = \nabla^4 u + \kappa^2 u$	$u_m^{\#}(r) = \left(r\sqrt{\kappa}\right)^{-n/2+1+m}\left(C_m ber_{n/2}(r\sqrt{\kappa}) + D_m bei_{n/2}(r\sqrt{\kappa})\right)$, m odd $u_m^{\#}(r) = \left(r\sqrt{\kappa}\right)^{-n/2+1+m}\left(C_m ber_{n/2-1}(r\sqrt{\kappa}) + D_m bei_{n/2-1}(r\sqrt{\kappa})\right)$, m even
Burger plate	$L\{u\} = \nabla^4 u - \mu^2 \nabla^2 u$	$u_m^{\#}(r) = E_m r^{2m-2} + F_m (\mu r)^{-n/2+1+m} I_{n/2-1+m}(\mu r)$

A_m to F_m are constant coefficients which will analyzed in a subsequent paper. It is worth pointing out that the formulas given in Table 2 for the zero order general solution of Winkler operator is effective for up to five dimensions. The same relations hold with ber, bei replaced by the Kelvin functions of the second kind ker, kei, respectively, for fundamental solutions. The higher order fundamental solution of Burger equation is alternations of the first and second terms of corresponding general solution by the higher order fundamental solutions of Laplace and Helmholtz operators.

The fundamental solutions of Winkler plate and Burger plate are given respectively by [5,6]. For vibration plate, the small vibration frequency means the approximation to linear steady deflection described by a biharmonic equation. For a Winkler plate on an elastic foundation, the small elastic foundation coefficient indicates that the general solution is close to that of a plate no resting on an elastic foundation. Ref. 5 has actually applied a BEM strategy based on the fundamental solution of the Winkler plate to analyze the biharmonic system equation, where the inhomogeneous (particular) solution is simply omitted, similar to idea in the aforementioned simplified BKM. The solution accuracy is quite high for a regular rectangular plate.

The Burger plate equation is a simplified model of von Karman equations for nonlinear deflection of plate under large loading, which assumes the plate has not in-plane movement at the boundary. By taking small Burger parameter, the nonsingular general solution of Burger plate approaches that of the biharmonic equation for the linear thin plate.

Now it is obvious that the present approximate strategy is explicitly grounded on the physical connections between different partial differential equations. The numerical validations of the biharmonic equations will be presented in a subsequent paper.

Remarks: It should be pointed out that we could greatly simplify the above-given standard form of general solutions involving some special functions. Thus, the computing effort for them is trivial. For Helmholtz-like problems, the BKM outperforms the DR-BEM and MFS significantly in terms of accuracy, symmetricity, efficiency, stability, and mathematical simplicity. The present study shows that the method is also very efficient for Laplace and biharmonic problems by a fairly good approximation via general solutions of Helmholtz-like operators with small system parameter to that of the corresponding non-Helmholtz-like operators. A mathematical analysis of this scheme will be given later. The major drawbacks of the BKM are severe ill-condition and costly full matrix for large system problems, which is a subject presently under investigation.

REFERENCES

1. W. Chen and M. Tanaka, New Insights into Boundary-only and Domain-type RBF Methods. *Int. J. Nonlinear Sci. & Numer. Simulation*, **1**(3), 145-151, (2000).
2. M.A Golberg and C.S. Chen, The method of fundamental solutions for potential, Helmholtz and diffusion problems. In *Boundary Integral Methods - Numerical and Mathematical Aspects*, (Ed. by M.A. Golberg), pp. 103-176, Comput. Mech. Publ., 1998.
3. P.W. Partridge, C.A. Brebbia and L.W. Wrobel, *The Dual Reciprocity Boundary Element Method*, Comput. Mech. Publ., 1992.
4. M. Itagaki, Higher order three-dimensional fundamental solutions to the Helmholtz and the modified Helmholtz equations, *Engineering Analysis with Boundary elements*, **15**, 289-293, (1995).
5. J.T. Katsikadelis and A.E. Armenakas, Plates on elastic foundation by BIE method, *J. Engng. Mech*., **110**(7), 1086-1105, 1984.
6. J. Sladek and V. Sladek, The BIE analysis of the Berger equation, *Ingenieur-Archiv*, **53**, 385-397, 1983.

Stress Recovery Based on Minimization of Complementary Energy

Zdzisław Więckowski
Department of Mechanics of Materials
Technical University of Łódź, Łódź, Poland
e–mail: zwi@ck-sg.p.lodz.pl

ABSTRACT

Summary A technique of stress recovery for a finite element solution is investigated. A smoothed, statically admissible stress field is computed by solving the local problem of minimization of complementary energy on patches of elements. The energy error of the approximate solution is estimated by the use of the recovered stress field. The method is illustrated by the example of the Poisson equation; numerical results are related to the problem of torsion of a prismatic bar.

The superconvergent patch recovery (SPR) method is a very popular technique of finding a stress field which is smoother and more accurate than the stress field related directly to the displacement field obtained by the finite element analysis. In SPR method, the improved stress field is usually considered in the form of polynomial (the degree of which is higher than the polynomial representing stresses in the original FE solution) which fits stress values at superconvergent points of elements belonging to a patch surrounding a node of the element mesh. Coefficients of the polynomial are found by the use of the least square method [1]. SPR approach can be enriched by a requirement that the recovered stress field should satisfy the equilibrium equations in an approximate (e.g. [2]) or exact (e.g. [3]) way. There are other recovery approaches where the equilibrium equations are satisfied on the element patch by recovered stresses. The equilibrium equations can be satisfied exactly by constructing the self-equilibrated element boundary tractions equivalent to those obtained from the kinematically admissible finite element solution and then finding the statically admissible stress field, related to the tractions, inside the element domain [4]. The equilibrium equations can also be satisfied in the weak sense like in the displacement-based finite element analysis—this procedure is known as the recovery by equilibration of patches (REP) [5].

In all the approaches mentioned above, the stress field obtained by the finite element analysis is used as input data in the recovery procedure. In contrast to these methods, the technique described in the present paper does not utilize stresses as input data but displacements which are of higher accuracy than stresses. The recovered stress field is found by minimizing the functional of complementary energy on the set of statically admissible stress fields where the displacements on the patch boundary are taken from the kinematically admissible finite element solution.

Let us consider two-dimensional physical problems described by Poisson's equation, $-\lambda\, u_{,\alpha\alpha} = f$, $\alpha = 1, 2$, where stresses (fluxes) satisfy the equilibrium (balance) equation of the form: $q_{\alpha,\alpha} = f$ with $q_\alpha = -\lambda\, u_{,\alpha}$. Let Ω_p denote the region occupied by an element patch where the stresses are to be recovered. For any patch Ω_p the following local minimization problem is solved: To find $\boldsymbol{q}_p^s \in Y$ such that $\boldsymbol{q}_p^s$ minimizes the functional of complementary energy

$$\Sigma(\boldsymbol{q}) = \frac{1}{2} \int\limits_{\Omega_p} \lambda^{-1}\, q_\alpha\, q_\alpha \,\mathrm{d}x - \oint\limits_{\partial\Omega_p} u_h\, q_\alpha\, n_\alpha \,\mathrm{d}s$$

on the following set of statically admissible stress (flux) fields:

$$Y = \left\{ q_\alpha \in L^2(\Omega_p): \quad q_{\alpha,\alpha} \in L^2(\Omega_p), \quad q_{\alpha,\alpha} = f \text{ on } \Omega_p \right\},$$

where u_h denotes the approximation of the displacement (potential) field and n_α is the unit vector outwardly normal to the patch boundary. The statically admissible fields of stresses are constructed by the use of the Prandtl stress function, ψ:

$$q_1 = \psi_{,2} + \bar{q}_1, \quad q_2 = -\psi_{,1} + \bar{q}_2 \tag{1}$$

where $\bar{q}_\alpha$ is a particular solution of equation $q_{\alpha,\alpha} = f$. In the case of triangular or quadrilateral elements with linear or bilinear interpolation functions, respectively, function ψ is approximated by the following polynomial:

$$\psi = \left[\begin{array}{ccccc} x & y & x^2 & x\,y & y^2 \end{array} \right] \left[\begin{array}{c} a_1 \\ \vdots \\ a_5 \end{array} \right]. \tag{2}$$

The above representation of function ψ means that both the components of vector $\boldsymbol{q}$ are linear functions of coordinates $x = x_1$ and $y = x_2$ while the finite element approximations gives these components as piecewise constant functions. After substituting equations (1) and (2) to the expression for functional Σ and calculating its first variation, we obtain the linear system of algebraic equations with the symmetric matrix. After calculation of the vector of coefficients $a_1, a_2, \ldots, a_5$, the components of stresses $q^s_{p\,\alpha}$ at the "central" node of the patch can be calculated and used as the nodal values so that the final recovered field of stresses, $\boldsymbol{q}^*$, can be written in the form

$$q_1^*(x,y) = \mathbf{N}\,\mathbf{q}_x, \quad q_2^*(x,y) = \mathbf{N}\,\mathbf{q}_y$$

where $\mathbf{N}$ are the same interpolation functions as used in the approximation of the displacement field, $\mathbf{q}_x$ and $\mathbf{q}_y$ denote vectors of nodal values of recovered stress components.

When the improved field of stresses is known, the error of the approximate solution can be estimated. The estimated error measured by means of energy norm can be expressed as follows:

$$\|\bar{\boldsymbol{e}}\| = \left(\int_\Omega \lambda^{-1} (\boldsymbol{q}^* - \boldsymbol{q}_h)^{\mathrm{T}} (\boldsymbol{q}^* - \boldsymbol{q}_h)\, \mathrm{d}x \right)^{\frac{1}{2}}.$$

As an example, the problem of torsion of the prismatic bar with triangular cross-section having equal sides is considered. All the above derivations are valid if we put $q_1 = \sigma_{31}$, $q_2 = \sigma_{32}$, $\lambda = 2\,G$ where G denotes the shear modulus, and u_h, which appears in expression for complementary energy, is the warp of the cross-section of the bar. Calculation have been made assuming that $G = 1$, the length of the cross-section edge is equal to 1, and the torsion angle for the unit length of the bar is equal to 1. Four uniform meshes generated automatically with element diameters $h = 0.25$, 0.1, 0.04 and 0.016 are utilized in the computations.

The relative error of the approximate solution, $\|\bar{\boldsymbol{e}}\|/\|\boldsymbol{q}\|$, has been estimated and compared with its exact value (the exact solution is known for the considered problem) for all the element meshes used in the calculations. The comparison is shown in Fig. 1. In the same figure, the diagram for

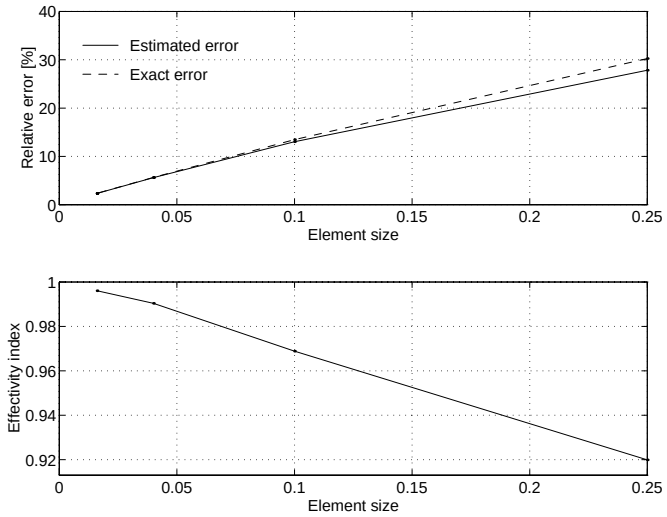

Figure 1: Energy error and effectivity index

the effectivity index, $\Theta \equiv \|\bar{\boldsymbol{e}}\|/\|\boldsymbol{e}\|$, which measures the accuracy of the error estimator, is also shown. In the last definition, $\|\boldsymbol{e}\|$ denotes the exact value of the error. The recovered stress field obtained in the case of rather coarse mesh for $h = 0.1$ is shown in Fig. 2 and compared with the exact solution.

As can be seen from the presented results, the recovery procedure described in the paper gives the smoothed stress field very close to the exact one and is characterized by the effectivity index for the error estimator which slightly differs from unity (0.920 .. 0.996 depending on mesh parameter h).

REFERENCES

[1] O.C. Zienkiewicz and J.Z. Zhu. The superconvergent patch recovery and *a posteriori* error estimates. Part 1: The recovery technique. *Int. J. Num. Meth. Eng.*, **33**, 1331–1364, (1992).

[2] N.-E. Wiberg, F. Abdulwahab and S. Ziukas. Enhanced superconvergent patch recovery incorporating equilibrium and boundary conditions. *Int. J. Num. Meth. Eng.*, **37**, 3417–3440, (1994).

[3] T. Kvamsdal, K.M. Okstad and K.M. Mathisen. Error estimation based on statically admissible stress fields. In J.-A. Désidéri et al., editors, *Numerical Methods in Engineering '96*, pages 14–20, Chichester. John Wiley & Sons, (1996).

[4] P. Ladeveze, G. Coffignal and J.P. Pelle. Accuracy of elastoplastic and dynamic analysis. In I. Babuška at al., editors, *Accuracy Estimates and Adaptive Refinements in Finite Element Computations*, pages 181–203, Chichester. John Wiley & Sons, (1986).

[5] B. Boroomand and O.C. Zienkiewicz. Recovery by equilibrium patches (REP). *Int. J. Num. Meth. Eng.*, **40**, 137–154, (1997).

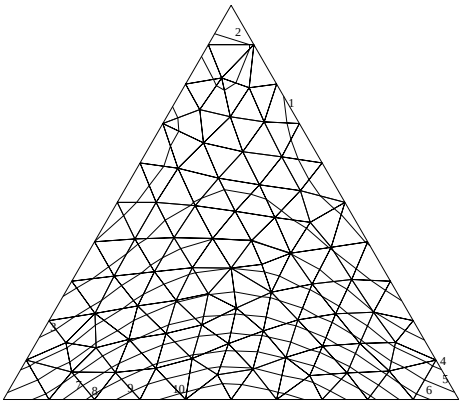

1: -1.80E-01 2: -1.20E-01 3: -6.00E-02 4: 0.00E+00 5: 6.00E-02
6: 1.20E-01 7: 1.80E-01 8: 2.40E-01 9: 3.00E-01 10: 3.60E-01

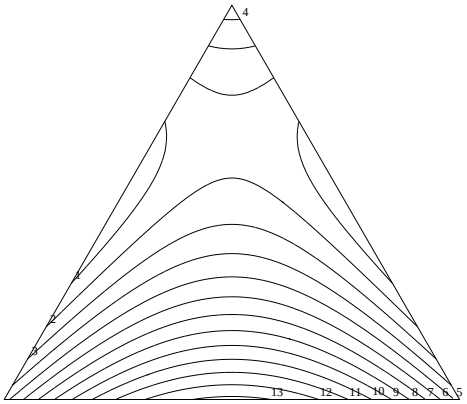

1: -1.80E-01 2: -1.30E-01 3: -8.00E-02 4: -3.00E-02 5: 2.00E-02
6: 7.00E-02 7: 1.20E-01 8: 1.70E-01 9: 2.20E-01 10: 2.70E-01

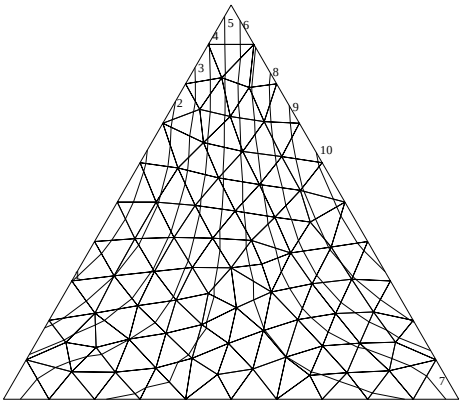

1: -3.10E-01 2: -2.40E-01 3: -1.70E-01 4: -1.00E-01 5: -3.00E-02
6: 4.00E-02 7: 1.10E-01 8: 1.80E-01 9: 2.50E-01 10: 3.20E-01

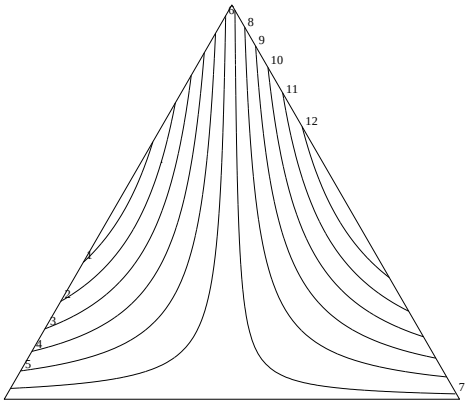

1: -3.40E-01 2: -2.80E-01 3: -2.20E-01 4: -1.60E-01 5: -1.00E-01
6: -4.00E-02 7: 2.00E-02 8: 8.00E-02 9: 1.40E-01 10: 2.00E-01

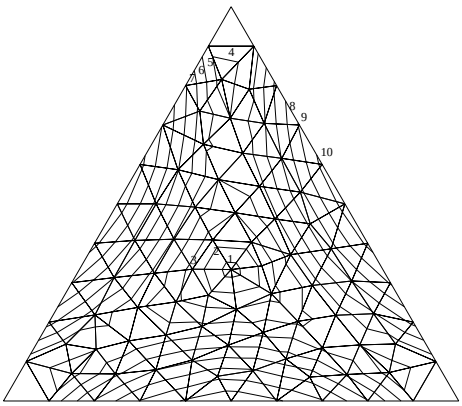

1: 2.00E-02 2: 6.00E-02 3: 1.00E-01 4: 1.40E-01 5: 1.80E-01
6: 2.20E-01 7: 2.60E-01 8: 3.00E-01 9: 3.40E-01 10: 3.80E-01

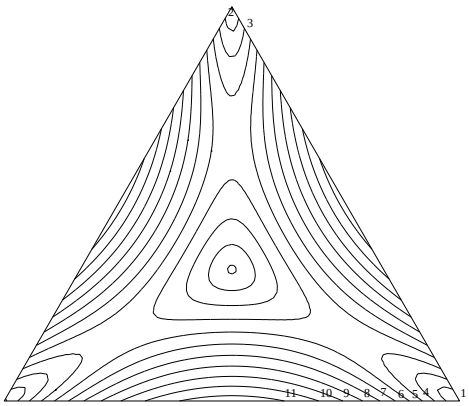

1: 1.00E-02 2: 5.00E-02 3: 9.00E-02 4: 1.30E-01 5: 1.70E-01
6: 2.10E-01 7: 2.50E-01 8: 2.90E-01 9: 3.30E-01 10: 3.70E-01

Figure 2: Recovered (left) and exact (right) stresses: σ_{31}, σ_{32} and $\sigma \equiv \sqrt{(\sigma_{31})^2 + (\sigma_{32})^2}$ (from top to bottom).

On *p*-hierarchical Solid Elements for Large Displacement Analysis of Thin Shells

Mats Ander* and Alf Samuelsson

Department of Structural Mechanics
Chalmers University of Technology, Göteborg, Sweden
e–mail: matsan@sm.chalmers.se

ABSTRACT

Summary A computer code for geometrically nonlinear analysis of thin structures using a *p*-hierarchical solid element approach has been developed using the MATLAB software. The *p*-hierarchical element formulation using integrals of Legendre polynomials as basis functions together with a Gauss-Lobatto quadrature has been implemented efficiently by aid of the MATLAB built in features for polynomials and multidimensional arrays. Numerical results for slender beams and thin shells will be presented

1.1 Introduction

A family of *p*-hierarchical solid elements has been implemented for geometrically nonlinear analysis. By use of integrals of Legendre polynomials as element basis functions [1] the conditioning properties of the element tangent stiffness matrix allows for analysis of thin shells. The key feature of the method is that only translational variables are employed on element and global structural level and that the finite deformations are expressed in terms of the displacement gradients on continuum level in a total Lagrange formulation [2]. The so called core equations where the displacement gradients act as 'material point' degrees of freedom are exact including geometrical nonlinearities. With this formulation a tangent stiffness matrix is deduced already at the core level. The core equations are independent of the element geometry and the choice of element basis functions. The core equations are transformed into finite element equations by use of a transformation matrix and by integration over the element volume in the reference configuration. In this transformation phase the displacement field approximation and the mapping of the element geometry enters. The transformation matrix consists of derivatives of the element basis functions. It follows that the transformation matrix for each integration point in the element is computed only once. Only a few elements are employed in the interior of the region. At the boundaries an exponential *h*-refinement is used.

1.2 *p*-hierarchical elements

In the present work the use of a *p*-hierarchical Legendre type solid element for thin shells is investigated. In the through thickness a low order polynomial approximation of the displacement field is tested. The solid element displacement field $\boldsymbol{u} = [u,v,w]^T$ is approximated

by $\boldsymbol{u} \approx \sum_i N_i^b v_i^b + \sum_j N_j^h v_j^h$ where N_i^b and N_j^h denotes the basic and hierarchical base functions respectively. The nodal degree of freedom number *i* is denoted by v_i^b while v_j^h is the j:th hierarchical degree of freedom. Note that the hierarchical base functions all have zero values at the basic nodes and that the hierarchical degrees of freedom do not associate to physical nodal points, but should simply be interpreted as unknown amplitudes of the hierarchical functions.
In the *p*-hierarchical formulation for the 3D solid element the basis functions can be distinguished into 27 groups. The first 8 includes the 8 standard tri-linear basis functions for the 8 vertices. The following 12 groups contain edge functions for the 12 edges, the next 6 groups base functions for the 6 faces and, finally, there is one group containing the internal volume basis functions. The number of base functions in the last 19 groups depends on the choice of polynomial degrees and hierarchical space. For the coded 3D solid element the polynomial degree is fixed to *q*=2 in the through thickness direction while it is varied from *p*=2 to *p*=9 in the other directions. This means that the implemented elements are restricted to model thin structures where a linear strain can be assumed through the thickness.

1.2.1 *p*-hierarchical shape functions for hexahedral elements

We define the cube $\{-1 \le x, h, V \le 1\}$, Figure 1, as being the standard element domain W_{st}.

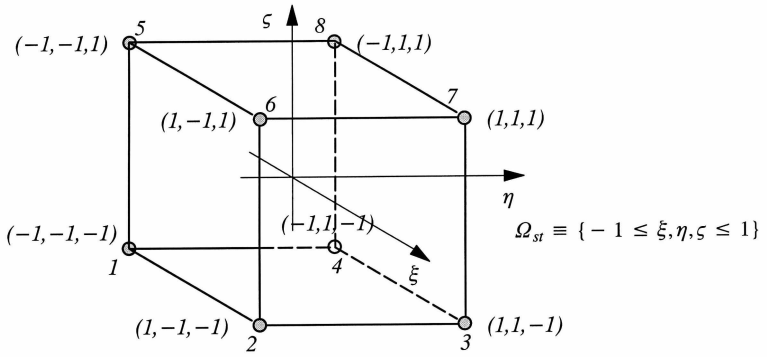

Figure 1. Standard hexahedral element W_{st}

The shape functions N_m are obtained as products of f-functions, Figure 2, as

$$N_m = f_i(x) f_j(h) f_k(z) \qquad (1)$$

The first two f-functions are the simple linear functions.

$$f_0(x) = \frac{1}{2}(1-x) \;\; ; \qquad f_1(x) = \frac{1}{2}(1+x) \qquad (2)$$

Higher order f-functions are defined as integrals of the Legendre polynomials

$$f_i(x) = \sqrt{\frac{2i-1}{2}} \int_{-1}^{x} P_{i-1}(t)dt \quad ; \text{i} = 2,3,\ldots, p \qquad (3)$$

Here P_{i-1} are the Legendre polynomials which can be generated from Rodrigues' formula:

$$P_n(x) = \frac{1}{n! \cdot 2^n} \frac{d^n}{dx^n} \left\{ (x^2 - 1)^n \right\} \qquad (4)$$

It follows that the f-functions (except the linear ones) vanish at the boundaries $x \pm 1$ and that the derivatives of the f-functions are orthogonal on the interval [-1,1].

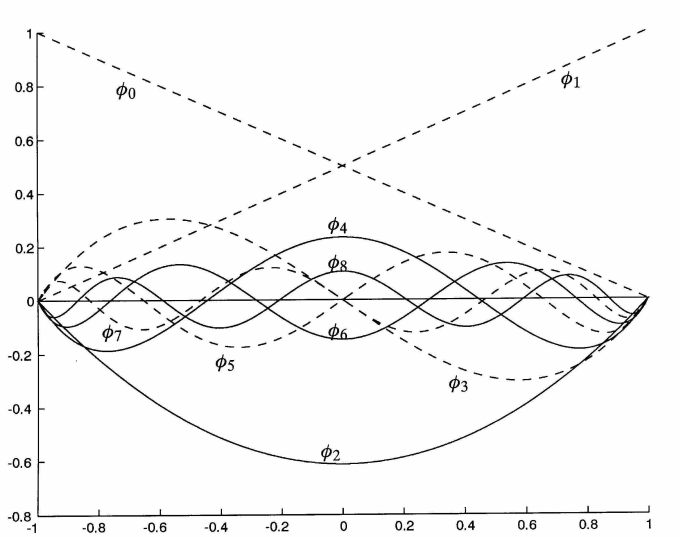

Figure 2. f-functions on the interval $-1 \le x \le 1$.

The base functions and their derivatives are deduced numerically using the MATLAB features for polynomials.

1.3 Numerical integration and continuation method

A Gauss-Lobatto quadrature procedure is adopted for the numerical integration [1] and a dominant displacement component driven continuation method is used for tracing the nonlinear structural response [3]. Secondary branches on the equilibrium path can be triggered by introducing imperfections in the structural geometry or in the load.

1.4 Numerical examples

A geometrically nonlinear analysis of a transversally loaded cantilever beam modelled with *p*-hierarchical Legendre type solid elements shows excellent agreement with an analytical non-linear beam solution. The developed code has been verified to work well for thin shells and beams in linear analysis. Numerical tests on the so called Scordelis and Lo cylindrical shell roof show that the present formulation gives accurate results in good agreement with analytical deep shell theory as well as with numerical results reported by other authors, see fig. and table below.

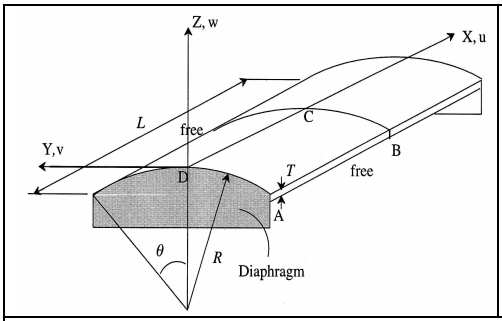

L = 6.0 m

T =0.03 m

R = 3.0m

q = 40°

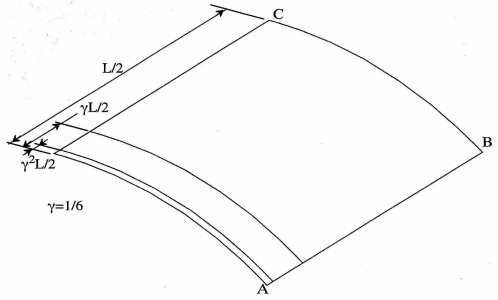

Scordelis and Lo cylindrical shell roof loaded by a uniformly distributed vertical load $f_Z = 0.625\times10^4$ Pa.

Graded 3-element mesh of one quarter of the shell.

Reference values for the vertical displacements $w_B = -0.0361m$, $w_C = 0.00541m$ from [4]

Polynomial degree p	NDOF	Displacement w_B	Displacement w_C	Potential energy p	Conditioning number of K
1-element with q = 2 and p = 5, 7, 9					
5	138	-0.035286	0.004714	-138.894	8.696367×10^7
7	249	-0.036136	0.005429	-144.468	9.817559×10^7
9	396	-0.036149	0.005438	-144.548	1.037179×10^8
3 -element graded mesh with q = 2 and p = 5, 7, 9					
5	414	-0.036049	0.005163	-142.311	1.100866×10^8
7	747	-0.036135	0.005437	-144.504	1.213742×10^8
9	1188	-0.036149	0.005440	-144.550	1.254000×10^8

REFERENCES

[1] B.A. Szabo and I. Babuska. *Finite Element Analysis.* Wiley, New York, (1991).

[2] M.K.A. Ander and A.G. Samuelsson. Finite element analysis of geometrically non-linear structures using translational variables. *Int. J. Num. Meth. Eng.*, **46**, 1367−1383, (1999).

[3] M. Ander. On postbuckling analysis of thin-walled structures, numerical and statistical approaches. Publication 99:16, Department of Structural Mechanics, Chalmers University of Technology, S-412 96 Göteborg, Sweden, (1999).

[4] J.-L. Batoz and G. Dhatt. *Modélisation des structures par éléments finis*. volume 3, Coques, Hermes, (1992).

Computational Mechanics and Artificial Neural Networks in Damage Detection in Rods

Grzegorz Piątkowski and Leonard Ziemiański
Department of Structural Mechanics
Rzeszów University of Technology, Rzeszow, Poland
e–mail: pgrzes@prz.rzeszow.pl, ziele@prz.rzeszow.pl

ABSTRACT

Summary This paper presents an application of Computational Mechanics and Artificial Neural Networks (ANN) [1] for non-destructive damage detection in rods. The identification method has been based on the analysis of propagation of wave in solids [2]. Special attention has been paid to preprocessing of time signals.

1 Introduction

Non-destructive methods of detection of change of material properties and damage in structural elements present an important and valuable tool. These methods allow estimating the state of a structure as well as predicting a period of safety usage. An ultrasonic method is one of the most often used non-destructive methods [3]. For structures such as rods, plates, shells another widely used method is the one based on structural waves propagation. In this method unlike in the classical method of ultrasonic testing, the wavelengths are large compared to the characteristic dimension of the structure and a wave pulse propagates along the whole structure. Moreover, the excitation of structural waves is at one point while the measurements of structural waves velocity are in a few other points instead of surface scanning used in ultrasonic testing. It simplifies the structural waves tests in rods, beams, plates and some other structures (Figure 1a).

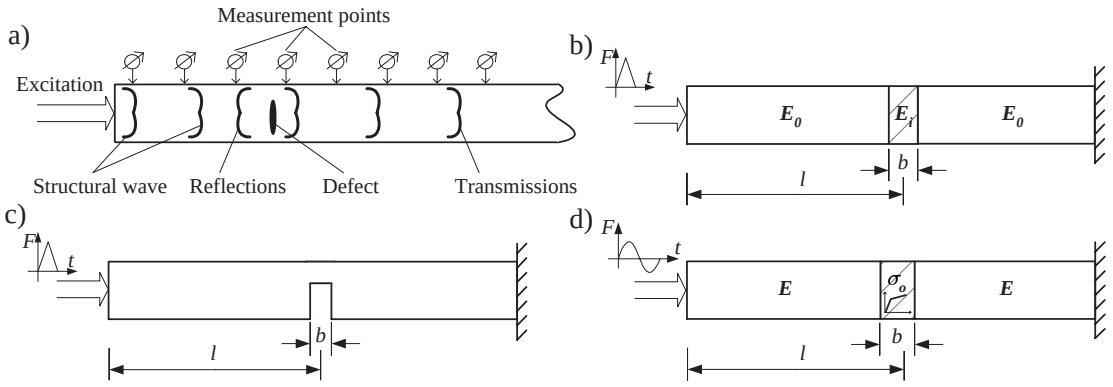

Figure 1: Structural waves propagation test

2 Neural networks in problems of damage detection

The Backpropagation ANNs with the Rprop learning algorithm have been applied. Neural networks with one or two hidden layers have been tested. The input vectors consisted of

preprocessed time signal. The outputs provided provided all parameters describing damage. Some of these parameters were identified by the network with satisfactory precision while other with a significant error.

Based on the previous research done by the authors [4, 5] cascade neural networks have been built to improve the generalisation of networks. The first network has been fed with input vector as for simple net. The first network's output is the most precisely determined parameter. The second network has got an input vector with additional value of parameter predicted by first net. The output of this network is the next desirable parameter. The cascade networks with two or three stages have been used (Figure 2).

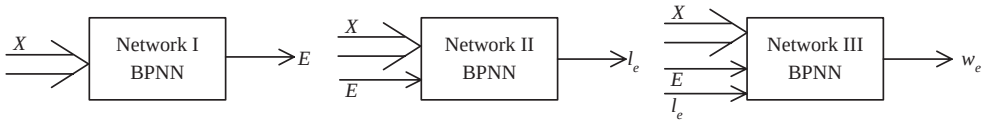

Figure 2: The three stage cascade network

3 Preprocessing of signals

One of the used methods of preprocessing input data was a compression of time signal [4, 5]. The compression has been performed by dedicated neural network called replicator shown in (Figure 3). Networks of architecture n-h-n have been learned to replicate at the output the time signal data points given at the input - the input variables have been mapped into the same output variables. The compression networks of 200-8-200 and 200-12-200 architectures have been created. After training the outputs from hidden neurons (see Figure 3) have been used as preprocessed data for damage identification net.

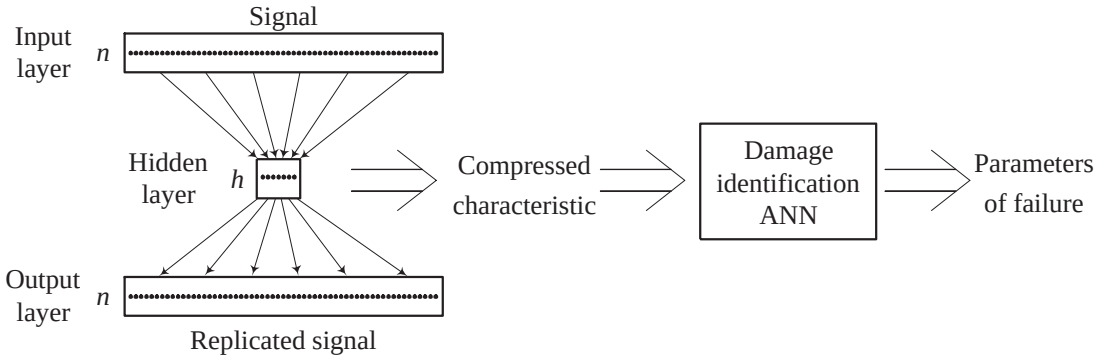

Figure 3: The use of replicator in damage identification problem

4 Damage detection in rod elements

4.1 Identification of stiffness changes

Numerical model of a rod with a constant cross-section has been considered. An elastic-plastic with isotropic hardening material model has been used [6]. Concentrated force with triangle characteristic and duration of 200μs have been applied to the free end of the rod (Figure 1b).

A failure, i.e. stiffness change of selected fragment of rod has been simulated by the change of Young's modulus (ΔE) for one or several consecutive finite elements (b). The location (l) of defect also has been changed. For these parameters dynamic responses of the numerical model have been calculated, and the velocities of wave propagation have been recorded in selected nodes. Differences between time signal of rod with defect (local change of stiffness) and model time signal (homogeneous rod) have been determined and described through two quantities: the shift of amplitude of a maximum of signal and the shift of time of appearance of a maximum for given signal. Such described vector was an input vector for neural network. At this stage separate neural networks have been built for different widths of simulated defect so an output vector consists of: Young's modulus value and location of element with changed Young's modulus. It was noticed that along with increase of defect width a network generalisation improved [4].

4.2 Identification of cross-section changes

The next analysed task was a rod with defect simulated as a notch. Removing of certain finite elements has simulated the failure of cross-section. Various width (b), various height (h) and various location (l) of notch have been considered (Figure 1c).

Table 1: Comparison of errors of cross-section parameters identification

St. par.	Height of defect		Location of defect		Width of defect	
	Learn	Test	Learn	Test	Learn	Test
	Standard net					
R^2	0.996	0.994	0.994	0.994	0.99	0.988
δ	0.0149	0.0177	0.0193	0.0192	0.0215	0.0232
	Cascade net					
R^2	1.000	0.999	0.999	0.997	0.994	0.986
δ	0.0043	0.0071	0.0094	0.0121	0.0165	0.0253

The input vector has been described with values of first three peaks of time signal [4] and by use of replicator. Both simple and cascade nets have been used at this stage. Better results have been obtained from neural networks with two hidden layers. The width of defect has no influence on the quality of results. Damage identification is significantly better in case of the use of cascade networks. In Table 1 the results of neural simulation are put together.

4.3 Identification of yielding zone

A group of finite elements with elasto-plastic material occurred inside the rod. The plastic-bilinear material model has been used. The Young's modulus and strain hardening modulus were constant. A failure has been simulated by the change of initial yield stress (σ_0). Width (b) and location (l) of defect have been changed (Figure 1d). A concentrated force with sine characteristic and duration of 400μs have been applied to the free end of the rod. The measured points have been located after the zone of yielding. For the identification networks the input vectors consisted of compressed time signals. A compression networks with 8 neurons in a hidden layer has been used.

The output vectors consisted of three parameters of failure (σ_0, b, l). When simple nets have been used, the yield strength parameter and the location of yield zone have been identified correctly. The width of defect has been identified significantly worse. The use of cascade networks improved the identification of width of defect (see Table 2).

Table 2: Learning errors of yielding zone parameters identification

St. par.	σ_0	Location	Width
	Standard net		
R^2	0.922	0.995	0.769
δ	0.0222	0.0117	0.097
	Cascade net		
R^2	1.000	1.000	0.886
δ	0.0039	0.0012	0.0679

5 Final remarks

On the basis of achieved results the following conclusions can be expressed: ANNs make it possible to use structural wave propagation analysis for detection and assessment of damage in structural elements, the ANNs developed in this paper has proved to be an effective tool to obtain parameters of failures of considered numerical models of rods, application of cascade networks can improve accuracy of neural approximation in both analysed cases, the presented methods of time signals preprocessing proved to be very useful in preparing of input vectors for neural networks.

REFERENCES

[1] Z. Waszczyszyn and L. Ziemiański Neural networks in mechanics of structures and materials - new result. *Computers and Structures*, v.79/22-25, 2261–2276, (2001).

[2] G. Yagawa and H. Okuda. Neural networks in computational mechanics. *Archives of Computational Methods in Engineering*, (3-4), 435–512, (1996).

[3] R.B. Thompson Quantitative ultrasonic nondestructive evaluation methods. Trans. ASME, *Journal of Applied Mechanics*, 1191–1201, (1983).

[4] L. Ziemiański and G. Piątkowski. Use of neural networks for damage detection in structural elements using wave propagation. In: B.H.V. Topping, editor, *Computational Engineering Using Metaphors from Nature*, 25–30, Edinburgh, Civil-Comp Ltd, (2000).

[5] B. Miller and L. Ziemiański. Neural networks in updating of a 12-storey frame model. In: B.H.V. Topping, editor, *Computational Engineering Using Metaphors from Nature*, 31–36, Edinburgh, Civil-Comp Ltd, (2000).

[6] *Theory and modeling guide*, Watertown, ADINA R&D Inc., (2000).

Form-Finding of Tensegrity Structures—A Review

A. Gunnar Tibert*
Department of Mechanics
Royal Institute of Technology, 100 44 Stockholm, Sweden
e-mail: gunnar.tibert@mech.kth.se

Sergio Pellegrino
Department of Engineering
University of Cambridge, Trumpington Street, Cambridge CB2 1PZ, U.K.
e-mail: pellegrino@eng.cam.ac.uk

ABSTRACT

Summary Seven form-finding methods for tensegrity structures are reviewed and classified as kinematical or statical. Kinematical methods are best suited to obtaining only configuration details of structures that are already essentially known. The force density method, one of the statical methods, is best suited when searching for new configurations, but offers no control over the element lengths.

Introduction

A tensegrity structure is any structure realised from cables and struts to which a state of prestress is imposed that imparts tension to all cables. In addition, the state of prestress stabilises the structure, i.e., provides first-order stiffness to all infinitesimal mechanisms. A key step in the design of tensegrity structures is the determination of their geometrical configuration, known as *form-finding*. Form-finding methods for tensegrity structures have been investigated by many authors, e.g., [1], but the various methods have not been previously classified or linked. Further information and more references can be found in [2].

Kinematical Methods

The characteristic of these methods is that the lengths of the cables are kept constant while the lengths of the struts are increased until a *maximum* is reached. Alternatively, the strut lengths are kept constant while the cable lengths are decreased until they reach a *minimum*.

- **Analytical Solutions**
  Analytical solutions can be obtained only for very simple structures, e.g., tensegrity prisms where the equilibrium configuration is determined by the relative rotation between the upper and lower regular polygon.
- **Non-Linear Programming**
  The form-finding of any tensegrity structure is turned into a constrained minimisation problem. Starting from a system for which the element connectivity and nodal coordinates are known, one or more struts are elongated, maintaining fixed length ratios, until a configuration is reached in which their length is maximised [3].

- **Dynamic Relaxation**
  A static problem is turned into a fictitious dynamic problem. Convergence is controlled by an appropriate choice of damping coefficients or, alternatively, by a technique called kinetic damping. The motion of the structure is initiated by an increase of the length of the struts, while the cable lengths are held constant [4].

Statical Methods

These methods are characterised by a relationship between equilibrium configurations of a structure with given topology and the forces in its members.

- **Analytical Solutions**
  A general solution of the relative rotation between the upper and lower polygon of tensegrity prisms was derived in [5]. Nishimura [6] used the force method and group representation theory to find analytical solutions to a number of spherical tensegrities and multi-stage tensegrity towers.

- **Force Density Method**
  The linear force density method, successfully used for form-finding of cable nets and membrane structures, was extended to tensegrity structures by Vassart [7]. To find a stable volume in three-dimensional space the force density matrix $\mathbf{D}$ of a structure, with given topology, must have a nullity $\mathcal{N} = 4$. Finding a set of member force densities which fulfil this condition is preferably done by symbolic software.

- **Energy Method**
  A mathematical energy potential for a tensegrity structure is set up, using force density and element length instead of elastic stiffness and element elongation [8]. This potential has a local minimum for a structure in d-dimensional space if a square matrix $\mathbf{\Omega}$ is positive definite with a nullity of $d + 1$. It was observed in [2] that $\mathbf{D} = \mathbf{\Omega}$. Using this method and group representation theory, Connelly and Back [9] compiled a complete catalogue of tensegrities with certain prescribed types of stability and symmetry.

- **Reduced Coordinates**
  A set of equilibrium equations relating the forces in the cables, but without showing explicitly the forces in the struts, can be obtained from virtual work. Sultan [10] used this method, which involves extensive symbolic computations, to find equilibrium configurations of a class of tensegrity towers.

Example: Truncated Tetrahedron

A simple, but important, form-finding example is that of the tensegrity version of a regular truncated tetrahedron, Figure 1. This structure was first constructed by della Sala in 1952 [11], and later studied by Calladine [12] when he formulated the extended Maxwell's rule. By measuring a physical model Calladine found that the ratio between the strut and cable lengths was 2.25. Pellegrino [3] used the kinematical method of non-linear programming to find the length ratio 2.2507,

and the force densities in the struts, truncating triangle cables, and cables connecting the triangles to be $q_s = -0.6672$, $q_t = 1$, and $q_l = 1.3795$, respectively. Using the force density method, assuming two types of cables and one type of struts, the condition for $\mathcal{N} = 4$ is

$$2\left(1+\frac{q_l}{q_t}\right)\left(\frac{q_s}{q_t}\right)^2 + \left[3+2\frac{q_l}{q_t}\left(3+\frac{q_l}{q_t}\right)\right]\frac{q_s}{q_t} + \frac{q_l}{q_t}\left(3+2\frac{q_l}{q_t}\right) = 0. \tag{1}$$

For a prescribed value of q_l/q_t, the value q_s/q_t is the solution to (1) which gives a positive semi-definite matrix $\mathbf{\Omega}$. Inserting $q_l/q_t = 1.3792$, $q_s/q_t = -0.6672$ is reobtained. The second step is to choose appropriate values of the four free coordinates; both regular and irregular final geometries can be found. Solving the analytic condition for the existence of a non-trivial prestress of the truncated tetrahedron by Nishimura [6] subject to the auxiliary condition of equal cable lengths gives the length ratio 2.2563. The corresponding force density relations are $q_l/q_t = 1.3794$ and $q_s/q_t = -0.6671$. The exact geometrical strut length of the regular truncated tetrahedron is $\sqrt{5} \approx 2.2361$. Hence, the geometry of the tensegrity version is different from that of the polyhedron, which clearly is seen in Figure 1.

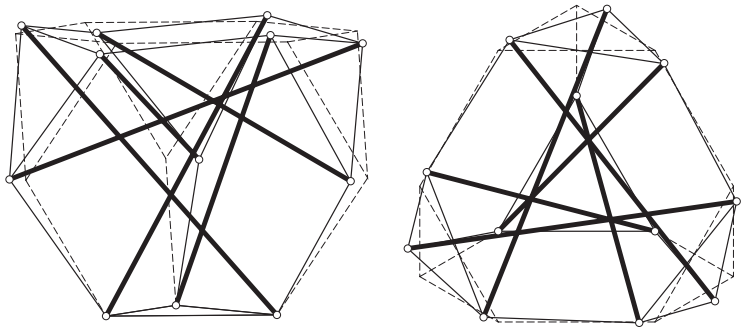

(a) Aerial view (b) Top view

Figure 1: Comparison of the regular truncated tetrahedron (dashed lines) and the tensegrity version. Note the distortion of the hexagonal faces.

Conclusions

Seven form-finding methods for tensegrity structures have been reviewed and classified into two categories. The first category contains kinematical methods, which determine the configuration of either maximal length of the struts or minimal length of the cables. The second category contains statical methods, which search for equilibrium configurations for which a state of self-stress can exist in the structure. The force density, which is found to be equivalent to energy method, is well suited to problems where the element lengths are not specified initially. New configurations are easy to find using the force density method, but it does not permit control of element lengths.

References

[1] R. Motro, S. Belkacem, and N. Vassart. Form finding numerical methods for tensegrity systems. In J. F. Abel, J. W. Leonard, and C. U. Penalba, editors, *Spatial, Lattice and tension structures, Proceedings of the IASS-ASCE International Symposium 1994*, pages 704–713, Atlanta, U.S.A., 1994. ASCE.

[2] A. G. Tibert and S. Pellegrino. Review of form-finding methods for tensegrity structures, 1991. Submitted to *International Journal of Space Structures*.

[3] S. Pellegrino. *Mechanics of kinematically indeterminate structures*. PhD thesis, University of Cambridge, Cambridge, United Kingdom, 1986.

[4] S. Belkacem. *Recherche de forme par relaxation dynamique des structures reticulees spatiales autoconstraints*. PhD thesis, L'Universite Paul Sabatier de Toulouse, Toulouse, France, 1987.

[5] R. Connelly and M. Terrell. Globally rigid symmetric tensegrities. *Structural Topology*, 21:59–78, 1995.

[6] Y. Nishimura. *Static and dynamic analyses of tensegrity structures*. PhD thesis, University of California at San Diego, La Jolla, U.S.A., 2000.

[7] N. Vassart. *Recherche de forme et stabilité des systèmes réticulés spatiaux autocontraints: Applications aux systèmes de tenségrité*. PhD thesis, Université des Sciences et Techniques du Languedoc, Montpellier, France, 1997.

[8] R. Connelly. Rigidity and energy. *Inventiones Mathematicae*, 66(1):11–33, 1982.

[9] R. Connelly and A. Back. Mathematics and tensegrity. *American Scientist*, 86(2):142–151, 1998.

[10] C. Sultan. *Modeling, design, and control of tensegrity structures with applications*. PhD thesis, Purdue University, West Lafayette, U.S.A., 1999.

[11] R. Marks and R. B. Fuller. *The Dymaxion World of Buckminster Fuller*. Reinhold Publications, New York, 1960.

[12] C. R. Calladine. Buckminster Fuller's "tensegrity" structures and Clerk Maxwell's rules for the construction of stiff frames. *International Journal of Solids and Structures*, 14(2):161–172, 1978.

Simulation of Shrinkage and Mechanical Properties of Paper

S. Heyden
Division of Structural Mechanics
Lund University, Lund, Sweden
e–mail: Susanne.Heyden@byggmek.lth.se

ABSTRACT

Summary Paper consists of bonded cellulose fibres in a network structure, oriented preferentially in a plane. A 2D network mechanics model and FEM is used for computational analysis of the shrinkage and elastic performance of paper.

Paper is a fibre network material consisting of bonded cellulose fibres. Cellulose fibres are moisture active, i.e. dimensions and mechanical properties are affected by the moisture content in the fibres. One characteristic feature of cellulose fibres is that they shrink more transversally than in the axial direction. This means that at a fibre crossing, the transverse shrinkage of one fibre tends to shorten the other fibre in its axial direction. Fibre phenomena like this transform to the sheet level in a non-trivial way. This work aims at understanding the relationship between micro-level parameters like fibre, bond and network geometry properties and global sheet properties. Focus is on shrinkage and elastic properties. To improve the understanding of the micro-macro interaction, two-dimensional network modelling and FEM is used.

A model network is composed of bonded fibres arranged in a random structure according to an arbitrary orientation distribution, see Figure 1. The fibres are modelled as linear elastic beam elements with arbitrary distribution in length, cross-section and stiffness. At the bond areas the fibres are assumed to act perfectly together, that is, there is no compliance in the bond layer. Due to this assumption the effect of the shrinkage of a crossing fibre can be taken into account by applying equivalent shrinkage forces at the opposite boundaries of the bond. The geometry of the network structure is periodic. This means that cyclic boundary and loading conditions can be used, making it possible to obtain relevant results even for small network cells. This is desirable due to the numerically heavy computations involved in the analysis. The modelling is described in detail in [1, 2]. The computer analysis consists of generation of the structure, calculation of equivalent shrinkage forces and analysis of elastic mechanical performance by FEM. By means of two further simulations the state of stress at restrained shrinkage and free shrinkage are determined. Output from the analysis is thus isotropic/orthotropic elastic parameters, free shrinkage and fibre segment stresses at free and restrained shrinkage respectively.

Unless the fibre shrinkage is the same in the transversal and axial directions sheet shrinkage will depend on the fibre orientation distribution. This phenomenon has been studied through networks where all fibres are oriented in two perpendicular directions. Figure 2 shows results from these simulations. Networks of density 40 mm/mm^2 were analysed and a unit fibre shrinkage of 1% transversal and no axial shrinkage was assumed. The variable on the x-axis is the part of the fibres that is oriented in the x direction. On the y-axis is the sheet shrinkage in the y direction. Simulated sheet shrinkage increases with the part of the fibres oriented in the perpendicular direction since the only mechanism in this case is transversal shrinkage shortening fibres. The simulation results, however, fall off from the dashed line which shows a simple analytic approximation neglecting double bonding and bending effects.

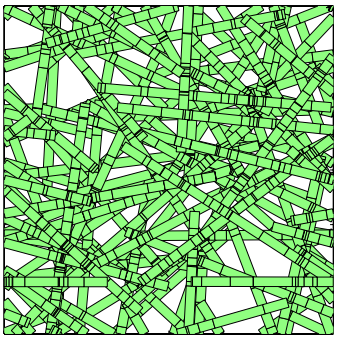

Figure 1: Example of model fibre network.

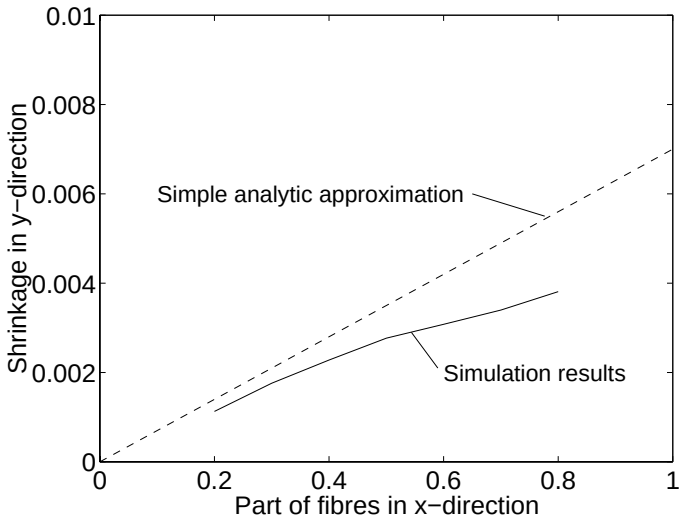

Figure 2: Sheet shrinkage plotted against fibre orientation ratio.

REFERENCES

[1] S. Heyden. Network Modelling for the Evaluation of Mechanical Properties of Cellulose Fibre Fluff. Doctoral thesis, Report TVSM-1011, Lund University, Division of Structural Mechanics, Lund, Sweden, (2000).

[2] L.I. Salminen, M.J. Alava, S. Heyden, P.J. Gustafsson and K.J. Niskanen. Simulation of Network Shrinkage. *To appear in Nordic Pulp and Paper Research Journal* .

Analysis of the Iosipescu test for studies of combined shear and compression of wood.

Federica De Magistris* and Lennart Salmén
STFI, Swedish Pulp and Paper Research Institute Inc.
Stockholm, Sweden
e–mail: fde@stfi.se

Department of Mechanics
Kungl Tekniska Högskolan, Stockholm, Sweden

ABSTRACT

Summary The Iosipescu method is a method used for testing of unidirectional composite material in shear**.** In our case tests using a modified Iosipescu shear-compression fixture were performed on wood. To test the reliability of the modified device a Finite Elements Analysis of the test, first in shear, was carried out and the results compared with the ones from experiments done on a particle board. The comparison will in the future be continued to incorporate the combined case of shear and compression.

1 Introduction

In mechanical pulping, wood fibers are repeatedly sheared and compressed at high temperatures in order to make them suitable for use as a papermaking pulp. The idea of this project is to study a combination of shear and compression of wood in order to determine under what conditions improvement of fiber collapse could be gained.

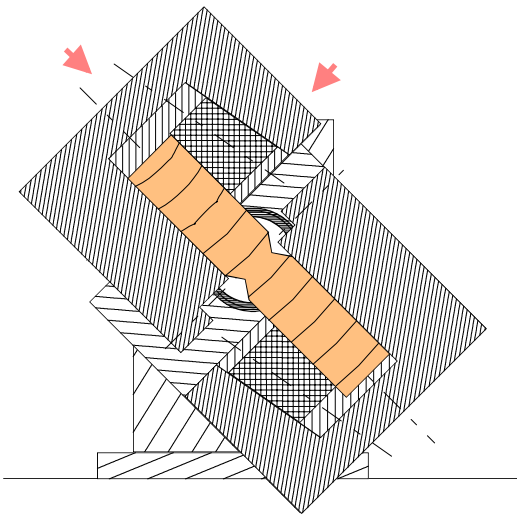

Figure 1. *New test setting for the Iosipescu shear test device*

In order to be confident on the results obtained with this new device, Fig 1, and to better understand the results a Finite Element model of the sample testing has been made and will be developed along with the tests. Shear test have been performed on particle board and the results have been compared with the solutions of the FE models

2 Finite element analysis

To investigate if proper deformation fields were reached by wood in the modified combined shear-compression Iosipescu device a Finite Element analysis has been performed. The software ABAQUS 5.8 was used. Three different 2D models [3,4,5], proposed in the literature to represent the Iosipescu device, with different load and boundary conditions, were analysed in order to choose the one that best represented the mechanical behaviour of the sample. For all models homogeneous and orthotropic materials were analyzed.

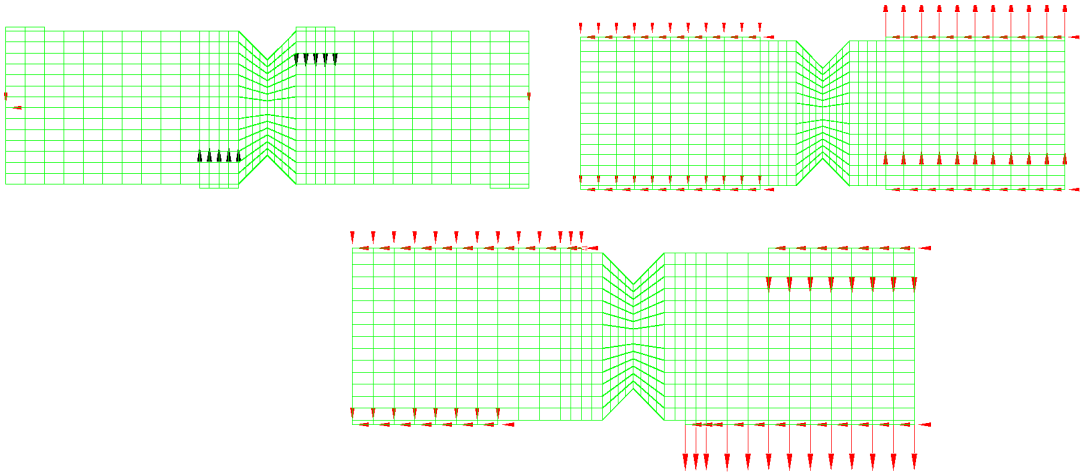

Figure 2. *Models for the Finite Elements Analysis of the Iosipescu test (force couple, left; symmetric loadings block, right; asymmetric loading blocks, bottom)*

3 Material and methods

The first step of the FE model has been to modelize a wood sample subjected to simple shear. The material model considered was wood viewed as an orthotropic material. The material constants were extrapolated from experimental data assigned as "orthotropic particle board" and are reported in Tab. 1. From experimental data G_{RT} has been determined while all the other caracteristic constant were, for the moment, estimated from this value in relation to typical characteristic of wood. The particle board was used in order to have a model of an orthotropic wood material without the annual ring structure of wood but with comparable material properties.

Table1. *Characteristic constant chosen for the FE analysis. Young and shear moduli are given in units of MPa*

	ER	**ET**	**EL**	**GRT**	**GRL**	**GLT**	**νRT**	**νRL**	**νLT**
FE model (orthotropic particles board)	11250	562,5	900	80	803	755	0,43	0,36	0,52

Different load and constrain conditions were analyzed and compared for the three different models. To check the results of these models, shear tests on an "orthotropic particle board" wood material was performed. Four samples were tested twice in shear to a load of 30 N both in "RL" and "RT" direction, the denomination was used to characterized the different cutting orientation of the sample from the particle board. The displacements where registered by Electronic Speckle Photography (ESP). By spraying black paint in a fine pattern on the wood previously painted in white the local displacements were possible to measure.

4 Results and discussion

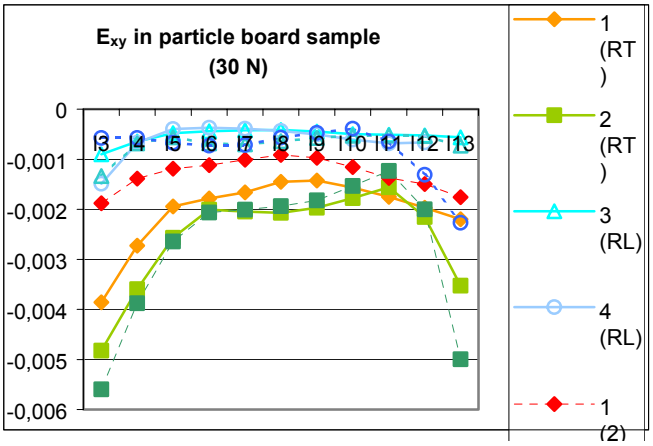

Figure 3. *Strain field of the "particle board", samples tested at 30 N*

In the following figures shear values from the experiments and from the analysis are shown, Fig. 3 and Fig. 4 respectively. For all the cases the shear values obtained at a load of 30 N are shown. The shear values are calculated in the section between the notches.

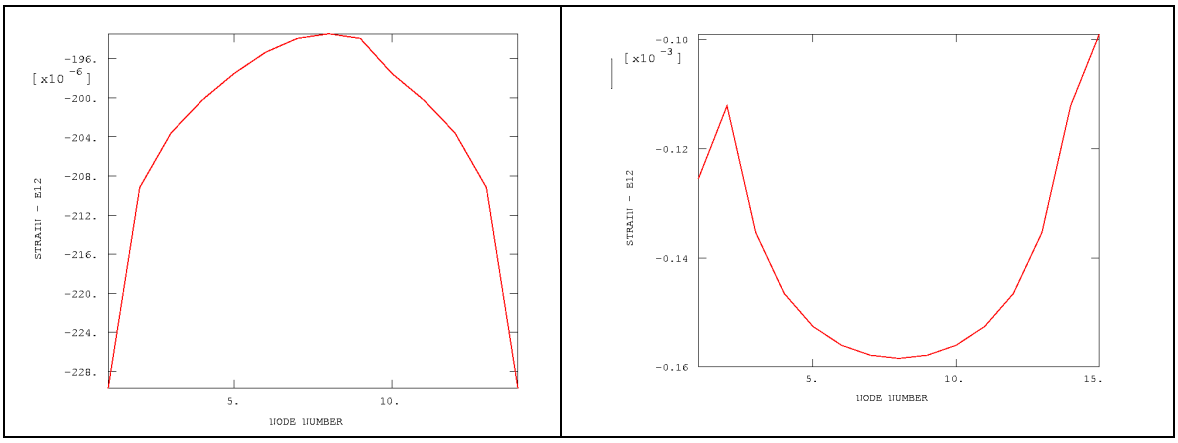

Figure 4. *Calculated strain field from Finite Elements Analysis of the "particle board" samples at a displacement of 0.04 mm. (RT orientation, left and RL orientation, right)*

As seen from the calculation of Fig. 4 the shape of the curves as well as the difference in shear between the RT and RL orientation are in agreement with the experimental results of Fig. 3. However the FE calculation are not in good agreement with the experimental data. This can bee due to the fact that the characteristic constants of the material are extrapolated from the shear modulus obtained from the test. Thus more experimental characteristic of the particle board are needed.

The model that represents the behaviour of the sample during the shear test in the best way was the one with asymmetric loadings blocks, see Fig. 2; in this model in fact the shear filed has the same shape that is founded in literature [5]. For particle board the results of the shear at a load of 30 N are shown in Fig. 6.

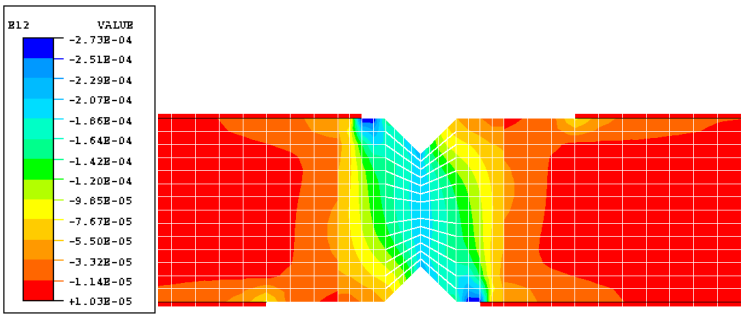

Figure 6. *Shear field for the model with asymmetric loading blocks at 30 N*

5 Conclusions

A Finite Element model with asymmetric loading blocks showed a solution closest to what is expected in on Iosipescu shear test, both in the shape of the strain field and in its absolute values. This model is chosen as a base model and will be further developed in a 3D model with introduction of a material model for the wood microstructure.

The mechanical behavior of wood is not jet fully understood and to make a proper model of its behavior, precise data for the FE analysis on simple deformation modes of wood will be needed.

REFERENCES

1. D. F. Adams and D. E. Walrath. Further Development of the Iosipescu Shear Test Method. *Exp. Mech.,* **27** (2): 113-119, (1987).

2. J. A. Barnes, M. Kumosa and D. Hull. Theoretical and Experimental Evaluation of the Iosipescu. Shear Test. *Comp. Sci. & Technol*., **28**: 251-268, (1987).

3. H. Ho, M. Y. Tsai, J. Morton and G. L. Farley. Numerical Analysis of the Iosipescu Specimen for Composite Material. *Comp. Sci. & Technol.,* **46**: 115-128, (1993).

4. M. Grédiac, F**.** Pierron and A. Vautrin. The Iosipescu In-plane Shear Test Applied to Composites: A New Approach Based on Displacements Field processing. *Comp. Sci. & Technol*., 51: 409-417, (1994).

5. Y. M. Xing, C. Y. Poon and C. Ruiz. A Whole-field Strain Analysis of the Iosipescu Specimen and evaluation of Experimental Errors. *Comp. Sci. & Technol*.,**47**: 251-259, (1993).

Modelling of Adhesive Joints in Timber Engineering

Erik Serrano and Per Johan Gustafsson
Division of Structural Mechanics
Lund University, Lund, Sweden
e–mail: erik.serrano@byggmek.lth.se

ABSTRACT

Summary The work presented concerns the modelling of adhesive joints in timber engineering applications. Numerical studies on the strength of various types of joints were performed. To obtain input data for the theoretical models used, experimental studies on the fracture behaviour of wood adhesive bonds where performed. The results show that wood adhesive bonds can be considered as being quasi-brittle, showing softening behaviour. Furthermore, strength, stiffness, fracture energy and shape of the softening curve are all important parameters for the strength of wood adhesive bonds.

Wood-adhesive joints play an important role in modern timber engineering. In order to add value to the raw material, several highly engineered wood-based products have been developed. Often these involve the use of adhesive joints. Typical examples of such reconstituted materials are glued laminated timber (glulam) and laminated veneer lumber (LVL), Figure 1. In each of these, adhesive joints are used both for lengthwise splicing and for interlaminar bonding. Another example of an adhesive joint application in timber engineering is that of glued-in rods which allow stiff and strong beam-to-column connections or column foundations to be obtained.

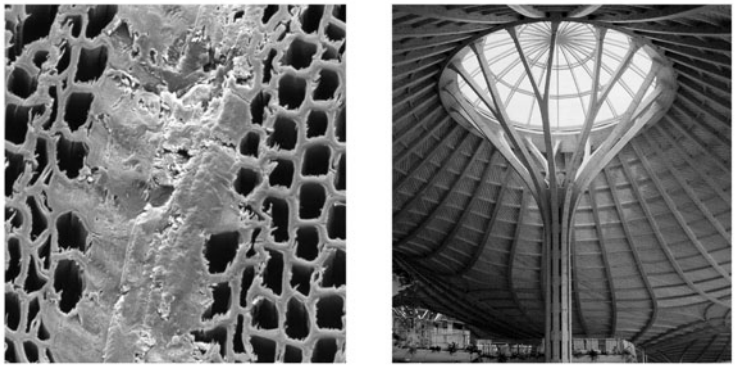

Figure 1: Phenol-resorcinol adhesives (left) are often used in the production of glulam (right).

In order to fully understand and model the behaviour of such structural elements as glulam beams, one must also understand the behaviour of their adhesive bond lines. Although adhesive bond lines often represent only a very small part of a structural component, they are often crucial parts for the strength and the reliability of the structural component. A typical adhesive bond line in timber engineering has a thickness in the range of 0.1–1 mm This is several orders of magnitude smaller than the scale of the structural components, one of approximately 0.1–10 m.

The work presented is an overview of a recently completed research project on wood adhesive joints [1] and concerns experimental and numerical studies of mechanical behaviour on both the above-mentioned scales. Also, methods for bridging the gap between the two scales, making it possible to incorporate knowledge of the mechanical behaviour of a thin bond line into analysis on the structural-component-size scale are discussed. Applications such as finger-joints, glued-laminated timber and glued-in rods are considered, Figure 2. The experimental studies include the testing of the fracture characteristics of wood-adhesive bonds, including both wood-to-wood bonds and glued-in rods of either steel or glass fibre reinforced polyester. The numerical studies relate to the strength of finger-joints, laminated beams and glued-in rods for timber structures.

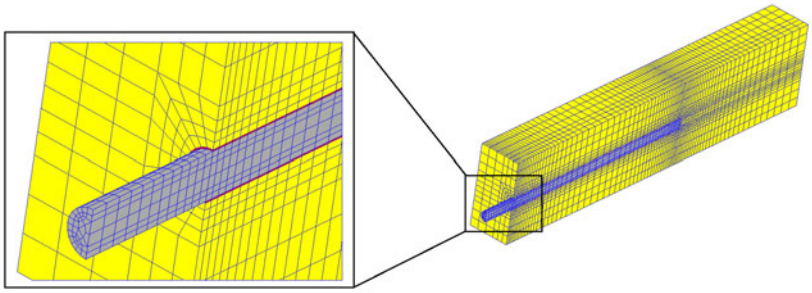

Figure 2: A finite element model of a glued-in rod.

The complete stress-displacement response of small specimens, particularly their fracture softening behaviour beyond peak stress, was recorded experimentally. Such responses were subsequently used as input to constitutive models based on nonlinear fracture mechanics and damage mechanics. The numerical analyses performed with these models show that the load-bearing capacity of wood-adhesive joints is highly influenced, not only by the local strength of the bond, but also by the material stifnesses involved, the geometrical shape of the adherends, by the fracture energy of the bond line and by the shape of the nonlinear stress-displacement relation.

REFERENCES

[1] Serrano, E. *Adhesive joints in timber engineering. Modelling and testing of fracture properties*. Doctoral Thesis. Report TVSM-1012. Division of Structural Mechanics, Lund University, Lund Sweden, 2000.

Strength Design of Glued-in Rods

Per Johan Gustafsson and Erik Serrano

Division of Structural Mechanics,
Lund University, Lund, Sweden
e–mail: bmpjg@byggmek.lth.se

ABSTRACT

Summary Axially loaded glued-in rods are used in timber structural design for joining or reinforcing heavy glue-laminated timber structural members. A European research program, 1998-2001, on the pull-out strength of glued-in rods included work on development of a calculation method before proposal of a design equation for the short term strength at constant climatic conditions. This work comprised various stress and strength analyses by the FEM and by hand calculation methods, experimental testing of fracture mechanics properties and testing of a large number of full-scale glued-in rod joints.

1. Introduction

Axially loaded glued-in rods are used in timber structural design for joining or reinforcing heavy glue-laminated timber structural members [1,2]. The rods are commonly made of threaded high strength steel bars, but also glass fibre bars were included in the testing program. Typical rod diameters are in the range of 8-30 mm and the glued-in length is commonly in the range of 10-30 times the rod diameter. The rod may be orientated along the grain of the wood, perpendicular to the grain or at some inclination, as indicated in Figure 1 showing the types of full-scale specimens and loading conditions included in the testing program.

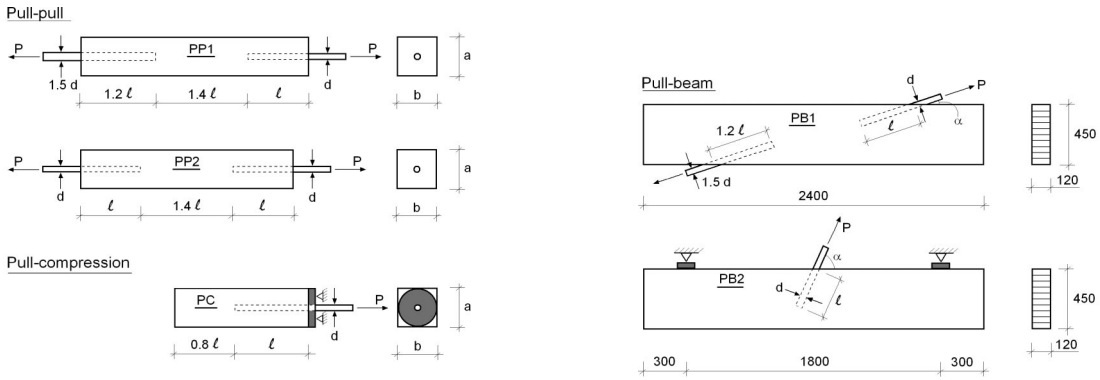

Figure 1. Glued-in rod test specimens.

2. Present study

3-D FE stress and fracture analysis were carried out for several joint geometries, loading conditions and glue-line material properties [4]. In these analyses the bond-line was modelled by a non-linear mixed mode fracture model, taking into account the localized gradual damage in

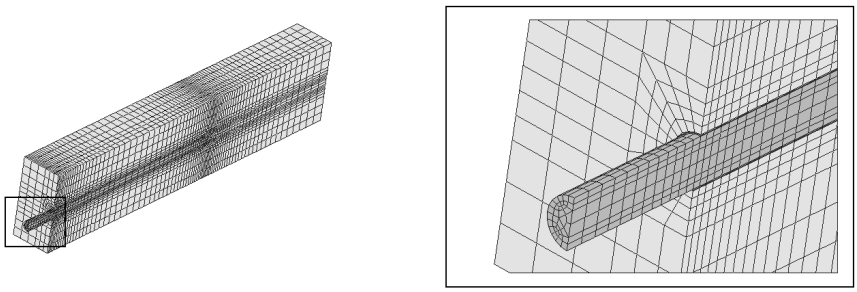

Figure 2. FE-model of a glued-in rod joint.

the bond layer, characterized by normal and shear stress vs normal and shear slip across the bond layer. The stress vs slip properties were quantified by four parameters: the local strength and fracture energy of the bond in pure shear and pure tension. The wood was modelled as a linear elastic orthotropic material. Figure 2 shows a FE-mesh used in the analysis.

The general goals before proposal of a strength design equation for the basic pullout strength were to find some method that has the qualities of being:

1. Simple, yet general.
2. Based on mechanics and with parameters with a physical meaning.
3. Reasonably accurate and in general give predictions on the safe side.

Striving towards these goals use of a combination of the 1D shear lag theory of Volkersen and quasi-nonlinear fracture mechanics [5] was investigated. In this theory the rod and the timber are assumed to act as overlapping bars connected by a shear layer, representing the adhesive bond line. The material properties of the two adherends are given by their axial stiffness in the direction of the rod: E_w and E_r representing the wood and the rod, respectively. The material properties of the bond layer are defined by its local shear strength, τ_f, and its shear fracture energy, G_f. A special case of this shear lag theory coincide with linear elastic fracture mechanics analysis and an other, opposite special case coincide with that of a ductile bond performance and uniform stress along the bond line.

Other less simple methods of analytical strength analysis were also studied, e.g. an extension of the above bar-shear lag theory by consideration to the shear strain in the wood, leading to a Timoshenko beam shear lag fracture model and a fourth order ordinary differential equation for the shear stress along the bond line.

Experimental tests of basic properties and fracture performance of the bond were carried for three adhesives: an epoxy, a polyurethan and a recorcinol/phenol [3]. In these tests specimens with short glued-in lengths, only 8 mm, were used in order to enable achieve uniform shear stress and recording of the entire stress vs slip curve, including the descending part with gradually decreasing stress as the deformation was increased. In Figure 3 is shown stress versus shear slip for the three adhesives using a rod made of steel glued-in parallel with the grain of the wood. The elastic pre-peak stress deformation was for all adhesives tested very small as compared with the post-peak deformation. The post-peak performance, in particular the slope of the first descending part of the curve, has a major influence of the ductility of the bond and is commonly of major importance for the load bearing capacity of a glued-in rod.

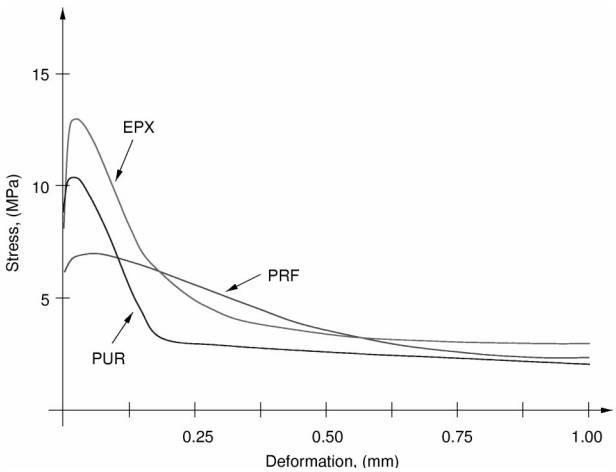

Figure 3. Local shear stress versus local shear slip.

The testing of full-scale glued-in rod specimens was carried out in cooperation with FMPA, Stuttgart, and SP, Borås. The testing program comprised more than 75 test series and 700 individual tests. In Figure 4 is the average strength values from test series relating to epoxy shown as the nominal bond shear stress at failure, $P_f/(\pi dl)$, versus a dimensionless number denoted ϖ. This number is defined by the length and diameter of the rod, the bond properties in terms of its local shear strength and fracture energy, and the elastic stiffness the wood and the rod. The curve indicated in the diagram represents a proposed design equation:

$$\frac{P_f}{\tau_f \pi dl} = \frac{\tanh(\varpi)}{\varpi}$$

where τ_f is the local bond shear strength and P_f the glued-in rod pull-out strength. In Table 1 is shown bond properties obtained by fitting experimental pull-out strength to the shear lag theory strength predictions.

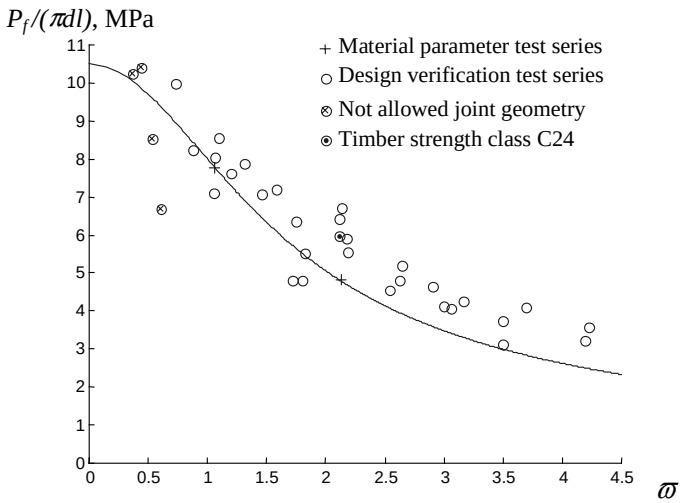

Figure 4. Pull-out strength test results and curve representing a strength equation.

Table 1. Local shear strength and fracture energy of rod to wood bond lines.

Adhesive	τ_f N/mm^2	G_f Nmm/mm^2
PRF	8.9	4.15
Epoxy	10.5	1.89
PUR	9.7	1.77

REFERENCES

1. P.J. Gustafsson and E. Serrano. Glued-in Rods for Timber Structures – Development of a Calculation Model. Report TVSM-3056, Div of Structural Mechanics, Lund University, Sweden 2001, pp 1-96.
2. P.J Gustafsson, E. Serrano, S. Aicher and C.-J. Johansson. A Strength Equation for Glued-in Rods. To be presented at the Timber Engineering RILEM Symposium, Stuttgart September 2001, pp 10.
3. E. Serrano. 'Glued-in Rods for Timber Structures. An Experimental Study of Softening Behaviour', Materials and Structures. 34 (238), May 2001, RILEM Publications, pp.228-234.
4. E. Serrano. 'Glued-in Rods for Timber Structures. A 3D Model and Finite Element Parameter Studies', Int. J. of Adhesion and Adhesives. 21(2) (2001) pp.115-127.
5. P.J. Gustafsson. 'Analysis of generalized Volkersen joints in terms of non-linear fracture mechanics', In 'Mechanical Behaviour of Adhesive Joints', proc. of Eur. Mech. Colloquium 227, 1987, Edition Pluralis, Paris, 1987, pp 323-338

Acknowledgement: The present study was carried out as a part of the European research project SMT4-CT97-2199, GIROD. The partners were SP Swedish National Testing and Research Institute, University of Stuttgart, University of Karlsruhe, TRADA Technology and Lund University.

Heat- and stress development in hardening concrete

Jan Arve Øverli
Department of Cement and concrete
SINTEF, Trondheim, Norway
e–mail: jan.a.overli@civil.sintef.no

ABSTRACT

Summary With focus on numerical simulations, this paper describes the hydration process of concrete and the subsequent response on the structure. There is a risk of cracking at early age due to the restrained volume changes. The hydration process, which results in a heat- and stress development in a structure, is simulated by means of the finite element method. An example is provided in this paper to exemplify the problem and the solution procedure.

During the hardening process of concrete energy is released as heat. The tensile strength of concrete is low. Due to temperature differences the concrete will tend to expand or contract and there is a risk of cracking of the concrete due to restrained volume changes from the temperature and shrinkage. When casting takes place upon an existing concrete structure, the relative stiffness will have an influence on whether or not cracks are formed. A typical problem is the casting of a wall on an existing slab, as illustrated in Figure 1. Keeping control of the cracking in early age concrete is important with respect to durability and therefore also on the lifetime of a concrete structure. Traditionally, prediction of early-age cracking has been based on temperature criteria. However, this is not sufficient because crucial factors like thermal dilation, shrinkage, mechanical properties and restraint conditions are not considered. For a reliable crack prediction at early ages a stress-strain criteria must be applied.

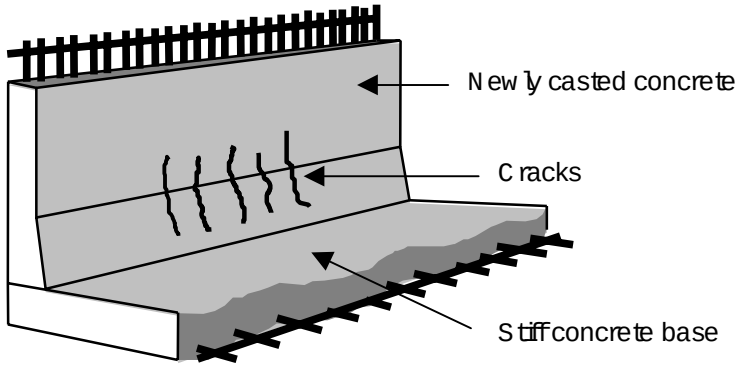

Figure 1 - Typical problem with cracking of concrete due to the hardening process.

On basis of the heat of hydration in the hardening concrete and the thermal boundary condition, the temperature distribution as a function of time can be calculated in a finite element analysis. To obtain reliable results, a simulation of hardening concrete structures has to take into account temperature development due to hydration, development of mechanical properties, creep and

shrinkage, and restraint conditions of the particular structure. This calls for well-documented material models. Within the Brite-Euram project IPACS [1] and the Norwegian NOR-IPACS [2] project a comprehensive laboratory test programme has been performed to identify parameters for models used in such calculations. Both thermal and mechanical properties have been investigated. Bosnjak [3] has implemented the material models in the finite element code Diana [4].

Concrete is a mixture of cement, water, aggregate (fine and coarse) and admixtures. The main compounds in cement are calcium silicates. In presence of water, a chemical reaction takes place between the cement and the water (hydration process), which in time produce a firm and hard concrete. The most important factors for temperature development in a newly cast structure are the cement content, thermal properties of concrete, geometry and size of structure, boundary conditions and initial conditions. Mechanical properties important in the analysis of hardening concrete are the strength, Young's modulus of elasticity and creep. In young concrete the development of these properties as function of time and temperature history is of great concern.

The influence of the mechanical responses on the temperature development in hardening concrete is negligible, and the thermal and mechanical problem may therefore be separated. The thermal problem is solved first, and results are used as input for the subsequent stress calculation. This is a so-called staggered analysis. The finite element method is adopted to solve the governing set of differential equations for the thermal and mechanical response of early age concrete. Since the thermal and mechanical problem is decoupled, the finite element discretisation may be done separately. However, to be efficient the same element mesh is normally used in both analyses. To avoid spatial oscillation of stresses, elements in the stress analysis then must have an order higher interpolation polynomial than element in the temperature analysis.

To determine the risk for cracking in concrete during the hardening process is a relevant problem for different types of structures. Typical structures are foundations, culverts in embankments or subsea tunnels. A numerical investigation of temperature and stress distribution in a culvert is presented in this paper. The structure is modelled and analysed by the general finite element program Diana [4].

Figure 2 shows the cross section and the finite element model under consideration. Due to symmetry only one half of the wall is modelled. The same element model is used both in the temperature and stress analysis. Solid elements describing linear variation of temperature and quadratic variation of stresses are used in this case. The exchange of temperature with surroundings is modelled by the conduction coefficient of boundary elements. Quadrilateral elements were used at the faces of three-dimensional model.

Different ways of modelling the structure and the restraint conditions is possible. In a culvert it would normally be sufficient with a two-dimensional temperature distribution. However, the stress distribution is three-dimensional. Therefore both the thermal and stress analyses must be performed with 3D models. The most important stress component is in the longitudinal direction of the culvert. Instead of a full 3D model, the analyses presented in this section employs a simplified model which is a "slice" of the wall with unit thickness. The analysis of the culvert in this work assumes free rotation of the cross section of the wall.

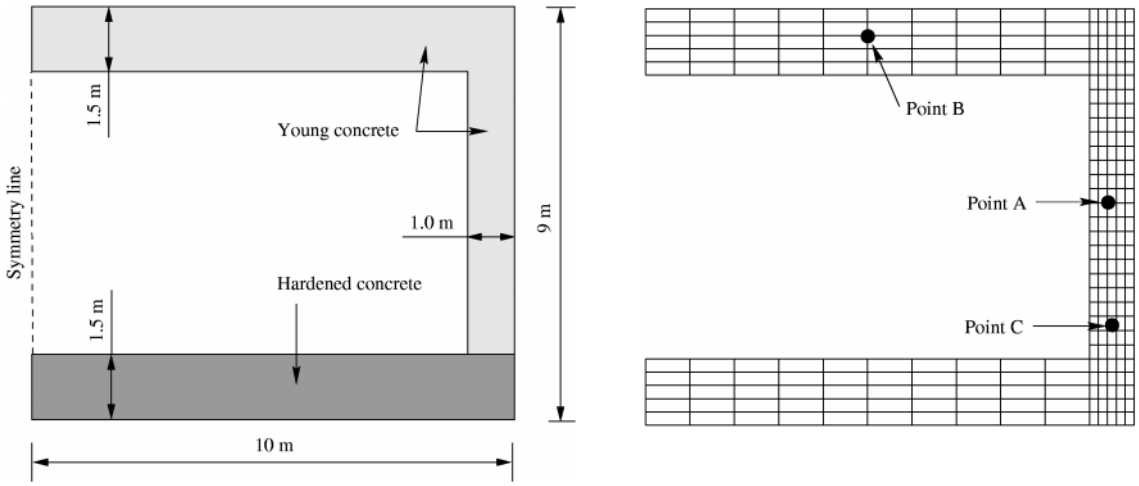

Figure 2 – Cross section geometry and finite element mesh of the culvert.

Typical material properties for concrete are employed in the analysis. The air temperature is constant 17°C. The hardened and young concrete has initial temperatures of 17°C and 20°C respectively. The formwork on the wall and the underside of the slab is removed after 36 hours. The culvert is analysed for a time period of 10 days.

Figure 3 illustrates results from the thermal analysis. The temperature development in two points, point A and B in Figure 2, in the middle of the cross-sections is given. The variation in development is due to the difference in thickness of the cross-section. As expected there is no significant heat exchange with the foundation slab.

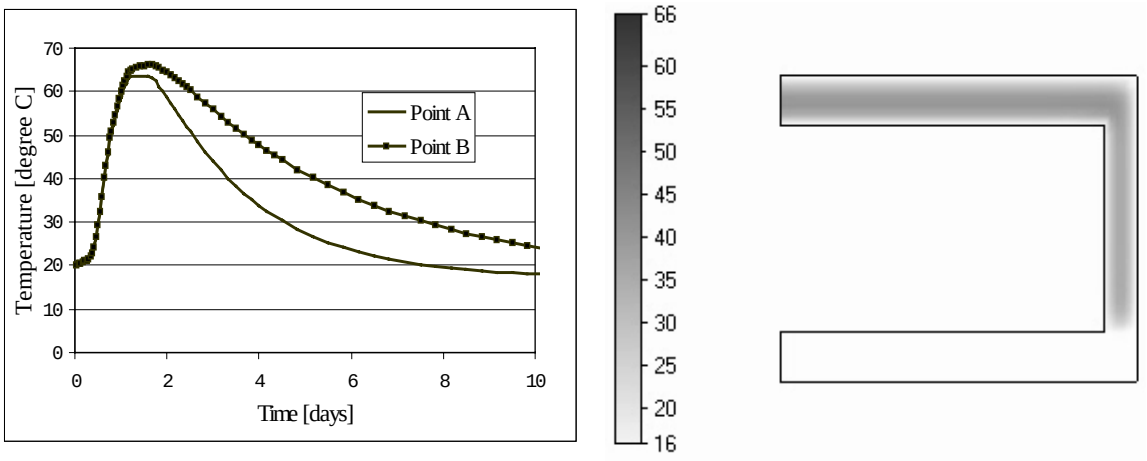

Figure 3 – Temperature development and distribution in the cross-section after 3 days.

The main objective for performing numerical analysis of young concrete is to estimate the risk for cracking due to volume changes in the hydration process. For the culvert in this example, stresses in the longitudinal direction can form vertical cracks. Figure 4 presents the longitudinal stress in the wall. During the expansion phase, when the concrete is heated, compressive

stresses are introduced in the young concrete. In the contraction phase, rather large tensile stresses develop in the cross-section. A maximum stress of 6.7 MPa is reached after 7 days. Typical tensile strength of concrete is in the range 2-5 MPa. Hence, vertical cracks will most likely occur in this culvert. As expected the largest tensile stresses are in the wall above the foundation. Since the foundation with hardened concrete is much stiffer than the wall with young concrete, the effect of restraining is higher in this area. In the figure it can be seen that in the area above the foundation, the complete thickness of the wall have high tensile stresses. Consequently cracks can form through the cross-section, which results in increased durability.

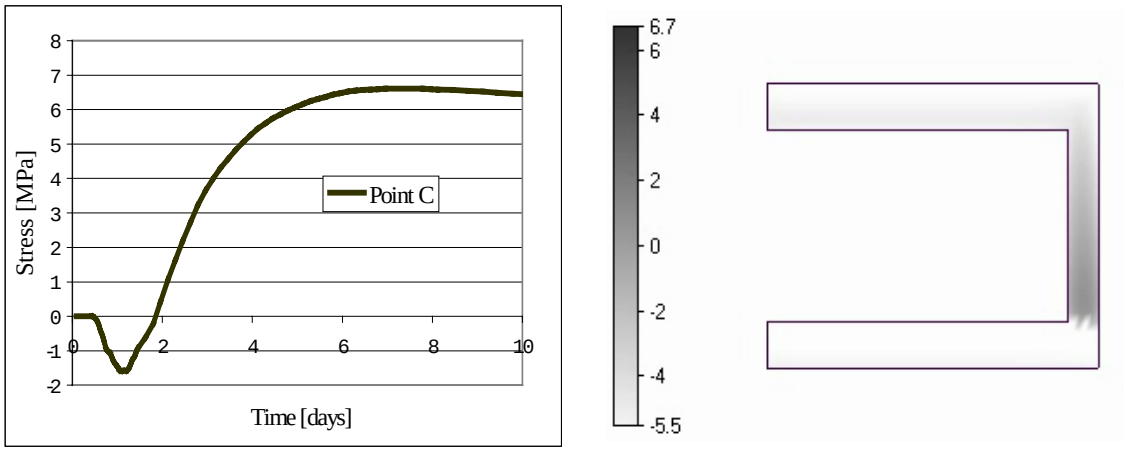

Figure 4 – Development and distribution of out-of-plane stress after 9 days in the wall.

This paper deals with numerical simulation of the heat and stress development in concrete during the chemical hydration process in concrete. The crucial factors in the prediction are thermal dilation, shrinkage, mechanical properties and restraint conditions. A culvert is analysed to exemplify the assumptions, difficulties and possibilities of employing a numerical analysis to estimate the risk of cracking at early age of a concrete structure. However, it must be emphasised that a difficult task and a major challenge in such analyses are to identify all the necessary material properties.

REFERENCES

[1] IPACS. Brite-EuRam project BRPR-CT97-0437. *Improved Production of Advanced Concrete Structures.* http://ipacs.ce.luth.se/index.html, (1997-2001).

[2] NOR-IPACS. A project supported by the Research council of Norway (NFR). *Improved Production of Advanced Concrete Structures,* (1997-2001).

[3] Diana 7.2. *User's Manual*, TNO Building and Construction Research, The Netherlands, http://www.diana.nl, (1999).

[4] D.Bosnjak. *Self-induced cracking problems in hardening concrete structures.* Dr.ing. thesis, Norwegian University of Science and Technology, Trondheim, Norway (2000).

Simulation of Wind Turbine Dynamics

Anders Ahlström
Department of Mechanics
Royal Institute of Technology, Stockholm, Sweden
e–mail: anders.ahlstrom@mech.kth.se

ABSTRACT

Summary A finite element model for simulation of the dynamic response of horizontal axis wind turbines has been developed. The aerodynamic model, used to transform the wind flow field to loads on the blades, is a Blade-Element/Momentum model. The model is rather general, and different configurations and wind conditions could easily be simulated. The model is primarily intended for use as a research tool when influences of specific dynamic effects are investigated.

Background

For a successful large-scale application of wind energy, the price of wind turbine energy must decrease in order to be competitive to the present alternatives. The behaviour of a wind turbine is made up of a complex interaction of components and sub-systems. The main elements are the rotor, tower, hub, nacelle, foundation, power train and control system, see figure 1. Understanding the interactive behaviour between the components provides the key to reliable design calculations, optimised machine configurations and lower costs for wind generated electricity. Consequently, there is a trend towards lighter and more flexible wind turbines, which makes design and dimensioning even more important [1].

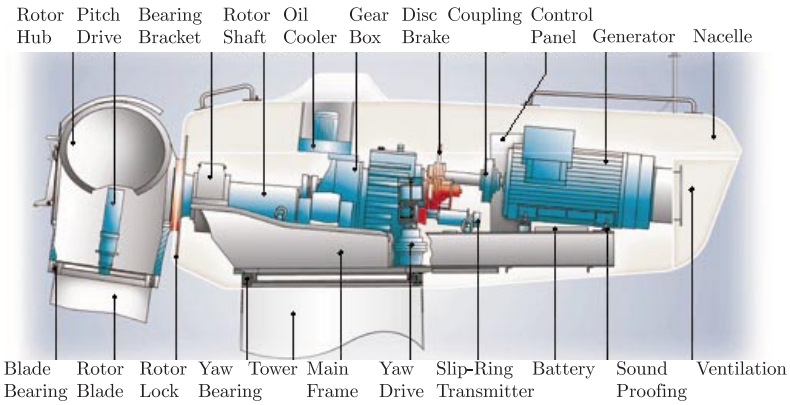

Figure 1: Wind turbine layout.

The goal of this ongoing project is to produce a model with such accuracy and flexibility that different kind of dynamic phenomena can be investigated. The majority of the present aeroelastic models are based on a modal formulation and a time domain solution. The modal formulation models are computationally time efficient because of the effective way of reducing degrees of freedom, DOFs. However, these modal models are primarily suited for design purposes and will,

because of the reduced DOFs, not be suitable for research areas where phenomena such as instabilities may be investigated. This project has chosen the finite element method as a means to accurately predict the wind turbine loading and response.

The calculation model is based on three computer programs:

- SOSIS-W for generation of the turbulent wind field [2].
- AERFORCE package for the calculation of aerodynamic loads [3].
- SOLVIA commercial finite element program for modelling of the structural dynamics [4].

Wind Field

It is very important for the wind industry to be able to describe the wind field properly. Turbine designers need the information to optimize the design of their turbines and turbine investors need the information to estimate their income from electricity generation.

SOSIS-W is an artificial wind data generator developed by Teknikgruppen AB [2]. The program is specially developed for providing time domain series with turbulent wind. SOSIS-W simulates three dimensional wind vectors, corresponding to gridpoints in a plane uniform cartesian grid, where the grid plane is perpendicular to the mean wind direction.

SOSIS-W creates three output files, one for each velocity component. The output data is arranged in rows and columns, where each row represents a time series and each element in a time series represents the velocity at a specific coordinate. Figure 2 shows an example of a grid net of size 4 x 4 and a rotor with its blades divided into 4 elements. However, in real simulations the resolution must be increased. Depending on the angle, phi, the time and the distance from the hub to the center of each blade element, the velocity will change in both space and time.

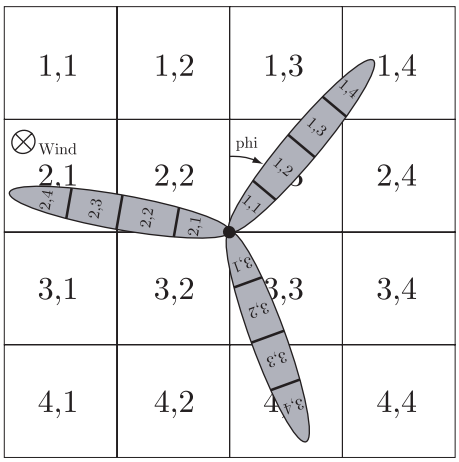

Figure 2: Example of a grid net of size 4 x 4 and a rotor with its blades divided into 4 elements.

Aerodynamics

Various methods may be used to calculate the aerodynamic forces acting on the blades of a wind turbine. The most advanced are numerical methods solving the Navier Stokes equations for the global as well as the flow near the blades. The two major approaches, for fast time simulations, to calculate the forces are the Actuator Disc Model and the Blade-Element Model.

The aerodynamic model used in this project is the Blade-Element/Momentum method which has been found very effective in comparative studies for wind turbine simulations. In spite of a number of limitations it is still the best tool available for getting good first order predictions of thrust, torque and efficiency for turbine blades under a large range of operating conditions.

The AERFORCE [3] package requires the input of airfoil aerodynamic data via tables as function of the angle of attack, the turbine blade and rotor geometry and wind and blade velocities. Calculation results are very dependent on the airfoil data, which is derived from experimental wind tunnel studies.

Extensions has been made to the BEM-method, in the AERFORCE package, to incorporate:

- Dynamic inflow: Unsteady modelling of the inflow for cases with unsteady blade loading or unsteady wind.
- Extensions to BEM-theory for inclined flow to the rotor disc (yaw model).
- Unsteady blade aerodynamics: The inclusion of 2D attached flow unsteady aerodynamics and a semi-empirical model for 2D dynamic stall.

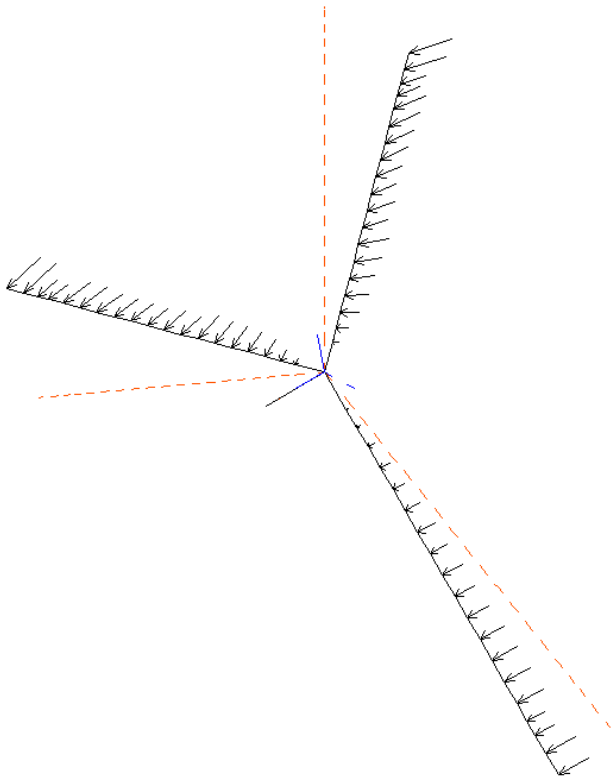

Figure 3: The aerodynamic forces acting on the rotor.

Structural Dynamics

As mentioned in the background to this paper a wind turbine is made up of a number of interconnected mechanical elements. The aerodynamics forces acting on the rotor will not only contribute

to the production of electrical power, they will also results in dynamic loads. To simulate the entire system, all motions must be taken into account.

The wind turbine is modelled using SOLVIA [4], which is a commercial finite element program for linear and nonlinear analysis of displacements, stresses and temperatures under static or dynamic conditions. The wind turbine is divided into three main parts, the tower, the nacelle and the rotor. The parts are then coupled at nodes where important bearing and rotationally DOFs are restrained. Figure 3 shows an example of the SOLVIA modelled rotor with the aerodynamic forces acting on each blade.

Conclusions

The combination of the three separate programs has produced a simulation package for wind turbine applications. Preliminary results indicate that the package is sufficiently accurate for the investigation of different kind of dynamic phenomena.

REFERENCES

[1] D. Eggleston and F. Stoddard. *Wind Turbine Engineering Design.* John Wiley & Sons, Chichester, (1997).

[2] I .Carlen. *SOSIS-W Version 1.3.*, Teknikgruppen AB, Sollentuna, Sweden, (2000).

[3] A .Björk. *AERFORCE: Subroutine Package for unsteady Blade-Element/Momentum Calculations TN 2000-07.* FFA, Bromma, Sweden, (2000).

[4] G. Larsson. *SOLVIA, Finite Element System Version 99.0, Report SE 99-6,* SOLVIA Engineering AB, Västerås, Sweden, (2000)

Analysis of Heat Losses in Multilayered Structures of a Pipeline Using Finite Element Method

I. Gabrielaitiene* and R. Kačianauskas
Department of Strength of Materials
Vilnius Gediminas Technical University, Vilnius, Lithuania
e−mail: irena.Gabrielaitiene@fm.vtu.lt

B. Sunden
Department of Heat and Power Engineering
Lund Technical University, Lund, Sweden
e−mail: Bengt.Sunden@vok.lth.se

ABSTRACT

Summary The steady state thermo-hydraulic flow in a pipe is investigated by the finite element method, where the main attention is focused on analysis of heat losses in a multilayered structure of a pipeline**.** A complex thermal finite element has been developed for this purpose and combined with thermo-hydraulic pipe element of the ANSYS code. The results for heat losses are presented and compared to analytical solution. Accuracy of the finite element model is also investigated.

Introduction

Evaluation of heat losses presents an important part of thermo-hydraulic flow analysis in engineering application***s*** such as district heating and cooling systems. The solution of this problem contains difficulties due to the multilayered, even multisolid**,** structure of the pipeline and due to different heat transfer modes having state-dependent characteristics. Some of these factors are neglected in engineering practise for simplicity reasons.

In analysis of heat losses in pipelines, numerical methods are frequently adopted to solve the fluid flow and heat transfer problems in pipelines separately [1-5]. A finite element formulation for temperature-independent fluid flow in piping systems is proposed in [1], while heat flow analysis in a pipe as an axisymmetric insulated cylinder is illustrated in [2]. Moreover formulae for the heat loss from a pipe with insulation and a ground surface thermal resistance are proposed in [3]. Detailed evaluation of heat losses by the finite element method with attention on heat flux distribution into the soil has been solved in [4] and transient analysis of a piping system is presented in [5]. The emphasis of this report was to develop a general finite element approach in modelling of thermo-hydraulic flow for analysis of heat losses in a multilayered structure of a pipeline.

Finite element approach to coupled thermo-hydraulic flow in pipe

Generally the fluid flow in a pipe and heat transfer involving conduction, convection and radiation is a simultaneous phenomenon. The finite element approach to this coupled steady-state non-linear problem may be written in the following form:

$$\begin{bmatrix} \boldsymbol{K}_{hyd}(\boldsymbol{P},\boldsymbol{T}) & \boldsymbol{0} \\ \boldsymbol{0} & \boldsymbol{K}_{ther}(\boldsymbol{P},\boldsymbol{T}) \end{bmatrix} \begin{Bmatrix} \boldsymbol{P} \\ \boldsymbol{T} \end{Bmatrix} = \begin{Bmatrix} \boldsymbol{W} \\ \boldsymbol{Q} \end{Bmatrix} \tag{1}$$

Here, [$\boldsymbol{P}$] and [$\boldsymbol{T}$] present nodal pressure and temperature vectors which have to be obtained by

solution of the problem (1). [***W***] and [***Q***] describe given nodal fluid and heat flow vectors reflecting given boundary conditions, while [K_{hyd}] and [K_{ther}] present hydraulic and thermal matrices reflecting physical properties of fluid and insulation.
The fluid physical properties, which are involved in both heat transfer and fluid flow analysis, depend on temperature and this aspect is important in design calculations.
In other words, fluid flow and heat transfer analyses are coupled due to variation of the above properties, where the coupling is built into the governing equations implicitly. The solution of model (1) requires an iterative sequential procedure.
The hydraulic matrix mainly depends on the fluid including fluid-pipe interaction properties. The physical nature of the thermal matrix is much more complicated. For an individual element *e* it reflects heat transfer through a multilayered**,** or even multisolid**,** structure of the pipe and environment and has the form of:

$$[K^{e}_{therm}] = \sum_{m=1}^{p} [K^{e}_{m}] \qquad (2)$$

Here, subscript *m* denotes all layers of insulation and environment structure producing thermal resistance**s**. On the other hand, individual layer**s** may contain different transfer modes. Each layer may produce a thermal matrix:

$$[K_m]=[K_1(h)+K_2+K_3+K_4] \qquad (3)$$

Here the $[K_1]$ matrix describes convection to the layer adjacent to a surface through the convection coefficient ***h***, $[K_2]$ reflects mass transport, while $[K_3]$ and $[K_4]$ describe conduction occurring in the flow longitudinal direction and normal to the flow direction**,** respectively.
For the fluid layer**,** the thermal matrix has the form: $[K_m]=[K_1(h)+K_2+K_3]$. For describing conduction in the insulation, the following matrix is used: $[K_m]=[K_4]$. For designing the combined effects of thermal radiation and natural convection from insulation surface**,** the thermal matrix has form of: $[K_m]=[K_1(h)]$.
Evaluation of heat losses provides the same sequence as thermal matrices. For the individual element *e:*

$$\{Q^{e}\} = \sum_{m=1}^{p} [K^{e}_{m}]\{T^{e}\} \qquad (4)$$

Implementation of the above scheme requires development of a complex thermal element. The model (1)-(3) can be applied to the solution with different level of coupling the thermal characteristics.

Solution of heat losses in multilayered structure of the heating pipe

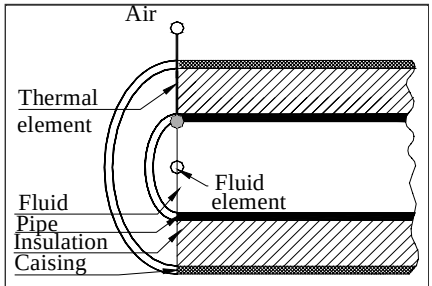

Fig. 1. Common insulated pipe

The most common pipes in use for district heating is insulated pipes with carrier of steel, insulation of poly-urethane and a casing of high density polyethylene. (Fig.1) In this case, the heat transfer from fluid to environment is a three-step process: from a warmer fluid to a wall, through the multilayered wall, then to a colder surrounding air.
The main problem occurring in a thermo-hydraulic finite element analysis of the pipe is that the existing finite element codes usually contain thermo-hydraulic pipe

element paying no attention to the structure of the pipe. In the framework of this paper the complex thermal element designing myltilayered structure of insulation has been proposed. It is compatible with the fluid element of the ANSYS code [6].

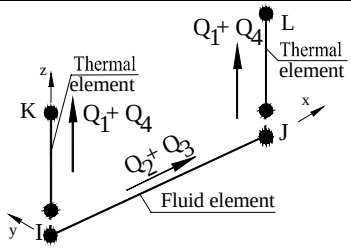

Fig.2 Complex thermal finite element and fluid element

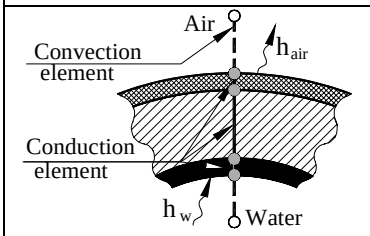

Fig.3 Complex thermal finite element

In the present study the analysis of heat losses is based on the following assumptions:

1. The heat transfer process from fluid to surrounding is only solved in the radial direction, therefore it presents a one-dimensional (axi-symmetric) problem.
2. The pipe is assumed to be placed in an underground culvert and the temperature of surrounding air in the culvert is assumed to be known.

The developed complex thermal element contains temperature-dependent thermal properties, while evaluation of heat losses is developed as separate postprocessor. A general scheme of the fluid element connecting pipe nodes I-J with the thermal element is presented in Fig. 2. Thermal elements K-I and L-J describe structure of insulation and environment as shown, in Fig.3. Here, heat transfer from fluid to wall describes fluid element, including flow - dependent convection coefficient. A set of conduction elements is needed to present the transfer of heat in the pipe, insulation and casing material, since properties of each material are different.

Heat transfer from the wall is represented by a convection element, which involves combined effects of natural convection and thermal radiation (Fig 3.)

Numerical example

A numerical example is applied to present the idea discussed in the previous section. Numerical examples are carried out for different diameters of the pipe (D20, D40, D80, D160 mm) and for a pipe length of 1 m. The temperature of the water is assumed to be 80^{o}C, temperature of the surrounding air is 30^{o}C. The properties of water are considered as follows: heat conductivity 0.684 [W/mK], specific heat 4313[J/(kgK)], density 993-937.2 kg/m3, viscosity 6.2-2.19$\times 10^{-4}$ [kg/ms]. The heat conductivity of steel pipe is 76 [W/mK], while heat conductivity of insulation and casing is 0.032 and 0.43 [W/mK], respectively.

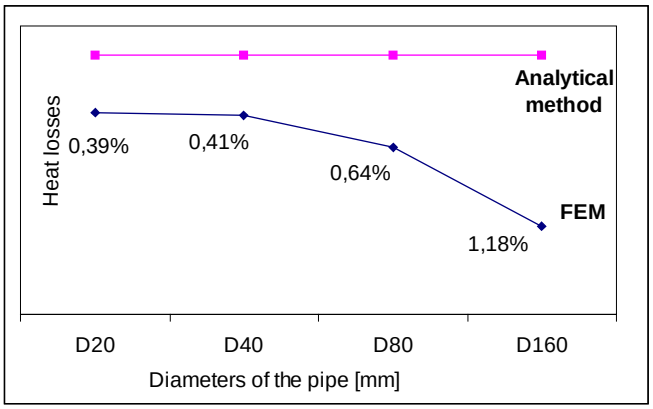

Fig.4 The comparison of the heat losses between the finite element results (FEM) and results by an analytical method

Fig. 4 shows the comparison of the losses between the finite element results and results by an analytical method for uncoupled problems. The influence of coupling by assuming a temperature dependent variation of density and viscosity is also investigated. The proposed problem is also tested by the analysis of a fragment of a heating network.

Accuracy of Finite Element Model
The accuracy of the finite element model for the estimation of the heat losses is examined for a few test examples by using different level of discretisation. The first test example defines the influence of discretisation of conduction element. The relative accuracy of heat flow decreases when the insulation thickness decreases, but remains independent on thermal conductivity of the insulation material. The second test defines the influence of discretisation of fluid element. Recommendations for longitudinal subdivision of the pipe section into fluid element are proposed as well.

Results and discussion
The finite element approach for thermo-hydraulic problem of a pipeline, mainly with a multilayered structure, with emphasis on analysis of heat losses has been developed. Theoretical investigation and numerical examples prove suitability of the above approach in engineering and advantages in comparison to the engineering method:

1. Multilayered structures of the pipe and surroundings are considered in the analysis of the heat losses.
2. Heat transfer modes at different level of coupling with the fluid flow by describing temperature dependent fluid characteristics can be investigated.
3. The finite element model with different accuracy may be used to estimate heat losses. However, the numerical examples are limited because real heating pipes are placed in underground culverts.

Acknowledgement
Financial support for this investigation by the Nordic Energy Research Programme is gratefully acknowledged.

REFERENCES

[1] S. Moaveni,. *Finite Element Analysis: Theory and Application with ANSYS*. Prentice-Hall, (1999)

[2] K.N. Huebner, E.A**.** Thornton., *The Finite Element Method for Engineers*, John Wiley and Sons, New York, (1982)

[3] G.E. Schneider, An Investigation into the Heat Loss Characteristics of Buried Pipes. *Journal of Heat Transfer Vol. 107, Translation of the ASME***,** pp. 696-699, (1985)

[4] E. Jonson, *Heat Losses from district heating system in small areas - Influence of pipe geometry and dimension* Lund Institute of Technology, Dept. of Heat and Power Engineering, Thesis for the degree of Licentiate of Engineering, (2001)

[5] B. Bohm, On transient heat losses from buried district heating pipes. *International Journal of Energy Research, 24*, pages 1311-1334, (2000).

[6] ANSYS. Theory Reference. Elements Reference Release 5.4. 1997 SAS IP, Inc.©

Finite element simulation of nonlinear moisture flow in orthotropic wooden materials

John Eriksson, Sigurdur Ormarsson and Hans Petersson
Department of Structural Mechanics
Chalmers University of Technology, Göteborg, Sweden
e–mail: johne@sm.chalmers.se

ABSTRACT

Introduction
Wood is a complex and moisture-sensitive material. This often causes problems in industry. In the sawmill industry, for example, moisture-related warping of sawn timber during drying is a serious problem. Accordingly, in analysing distortion of timber boards or of wood products such as doors, window frames, and the like it is of substantial interest to have through knowledge of the distribution of the moisture content (MC) and of its variation over time. Simulations here need to take account of the fibre orientation, the orthotropy of the wood and variations in the material parameters as a function of moisture and temperature. This suggests use of full 3D non-linear diffusion model for analysing the moisture flow below the saturation point. Figure 1 shows the material directions **l**, **r**, **t** in wood. Most of simulation tools currently available are based on calculations of average MC or of one-dimensional moisture flow [1]. The influence of temperature, although it can be important, is not studied here.

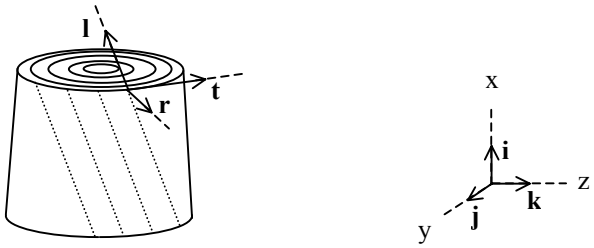

Figure 1. The local and the global coordinate systems.

Theory
The non-linear diffusion equation for the moisture content w can be written as [2]

$$\frac{\partial w}{\partial t} = \mathrm{div}(\mathbf{D}_w(w)\nabla w) + Q \tag{1.1}$$

where the source term Q, or the general moisture rate per unit volume and second, is added to the equation. ∇w is the moisture gradient vector and $\mathbf{D}_w$ the diffusivity matrix. For anisotropic material the matrix $\mathbf{D}_w$ generally has nine independent coefficients. In this study, the wood involved is assumed to be an orthotropic material and the $\mathbf{D}_w$ matrix to be given by

$$\overline{\mathbf{D}}_w(w) = \begin{bmatrix} D_l(w) & 0 & 0 \\ 0 & D_r(w) & 0 \\ 0 & 0 & D_t(w) \end{bmatrix} \tag{1.2}$$

where the subscripts l, r and t stand for the longitudinal, radial and tangential directions, respectively.
The constitutive equation for moisture flow below the fibre saturation point is

$$\mathbf{q} = -\mathbf{D}_w(w)\nabla w \tag{1.3}$$

where **q** is the moisture flux vector. The amount of moisture passing through a unit surface area per unit of time is denoted as $q_n = \mathbf{q}^T\mathbf{n}$, where **n** is the outward normal to the surface, see [3] for details. The transformation between the orthotropic directions and the global coordinate system is given by

$$\begin{bmatrix}\mathbf{l}\\ \mathbf{r}\\ \mathbf{t}\end{bmatrix} = \mathbf{A}^T\begin{bmatrix}\mathbf{i}\\ \mathbf{j}\\ \mathbf{k}\end{bmatrix} \tag{1.4}$$

where **l**, **r**, **t** and **i**, **j**, **k** are the unit vectors along the axes of the local and the global coordinate systems, respectively. The transformation matrix **A** consists of nine direction cosines that take into account the effect of annual rings, spiral grain and the conicity of the log [4]. When the flow and the moisture gradient vectors are transformed to the local coordinate system, the following relationship is obtained:

$$\overline{\mathbf{q}} = \mathbf{A}^T\mathbf{q} \tag{1.5}$$

$$\overline{\nabla}\overline{w} = \mathbf{A}^T\nabla w \tag{1.6}$$

Combining Eqs. (1.3)–(1.6) yields to the relationship between the global and the local diffusivity matrix.

$$\mathbf{D}_w(w) = \mathbf{A}\overline{\mathbf{D}}_w(w)\mathbf{A}^T \tag{1.7}$$

The moisture content can be approximated by $w(x,y,z,t)=\mathbf{N}(x,y,z)\cdot\mathbf{a}(t)$ where **a** is a vector containing all the moisture values at the nodal points and $\dot{\mathbf{a}}$ is the time derivative of the vector **a**. Multiplying Eq. (1.1) by a weight-function vector chosen according to the Galerkin method, and then integrating and applying the Green-Gauss theorem yields

$$\left(\int_V \mathbf{B}^T\mathbf{D}_w(w)\mathbf{B}dV\right)\mathbf{a} = -\int_S \mathbf{N}^T\mathbf{q}^T\mathbf{n}dS + \int_V \mathbf{N}^T Q dV - \left(\int_V \mathbf{N}^T\mathbf{N}dV\right)\dot{\mathbf{a}} \tag{1.8}$$

The matrix **N** contains the global shape functions for the moisture content, and **B** is given by $\mathbf{B} = \nabla\mathbf{N}$. V and S refer to the volume and the boundary surface, respectively, of the body in question. Equation (1.8) can in brief form be written as

$$\mathbf{K}\mathbf{a} + \mathbf{C}\dot{\mathbf{a}} = \mathbf{f} \tag{1.9}$$

If convection at the boundary is considered in Eq. (1.8), **K** and **f** need to be modified. The flux there can be expressed by the convection boundary condition $q_n = \alpha(w - w_\infty)$, where α is a convection coefficient dependent on a variety of conditions. The terms to be added due to the convection condition are $\mathbf{K}_c = \int_{S_c}\alpha\mathbf{N}^T\mathbf{N}dS$ and $\mathbf{f}_c = w_\infty\int_{S_c}\alpha\mathbf{N}^T dS$, see [3]. Thus, Eq. (1.8) can be modified to

$$(\mathbf{K} + \mathbf{K}_c)\mathbf{a} + \mathbf{C}\dot{\mathbf{a}} = \mathbf{f} + \mathbf{f}_c \tag{1.10}$$

The method chosen to solve the equation system (1.9) or (1.10) is a standard finite difference scheme. The time domain is divided up by different time points t_1, t_2, t_3, …,t_n, on the time axis. Various types of finite difference schemes with differing characteristics can be obtained, considering either Eq. (1.8) or Eq. (1.10) at time $t = t_n + \beta\Delta t_n$ and choosing the parameter β so that $1 \geq \beta \geq 0$. The moisture at time step n+1 is denoted as $\mathbf{a}^{n+1}$ and, if the moisture at step n denoted $\mathbf{a}^n$ is known, can be found according to [5] or [6] as

$$\left(\frac{\mathbf{C}}{\Delta t} + \beta\mathbf{K}\right)\mathbf{a}^{n+1} = \left[\frac{\mathbf{C}}{\Delta t} - (1-\beta)\mathbf{K}\right]\mathbf{a}^n + (1-\beta)\mathbf{f}^n + \beta\mathbf{f}^{n+1} \tag{1.11}$$

In the examples given below $\beta = 0.5$ is selected which means that the scheme is unconditionally stable.

Implementation

Thus far, only 2D cases have been considered. Implementation is performed analogous with CALFEM, in a Matlab environment, using bilinear elements.

The annual rings of the sawn timber boards studied are represented as ellipses, see Fig.3. The shape of the ellipses can be described by γ, the ratio of a^r and b^r.

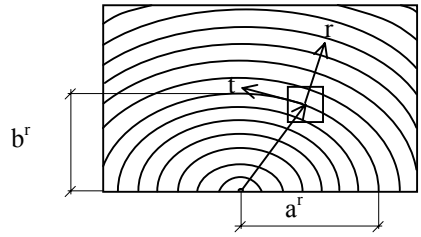

Figure 3. *Material direction model in 2D, pith location and the lengths* a^r *and* b^r *defining one annual ring.*

Verification example

Verification can be achieved by comparing a case of transient moisture flow with a known analytical solution. The case studied is a rectangle with a constant initial MC of 1 and a boundary MC of 0. The solution to this problem can be found by use of eigenfunctions. A check of the analytical solution by use of Parseval's identity was performed, see [7] for details. The material was assumed to be isotropic with a diffusivity of $7.78 \cdot 10^{-7}$, and the dimensions of the rectangle were taken to be 0.1x0.05. A MC-profile at y = 0.025, t = 150 (Δt = 0.5) shows convergence with the FE solution, see Fig.4.

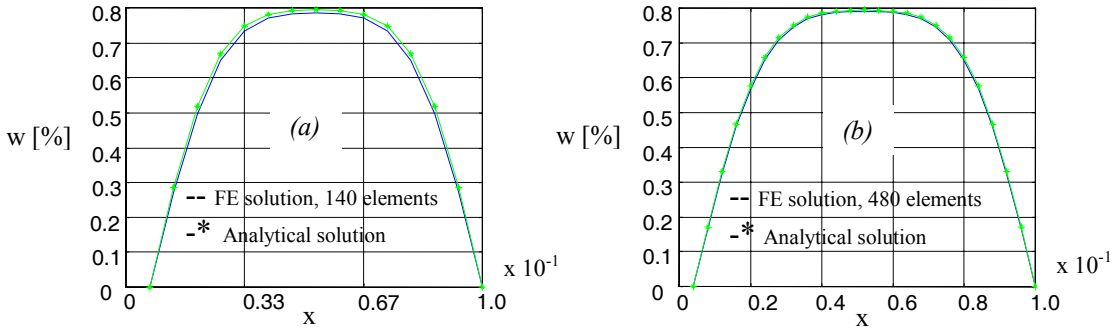

Figure 4. *Analytical and FE solution of a transient moisture flow problem, (a) 140 elements (b) 480 elements.*

Comparison for a 2D example of solutions using linear versus nonlinear diffusion coefficients.

The case studied was a 100x50 mm^2 board with the diffusion coefficients [1] shown in Fig.5. The boundary condition was set to an MC of 8% and the initial condition to an MC of 27%.

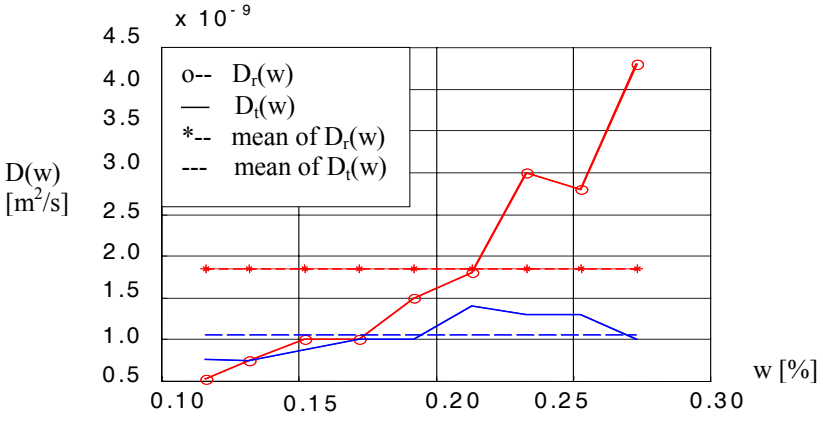

Figure 5. *Influence of moisture content on the diffusion coefficients.*

For the MC range for which no measured data were available, a least square extrapolation fit was performed. The influence of pith location was also studied, the MC of two different boards dried in the same manner and equal in their material parameters but with differing pith locations being compared.

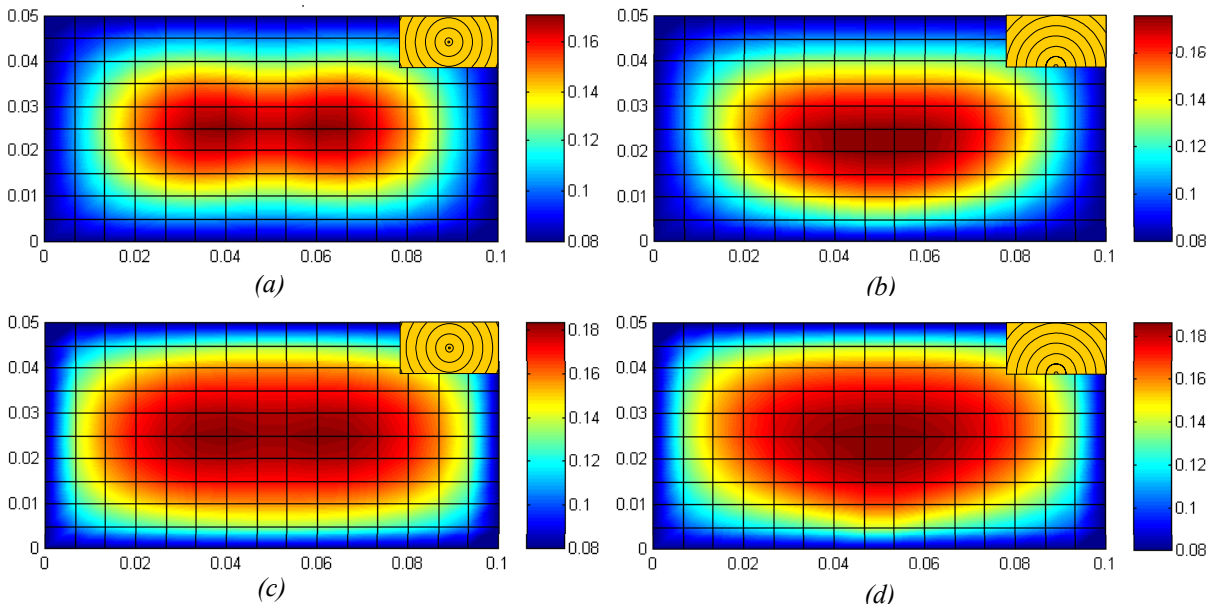

Figure 6. *Moisture content of boards subjected to a sudden drop in boundary MC and dried for 39 hours*
(a) Linear coefficients and pith in the middle of the cross-section
(b) Linear coefficients and pith at the centre of the lowest edge
(c) Nonlinear coefficients and pith in the middle of the cross-section
(d) Nonlinear coefficients and pith at the centre of the lowest edge.

In the simulations presented, circular annual rings were assumed ($\gamma = 1$). The results shown in Fig.*6(a)-(d)* indicate pith position to be of importance for the MC profile and nonlinearity to affect the MC profile considerably. Table 1 summarises the results of the simulations performed.
When the MC of a node close to the boundary is plotted versus time for the four cases just considered, the node could be seen to dry faster at the beginning in cases *(c)* and *(d)* but to dry faster in cases *(a)* and *(b)* as time progresses. This result is expected on the basis of the variation in diffusivity parameters that is shown in Fig.5. If $\gamma = 0.5$, that is if the annual ring representation is elliptical and if all the other prerequisites are the same as in Fig.6*(c),* the average MC at time 39 hours increases, see Tab.1.

Table 1. *Average MC for two pith locations as solved using a linear and a nonlinear technique and an example of elliptical annual rings as solved by a linear technique (the boundary nodes not being considered in the average).*

Case	Fig.6*(a)*	Fig.6*(b)*	Fig.6*(c)*	Fig.6*(d)*	Fig.6*(a)* but $\gamma = 0.5$
Average MC [%]	12.8	13.2	15.2	15.2	13.8

REFERENCES

[1] Anders Rosenkilde. *Mätningar av fuktkvotsgradienter och ytfenomen vid virkestorkning*. Licentiate thesis, Report TRITA-BYMA 1996:1, Stockholm, Byggnadsmaterial KTH (1996).

[2] J. Arfvidsson, J. Claesson. *Isothermal moisture flow in building materials: modelling, measurements and calculations based on Kirchhoff's potential*. Building and environment 35 (2000) 519-536.

[3] N.S. Ottosen and H. Petersson. *Introduction to the Finite Element Method*. Prentice-Hall, New York, (1992).

[4] Sigurdur Ormarsson. *Numerical analysis of moisture-related distortions in sawn timber*. Doctoral thesis, Publication 99:7, Göteborg, Structural Mechanics, CTH (1999).

[5] Alf Samuelsson, Nils-Erik Wiberg. *Finite element method*. Studentliteratur, Lund, (1998).

[6] O.C.Zieniewicz, R.L.Taylor. *The finite element method.* volume 2, fifth edition, solid mechanics, pages 413-423. Butterworth Heinemann, (2000).

[7] Gunnar Sparr, Annika Sparr. *Kontinuerliga system*. Studentliteratur, Lund, (1999, 2000).

Coupled versus uncoupled heat and mass transfer in capillary-porous materials

Kristian Krabbenhoft[*,†] **and Lars Damkilde**[‡]

Department of Civil Engineering
Technical University of Denmark, Lyngby, Denmark
e–mail: [†]kk@byg.dtu.dk, [‡]ld@byg.dtu.dk

ABSTRACT

Summary The simultaneous transfer of heat and mass in capillary-porous materials can be described by three coupled differential equations with saturation, gas pressure, and temperature as variables. In this abstract it is demonstrated how, under certain circumstances, it is crucial to include these couplings for a satisfactory description of the overall behaviour of the system.

An accurate description of simultaneous heat and mass transfer in porous media is essential to a wide class of problems. These include industrial processes such as the drying of building materials, food stuffs, and other agricultural products. Other examples include concrete hardening, multiphase flow in soils, and pressure increases in concrete subjected to extreme conditions such as fire. Whereas heat and mass transfer as independent uncoupled phenomena can be described relatively easily, the complexity of the models grows significantly when the full coupling between moisture content, gas pressure, and temperature is taken into consideration.
In this work we use the model put forward by Whitaker [1]. Here a representative average volume of the porous medium in question is considered, see Figure 1. Starting from the microscopic balance equations these are then averaged over the representative volume. This yields a set of macroscopic conservation equations for the total water content (liquid and vapour), dry air, and enthalpy. These can be written as

Total water:

$$\frac{\partial}{\partial t}\left(\varepsilon_w \rho_w + \varepsilon_g \rho_v\right) + \nabla \cdot \left(\rho_w \boldsymbol{v}_w + \rho_v \boldsymbol{v}_v\right) = 0 \tag{1}$$

Enthalpy:

$$\rho C_p \frac{\partial T}{\partial t} + \left(\rho_w c_{pw} \boldsymbol{v}_w + \rho_g c_{pg} \boldsymbol{v}_g\right) \cdot \nabla T = \nabla \cdot \left(\mathsf{K}_{\text{eff}} \cdot \nabla T\right) - \Delta h_{\text{vap}} \left(\frac{\partial}{\partial t}\left(\varepsilon_w \rho_w\right) + \nabla \cdot \left(\rho_w \boldsymbol{v}_w\right)\right) \tag{2}$$

Dry air:

$$\frac{\partial}{\partial t}\left(\varepsilon_g \rho_a\right) + \nabla \cdot \left(\rho_a \boldsymbol{v}_a\right) = 0 \tag{3}$$

Here, subscripts $\alpha = w, g, v, a$ refer to liquid water, gas, vapour, and dry air respectively. ρ_α are the intrinsic phase average densities, $\boldsymbol{v}_\alpha$ the velocities, and ε_α are the volume fractions with $\varepsilon_w + \varepsilon_g = \varphi$ where φ is the porosity. As for the enthalpy conservation equation ρ is the average density, C_p the average specific heat, $c_{p\alpha}$ the specific heat of the different species, T the temperature, K_{eff} the effective conductivity, and Δh_{vap} the heat of evaporation. The liquid water and gas velocities are determined by Darcy's law

$$\boldsymbol{v}_w = -\frac{\mathsf{K}\mathsf{K}_{\text{rw}}}{\mu_{\text{w}}}\left(\nabla p - \nabla p_c\right), \qquad \boldsymbol{v}_g = -\frac{\mathsf{K}\mathsf{K}_{\text{rg}}}{\mu_{\text{g}}}\nabla p \tag{4}$$

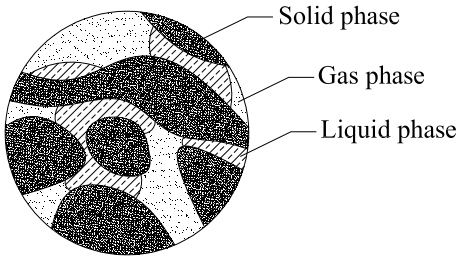

Figure 1: Averaging volume.

where the effective permeability matrices $\mathsf{KK}_{\mathrm{r}\alpha}$ are the product of the intrinsic permeability K, which depends only on the structure of the porous medium, and the relative permeabilities $\mathsf{K}_{\mathrm{r}\alpha}$ which depend on the saturation. Both K and $\mathsf{K}_{\mathrm{r}\alpha}$ are diagonal matrices. The viscosities are given by μ_α. The motion of the liquid water is due to gradients in the total liquid pressure, i.e. gradients in the difference between total gas pressure p and capillary pressure p_c, whereas gradients in total gas pressure alone results in motion of the gas species. Furthermore, following Fick's law for a binary mixture of gases (air and vapour) the relative average velocities of the these species are related to the average total gas species velocity as

$$\boldsymbol{\rho}_v \boldsymbol{v}_v = \rho_v \boldsymbol{v}_g - \rho_g \mathsf{D}_{\text{eff}} \nabla \left(\frac{\rho_v}{\rho_g} \right), \qquad \rho_a \boldsymbol{v}_a = \rho_a \boldsymbol{v}_g - \rho_g \mathsf{D}_{\text{eff}} \nabla \left(\frac{\rho_a}{\rho_g} \right) \tag{5}$$

The system is closed by the thermodynamic relations

$$p_a = \frac{\rho_a R T}{M_a}, \quad p_v = \frac{\rho_v R T}{M_w}, \quad p = p_a + p_v \tag{6}$$

and the equations of state

$$p_c = p_c(s, T), \qquad p_v = p_v(s, T) \tag{7}$$

where $s = \varepsilon_w / \varphi$ is the saturation. The capillary pressure-saturation curves are usually determined experimentally, but a good first guess can also be made on the basis of the structure of the porous medium. An example of this is wood which has a rather regular cell structure and where there is a good correlation between analytically and experimentally determined capillary pressure-saturation relations.

The three coupled conservation equations can be discretized in space by finite elements such that the following system of ordinary differential equations is obtained

$$\begin{bmatrix} \boldsymbol{C}_{ll} & \boldsymbol{C}_{le} & \boldsymbol{C}_{la} \\ \boldsymbol{C}_{el} & \boldsymbol{C}_{ee} & \boldsymbol{C}_{ea} \\ \boldsymbol{C}_{al} & \boldsymbol{C}_{ae} & \boldsymbol{C}_{aa} \end{bmatrix} \begin{bmatrix} \dot{\boldsymbol{s}} \\ \dot{\boldsymbol{p}} \\ \dot{\boldsymbol{T}} \end{bmatrix} + \begin{bmatrix} \boldsymbol{K}_{ll} & \boldsymbol{K}_{le} & \boldsymbol{K}_{la} \\ \boldsymbol{K}_{el} & \boldsymbol{K}_{ee} & \boldsymbol{K}_{ea} \\ \boldsymbol{K}_{al} & \boldsymbol{K}_{ae} & \boldsymbol{K}_{aa} \end{bmatrix} \begin{bmatrix} \boldsymbol{s} \\ \boldsymbol{T} \\ \boldsymbol{p} \end{bmatrix} = \begin{bmatrix} \boldsymbol{r}_l \\ \boldsymbol{r}_e \\ \boldsymbol{r}_a \end{bmatrix} \tag{8}$$

Here the subscripts l, e, and a refer to the physical quantities of liquid, enthalpy, and air respectively. As state variables we have used saturation, temperature, and total gas pressure, and the $\boldsymbol{C}$ and $\boldsymbol{K}$ matrices depend nonlinearly upon these state variables. For the time discretization Lee's three-level time stepping scheme is applied

$$\boldsymbol{x}^{n+1} = -\left(\boldsymbol{K}^n + \tfrac{3}{2\Delta t} \boldsymbol{C}^n \right)^{-1} \left(\boldsymbol{K}^n \boldsymbol{x}^n + \boldsymbol{K}^n \boldsymbol{x}^{n-1} - \tfrac{3}{2\Delta t} \boldsymbol{C}^n \boldsymbol{x}^{n-1} + 3\boldsymbol{r}^n \right) \tag{9}$$

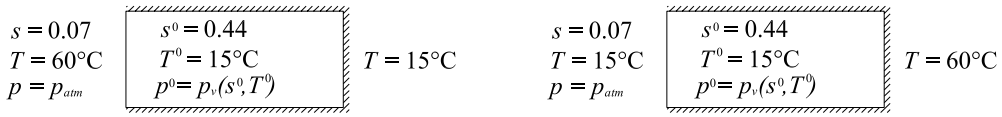

Figure 2: Drying configurations (a) and (b).

Next, an example concerning the drying of a 20 cm one-dimensional slab of softwood is given. Wood is a highly hygroscopic material and as such a complete analysis also needs to account for the transfer of bound water in the cell wall. In this case, however, we consider only the transfer of free water above the fiber saturation point. Two different configurations as shown in Figure 2 are considered. In (a) a temperature of $60°\mathrm{C}$ is maintained at the left end whereas the temperature at the right end is $15°\mathrm{C}$, and in (b) these boundary conditions are then reversed. The initial saturation is $s = 0.44$ corresponding to a moisture content of MC $= 90\%$. For the material values used in the simulations we refer to [2]. To illustrate the effect of the temperature gradients both a fully coupled and an uncoupled computation is performed for each configuration. In the uncoupled computation the transfer equations are still nonlinear in s, T, and p, but the changes in the individual physical quantities occur only as a result of gradients in these quantities. This means that e.g. flow of gas due to temperature gradients does not occur which under certain circumstances is a seriously flawed assumption.

The results of the computations for the two configurations are shown in Figure 3 (a) and (b). Several observations can be made. Whereas the uncoupled simulation for configuration (a) shows a more rapid drying than is the case with the use of the coupled transfer equations, the opposite is the case for configuration (b). Also, for the uncoupled simulation configuration (a) seems to be the most favourable, whereas the opposite is clearly the case for the coupled simulation. The explanation for these differences lies primarily in the equation of motion for the dry air species.

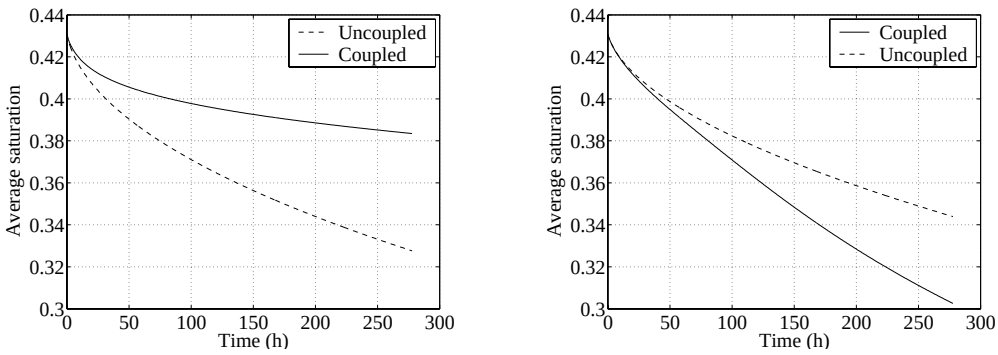

Figure 3: Results of drying simulation for configurations (a) and (b).

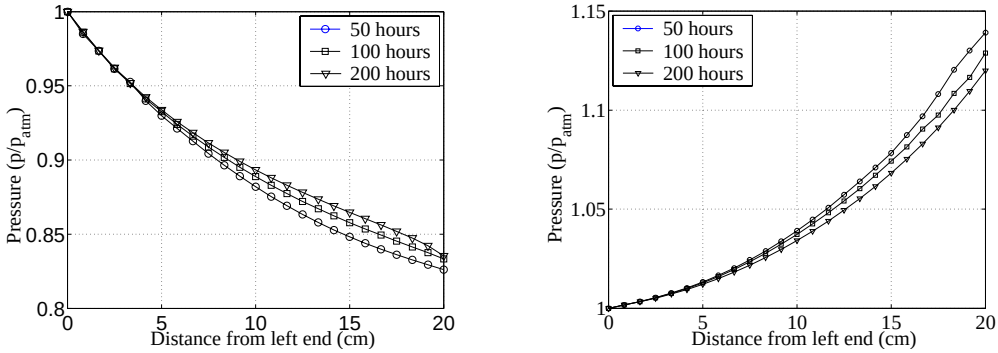

(a) (b)

Figure 4: Drying configurations (a) and (b).

Rewriting (5) in terms of pressures, we have

$$\begin{aligned} \rho_a \boldsymbol{v}_a &= \frac{pM}{RT}\boldsymbol{v}_g - \frac{M_a M_w}{MRT}\mathsf{D}_{\text{eff}}\left(\frac{p_v}{p}\nabla p - \nabla p_v\right) \\ &\simeq -\left(\frac{pM}{RT}\frac{\mathsf{K}\mathsf{K}_{\text{rg}}}{\mu_{\text{g}}} + \frac{M_a M_w}{MRT}\frac{p_v}{p}\mathsf{D}_{\text{eff}}\right)\nabla p + \frac{M_a M_w}{MTR}\left(\frac{\partial p_v}{\partial T}\right)\mathsf{D}_{\text{eff}}\nabla T \end{aligned} \tag{10}$$

Here we have used the fact that $\partial p_v/\partial s \simeq 0$. Equation (10) expresses the fact that flow of air is owed to both pressure and temperature gradients, and in such a way the transfer will occur towards decreasing pressures and increasing temperatures. For configuration (a) the temperature gradients will cause a transport of air out of the slab and the resulting under-pressure shown in Figure 4 (a) is obviously quite unfavourable. For configuration (b) the situation is the opposite. Here an over-pressure develops at the right end, see Figure 4 (b), which has a positive effect both regarding the transport of water and gas. As for the uncoupled problems, the flow of gas is independent of the temperature distribution and the large under-pressure in case (a) never occurs. Similarly, the pressures in case (b) are also moderate. The result is two quite similar drying histories with case (a) being slightly more rapid since heat is here supplied at the left end of the slab where the bulk of the evaporation takes place.

The conclusions are as follows. In drying processes with considerable temperature variations the coupling between gas pressure and temperature can influence the results significantly, and as shown through an example it is not possible to make any general statements of whether this influence will increase or reduce the computed drying times.

REFERENCES

[1] S. Whitaker. Simultaneous heat, mass, and momentum transfer in porous media: A theory of drying. *Advances in Heat Transfer*, **13**, 119–203, (1977).

[2] P. Perré and I. W. Turner. TransPore: A generic heat and mass transfer computational model for understanding and visualising the drying of porous media. *Drying Technology*, **17**(7&8), 1273–1289, (1999).

A concrete material model for impact loading conditions

M. Polanco-Loria
Department of Fracture Mechanics and Materials Testing
SINTEF, Materials Technology, Trondheim, Norway
e–mail: mario.polanco@matek.sintef.no

O. S. Hopperstad and T. Børvik
Department of Structural Engineering
Norwegian University of Science and Technology, Trondheim, Norway

ABSTRACT

Summary This paper describes a new concrete material model specially developed to handle impact loading situations. The main feature of this model is the simplicity to include pressure sensitivity, strain rate dependency and damage behaviour effects characteristics of concrete materials. Based on the numerical predictions so far, this model represents a good compromise between simplicity and accuracy for large-scale numerical analysis of structures under impact loading.

INTRODUCTION

It is well known that concrete exhibits a rate-dependent behaviour when subjected to high rate straining, with significant increase of dynamic strength. This particular behaviour is rather important under impulsive loading, as it occurs when structures are subjected to impacts or explosions (e.g. strain rates $\dot{\varepsilon} > 1\ s^{-1}$). For these strain rates dynamic strength can be enhanced, with respect to the static one, up to at least 80 % in tension and 25 % in compression.

On the other hand, under a multiaxial state of stress the damage mechanisms activated are highly dependent on the loading path. Mazars [1] proposes an interesting classification to illustrate which are the main damage modes involved depending on the loading state as shown in Table 1. The complexity of a numerical model will depend on the objectives to simulate the basic mechanism involved in a certain type of problems or in the generality to consider all types of loading. In particular, for impact and penetration problems these three mechanisms: cracking, shearing and compaction are present at the same time, see Fig. 1. In addition, the modelling complexity is increased because strain rate effects (different for each mechanism) should be included.

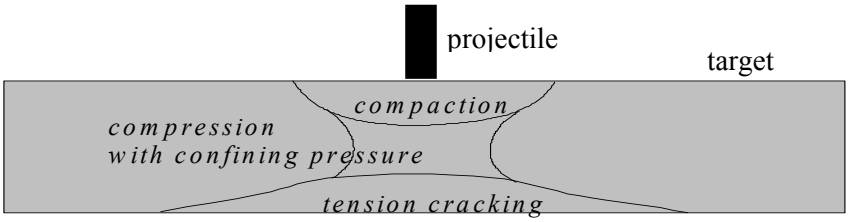

Fig. 1 Mechanisms activated during impact

Table 1 Main damage mechanisms

Type of loading	Particularity	Local damage mode	loading examples
A: tension and compression (low lateral pressure) • uniaxial • biaxial • triaxial	extensions brittle/softening behaviour	cracking mode I and mode I+II (debonding+branching)	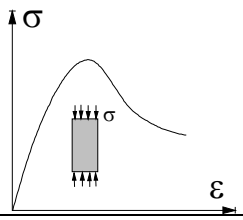
B: compression, moderate-high lateral pressure • triaxial	no extension "ductile" behaviour	cracking mainly in mode II and III (branching)	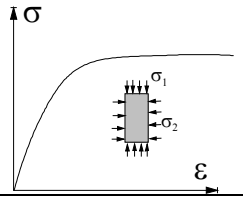
C: hydrostatic pressure in compression • triaxial	no extension hardening and stiffening	consolidation of the microporous structure	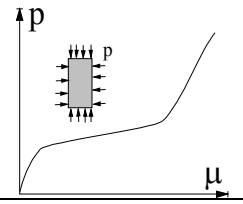

Based on these arguments this paper introduces a new concrete material model representing a nice compromise between simplicity and accuracy for concrete structures exposed, in particular, to impact loading conditions.

THE CONCRETE MODEL

The concrete model proposed [2] is an enhanced version of the original model of Holmquist et al. [3] and it uses a factorised formulation as follows:

$$\sigma_{eq}^{*} = F_{pressure}\, F_{rate}\, F_{J3} \tag{1}$$

In particular, for the pressure sensitivity the proposal consists of working with one simple continuous function defined as:

$$F_{pressure} = B\, \left\{P^{*} + T^{*}(1-D)\right\}^{N} \tag{2}$$

The material parameters B, T^{*} and N are calibrated from classical results from the literature. The rate sensitivity adopts the formulation proposed by Camacho and Ortiz [4] and largely used by Borvik for metals [5]:

$$F_{rate} = \left[1 + \dot{\varepsilon}^{*}\right]^{C} \tag{3}$$

Finally, a reduction of the shear strength on the compressive meridian can be considered by introducing an elliptic function F_{J3} depending on the deviatoric polar angle θ and the normalized out-of-roundness parameter, e, as proposed by Willam and Warnke [6] defined as:

$$F_{J3} = \frac{2(1-e^2)\cos\theta + (2e-1)\left[4(1-e^2)\cos^2\theta + 5e^2 - 4e\right]^{1/2}}{4(1-e^2)\cos^2\theta + (1-2e)^2} \quad (4)$$

The damage behaviour is treated separately according to each mechanism. For this purpose, three damage internal variables: D_T, D_S and D_C, representing the brittle, shear and compaction damage, respectively, are introduced.

Tensile damage

$$D_T = \begin{cases} 0 & \text{if} \quad P^* > -T^*(1-D) \\ 1 & \text{if} \quad P^* \le -T^*(1-D) \end{cases} \quad (5)$$

Shear damage

$$D_S = \sum \frac{\Delta\varepsilon_{eff}^p}{\varepsilon_p^f} \quad (6)$$

Pore compaction

$$D_C = \sum \frac{\Delta\mu^p}{\mu_{lock}} \quad (7)$$

Total damage

$$D = Max\left(D_T, \sqrt{\frac{D_S^2 + D_C^2}{|D_S + D_C|}}\right) \quad (8)$$

NUMERICAL SIMULATION OF A PENETRATION PROBLEM

The penetration computations are based on a test performed by Hanchak et al. [7] where a square reinforced concrete plate of 610x610x178 mm was impacted. Three layers of square-pattern reinforcement steel rods with a diameter of 5.6 mm were used. The uniaxial compressive and tensile strength of the concrete was $f_c = 48$ MPa and $f_t = 4$ MPa, respectively. In addition to the pressure-compaction curves, triaxial tests were performed under various confining pressure levels so that shear strength-pressure curves could be established.

A 30-mm, smooth-bore powder gun was used to launch a 0.50 kg ogival-nose steel projectiles with a length of 143.7 mm and a diameter of 25.4 mm. The striking velocity was 434 m/s. 2D axisymmetric elements were used in the computations. In total 5000 elements were used. The erosion element option of LS-DYNA was adopted in the numerical calculations. The numerical model predicts a residual velocity of 205 m/s, which compares fairly well with the experimental residual velocity of 214 m/s reported by Hanchack, see Fig. 2. Consequently, the present model represents a good compromise between simplicity and accuracy for large-scale numerical analysis of structures under impact loading. However, further numerical validation tests are still needed.

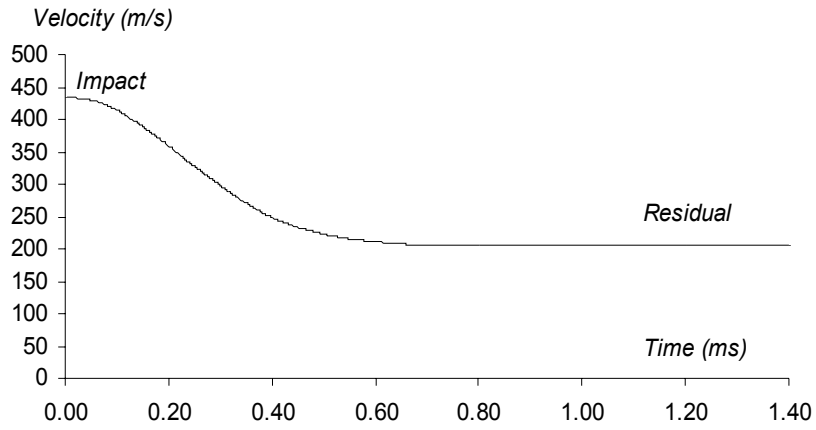

Fig. 2 Residual velocity of the projectile after perforation

ACKNOWLEDGMENTS

The authors gratefully acknowledge Dr. T. Berstad at Livermore Software Technology Corporation for the numerical implementation of the present model in LS-DYNA.

REFERENCES

[1] Mazars J. (1984) "Application de la mecanique de l'endommagement au comportement nonlineaire et la rupture du beton de structure" These de Doctorate d'Etat, LMT, Universite de Paris, France.

[2] Polanco-Loria M. (2001) "Improvements to the HJC concrete model in LS_DYNA" SINTEF report STF24 F01286, Trondheim, Norway.

[3] Holmquist T.J., Johnson G.R. and Cook W.H. (1993) "A computational constitutive model for concrete subjected to large strains, high strain rates and high pressures" Proceedings of 14th International Symposium on Ballistics, Quebec, Canada.

[4] Camacho G.T. and Ortiz M. (1997) "Adaptive Lagrangian modelling of ballistic penetration of metallic targets" Computer Methods in Applied Mechanics and Engineering, Vol. 142, pp. 269-301.

[5] Børvik T. (2000) "Ballistic penetration and perforation of steel plates" Ph.D. Dissertation, The Norwegian University of Science and Technology, Norway.

[6] Willam K.J. and Warnke E.P. (1975) "Constitutive model for the triaxial behaviour of concrete" International Association of Bridges and Structural Engineers, seminar on concrete structures subjected to triaxial stresses, IABSE Proc. 19, Italy.

[7] Hanchak S.J., Forrestal M.J., Young E.R. and Ehrgott J.Q. (1992) "Perforation of concrete slabs with 48 MPa and 140 MPa unconfined compressive strengths" International Journal of Impact Engineering, vol. 12, no. 1, pp. 1-7.

CONTACT MECHANICAL APPROACH TO DETERMINE ELASTIC MODULI OF PAPER ROLLS

K. Ärölä* and R. von Hertzen
Department of Mechanical Engineering
Helsinki University of Technology, Espoo, Finland
e–mail: kilwa.arola@hut.fi, rvhertz@csc.fi

M. Jorkama
Metso Paper Inc., Järvenpää, Finland
e–mail: marko.jorkama@metso.com

ABSTRACT

Summary A wound roll of paper is loaded against a nip roller and the measured values of the nip width and the roll indentation are compared with the corresponding calculated values. The numerical problem is solved using the Finite Element Method in conjunction with the Panagiotopoulos process. A suitable form of the incremental stress-strain relation will be discussed. A least squares fit to the experimental results is used to determine values for the paper roll elastic moduli.

INTRODUCTION

Winding a flexible web into a compact roll is a widely used process for materials such as paper, thin films and magnetic tapes. By the aid of winding models [1,2] one can analyse the internal stress state of the roll, which is an important part of the defect free roll structure design. Winding models can predict several roll defects directly, and will help to understand many others.

Every winding model needs a proper constitutive law for the material wound and numerical values for the material parameters. The earliest models were based on the assumption that the wound roll could be treated as a linear, plane strain and orthotropic medium. Later the radial modulus of a wound roll was modeled as a nonlinear function of the radial stress or strain [3] and also viscoelastic effects were accounted for [4]. A common feature of modern winding is the presence of a nip in the winding path. It should be noted that the nip-induced stresses destroy the rotational symmetry of the stress field of the wound roll. Therefore, shear stresses are generated into the roll. Since the conventional models concentrate solely on cases with rotational symmetry, the information on elastic constants in the literature is restricted to the tangential and radial moduli. However, there is an increasing interest and need for models of winding with a nip so that the values of the shear moduli and Poisson's ratios also become important. It has been shown recently, in particular, that the value of the shear modulus of the roll may have a marked effect on the nip width [2].

The aim of the present work is to present a method for the determination of the elastic moduli of the roll by comparing the results of roll compression tests with those of a nonlinear FE-model in the sense of a least squares fit.

THEORY

The basic contact configuration of a paper roll and a nip roller is shown in Figure 1, which shows the wound roll pressed against the steel drum.

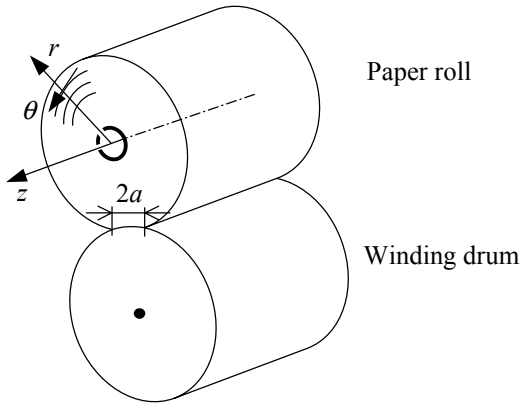

Figure 1. Nip contact configuration and the coordinate system used.

Let us consider first a general stress-strain relation of an orthotropic nonlinearly elastic material. In a plane strain state, some distance away from the roll ends, the incremental constitutive equation in the principal directions of the material can be written as

$$\begin{bmatrix} \Delta\sigma_r \\ \Delta\sigma_\theta \\ \Delta\tau_{r\theta} \end{bmatrix} = \begin{bmatrix} E_{rr} & E_{r\theta} & 0 \\ E_{\theta r} & E_{\theta\theta} & 0 \\ 0 & 0 & G_{r\theta} \end{bmatrix} \begin{bmatrix} \Delta\varepsilon_r \\ \Delta\varepsilon_\theta \\ \Delta\gamma_{r\theta} \end{bmatrix}. \qquad (1)$$

In general, all the coefficients E_{rr}, $E_{r\theta}$, $E_{\theta r}$, $E_{\theta\theta}$ and $G_{r\theta}$ may depend on the strain components ε_r, ε_θ and $\gamma_{r\theta}$. For a hyperelastic material one can derive the stresses from an elastic potential function so that $E_{r\theta} = E_{\theta r}$. One may ask, of what form are the terms E_{rr}, $E_{r\theta}$, $E_{\theta r}$, $E_{\theta\theta}$ and $G_{r\theta}$ in the case of a paper roll? No general answer exists so far. Pfeiffer, for example, suggests [5] the relations

$$E_{rr} = K_1 K_2 \, e^{-K_2 \varepsilon_r} = K_2 (K_1 - \sigma_r) \qquad (2)$$

$$E_{r\theta} \approx E_{\theta r} \approx 0 \,. \qquad (3)$$

Instead of equation (2) Hakiel prefers the relation [1]

$$E_{rr} = c_0 + c_1 \sigma_r + c_2 \sigma_r^{\,2} \,. \qquad (4)$$

In the present work we consider the parameters $E_{\theta\theta}$, $E_{r\theta}$ and $G_{r\theta}$ as constants and employ equation (2) for the radial modulus.

Our numerical solution of the compression experiment consists of two main steps as described below:

- The elastic solution, i.e. the flexural matrix for the discretized contact surface is calculated using FEM.
- The contact stress distributions are calculated using the Panagiotopoulos iteration utilizing the flexural matrix.

The winding steel drum can be considered as rigid when compared to the paper roll. The finite element mesh of the roll cross section is shown in Figure 2. The calculated contact pressures are used to update the stress and strain state of the material and a new elastic solution is sought. This process is repeated until a prescribed accuracy in the contact force distribution is obtained.

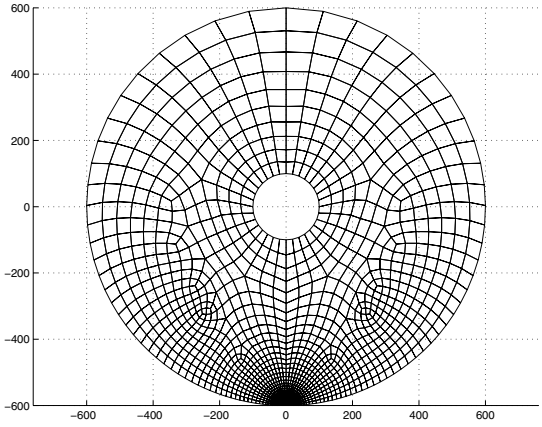

Figure 2. Cross section of the paper roll meshed with four node quadrilateral elements.

Typically six or seven material iterations are needed to reach a relative change ≤ 10^{-6} of forces in successive iterations. Note that a wound roll represents a strongly pre-stressed body of material. Therefore, it is important to account for the initial strains in the solution procedure. If the wound-in-tension history of a roll is known, one can account for the initial strains of a finished axisymmetric roll using Hakiel's model; otherwise, experimentally determined (pull tab) values must be used.

Calculations show that the value of $E_{r\theta}$ has practically no effect, whereas $G_{r\theta}$ has a significant effect on the contact width and indentation depth. Hence, it is evident that the value of $G_{r\theta}$ can be determined by a least squares fitting to measured data. The residual error to be minimized is

$$e = \sum_{i=1}^{N} \left\{ \left[a_i - a(G_{r\theta}; P_i) \right]^2 + \left[\delta_i - \delta(G_{r\theta}; P_i) \right]^2 \right\} \tag{5}$$

or

$$e = \sum_{i=1}^{N} \left\{ \left[P_i - P(G_{r\theta}; a_i) \right]^2 + \left[\delta_i - \delta(G_{r\theta}; a_i) \right]^2 \right\}. \tag{6}$$

Here a_i and δ_i denote the measured values of the nip half-width and the roll indentation, respectively, for the line loads P_i ($i = 1,\ldots,N$) used in the compression experiment, whereas

$a(G_{r\theta}; P_i)$ and $\delta(G_{r\theta}; P_i)$ denote the corresponding numerically computed values. Note that in place of $G_{r\theta}$ in eqs (5) and (6) there may be several unknown elastic parameters. In practice, however, the computational cost may be reduced by taking the values of K_1 and K_2 from a stack test and the value of $E_{\theta\theta}$ from a machine direction tensile test.

EXPERIMENTAL SETUP

The experimental setup resembles the configuration shown in Figure 1. A paper roll of radius R_1 rests on a nip roller of radius R_2. A compressive load is applied from the core chucks to the roll. The resulting nip load P is calculated from the roll weight and the core load. The distance x of the roll top from a fixed point is measured with a high precision laser sensor (resolution < 10 μm). It is assumed that the nip and core loads do not cause any significant deformation at the roll top. Hence, the nip compression can be calculated from the measured value of x. The nip width was measured using the Pressurex Micro Film. The smallest measurable pressure with this film is 13.8 kPa and, hence, also the nip edges could be quite accurately detected. The evenness of the nip distribution was checked by measuring the nip width from three locations of the roll: both edges and the center. The initial internal pressure distribution of the roll was estimated by pull tab measurements. The total number of pull tabs was 10. Near the roll periphery the internal pressure was measured at 50 mm spacings. The nip roller diameter was 0.425 m and the roll diameter 1 m.

CONCLUSIONS

An indirect method for determining the values of elastic moduli of a paper roll is presented. In particular, the value of the shear moduli $G_{r\theta}$ is rarely reported in existing literature, and yet it is an important parameter in modern winding models including the nip action. The present method can in principle be utilized in an automated on-line measurement system.

REFERENCES

[1] Z. Hakiel. Nonlinear Model for Wound Roll Stress. *TAPPI Paper Finishing and Converting Conference Proceedings,* pages 9-15, (1986).

[2] M. Jorkama. Contact Mechanical Model for Winding Nip. *Acta Polytechnica Scandinavica*, **Me 146**, (2001).

[3] J.D. Pfeiffer. Prediction of Roll Defects from Roll Structure Formulas. *TAPPI Journal*, **62**, No. 10, pages 83-88, (1979).

[4] W.R. Qualls, and J.K. Good. An Orthotropic Viscoelastic Winding Model Including a Nonlinear Radial Stiffness. *Journal of Applied Mechanics*, **64**, pages 201-208, (1997).

[5] J.D. Pfeiffer. Measurement of the K2 Factor for Paper. *TAPPI Journal*, **64**, No. 4, pages 105-106, (1981).

Truss Optimization with constraints on eigenfrequencies, displacements, stresses and buckling.

Niels L. Pedersen* and Anders K. Nielsen
Department of Mechanical Engineering, Solid Mechanics
Technical University of Denmark
Nils Koppels Allé, Building 404, DK–2800 Kgs. Lyngby, Denmark
email: nlp@mek.dtu.dk

ABSTRACT

Summary We consider general 3D truss structures. The design variables are the cross–sections of the truss bars together with the joint coordinates and these design variables are considered to be continuos variables. Using the design variables we will simultaneously do size optimization (areas) and shape optimization (joint positions). The structures are subjected to multiple load cases and the objective of the optimizations is minimum mass with constraints on eigenfrequencies (possible multiple), displacements and stresses.

1. Introduction

Optimization of trusses using numerical methods has been an active area of research since it was initiated by the work of [2] and of [3]. In the paper [5] it was shown that we have the possibility of simultaneously using the area of the cross section of the bar and the joint coordinates as the design variables. A large number of papers have been published in the area of truss optimization, for a review see [1] and references therein. There is however a very limited amount of papers dealing with the introduction of constraints on eigenfrequencies in connection with the optimization of truss structures, but from a practical point of view it seems reasonable to include this. The introduction of constraints on eigenfrequencies also have the possibility of removing the degenerated structures you might find in optimization. The main contribution of the present paper is the inclusion of constraints on eigenfrequencies, in a general setting of truss optimization. In the following sections we give an outline, for a more thorough explanation see [7].

2. Stress Constraints

If a bar is in tension we have an simple constraint specifying that the stress ($\sigma > 0$) must be smaller than a stress related to the yield stress (σ_y).

$$\sigma \leq \sigma_y/\gamma \tag{1}$$

where γ is a safety factor. In compression we have a similar limit on the stress but we also want to avoid buckling in the slender members. To be able to make a more clear comparison between the optimized structures shown in the example and the actually used designs we will apply a stress constraint that is given by the Danish standards DS409,DS410 and DS412. In figure 1 we show the allowable compressive stress in bars for different profile types together with the allowable stress for the ideal truss.

$$\frac{d\omega^2}{dh} = \{\phi\}^T\left(\frac{d[S]}{dh} - \omega^2\frac{d[M]}{dh}\right)\{\phi\} \tag{2}$$

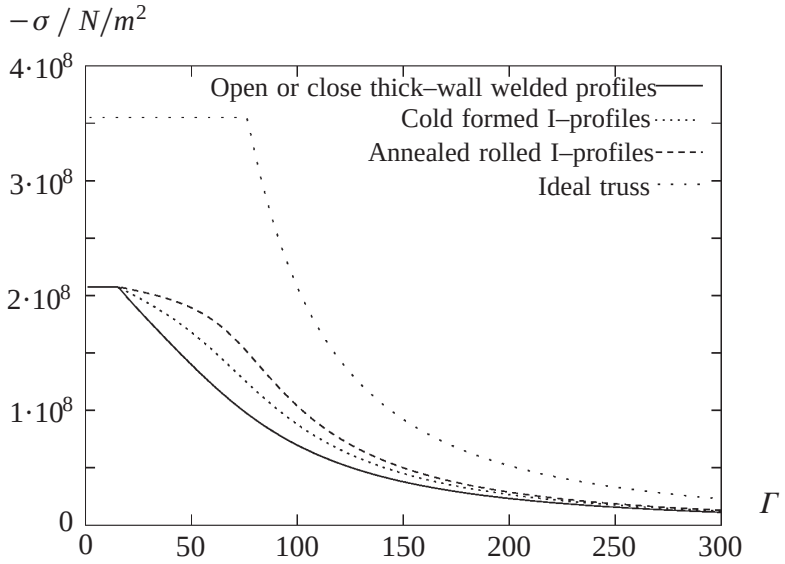

Figure 1. Allowable compressive stress in bars as a function of slenderness ratio, Γ , using DS409,410,412. (Steel S355, $\sigma_y = 3.55\ 10^8\ N/m^2$ $E = 2.1\ 10^{11}\ N/m^2$).

3 Sensitivities

When we are using SLP (Sequential Linear Programming). as the optimization method we need the sensitivities of the objective as well as of the constraints with respect to the design parameters. Most of the sensitivities can be found straight forward, see e.g. [4]. In the following we will only describe the sensitivities of eigen frequencies. If we have a distinct eigenpair, $(\omega^2, \{\phi\})$, then the sensitivity with respect to a design parameter, h , is given by

where $[M]$ is the mass matrix and $[S]$ is the stiffness matrix, and we have assumed the normalization of the eigenvector . If we have a multiple eigen frequency we can not use (2). The derivation below is primarily taken from [6]. We will assume that we have a double eigenfrequency with two corresponding eigenvectors, $(\omega^2, \{\phi\}_1, \{\phi\}_2)$. The derivations for higher order of multiplicity can be done in a similar way. We will again assume that the eigenvectors are normalized and that the two eigenvectors are orthogonal.

$$\{\phi\}_1^T[M]\{\phi\}_1 = 1 \quad \{\phi\}_2^T[M]\{\phi\}_2 = 1 \quad \{\phi\}_1^T[M]\{\phi\}_2 = 0 \tag{3}$$

The problem is that any linear combination of the two eigenvectors will also be an eigenvector with the same eigenfrequency.

$$\{\bar{\phi}\} = c_1\{\phi\}_1 + c_2\{\phi\}_2 \tag{4}$$

$$c_1^2 + c_2^2 = 1 \Rightarrow \{\bar{\phi}\}^T[M]\{\bar{\phi}\} = 1 \tag{5}$$

The sensitivity is therefore not only related to the change in the design space, given by the change in design parameter h , but also by the choice of the eigenvector. Only for two specific eigenvectors will the sensitivities have physical meaning. By inserting (4) in the sensitivity (2) we get

$$\frac{d\omega^2}{dh} = c_1^2 g_{11} + c_2^2 g_{22} + 2c_1c_2g_{12} \tag{6}$$

$$g_{nm} = \{\phi\}_n^T\left(\frac{d[S]}{dh} - \omega^2\frac{d[M]}{dh}\right)\{\phi\}_m \tag{7}$$

To find the extreme values of (6) we differentiate with respect to the two constants, c_1, c_2, and set this equal to zero.

$$\begin{bmatrix} g_{11} & g_{12} \\ g_{12} & g_{22} \end{bmatrix} \begin{Bmatrix} c_1 \\ c_2 \end{Bmatrix} = \begin{Bmatrix} 0 \\ 0 \end{Bmatrix} \tag{8}$$

We now solve the eigenvalue problem (8) and find the eigenpairs.

$$(g_a, \{c\}_a) \quad , \quad (g_b, \{c\}_b) \tag{9}$$

The physical sensitivities of the double eigenfrequency is given directly by g_a and g_b, and the corresponding eigenvectors are given by (4) with the constants taken from the vectors $\{c\}_a$ and $\{c\}_b$.

4 Example

In this example we will compare an optimized result to a real life application. In the spring of 2001 the national football stadium of Denmark was fitted with a roof. The size of the roof is $140\ m \times 95\ m$. The actual end beam used in the roof is shown in figure 2 and has a mass of 65 metric ton. The roof is supported at four points indicated by balls in figure 2.

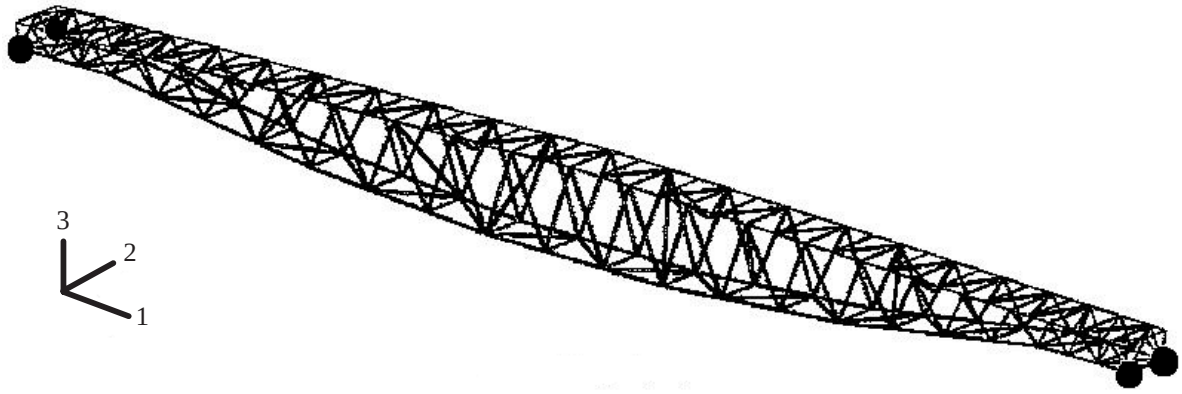

Figure 2. Original end beam of the folding roof, mass 65 metric ton.

To be able to compare the designs from optimization with the design in figure 2 we will constrain the optimization so that it will fulfill the same safety as specified by Danish standard (DS409–412). According to the standards we have six loads:

- Snow load, $\{F_s\}$ (900 N/m^2)
- self–weight, $\{F_g\}$
- Lift due to wind, $\{F_{wl}\}$ (wind speed 24 m/s)
- Downward force due to wind, $\{F_{wd}\}$
- Horizontal wind load, $\{F_w\}$
- Horizontal force, $\{F_c\}$ (3500 N/m)

From these loads we get three different load cases:

$$\text{Load case 1}: \{F_g\} + \{F_c\} + 1.5\{F_s\} + 0.5\{F_{wd}\} + 0.5\{F_w\}$$
$$\text{Load case 2}: \{F_g\} + \{F_c\} + 0.5\{F_s\} + 0.5\{F_{wd}\} + 1.5\{F_w\}$$
$$\text{Load case 3}: \{F_g\} + \{F_c\} + 1.5\{F_{wl}\} + 0.5\{F_w\}$$

The constraints on the eigenfrequency is that the first eigenfrequency should be greater than 1 *Hz*. At the same time we will apply the displacement constraint that the maximum deflection is 1/200

of the total span of the beam. Figure 3 shows the optimized structure, it should be noted that nodes which are loaded or constrained are not allowed to change position. From figure 3 we see that the design has changed compared to figure 2. The original beam had a maximum height of 6.75 m this is in the optimized design reduced to 5.85 m . At the same time the width of the lower flange is reduced from 3.40 m to 1.66 m . The objective (mass) of the optimization was reduced to 41.2 metric ton. For this example the constraints on displacement and eigenfrequency is not active so the design is fully controlled by the stress constraints.

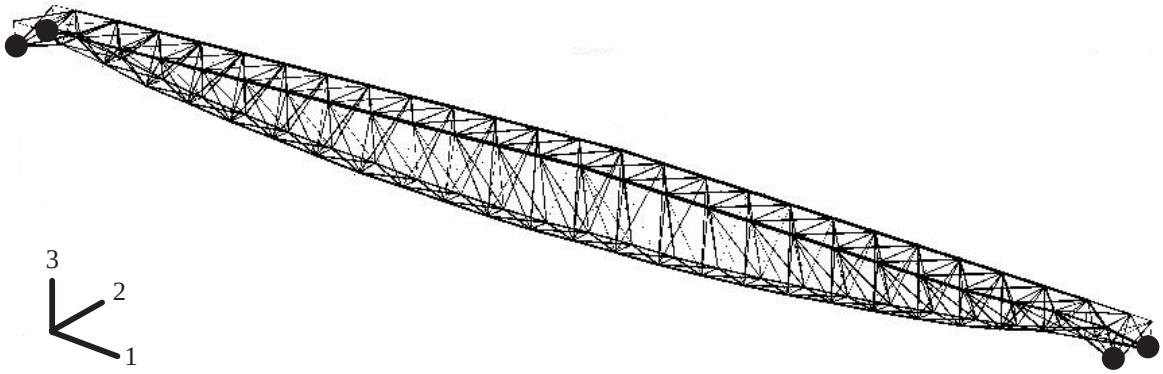

Figure 3. Optimized design of end beam, mass 41.2 metric ton.

Acknowledgments. The work of Niels L. Pedersen was supported by the Danish Technical Research Council through the THOR–programme (Technology for Highly Oriented Research): "Systematic design of MEMS". This support is highly appreciated.

REFERENCES

[1] Bendsøe, M. P., Ben–Tal, A. and Zowe, J. (1994) "Optimization methods for truss geometry and topology design". *Structural Optimization* **7**, 141–159

[2] Dorn, W., Gomery, R. and Greenberg, M. (1964) "Automatic design of optimal structures". *J. de Mecanique* **3**, 25–52

[3] Fleron, P. (1964) "The minimum weight of trusses". *Bygningsstatiske Meddelser* **35**, 81–96

[4] Nielsen, A. K. (2001) "Tredimensionale gitterkonstruktioner: optimering for minimum mass med restriktioner på dynamiske og statiske egenskaber". Master thesis, Department of Mechanical Engineering, Solid Mechanics, Technical University of Denmark, (In Danish)

[5] Pedersen, P. (1970) "On the minimum mass layout of trusses". *AGARD–CP–36–70*

[6] Pedersen, P. (1994) "Non–Conservative Dynamic Systems: Analysis, Sensitivity Analysis, Optimization". Lecture notes from IUTAM fifth summer school on mechanics, Concurrent Engineering Tools for Dynamic Analysis and Optimization, Aalborg University.

[7] Pedersen, N.L. and Nielsen, A.K. (2001) "Optimization of practical trusses with constraints on eigenfrequencies, displacements, stresses and buckling". (submitted)

On sensitivity computations of geometrically and materially non-linear structural response

Sami Pajunen
Department of Mechanical Engineering
Tampere University of Technology, Tampere, Finland
e–mail: sami@mohr.me.tut.fi

ABSTRACT

Summary In this study we consider the design sensitivity analysis of structures exhibiting large deflections. Based on governing FEM equilibrium equations and direct differentiation method, we derive both total and incremental sensitivity formulas for elastic and elasto-plastic responses, respectively.

Introduction

The design sensitivity analysis is an essential part of a general optimisation problem. A well-posed, standard-form optimisation problem can be solved using a suitable mathematical minimisation algorithm, whereas the data regarding the physical character of the problem is brought into the computation via requested function values and their derivatives with respect to design variables. In a general structural optimisation problem, the finite element method serves as a standard tool for evaluating the objective and constraint function values and their design derivatives.

In this study we concentrate on design sensitivity analysis of quasi-static structural systems that are discretised using the finite element method. We consider the displacement sensitivity both for large deflection problems as well as rate-independent elasto-plasticity. However, we restrict the discussion on problems that exhibit monotonically increasing unique load-deflection paths, i.e. we handle only structures that are not prone to buckling. As concluded in many research papers, see e.g. [1,2], the direct differentiation method (DDM) is superior to the adjoint system method, especially in elasto-plastic problems. Indeed, throughout this study also we use the DDM.

Displacement sensitivity

During the minimisation process, the design derivative $\mathrm{d}\mathbf{q}/\mathrm{d}\mathbf{x}$ of nodal displacements $\mathbf{q}$ with respect to design variables $\mathbf{x}$ at the final load level $\lambda_{k+1}\mathbf{p}_{\mathrm{ref}}$, say, is needed. Here $\mathbf{p}_{\mathrm{ref}}$ is the reference load vector, λ is the external load factor and the subscript denotes increment number. In the so called total sensitivity approach, the governing equilibrium equation

$$\mathbf{r}(\mathbf{q}) - \lambda\mathbf{p}_{\mathrm{ref}} = \mathbf{0} \tag{1}$$

is differentiated with respect to design variable vector $\mathbf{x}$ leading, after standard manipulation, to

$$\mathbf{K}_{\mathrm{T}}\frac{\mathrm{d}\mathbf{q}}{\mathrm{d}\mathbf{x}} = -\frac{\partial\mathbf{r}}{\partial\mathbf{x}}. \tag{2}$$

In above $\mathbf{r}$ is the internal nodal force vector and $\mathbf{K}_T$ is the tangent stiffness matrix.

After regular path continuation up to desired load level $\lambda_{k+1}\mathbf{p}_{ref}$, the design sensitivity can be obtained from (2) just by formulating the right-hand side of (2) for the used element type and adopting an already manipulated stiffness matrix $\mathbf{K}_T$. Thus, whenever the total sensitivity approach gives appropriate results, it should be adopted because of its low computational costs. Because the total sensitivity approach is based on differentiation of the equilibrium equation at fixed but arbitrary state, the obtained sensitivity equation (2) can not give accurate results if the nodal displacements are somehow history-dependent. For example, in elasto-plastic problems (2) must not be used.

Opposite to the total sensitivity scheme, path-dependent problems can be handled using an accumulated sensitivity approach that is incremental in nature. To begin with, we first write the equilibrium equation (1) in an incremental form as

$$\Delta\mathbf{r}_{k+1} = \lambda_{k+1}\mathbf{p}_{ref} - \mathbf{r}_k, \tag{3}$$

in which the right-hand side terms contain fixed values of external and internal force vectors at equilibrium states k and k+1 and the left-hand side term is due to the iteration process from equilibrium state k to k+1. Differentiation of (3) with respect to design variable vector $\mathbf{x}$ leads us, after some computations, to

$$\left(\mathbf{K}_T\right)_{k+1}\frac{d\Delta\mathbf{q}_{k+1}}{d\mathbf{x}} = -\left(\mathbf{K}_g\right)_{k+1}\frac{d\mathbf{q}_k}{d\mathbf{x}} - \int_V \mathbf{B}_{k+1}^T\frac{d\boldsymbol{\sigma}_k}{d\mathbf{x}}dV - \frac{\partial\mathbf{r}_{k+1}}{\partial\mathbf{x}}. \tag{4}$$

Using (4) it is straightforward to compute the required design derivative at equilibrium state k+1 as

$$\frac{d\mathbf{q}_{k+1}}{d\mathbf{x}} = \frac{d\mathbf{q}_k}{d\mathbf{x}} + \frac{d\Delta\mathbf{q}_{k+1}}{d\mathbf{x}}. \tag{5}$$

In (4) $\mathbf{K}_g$ is the geometric stiffness matrix , $\mathbf{B}$ is the kinematic matrix and $\boldsymbol{\sigma}$ is the vector of stresses. Compared to total sensitivity formula (2), one additional stress sensitivity term $d\boldsymbol{\sigma}/d\mathbf{x}$ is required in the incremental approach (4). Indeed, this single term contains all the information concerning the adopted constitutive model. Computation of this term during the elasto-plastic analysis can be briefly described as follows.

Stress sensitivity

Up to equilibrium state k the stress is updated as

$$\boldsymbol{\sigma}_k = \boldsymbol{\sigma}_{k-1} + \Delta\boldsymbol{\sigma}_k, \tag{6}$$

in which the increment $\Delta\boldsymbol{\sigma}_k$ is accumulated during the increment from equilibrium state k to k+1. Differentiation of (6) with respect to design variable vector $\mathbf{x}$ gives

$$\frac{d\boldsymbol{\sigma}_k}{d\mathbf{x}} = \frac{d\boldsymbol{\sigma}_{k-1}}{d\mathbf{x}} + \frac{d\Delta\boldsymbol{\sigma}_k}{d\mathbf{x}}, \tag{7}$$

in which the latter derivative is dependent on the used elasto-plastic stress updating algorithm. In the case of explicit time integration algorithm, the latter derivative can be written, after some manipulations, as

$$\frac{d\boldsymbol{\sigma}_k}{d\mathbf{x}} = \sum_{i=1}^{k}\mathbf{D}_i^{cont}\mathbf{B}_i\frac{d\Delta\mathbf{q}_i}{d\mathbf{x}}. \tag{8}$$

In (8) $\mathbf{D}^{\text{cont}}$ is the continuum elasto-plastic material stiffness matrix following from the explicit stress updating analysis. The formulas (4), (5) and (8) together serve as the so called incremental sensitivity algorithm.

Examples

At this point, we adopt two examples to present some typical results of non-linear response sensitivity. The first example, a two-bar truss [1] depicted in Figure 1, offers a highly suitable test for the accuracy of the sensitivity algorithms because the sensitivity of vertical displacement v of node 2 with respect to bar cross-sectional area $A = A_1 = A_2$ can be expressed for large displacements in closed form as

$$\frac{\mathrm{d}v}{\mathrm{d}A} = -\frac{v}{A}\,\frac{\frac{1}{2}v^2 + \frac{3}{2}Hv + H^2}{\frac{3}{2}v^2 + 3Hv + H^2}. \tag{9}$$

When deriving (9), a linear constitutive relationship between Green-Lagrangian (GL) strains and second Piola-Kirchhoff (PK) stresses is assumed. We test the total sensitivity approach (2) with fixed design variable values A_1 and A_2 and an increasing external load P as shown in Figure 1. Because our aim is to handle only pre-buckling range, we follow the sensitivity path, depicted in Figure 2, up to load value P = 0.95 kN with increments of 0.05 kN, while buckling would occur at P_{cr} = 0.981 kN. As expected in the light of the theory, the obtained numerical sensitivity path is coincident with the analytical one.

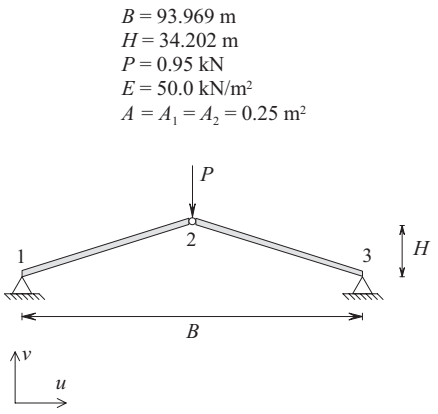

Figure 1. Symmetric two-bar truss.

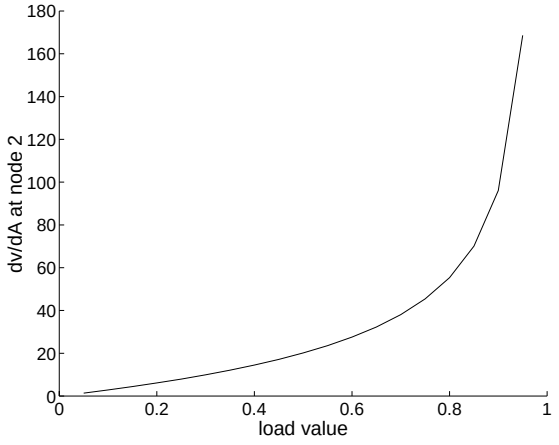

Figure 2. Vertical displacement sensitivity with respect to cross-section area as a function of load value.

In order to highlight the results of sensitivity analysis at elasto-plastic range, we use the very simple example problem shown in Figure 3. For the material, we assume a bilinear GL-stress-PK-strain curve with slopes E and E_{t} at elastic and elasto-plastic ranges, respectively, and a yield stress σ_{y} as depicted in Figure 3. We consider the structure up to load level P = 10 kN with load steps of 1 kN. The sensitivity path in Figure 4 is computed using the incremental sensitivity approach (4). The results are coincident with the analytical ones, see e.g. [3, pp.142-144].

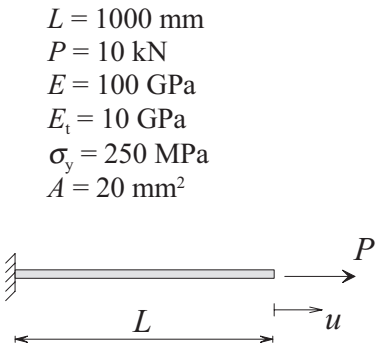

Figure 3. Stretched elasto-plastic bar test example.

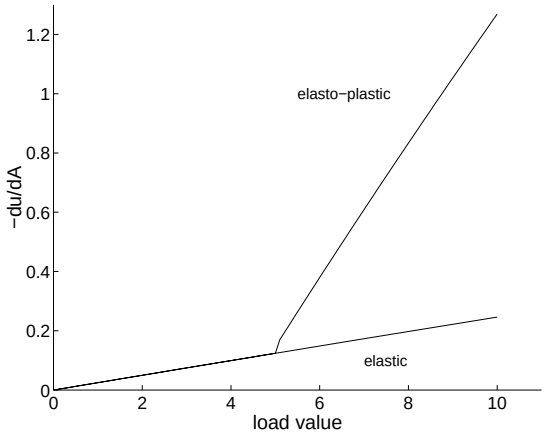

Figure 4. Design sensitivity for the elasto-plastic bar problem.

Conclusions

In this brief report we have discussed on some central phases of non-linear sensitivity analysis. From the major formulas (2) and (4) we can see clearly that for geometrically-only non-linear problems the sensitivity analysis requires only rather light computations; though the path-following procedure is incremental, the sensitivity analysis has to be performed only once at the final load level. For the materially non-linear case, the sensitivity analysis is considerably more complex because the stress sensitivity term (7) is path-dependent. Consequently, the whole sensitivity analysis has to be carried out incrementally. The very form of the stress sensitivity is dependent e.g. on the used constitutive time integration method and from the fact whether updated or total lagrangian approach is used. The incremental approach has also some other non-trivial aspects, such as a sensitivity jump at the yield load level, that are to be studied and discussed in forthcoming papers.

REFERENCES

[1] M. Kleiber, T.D. Hien and E. Postek. Incremental finite element sensitivity analysis for non-linear mechanics applications. *Int. J. Numer. Meth. Eng.*, **37**, 3291-3308, (1994).

[2] J.J. Tsay and J.S. Arora. Nonlinear structural design sensitivity analysis for path dependent problems. Part 1: General theory. *Comput. Meth. Appl. Mech. Eng.*, **81**, 183-208, (1990).

[3] M. Kleiber, H. Antúnez, T. D. Hien and P. Kowalczyk. *Parameter Sensitivity in Nonlinear Mechanics: theory and finite element computations.* John Wiley & Sons, Chichester, (1997).

Optimum Design of Cold-Formed Steel Z-shape Purlin using Genetic Algorithms

Wei Lu* **and Pentti Mäkelainen**
Laboratory of Steel Structures, Department of Civil and Environmental Engineering
Helsinki University of Technology, Espoo, Finland
e–mail: luwei@cc.hut.fi, pentti.makelainen@hut.fi

Jyrki Kesti
Rautaruukki Oyj, Steel Structure Division / R&D
Helsinki, Finland
e–mail: jyrki.kesti@rautaruukki.com

ABSTRACT

Summary The objective of this paper is to apply the genetic algorithm to optimize the dimension of cold-formed Z-shape purlin under gravity load. The objective function, the design variables and the constraints are described. The formula that is used to transfer the constraint problem to the unconstraint problem is given. The design example is presented and the optimization results are obtained.

Introduction. Roof systems commonly used throughout the world often consist of cold-formed steel C and Z-section purlins fastened to high tensile profiled steel sheeting. Many bends along the flange and web, and using the multiple lip stiffeners will make the section very resistant to the local buckling and less prone to twist under the uplift wind load and gravity load. The multiple choices of the cross section raise the questions of the optimal shape. Due to the complex constraints of the design of the cold-formed steel purlin based on the Eurocode 3, Part 1.3 [1], the Genetic Algorithm (GA) is used to optimize the dimension of the Z-section purlin. GA is general-purpose, derivative-free, stochastic, search algorithm [2][3] and starts from randomly choosing initial population that consists of candidate solutions to the problem in hand. Each individual in the population is characterized by a fixed length binary bit string that is called chromosome. These chromosomes are evaluated by means of a fitness function. A new generation of chromosomes is created by combining the fittest individuals from the previous population. Evolutionary operators such as selection, crossover, and mutation are used to create this new population. Besides, 'Elitism' may be incorporated into the algorithm to avoid losing the best individual. These processes continue until the specified level of fitness arrives.

Optimization formulation. The dimension of the Z-section of the cold-formed purlin shown in Figure 1 will be optimized using GA. The purlin is assumed continuous over the two spans and is under the gravity load as shown in Figure 2.

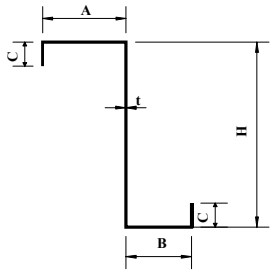

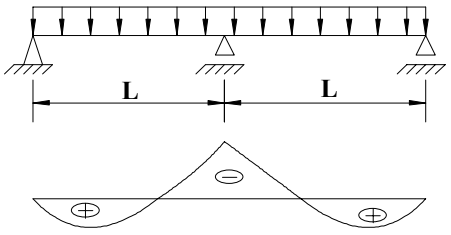

Figure 1 Dimension of the Z-section **Figure 2 Two span purlin under gravity load**

The objective of our problem is to develop a set of design curves that minimizes the total purlin weight, $W = \rho \cdot A_g \cdot (2 \cdot L)$, while satisfying the Eurocode 3 specification. From these design curves, the optimum dimension can be easily determined under the given load.

Since the GA is suitable for unconstraint optimization problem, the constraint problem mentioned above should be transformed into unconstraint problem by using penalty function. According to [4], the objective function including the penalty function is defined as

$$\overline{F} = W + W \cdot (1 + K \cdot CC)$$

where $\overline{F}$ is the modified objective function and CC is constraint violation function and $CC = \sum c_i$, in which c_i are the constraint violations and can be expressed as

$$c_i = \begin{cases} 0 & \text{if } \alpha_i = 0 \\ \alpha_i & \text{if } \alpha_i > 0 \end{cases}$$

where α_i is the normalized constraints. The constant, K, is set to 10.

Demonstrate design example. The standard GA, which is based on bit representation, multiple-point crossover, bit-flip mutation and roulette wheel selection (with elitism) is used to optimize the Z-shape purlin with $L = 4500$ mm under 2 kN/m of gravity load. The yield strength is 350 MPa and the Young's modulus is 210 GPa. Table 1 shows the results for 20 runs, where one run is defined as one completely running of GA.

Table 1 shows that the optimized dimension for the cross section is the thickness of 1.8 mm, the height of 170 mm for the web, the length of 55 mm for the flange and the depth of 22 mm for the lip, i.e. the ratio of C to A is 0.40. Besides, most part of source code of GA-based design are made by Matlab except that the calculation of the section properties is taken from [5].

Table 1 Optimization results for 20 runs

No. of run	t (mm)	H (mm)	A (mm)	C (mm)	A_g (mm^2)	$Weight$ (kg)
1	1.8	190	58	16.24	574.63	405.98
2	1.9	170	54	18.90	564.46	398.79
3	1.7	190	59	20.06	558.55	394.61
4	1.6	200	61	24.40	560.81	396.21
5	2.2	140	48	26.40	594.98	420.36
6	1.6	200	61	24.40	560.81	396.21
7	1.6	200	61	24.40	560.81	396.21
8	1.8	170	55	22.55	551.08	389.34
9	1.6	200	61	24.40	560.81	396.21
10	2.6	130	46	21.16	639.01	451.46
11	1.6	200	61	24.40	560.81	396.21
12	1.4	220	65	37.70	564.09	398.53
13	1.9	170	54	18.90	564.46	398.79
14	1.4	220	65	36.40	560.56	396.03
15	1.4	220	65	37.70	564.09	398.53
16	1.5	210	63	30.87	564.69	398.95
17	**1.8**	**170**	**55**	**22.00**	**549.15**	**387.97**
18	1.7	190	59	20.06	558.55	394.61
19	2	160	53	17.49	565.10	399.24
20	**1.8**	**170**	**55**	**22.00**	**549.15**	**387.97**

Conclusions. This paper shows that the genetic algorithm can be used to optimize the dimension of the Z cross section of cold-formed purlin. This GA-based design method can be applied further to develop a set of design curves, from which the optimum dimension can be easily determined under the given load. Besides, this method can be also applied to optimize the other shape of cold-formed steel purlin.

REFERENCES

[1] *ENV 1993-1-3: General Rules. Supplementary Rules for Cold-formed Thin Gauge Members and Sheeting.*, (1996).

[2] M. Mitchell. *An Introduction to Genetic Algorithms.* Cambridge (MA) MIT Press, (1998).

[3] B. Cogan. The Evolution of Genetic Algorithms. *Scientific Computing World,* May/June, 28-31, (2001).

[4] V. K. Koumousis and P. G. Georgion. Genetic Algorithms in Discrete Optimization of Steel Truss Roofs. *Journal of Computing in Civil Engineering*, **8**, 309-325, (1994).

[5] B. Schafer. Elastic Buckling of Thin-Walled Structures. *http://www.ce.jhu.edu/bschafer/finite_strip/finite_strip.htm*

On geometry of a totally damaged zone near a mode III crack tip in creep-damage coupled problem

Stepanova L.V.
Department of Continuum Mechanics
Samara State University, Samara, Russia
e–mail: lst@ssu.samara.ru

ABSTRACT

Summary The asymptotic solution to a mode III crack growth problem in a creeping solid in the framework of the continuum damage mechanics is presented. The solution is based on introducing a self – similar variable proposed by Riedel for the creep power constitutive law coupled with the power kinetic law of the damage evolution. The asymptotic expansions of the stress tensor components and the integrity parameter for large distances from the crack tip are obtained. It is shown that a totally damaged zone near the crack tip does exist. The geometry of the totally damaged zone is given.

Recently a number of papers devoted to the static and growing crack problems coupling elasticity, plasticity and creep with damage in the framework of continuum damage mechanics have gained [1-8]. Effects of the damage evolution on the stress – strain state and vice versa are of interest to study. From the practical point of view it is important to have an estimation of the crack growth rate. Some characteristic features related to the two – dimensional damage coupled crack problems can be outlined. It is shown [1-4] that the effect of the damage evolution on the stress – strain state near the crack tip appears as either smoothing the stress singularity near the crack tip or its significant reduction. The following feature inherent in the considered class of the problems is the presence of a totally damaged zone where all stress tensor components and the integrity parameter are equalled to zero [1], [2]. Determination of the shape of the totally damaged zone or the active damage process zone is worthy of notice. In [6], [7] where asymptotic fields of stress, creep strain rate and damage of a mode I creep crack in steady-state growth are analyzed according to the experimental observation on the damage distribution around a mode I creep crack in steady-state growth contour of the damage field is represented by a semi-ellipse in front of the crack and by a wake parallel to the crack plane behind the crack. Thus, the problem of determining the configuration of the totally damaged zone or the progressively damaged zone still remains unsolved. The present paper is concerned with an asymptotic analysis of the stress, creep strain rate and the integrity parameter fields at large distances from the crack tip. The asymptotic analysis is based on a self – similar variable proposed by Riedel [8]. The asymptotic fields allow to obtain the configuration of the totally damaged zone modelled in the vicinity of the crack.

Let us consider a semi-infinite crack in an infinite body in a material with constitutive equations formulated on the basis of the creep power law in the framework of continuum damage mechanics

$$\dot{\varepsilon}_{ij} = \frac{3}{2} B \left(\frac{\sigma_e}{\psi} \right)^{n-1} \frac{s_{ij}}{\psi}, \tag{1}$$

where ψ is the integrity parameter; $\dot{\varepsilon}_{ij}$ is the creep strain rate tensor components; s_{ij} is the stress deviator tensor components; $\sigma_e = \sqrt{3 s_{ij} s_{ij}/2}$ is the stress intensity; B, n are the material constants.

The initial conditions have the form

$$\sigma_{ij}(r,\theta,t=0)=\left(\frac{C^*}{BI_nr}\right)^{1/(n+1)}\overline{\sigma}_{ij}(\theta,n), \tag{2}$$

where C^* is the path-independent integral of the steady state creep theory, I_n is the function depending on n and defined as dimensionless C^*-integral, $\overline{\sigma}_{ij}(\theta,n)$ is the functions known from the Hutchison-Rice-Rosengren (HRR) [9]; r, θ are the polar coordinates in the vicinity of the growing crack. Asymptotic conditions at $r\to\infty$ are determined by the HRR-solution to the problem without considering the damage accumulation process ($\psi\equiv 1$) and are given by (2).

Note the asymptotic condition (2) is a hypothesis according to which the stress field away from the crack tip is the stress field near the crack tip of a static crack in material with the creep power constitutive law. However, the problem being investigated is the creep crack growth problem. Thus, the truth of the hypothesis (2) or its incorrectness should be proved by the solution.

It is found [8] that there is a self-similar variable

$$R=\frac{r}{k(n)\,(At)^{(n+1)/m}} \tag{3}$$

for the initial and boundary conditions (2), where $k(n)=C^*/(BI_n)$; A,m are the constants of the damage evolution law

$$\frac{d\psi}{dt}=-A\left(\frac{\sigma_e}{\psi}\right)^m. \tag{4}$$

For the case the stress tensor components and the integrity parameter are represented as

$$\sigma_{ij}(r,\theta,t)=(At)^{(n+1)/m}\,\hat{\sigma}_{ij}(R,\theta),\qquad \psi(r,\theta,t)=\hat{\psi}(R,\theta),$$

where $\hat{\sigma}_{ij}(R,\theta)$ and $\hat{\psi}(R,\theta)$ are the dimensionless function of R,θ and should be obtained from the solutions of different boundary value problems.

It is expedient to start study of phenomenon with the most simple problem from mathematical point of view — a mode III crack problem. Therefore, let us consider the subcritical creep mode III crack growth in a solid with damage.

One can find asymptotic expansions of the effective stress tensor components and the integrity parameter at large distances from the crack tip R (at large distances in comparison with a characteristic length of the totally damaged zone, but at as yet small distances in comparison with a characteristic length of the body or the crack length). By virtue of the fact that the totally damaged zone near the crack tip does exist it is not possible to seek for the asymptotic expansions in the vicinity of the crack tip. Thus, the asymptotic expansions of the stress tensor components and integrity parameter asymptotic expansions are sought in the form

$$\begin{gathered}\frac{\tau_{ij}}{\psi}(R,\theta)=R^s f_{ij}^{(0)}(\theta)+R^{s_1}f_{ij}^{(1)}(\theta)+R^{s_2}f_{ij}^{(2)}(\theta)+...,\\ \psi(R,\theta)=1-R^q g^{(0)}(\theta)-R^{q_1}g^{(1)}(\theta)-R^{q_2}g^{(2)}(\theta)-...\quad (R\to\infty, s<0).\end{gathered} \tag{5}$$

The geometry of the totally damaged zone for different values of the material constants is determined by the equation

$$\psi(R,\theta) = 1 - R^q g^{(0)}(\theta) - R^{q_1} g^{(1)}(\theta) - R^{q_2} g^{(2)}(\theta) = 0. \tag{6}$$

It is found that $s_1 = s + sm$, $s_2 = s + 2sm$ and $q = sm$, $q_1 = 2sm$, $q_2 = 3sm$. It is obtained that HRR-solution does not govern the configuration of the totally damaged zone. Thus, the remote boundary condition is assumed to be

$$\sigma_{ij}(r,\theta,t) \to \tilde{C} r^s \overline{\sigma}_{ij}(\theta). \tag{7}$$

The self-similar variable $R = r(tA\tilde{C}^m)^{1/sm}$ can be introduced for the case. The asymptotic expansions (5) are again used and new values of the eigenvalue s leading to the "convergent" contours of the totally damaged zone for the different values $n,\ m$ are found.

Table. The eigenvalues obtained for different values of the material constants.

$n = m = 1$	$s = -1.5$
$n = 2,\ m = 0.7n$	$s = -1.2303$
$n = 3,\ m = 0.7n$	$s = -1.1830$
$n = 4,\ m = 0.7n$	$s = -1.1648$
$n = 5,\ m = 0.7n$	$s = -1.1553$
$n = 6,\ m = 0.7n$	$s = -1.1495$
$n = 7,\ m = 0.7n$	$s = -1.1455$
$n = 8,\ m = 0.7n$	$s = -1.1425$
$n = 9,\ m = 0.7n$	$s = -1.1405$
$n = 10,\ m = 0.7n$	$s = -1.1390$

It can be concluded the HRR-field does not govern the geometry of the totally damaged zone. The new stress asymptotic at infinity is found. It is shown that it is precisely the stress asymptotic that governs the configuration of the totally damaged zones for different values of the material constants. The geometry of the totally damaged zone is given in Figure 1-2, where the following notations are accepted: 1 — the configuration of the totally damaged zone given by the two-term asymptotic expansion for the integrity parameter; 2 — the configuration of the totally damaged zone given by the three-term asymptotic expansion for the integrity parameter; 3 — the configuration of the totally damaged zone given by the four-term asymptotic expansion for the integrity parameter.

REFERENCES

[1] V.I. Astafjev, T.V. Grigirova and V.A. Pastuchov. Influence of continuum damage on stress distribution near a tip of a growing crack under creep conditions. In: Cocks, A.C.F., Ponter, A.R.S. (Eds.), *Mechanics of Creep and Brittle Materials*, pages 49–61, vol. 2, Elsevier. London, (1991).

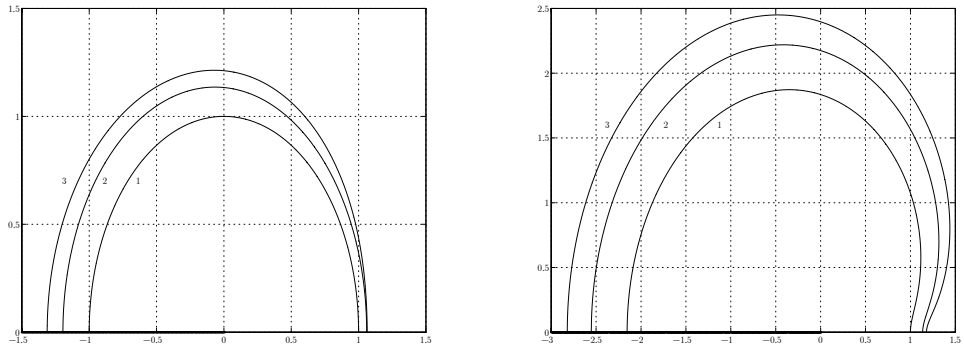

Figure 1: The geometry of the totally damaged zone for $n = m = 1$ and $n = 3,\ m = 0.7n$.

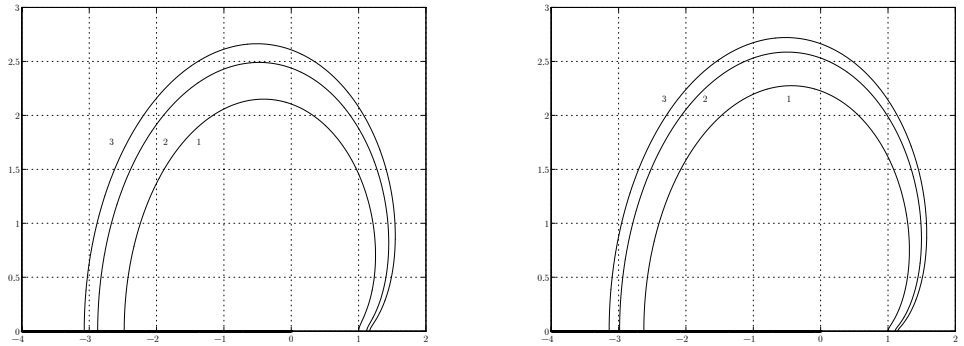

Figure 2: The geometry of the totaly damaged zone for $n = 5, 7$ and $m = 0.7n$.

[2] V.I. Astafjev and T.V. Grigirova. Stress and damage distribution near the tip of a crack growing under creep. *Izv. RAN. MTT*, **3**, 160–166, (1995).

[3] J. Zhao and X. Zhang. The asymptotic study of fatigue crack growth based on damage mechanics. *Eng. Frac. Mech.*, **50**, 131-141, (1995).

[4] J. Zhao and X. Zhang. On the process zone of a quasi-static growing tensile crack with power-law elastic-plastic damage. *Int. J. of Fracture*, **108**, 383-395, (2001).

[5] L.V. Stepanova and M.E. Phedina. Self - similar solution of the damage-creep coupled boundary value problem of mode III crack. *Vestnik SamGU*, **4(18)**, 128-145, (2000).

[6] S. Murakami, T. Hirano and Y. Liu. Asymptotic fields of stress and damage of a mode I creep crack in steady-state growth. *Int. J. Solids Structures*, **37**, 6203-6220, (2000).

[7] S. Murakami, Y. Liu and M. Mizuno. Computational methods for creep fracture analysis by damage mechanics. *Comput. Meth. Appl. Mech. Engrg*, **183**, 15-33, (2000).

[8] H. Riedel. *Fracture at high temperature*. Berlin: Springer, (1987).

[9] J.R. Rice and G.F. Rosengren. Plane strain deformation near a crack tip in a power-law hardening material. *J. Mech. Phys. Solids*, **16**, 1-12, (1968).

Modelling Simultaneous Tensile and Compressive Failure Modes of the Split Cylinder Test

Lennart Østergaard*, John Forbes Olesen and Henrik Stang
Department of Civil Engineering
Technical University of Denmark, Lyngby, Denmark
e–mail: los@byg.dtu.dk

ABSTRACT

Summary The split cylinder test has been modelled in a fem-program using the fictitious crack model by Hillerborg [1] in combination with a Coulomb plastic yield condition. It is shown that under certain circumstances the peak load determined from the split cylinder test is not uniquely correlated to the tensile strength. Moreover, the stress crack opening relationship of the material has a significant influence on the peak load. The results indicate that care should be taken when using this test method.

INTRODUCTION

The split cylinder test is widely used for determination of the tensile strength of concrete and other cementitious materials. The test is conducted by loading a standard cylindrical specimen with a line load on two diametrically opposite generatrices, see Figure 1a . This loading condition produces tensile stresses perpendicular to the loading plane, and at some load level, splitting of the specimen occurs. However, also compressive failure occurs near the loading strips and produce two failure wedges, see Figure 1b. Thus, the failure mode is not a pure tensile failure, and the peak load is therefore influenced by the width of the loading strips, the compressive strength, the friction angle and the cohesion of the material. The tensile splitting is governed by a crack propagating in the plane of loading. Crack propagation is described by Hillerborg in [1] introducing the stress crack opening relationship as a material characteristic. It turns out that the stress crack opening relationship of the material influences the peak load significantly due to the influence on the crack propagation. The purpose of this paper is to investigate the influence of the stress crack opening relationship on the behavior of the split cylinder test.

ANALYSIS

Traditionally, the tensile strength is obtained from the peak load of the split test using a linear elastic model. If the loads are assumed to be ideal line loads, the elastic solution is given by $f_{sp} = 2P_u/(\pi hD)$, [2], where P_u is the peak load, h is the height of the specimen and D is the specimen diameter. The split tensile strength, f_{sp}, is equal to the true tensile strength if the material under consideration is perfectly brittle. However, this is not achievable in practise, and reduction factors are commonly used to correct f_{sp}. If the material under investigation behaves as a modified coulomb material, a plastic solution will be applicable as described in Nielsen, [3]. In this case, a minimized upper bound solution, based on the failure mechanism shown on Figure 1 or the exact solution based on a slip line field derived by Izbicki [4] may be applied. Also a

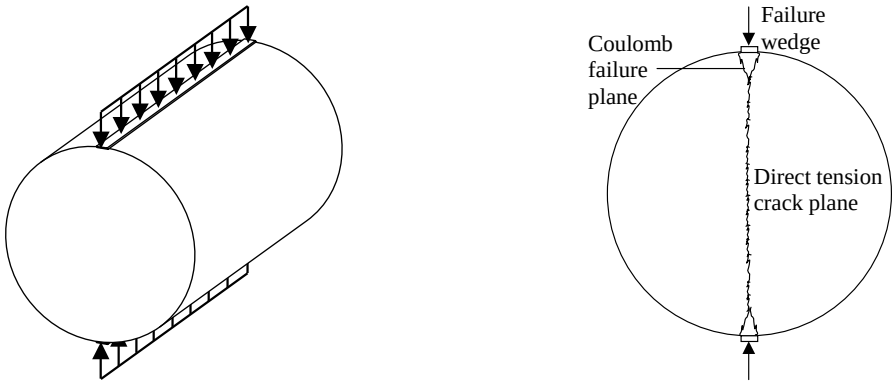

(a) (b)

Figure 1: Loading of the split cylinder (a) and failure mode (b)

fracture mechanical solution based on the fictitious crack model has been developed by Rocco et al [2]. They offer a formula which has been calibrated to fit the results of their numerical model. The above mentioned models are compared with the numerical model presented here.

The present numerical model is illustrated in Figure 2a where the failure mode in Figure 1b has been adopted. One quarter of a cylinder is modelled. The model is simply supported on the radial sections and the splitting crack is modelled using interface elements on the vertical radial section.

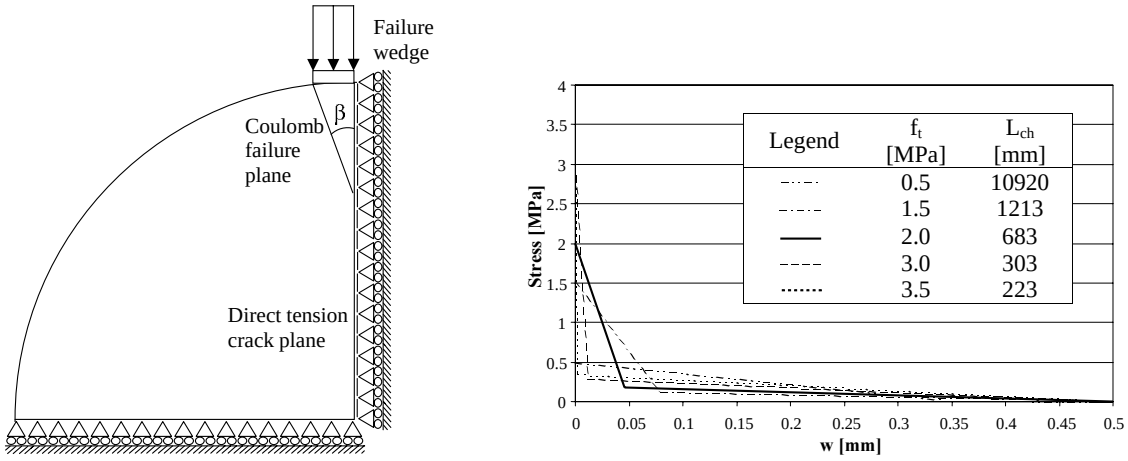

(a) (b)

Figure 2: Model used in the finite element analysis (a) and the applied stress-crack opening relationships with $G_f = 91\frac{N}{m}$ (b), as given by the area under the curve.

The interface elements are given zero thickness before cracking. Cracking is initiated when the normal traction in an element reaches the tensile strength. After the tensile strength has been reached the normal traction is governed by one of the prescribed stress-crack opening relation-

ships shown in Figure 2b. These bilinear stress-crack opening relationships all represent the same fracture energy and the same normalized slope of the second branch; the normalization with respect to the tensile strength. They differ in tensile strength and the initial slopes are adjusted in order to keep the fracture energy constant. Thus, the curves represent different ratios between tensile strength and fracture energy. The characteristic length $L_{ch} = EG_f/f_t^2$ reflects the material brittleness.

After a certain propagation of the splitting crack, a compressive failure occurs as shown in Figure 1b. This failure is an integrated part of the failure of the split cylinder, and must be modelled. Interface elements are used on the side of the wedge shown in Figure 2b and a coulomb frictional criterion is specified. The compressive strength is determined from the tensile strength using a standard empirical formula, $f_c = (f_t/0.35)^2$. The cohesion, c, the friction angle, φ, and the angle of the side of the wedge, β that minimizes the upper bound solution, [3], are given by $c = \frac{f_c}{4}, \varphi = 37\ ^\circ, \beta = 26.5\ ^\circ$. The model has been implemented in the finite element program DIANA and calculations have been performed with the stress-crack opening relationships shown in Figure 1. The calculations are controlled by adaptive control of the crack opening at the center of the cylinder. The results will be discussed in the next section.

DISCUSSION

The results of the finite element calculations show that the peak-load is strongly influenced by the ratio between tensile strength and fracture energy of the material under consideration, see Figure 3a and 3b. It is seen how in all cases a yield plateau is eventually reached. This is an artifact of the model due to the ideal plastic assumption of the compressive failure. Only the first peak of the curves is ascribed physical meaning. The example in Figure 3a with a tensile strength of 2.5 MPa shows a clear distinction between the tensile crack propagation and the later compressive - plastic - failure. First the crack propagates through the cylinder, which results in an unloading (the first peak), whereafter stresses again build up and finally, a compressive failure occurs. For $f_t = 1.0$ MPa, there is no clear distinction between the two failure modes. They occur simultaneously but eventually, the load carried by the specimen drops to the load carried by the modified Coulomb plastic failure plane, when the crack is widely open and stress free.

Figure 3b shows the first peak for different choices of tensile strength and softening behavior. Also, the linear elastic solution, the plastic solutions from [3] and [4] and the model based on a pure fictitious crack analysis, [2], are shown. The cohesive model is only shown in the range of 3.0-3.5 MPa, where it is close to the results of the numerical model and the linear elastic analysis. The reason is that the model is not valid for lower values of f_t in combination with the present selection of the remaining parameters. This is due to a build-in singularity that breaks down the model for some sets of parameters. The model results of this paper are seen to undergo a transition from plastic to brittle behavior. For low tensile strengths, where the f_t/G_f-ratio is low, it is seen how the result fits the plastic model (Izbicki), while the model fits the linear elastic results for high tensile strengths. The latter is expected since the stress crack opening relationships in these cases model very brittle materials. However, for a normal choice of parameters ($f_t = 2.0\ MPa$), it is seen that the result is neither plastic, nor elastic, but in fact quasi-brittle. It is also seen how

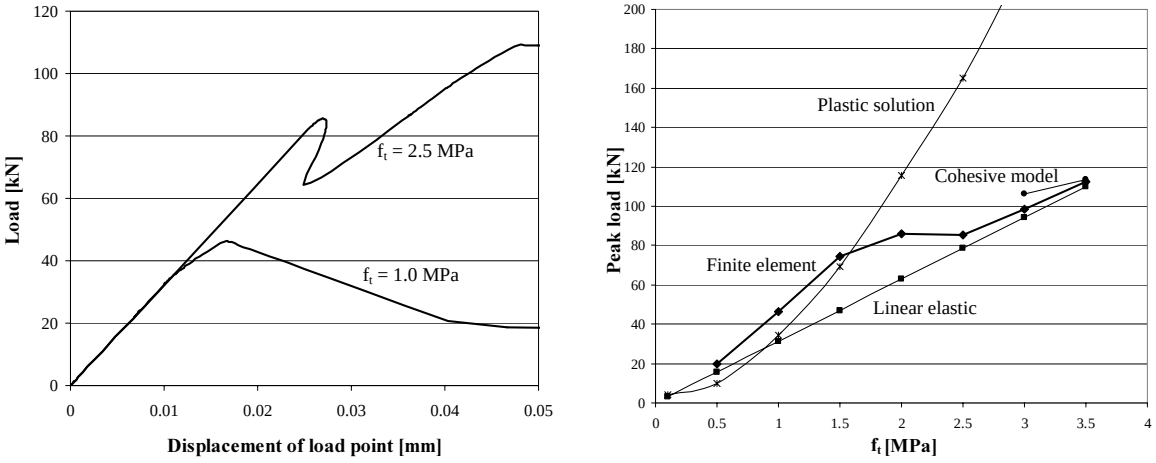

(a) (b)

Figure 3: Load-displacement curves for different stress-crack opening relationships (a) and peak load as function of tensile strength (b)

this plastic-elastic transition results in a flat plateau, where the change in tensile strength has little influence on the peak load. These problems will be revealed if the test method is used for concrete in early age, since the f_t/G_f-ratio is higher than for mature concrete. It is also well known that f_t is independent of G_f, e.g. it is possible to change the latter by adding fibers or changing aggregate size without changing the tensile strength.

CONCLUSIONS

Potential problems with the split cylinder test method have been identified. This is due to the fact that the peak load of the test is influenced not only by the tensile strength, but also by the stress crack opening relationship, and thus the fracture energy of the material. Further investigations are needed to confirm these results.

REFERENCES

[1] A. Hillerborg, M. Modéer and P. E. Petersson. Analysis of crack formation and crack growth in concrete by means of fracture mechanics and finite elements. *Cement Concr Res*, **6**, 773–782, (1976).

[2] C. Rocco, G. V. Guinea, J. Planas and M. Elices. Review of the splitting-test standards from a fracture mechanics point of view. *Cement Concr Res*, **31**, 73–82, (2001).

[3] M. P. Nielsen. Limit Analysis and Concrete Plasticity. Second edition. London. CRC Press (1999).

[4] R. J. Izbicki. General Yield Condition: I. Plane Deformation. *Bull. Acad. Pol. Sci. Ser. Sci. Tech.*, **20**, No. 7-8, (1972).

Geometric and material instabilities in tensile loaded cracked shells

B.Skallerud*, **T.Holmås**

* Department of Applied Mechanics
Norwegian University of Science and Technology, Norway
e–mail: bjorn.skallerud@mtf.ntnu.no
MARINTEK Marine Structures
SINTEF, Norway

ABSTRACT

Summary In the present study some preliminary results of finite element analyses of cracked sheets loaded in tension are presented. The sheets response are governed by the combined effect of buckling, ductile tearing, and plastic deformations.

INTRODUCTION

Thin plates loaded in tension are in most cases not associated with instable response (disregarding softening material and necking effects). Introducing cracks perpendicular to a dominating tensile load may lead to instable behaviour. This is caused by two phenomena. First, the crack makes the material above and below the crack faces prone to buckling due to compressive stresses parallel to the crack. Second, in a ductile material crack growth occcur during increasing applied load, eventually reaching some limit point. In combination, these two effects may also interact, and in order to calculate reasonable capacities, these effects have to be accounted for simultaneously in the simulation. Hence, in the finite element analysis nonlinear geometry, elasto-plastic shell behaviour, and ductile tearing have to be combined. In this respect, it is the modeling and simulation of the ductile tearing that is most challenging[1][2][3][4][5]. Many approaches are available, classified as critical crack tip opening angle, cohesive zones, and nonlinear springs. The latter approach is employed herein, combined with the ANDES thin shell formulation and stress resultant plasticity modelling presented by Skallerud and Haugen[6].

MODELING AND SIMULATION

The physics of creating new material surfaces (i.e. breaking of atomic bonds) during a fracture process is complicated, and at present mesoscopic or continuum mechanics are employed. But micromechanical models are under development. A very important effect in (ductile) fracture is linked to the concept of constraint. The higher the constraint around a plastic zone near a crack tip is, the higher is the stresses. Hence, this affects the damage dissipation and fracture capacity. The familiar fracture toughness thickness dependency is an example of this. In thin sheets the constraint is low, and the ductile failure approaches a rupture mode of slant localised plastic deformations. In many applications of cracked thin shells there is a need for caclulationg crack growth of magnitude up to meters in order to predict ultimate capacity. The bulk of numerical studies of ductile fracture is limited to predicting a few millimetres of crack growth, using 1/10-millimeter finite element sizes in

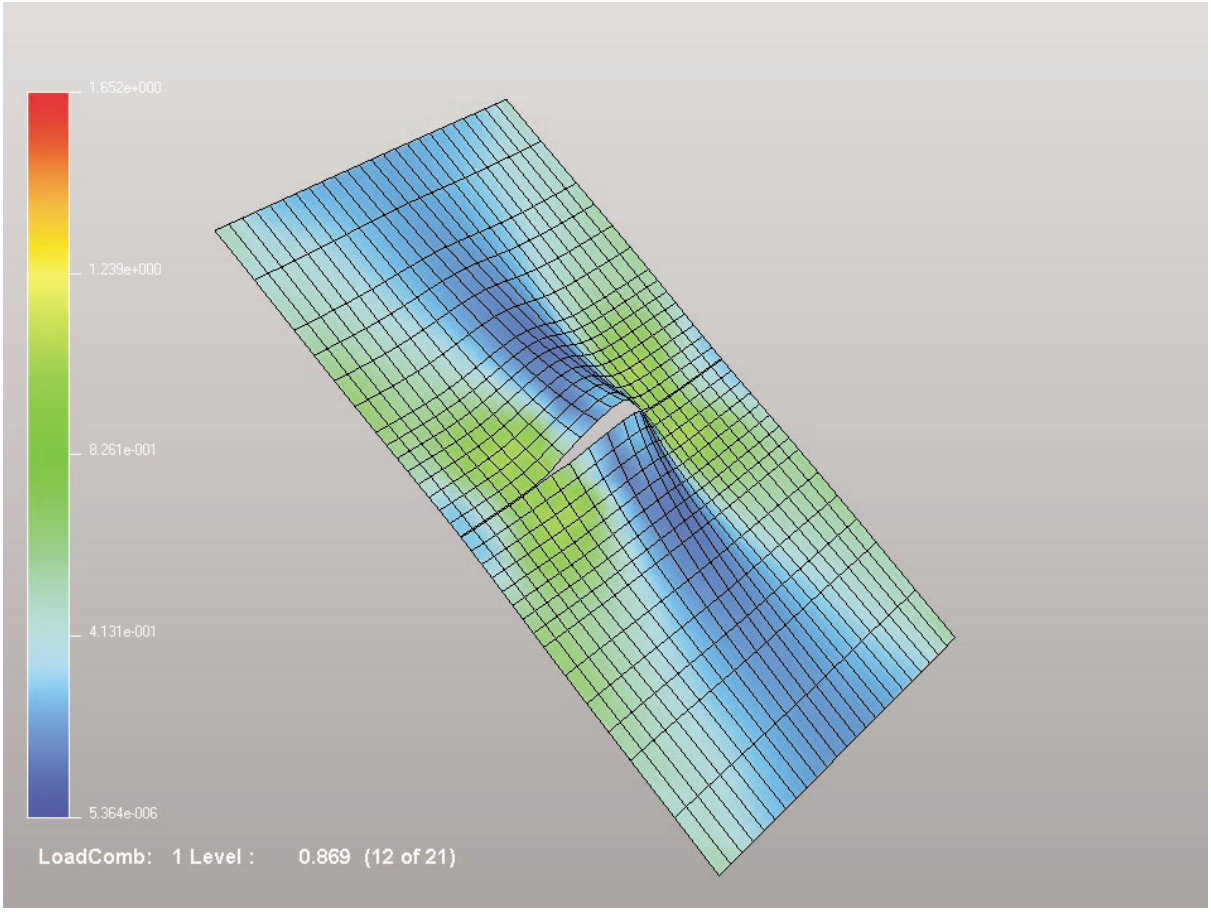

Figure 1: Center cracked aluminium plate with local buckling and tearing crack growth.

the crack growth regions. This is not feasible in predicting large scale crack growth. The present modeling is based on nonlinear springs with a softening behaviour that mimics the stress carrying capability approaching zero as the crack grows through the elements. The spring model is calibrated to resemble the damage growth in the sheet at a given thickness (governing constraint). Furthermore, with such softening behaviour the mesh sensisitivity has to be accounted for. This may be done by calibration to a test. Alternatives exist that reduce the mesh sensitivity (introducing other length scale parameters, visco-plastic regularisation etc). Fig.1 shows the case analysed herein. It is a rectangular aluminium sheet (Al 2024-T3) of thickness 2.3mm. A central trough crack is introduced, and tensile loading is applied. Fig.1 depicts the deformed coarse finite element mesh used (see [6] for formulation). It is noted that significant ductile grack growth has evolved and transverse local buckling is present. Reasonable ulitmate load prediction compared to test results is obtained.

REFERENCES

[1] A.L.Gurson. Continuum theory for ductile rupture by void nuckleation and growth – Part I, yield criteria and flow rules for porous ductile media. *J Engng Mater and Techn.*, **99**, 2–15, (1977).

[2] B.R.Shesradi and J.C.Newman Jr. Analysis of buckling and stable tearing in thin sheet materials. *Fatigue and Fracture Mechanics*, **ASTM STP 1332**, 114–134, (1999).

[3] T.Siegmund and W.Brocks. The role of cohesive strength and separation energy for modeling of ductile fracture. *Fatigue and Fracture Mechanics*, **ASTM STP 1360**, 139-151, (2000).

[4] A.S.Gullerud, R.H.Dodds Jr, R.W.Hampton, and D.S.Dawicke. 3-D finite element modeling of ductile crack growth in thin aluminum materials. *Fatigue and Fracture Mechanics*, **ASTM STP 1360**, 85–101, (2000).

[5] V.Tvergaard. Crack growth predictions by cohesive zone model for ductile fracture. *J Mech and Phys of Solids*, **49**, 2191–2207, (2001).

[6] B.Skallerud and B.Haugen. Collapse of thin shell structures - stress resultant plasticity modelling within a co-rotated ANDES finite element formulation. *Int.J. Numerical Meth Engng*, **46**, 1961–1986, (1999).

Non-local approach for damage simulation in ductile materials

J. Jackiewicz[*] and M. Kuna[**]

[*]Department of Mechanical Engineering,
Bydgoszcz University of Technology and Agriculture, Bydgoszcz, Poland
e–mail: jj-kms@mail.atr.bydgoszcz.pl (j.jackiewicz@imm.tu-freibeg.de)
[**]Institute of Mechanics and Machine Components,
Freiberg University of Mining and Technology, Freiberg, Germany
e–mail: kuna@imm.tu-freiberg.de

M. Scherzer[**]

e–mail: scherzer@imm.tu-freiberg.de

ABSTRACT

Summary To overcome shortcomings of classical theories for local fracture mechanics and continuum damage mechanics, a non-local model for damage simulation in elastic-plastic materials with micro-defects is proposed. This model is suited to solve engineering problems when plasticity occurs to large extent and the global concepts of fracture mechanics are no longer valid. The model is based on the non-local continuum theory, which employs a homogenization technique with selection methods of evolutionary algorithms. The homogenization technique with the selection methods has been used for the following reasons: (i) to enforce the consistency conditions during the integration of the stress tensor over a loading increment and (ii) to improve modeling of the internal energy dissipation in the context of the finite plastic strain problem.

Analysts and designers in the engineering industry want not only more accurate but more universal ways to analyze the various problems of fracture mechanics. Since fracture mechanics essentially relies on continuum mechanics concepts for global phenomena, an improved modeling of local phenomena at stress concentration, which are observed in engineering materials of structures, is necessary. It should be noted, that in many cases, encountered in classical elastic-plastic fracture mechanics, the stress field does not agree with plane strain HRR solution well. In other word, the classical J-integral concepts may not be directly applicable as fracture parameter. The main reasons are: (i) the influence of the stress triaxiality at the crack tip, which depends on geometry and loading of the cracked structure, and (ii) the influence of unloading, which occurs during cyclic loading or crack growth. When micro-damage phenomena in the ductile materials are considered, the inherent complexity of the hierarchical analysis makes this approach impractical.

Recently, continuum damage mechanics has been proposed to deal with the relevant problems by taking into account the local deformation and failure behavior of structural materials, concerning micro-scale materials models (see in [2, 3 and 4]). Please note that the evolution of the micro-damage phenomena can be numerically approximated to that extent, in which microscopic phenomena are described macroscopically.

To solve these problems, a transfer from a measure of fracture parameters for small laboratory specimens to evaluating the safety of large structural components is very important. Additionally, this transfer requires taking into consideration the size effect. The size effect is a problem of scaling, which performs an important role in every physical theory. Up to known, in most of mechanical engineering branches the problem of scaling has been less pressing because the structure or structural components can only be tested at full size. The size effect in ductile materials characterizes a capability of the energy absorption. It is known, that the small structures have larger ductility then the larger ones. Particularly, the size effect on energy absorption capability is important for blast and impact.

Moreover, the macroscopic description of distributed cracking or other types of damage in structural materials requires constitutive models that exhibit strain softening. Strain softening behavior is characterized by a decrease of stress at increasing strain or in general a loss of positive definiteness of the tangential moduli matrix of material. This behavior is observed macroscopically in many materials, including various metals, which exhibit void nucleation and growth in large strains. If the tangent modulus loses positive definiteness, then computational difficulties follow as a result of that the Newton-Raphson procedure often fails to converge to one equilibrium state. For initial boundary value problems, the softening response leads to a change in type of governing partial differential equations. Under quasi-static loading conditions, a loss of ellipticity of the governing equations is associated with a bifurcation. Additionally, when the boundary value problems are not well posed, the results of finite element calculations turn out to be dependent on the mesh spacing.

Many attempts to characterize the degradation of material stiffness by local inelastic continuum theories, such as plasticity or continuum damage mechanics, have been unsatisfactory because the phenomena of strain localization are difficult to describe precisely. Namely, it is difficult to describe the response of the material in such cases, in which the physical quantities (influenced on strain softening) are distributed into infinitesimal zones. Hence, a realistic prediction of the failure of structures caused by progressive damage requires an application of localization limiters, which give results independent of the mesh spacing. The localization limiters force the strain-softening region to have a certain minimum finite size and thus ensure the energy dissipation at failure to be finite. Therefore, they allow taking into account the influence of the length scale associated with descending steeply strain field on the stress distribution at the microscopic level. Two basic types of localization limiters may be applied:

- *integral limiters*, based on non-local constitutive equations,
- *differential limiters*, based on higher order derivatives of the strain tensor.

It is worthwhile to stress that one of the alternatives to the approach of localization limiters is the micro-polar continuum description. The most promising way for damage simulation in ductile materials seems to be an application of the non-local approach.

Improved spatial resolution for non-local analysis

The non-local continuum consists of multi-continuum points conceived as having properties associated with a certain representative volume of the material. The size of this volume has to be large enough in order to represent its local micro-properties by their mean values defined as meso-properties through continuous variables. Special homogenization functions are used in the non-local effective description of the material. Moreover, these functions are limited to the prediction of the macro-defects initiation in cleavage and ductile modes. It seems that smooth

approximation functions have a clear advantage (see in [1]). The homogenization technique consists in defining some variables in the constitutive equations by spatial averaging over the representative volume according to the evolution adaptive scheme for (*i*+1)*th* updated and (*i*)*th* previous variables. This scheme is represented by the following equations:

$$\left\langle \bullet \left(\boldsymbol{x}_{(i)} \right) \right\rangle_{NL} = \int\limits_{{}_{R}V\left(\boldsymbol{x}_{(i)} \right)} \alpha^{*} \left(\boldsymbol{x}_{(i)}, \boldsymbol{s} \right) \left[\bullet \left(\boldsymbol{x}_{(i)} + \boldsymbol{s} \right) \right] dV(\boldsymbol{s}),$$

$$\left\langle \bullet \left(\boldsymbol{x}_{(i+1)} \right) \right\rangle_{NL}^{(UL)} \overset{(EA)}{=} \int\limits_{{}_{R}V\left(\boldsymbol{x}_{(i+1)} \right)} \alpha^{*} \left(\boldsymbol{x}_{(i+1)}, \boldsymbol{s} \right) \left\langle \bullet \left(\boldsymbol{x}_{(i+1)} + \boldsymbol{s} \right) \right\rangle_{NL} dV(\boldsymbol{s}),$$

$$\left\langle \bullet \left(\boldsymbol{x}_{(i+1)} \right) \right\rangle_{NL}^{(UL)^{*}} \overset{(EA)}{=} \int\limits_{{}_{R}V\left(\boldsymbol{x}_{(i+1)} \right)} \alpha^{*} \left(\boldsymbol{x}_{(i+1)}, \boldsymbol{s} \right) \left\langle \bullet \left(\boldsymbol{x}_{(i+1)} + \boldsymbol{s} \right) \right\rangle_{NL}^{(UL)} dV(\boldsymbol{s}),$$

where:

$$\alpha^{*} \left(\boldsymbol{x}, \boldsymbol{s} \right) = \alpha^{*} \left(\boldsymbol{\zeta} \equiv \boldsymbol{s} - \boldsymbol{x} \right) = \frac{e^{-(\boldsymbol{\zeta}/(\lambda\, \Delta\boldsymbol{\zeta}))^{2}} - e^{-(\Delta\boldsymbol{\zeta}/(\lambda\, \Delta\boldsymbol{\zeta}))^{2}}}{1 - e^{-(\Delta\boldsymbol{\zeta}/(\lambda\, \Delta\boldsymbol{\zeta}))^{2}}} \; -$$

weight function, which defines the averaging,

$\Delta\boldsymbol{\zeta}$ - parameter, which determines a size of the influence domain,

λ - parameter of scale.

The weight functions contain minimum number of nodes within their domain of influence. When a larger value for $\Delta\boldsymbol{\zeta}$ is chosen, so that the weight function incorporates more neighboring nodes.

The presented formula is sensitive on numerical disturbances. Therefore two homogenization levels are used. The first in nodes between elements and the second to accurate describe the process of internal dissipation energy in the material, which is directly connecting to the size effect. Moreover, the special hybrid elements are used, which contain proper shape functions averaging this process. Please note that the representative volume in the non-local continuum corresponds to the representative volume in the statistical theory of heterogeneous materials.

Assuming, that there are imaginary rays penetrating the examining body from different angles, the homogenization technique is incorporated in the implementation of the finite element method. Furthermore, this technique is improved by employing special transformation functions for adjacent nodes and Gauss integrating points. Formulating of the resulting local (single node) and non-local (multi-node) state parameters allows a systematic approach to non-classical description of the ductile material with micro-defects. The non-classical state-space parameters obey certain inequalities and sum rules. The networks of interactions between: distinguished nodes of representative volumes are described by joint distribution functions in the state parameter-space in that way like variance and covariance tensors. Interactions lead to superposition states, which comprise local coherence but also non-local entanglement. The average variance and covariance tensors are distinguished entirely from their counter-pairs. Non-local entanglement should get operational parameters when it is a need to switch between local and non-local features of quantities by changing their so called perspective (plastic reloading and elastic unloading).

Size effect

For ductile materials the size effect is determined by an internal length scale for the material by means of localization limiters. Please note that for brittle materials the size effect is involved by the weakest link idea and the distribution of the largest microscopic crack appearing in each representative volume of the material. This distribution of non-local strength of representative volumes is described by the Weibull statistics.

Application examples

The ideas given in the previous sections are verified by various case studies of the finite strain, large deformation and incremental theory of plasticity. Examples of these case studies are presented namely a finite element simulation of ductile crack growth in a compact tensile specimen, a finite element simulation of cleavage fracture in a notched tensile specimen and finite element simulations of the damage evolution in the plane-strain perforated block and classical axi-symmetric tensile test specimens.

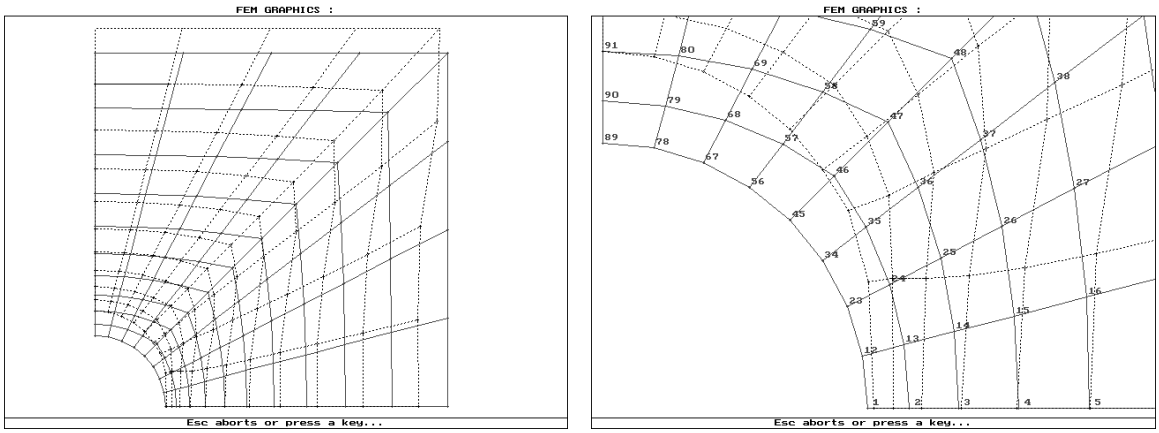

Figure. Initial and deformed finite element meshes of the plain-strain perforated block for Gurson model of the damaged material

REFERENCES

[1] R. de Borst. Some recent issues in computational failure mechanics. *Int. J. Numer. Meth. Eng.*, **52**, 63-95, (2001).

[2] G. Bernauer and W. Brocks. *Numerical Round Robin on Micro-Mechanical Models, Phase II, Results of Task A*. Technical Note GKSS/WMS/00/5, Geesthacht, (2000).

[3] J. Jackiewicz. Numerical aspects of non-local modeling of the damage evolution in elastic-plastic materials. *Comput. Mater. Sci.*, **19**, 235-251, (2000).

[4] A. Sherry. *Guidance on local approach methods, Appendix 17*. R/H/R6 Report, AEA Technology, (1999).

On Crack Tip Stress Releasing

Pauli Pedersen
Department of Mechanical Engineering, Solid Mechanics
Technical University of Denmark
Nils Koppels Allè, Building 404, DK-2800 Kgs.Lyngby, Denmark
email: pauli@mek.dtu.dk

ABSTRACT

Summary The method of hole drilling near the crack tip is often used in fatigue damage repair, see Shin et al., 1996. In a recent paper by Thomas et al., 2000 optimum location of the drilled holes are discussed. In this paper we focus on the shape of a single hole centered at (or in front of) the crack tip. With shape optimization it is shown that the stress field, at the crack boundary can be significantly improved.

1 Introduction

The method of hole drilling near the crack tip is often used in fatigue damage repair. In the survey by Shin et al., 1996 comparisons with alternative methods are presented and it is concluded that hole drilling was most effective. A number of experimental results are presented. In a recent paper by Thomas et al., 2000 optimum location of the drilled holes are discussed, and the specific problem of a center cracked plate is studied with four relatively large holes (20-40 mm) placed symmetrically relative to the crack. Only circular holes are applied. From shape optimization we know that the circular shape is by no means optimal, see Pedersen, 2000 and Pedersen, 2001.

It is therefore important to find the shape of a hole, which in the most effective way, releases the stress concentration. We shall restrict the description to the elementary case shown in figure 1. A simple parametrization, used in earlier shape optimizations, is applied and it is shown that an almost uniform stress state can be obtained along the boundary of the hole. The shape of the hole is described by the super-elliptic equation

$$(x/a)^\eta + (y/b)^\eta = 1 \tag{1}$$

where the x direction is the direction of the crack, as shown in figure 1. If we use a square design domain $a = b$ (super-circle), then the only design parameter is η. We analyzed three designs corresponding to $\eta = 2$ (circular), $\eta = 2.5$ (optimized) and $\eta = 6$. Values for relative maximum strain energy densities for the three designs are 1.00, 0.67 and 1.13 corresponding to relative maximum tangential stresses 1.00, 0.82 and 1.06. We note that considerably better distributions of stresses can be obtained. Even more uniform fields along the hole boundary can be obtained when more design parameters are included.

The objective of the optimal shape design in relation to cracks is not completely clear. At first we may argue that the objective should be to minimize the stress intensity factor. However, for non-sharp crack tips the interpretation of the stress intensity factor is not clear. Thus we choose to

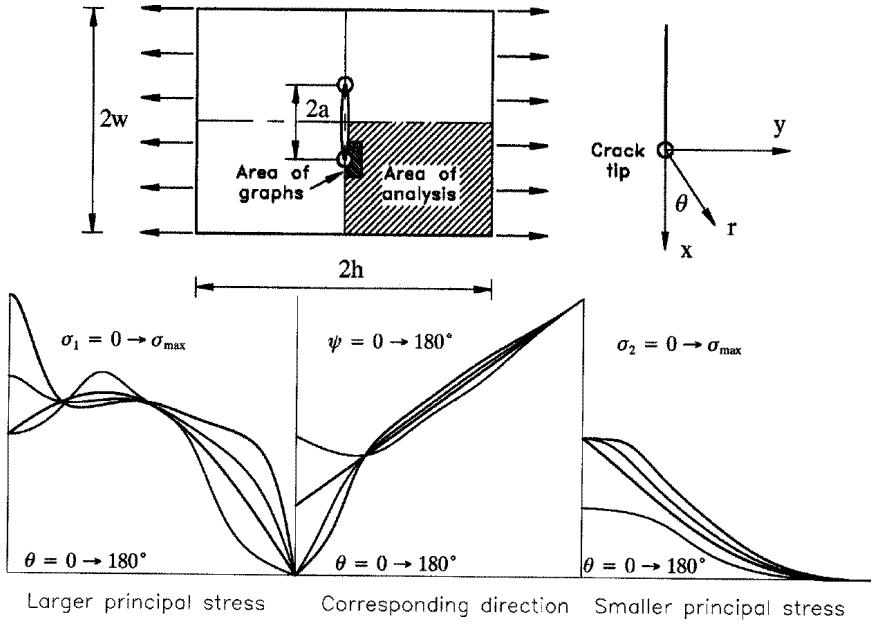

Figure 1: The analyzed elementary case with $w = 100mm$, indicating also the area of the graphs (hole size $\simeq 1mm$) . Analytical stress fields at the crack tip (without hole) as a function of θ are shown for four cases of orthotropy and for isotropic material. In the σ_2 graph, from below we have $E_C/E_T = 0.25, 0.5, 1.0, 1.5, 2.0$, respectively.

minimize the maximum tangential stress at the boundary of the drilled hole. In the case of plane stress this also corresponds to minimizing the maximum von Mises stress or the energy density. For the cases of non-isotropic materials it seems most relevant to minimize the maximum energy density.

2 Sensitivity of the optimal shape

The example shown in the introduction is based on a number of assumptions and a study of the sensitivity to these assumptions is needed. We will discuss the influence from the external load and size of the hole, from material power law non-linearity, from material anisotropy, and from the allowable domain of the hole. Graphical illustrations will only be given in the lecture.

2.1 Influence from the external load and size of the hole.

Different external loads can be examined, either given stresses (forces) or given forced displacements. As expected only little influence is seen as long as the crack is loaded mostly in mode I. This follows from the fact that the near crack tip field will, as a function of the external load, only change with a common factor (the stress intensity factor). Optimization for cracks in mode II, mode III and combined modes needs further studies.

In table 1 we show the relative concentration of the energy density, for different size of the holes and for two alternative load cases. In all cases the best of the analyzed designs correspond to a

super-elliptic power of $\eta = 2.5$. Relative to the size of the hole (0.5 , 1.0 , 1.5 and 2.0 mm), with the 1 mm size as reference, we got 1.92 , 1.00 , 0.68 , 0.52 , and larger holes naturally give a more efficient stress release. The size of the hole is assumed to be determined by alternative considerations.

Shape parameter		$\eta = 2.0$	$\eta = 2.25$	$\eta = 2.5$	$\eta = 3.0$	$\eta = 3.5$	$\eta = 4.0$	$\eta = 4.5$
size	stress load	1.0	0.857	**0.840**	0.876	0.934	0.994	1.05
0.5 mm	displ. load	1.0	0.854	**0.835**	0.863	0.916	0.973	1.03
size	stress load	1.0	0.857	**0.843**	0.894	0.970	1.05	1.13
1.0 mm	displ. load	1.0	0.852	**0.833**	0.875	0.944	1.02	1.09
size	stress load	1.0	0.856	**0.842**	0.895	0.974	1.06	1.14
1.5 mm	displ. load	1.0	0.850	**0.830**	0.872	0.943	1.02	1.10
size	stress load	1.0	0.854	**0.841**	0.894	0.973	1.06	1.15
2.0 mm	displ. load	1.0	0.847	**0.826**	0.866	0.937	1.01	1.09

Table 1: Relative values of maximum energy density (for circle, $\eta = 2$, the value is set to 1.0) . Corresponding values for stress are equal to the square-root of the shown values. Optimized values are shown in bold.

2.2 Influence from material power law non-linearity.

We also obtain results based on analysis with material non-linearity. As expected from earlier results (Pedersen, 2001) the optimal shape of the hole is rather insensitive to the power p $(p \leq 1)$ of the non-linearity. We still obtain almost uniform energy density (here von Mises stress) along the boundary of the hole. The isolines show equal levels of reduced stiffness, described by the factor $(\epsilon_e/\epsilon_0)^p$, where ϵ_e is effective strain and ϵ_0 is the corresponding value that gives the transition from linearity to non-linearity. The assumptions behind the calculations leading to the results analyzed for $\eta = 2, 2.5, and\ 6$ (as for the linear material) correspond to deformation theory with a power law of $p = 0.1$ Relative values for these results are for the squared maximum von Mises stress 1.0, 0.98, 1.11 and for the minimum stiffness reduction factors 0.305, 0.336, 0.280.

2.3 Influence from material anisotropy.

It is expected that anisotropic material behaviour will influence the optimal shape to a large extend, see Pedersen et al., 1992. When the material is stiffer in the crack direction we see little influence on the optimal shape, but when it gets more flexible in the crack direction the influence is pronounced. We found that an energy concentration will always appear for simple super-elliptic designs. With one modification function to the shape of the hole, as described in details in Pedersen et al., 1992, we obtain designs with almost uniform energy density along the hole boundary. A study of the stress fields at a crack tip for this anisotropic case, may give an understanding for the need of more advanced designs for these cases. From the results, a two parameter description seems sufficient.

2.4 Influence from the allowable domain of the hole.

By including the elliptic half-axes a, b as design parameters (the added condition of $ab = constant$ practically fixes the area of the hole), we may further improve the levels of squared von Mises stress. In all cases we obtain almost uniform distribution along the highly stressed boundary. The results corresponding to $a/b = 1.0, 0.9, 0.8, 0.7, 0.6, and\ 0.5$, give the resulting relative maximum values $1.0, 0.92, 0.84, 0.75, 0.66, and\ 0.59$, and thus the super-ellipse has distinct advantages over the super-circle. The optimal super-elliptic power η change with the ratio a/b and for the solutions referred, we got $\eta = 2.5, 2.4, 2.3, 2.15, 2.10, 1.95$, respectively.

The same six designs were analyzed based on a strong material non-linearity $(\sigma_e/\sigma_0)^{10}$ and again almost constant von Mises stress were obtained along the boundary, although now decreased with almost a factor of four. Relative to the results given for the linear solution. The values with the non-linear solution were $0.24, 0.23, 0.22, 0.21, 0.20, 0.18$, respectively. The strong non-linearity levels out the difference, but still the possibility for smaller ratios a/b gives a better solution.

3 Conclusions

With illustrative examples we have shown that the stress field, at the boundary of a drilled stress releasing hole, can be significantly improved. To a large extend the one parameter super-elliptic shape is able to return a field of constant tangential stress along the boundary. A shape like this will diminish the possibility for further fatigue crack initiation.

References

Pedersen, P., Tobiesen, L., and Jensen, S. H. (1992). Shapes of orthotropic plates for minimum energy concentration. *Mechanics of Structures and Machines* 20(4):499–514.

Pedersen, P. (2000). On optimal shapes in materials and structures. *Structural Optimization* 19:169–182.

Pedersen, P. (2001). On the influence of boundary conditions, Poisson's ratio and material non-linearity on the optimal shape. *Int. J. of Solids and Structures* 38(3):465–477.

Shin, C. S., Wang, C. M., and Song, P. S. (1996). Fatigue damage repair: A comparison of some possible methods. *Int. J. of Fatigue* 18:535–546.

Thomas, S., Mhaiskar, M., and Sethuraman, R. (2000). Stress intensity factors for circular hole and inclusion using finite element alternating method. *Theoretical and Applied Fracture Mechanics* 33:73–81.

Identification of normal forces in members of lab tested models of bridge truss girders

Wojciech Siekierski
Department of Bridges
Poznan University of Technology, Poznan, Poland
e–mail: siekiers@sol.put.poznan.pl

ABSTRACT

Summary Lab tests of two models of bridge truss girders are summarised. Local detailed FEM analysis of normal stress distribution was necessary to assess normal forces basing on recorded strains. The forces were also compared to results obtained from simpler numerical model of the girders.

Bridge truss girders differ from "building" truss girders. Significant internal forces they carry and constructional requirements (for example: eccentricity limitations) result in necessity of relatively big gusset plates. Many of such bridges are in service in Poland. Tests of two models of bridge truss girders (Fig.1) were carried out in the Institute if Civil Engineering of Poznań University of Technology. Girder "A" was built of I–members (IPE120). Girder "B" had the same layout and increased stiffness of members along the 10-3-7-15 line (see Fig.1).

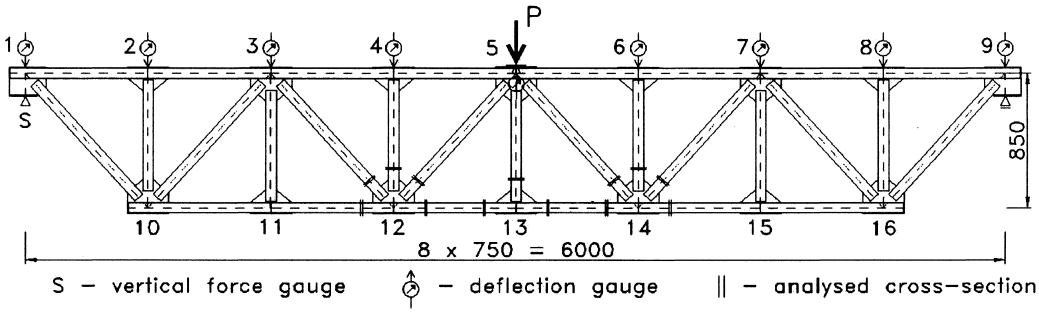

Fig.1. Basic dimensions of girders and test layout

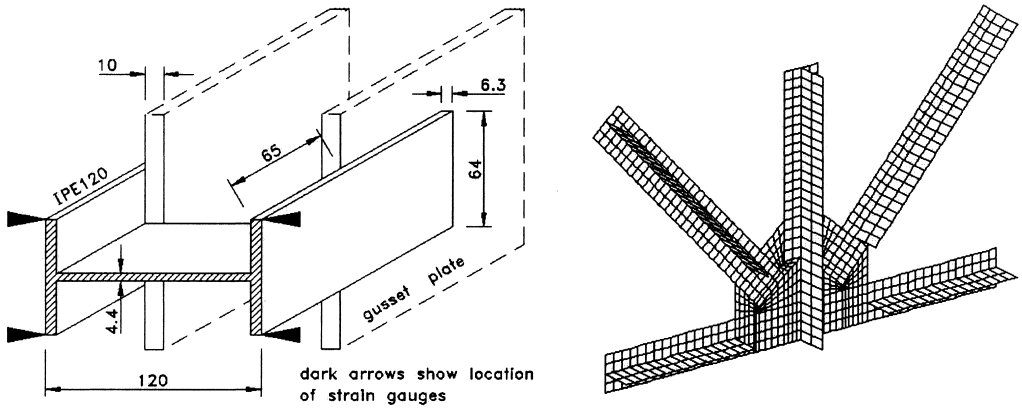

Fig.2. Left: analysed cross–section (hatched) [mm]; note that member web is discontinued at the edge of gusset plate. Right: shell–element FEM model of node 12 (see Fig.1) used for the additional analysis.

Though the main aim was to assess the joint size influence on global stiffness, strains at the cross–sections indicated in Fig.1 were also recorder to verify internal forces distribution. The forces obtained on the basis of recorded strains were to be verified with plane–frame FE model.

Since the normal stress distribution at the analysed cross–sections was non–linear [2], the recorded data (strains at flange edges) were insufficient to assess actual normal forces correctly. To identify actual normal stress distribution, shell–element FE models of nodes 12 and 13 were analysed. The nodes were virtually cut out of the structure at members midspan. Centre parts of gusset plates were clamped and normal forces applied subsequently to bottom flanges and cross bracing ends. Structural detail of element–to–gussset plate connection and the FE model of node 12 are shown in Fig.2. Calculations were carried out in Poznań Supercomputing and Networking Centre, using Abaqus [3].

Table 1 gives normal forces calculated on the basis of recorded strains assuming linear normal stress distribution, values corrected after local FEM analysis and those obtained from analysis of plane–frame FE models of girders.

Table 1.

Member ↓ / Girder →	Normal force [kN]					
	Assuming linear stress distribution		After additional FEM analysis		Calculated: plane–frame FE model	
	"A"	*"B"*	"A"	*"B"*	"A"	*"B"*
bottom flange (12)-11	79.6	*78.3*	62.9	*61.9*	61.9	*61.9*
cross bracing (12)-3	55.1	*56.9*	43.0	*44.4*	45.9	*46.1*
cross bracing (12)-5	-47.5	*-46.1*	-44.2	*-42.9*	-45.4	*-44.3*
bottom flange (12)-13	133.7	*132.8*	123.0	*122.2*	122.7	*122.4*
bottom flange (13)-12	129.9	*129.2*	119.5	*118.9*	122.7	*122.4*

Note: negative sign marks compression.

Table 1 shows that additional analysis helped to establish actual normal force basing on the edge strains recording. "Recorded" normal forces obtained assuming linear stress distribution differ from calculated ones by 5÷25%, while after additional analysis – by 2÷6%.

It is possible to verify lab test results with relatively simple FE model of the tested structure. However, in such cases, additional local detailed modelling may be necessary. Sometimes this approach is more effective than detailed modelling of the whole structure.

REFERENCES

[1] Macha E., Nowicki A., Szata M.: *Pomiary tensometryczne materiałów i konstrukcji przy obciążeniach statycznych*, Wrocław, Politechnika Wrocławska, 1977.

[2] Jastrzębski P., Mutermilch J., Orłowski W.: *Wytrzymałość materiałów*, Warszawa, Arkady, 1974.

[3] *Abaqus Users Manual*, 1999.

Parallel strategies in structural linear and non-linear analysies

J.Y. Cognard*, A. Poulhalec
E.N.S. Cachan - Antenne de Bretagne, campus de Ker Lann, 35170 Bruz, France
e-mail: cognard@bretagne.ens-cachan.fr

P. Verpeaux
CEA Saclay, DMT/SEMT, 91191 Gif sur Yvette Cedex, France
e-mail: pv@semt2.smts.cea.fr

ABSTRACT

Summary We present parallel strategies suited to the simulation of a wide class of non-linear problems. On one hand, a domain decomposition technique or a parallel direct solver are used to efficiently solve large linear global problems. On the other hand, in order to have a well-balanced load for the integration of the constitutive laws we propose to use a kind of second domain decomposition. The implementation of these strategies are carried out starting from the parallel language of the finite element code CAST3M.

Introduction

The numerical costs of complex non linear Finite Element simulations can be reduced by using efficient numerical strategies, and by using parallel computers whose performances increase rapidly [7]. However, one observes generally that the parallelization of existing codes leads to complex developments, and that good parallel performances are usually obtained at the expense of portability.

The objective of this communication is to present a parallel approach suited to the simulation of a wide class of non-linear problems for quasi-static response. It is based on the use of two domain decompositions which goal is to balance the computation load over the various processors by limiting the redistributions of the tasks. A good load balancing of the tasks as well as keeping the communications as low as possible are key to an effective parallel algorithm.

Parallel approach using two domain decompositions

Non-linear problems are usually solved using the so-called incremental methods, which split the studied time interval in a series of several increments of time. Using a guess for the displacement leads to a time-independent non-linear problem, which is solved by means of NEWTON type iterative methods. This algorithm leads mainly to solve two types of sub-problems, which can be time consuming for large number of degrees of freedom and for strongly non-linear constitutive laws, i.e. for industrial type problems. The proposed parallelization strategy uses the mechanical properties of these two types of sub-problems.

On one hand, domain decomposition techniques [4] can be used to solve the linear global problems. In order to be compatible with the BFGS type convergence speed-up strategies we have chosen a direct resolution of the condensed problem where we can reuse existing modules of the sequential code. Moreover, this technique gives the same numerical solution that the

direct approach and multifrontal factorization techniques provide good numerical performances for sequential and parallel approaches [1].

On the other hand, the CPU time spent to integrate the constitutive laws depends on several parameters: the material behavior, the position of the integration point in the structure, the history of the loading path, … Therefore, for complex simulations, it is nearly impossible to predict the space evolution of the numerical cost of this part with respect to the increments. In order to have a well-balanced load during the integration of the constitutive laws, without communication, we propose the use of a kind of second domain decomposition (decomposition in blocs of elements) [3]. An optimization of the communications between the two domain decompositions is necessary to obtain good numerical performances.

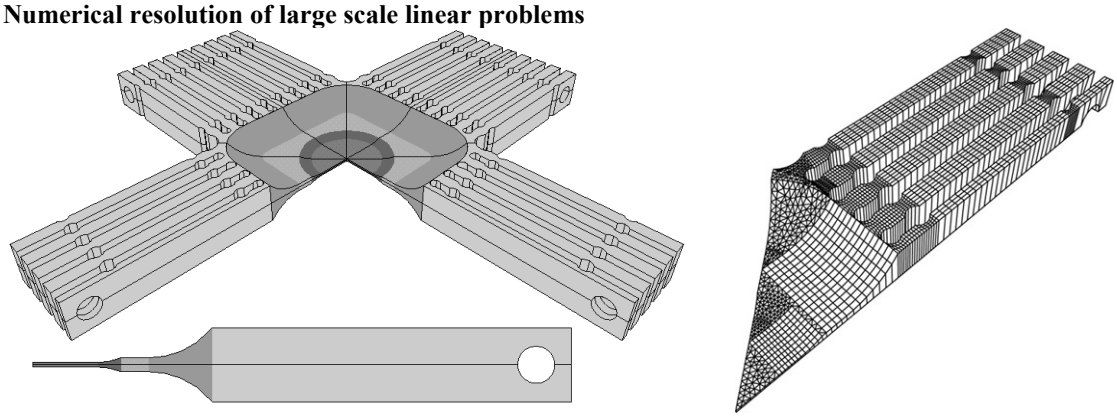

Figure 1: Geometry of the biaxial tensile specimen and model with 49 689 d.o.f.

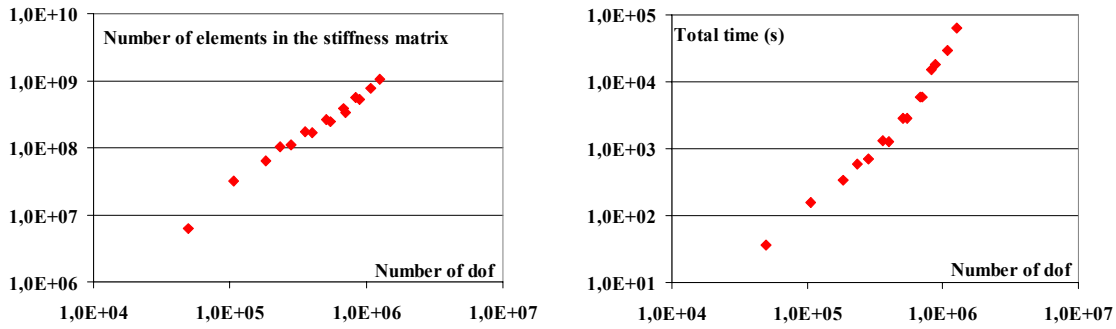

Figure 2: Numerical results for elastic linear computations

The computational cost of the factorization of the stiffness matrix quickly increases with the number of degrees of freedom and often takes an important part in the complete CPU time of non linear simulations. In order to limit fill in the factorization of the matrix, which has a great influence on the numerical cost for large scale problems, a “nested dissection” ordering approach [5] has been implemented. The principle is to carry out a partition of a mesh in two zones separated by an interface. The order of classification of the nodes is initially the nodes of a zone, then the nodes of the other zone, then those of the interface. The two zones being uncoupled, during factorization each one will be factorized independently, then the factorization of the interface will ensure the coupling of the zones. It is in the interface that some zeros will remain at the factorization step. The process is then repeated recursively on each zone. In order to minimize the complete size of the factorized matrix, well-balanced sub-domains are

requested and the size of the interfaces have to be minimize. This optimization problem is carried out using a Monte Carlo method. In fact, this strategy is similar to a domain decomposition technique.

Tests of a "multithreads" parallel version of this linear solver have been carried out on an IBM-SP2-WH2 with 4 processors and 4 Gb shared memory. A biaxial tensile specimen (Figure 1) [2] has been used. The symmetries allow us to study only one-sixteenth of the specimen. Displacements are prescribed on one part of the bores that are drilled into the combs. Figure 2 presents, the size of the problem and the walk-clock time with respect to the number of d.o.f.. On such a computer, for meshes up to 500 000 d.o.f. a speed-up of more than 2 is reached with 4 processors (the parallelization of the ordering phase can increases the speed-up). For larger problems the management time of the virtual memory (swap on disk) is penalizing for the walk-clock time, but it allows to solve large problems.

Parallel implementation and an example of non linear simulation

In order to allow an easy development of parallel applications by using modules of the sequential code, an extension of the user language of the code CAST3M has been done [2, 3]. The idea is to develop a machine-independent parallel programming language, which allows the user of the code to distribute computations over the different processors of a parallel computer, knowing that the system ensures the coherence of data during the sequence of tasks while limiting waiting phases of applications. Thus he can reuse directly a great part of the sequential code (the pre processor, the post processor and computational modules) to experiment parallel strategies. The propounded system, that takes into accounts the capabilities of the various computers types, allows two levels of parallelization: the user level and the programming level only used for fine performance tuning.

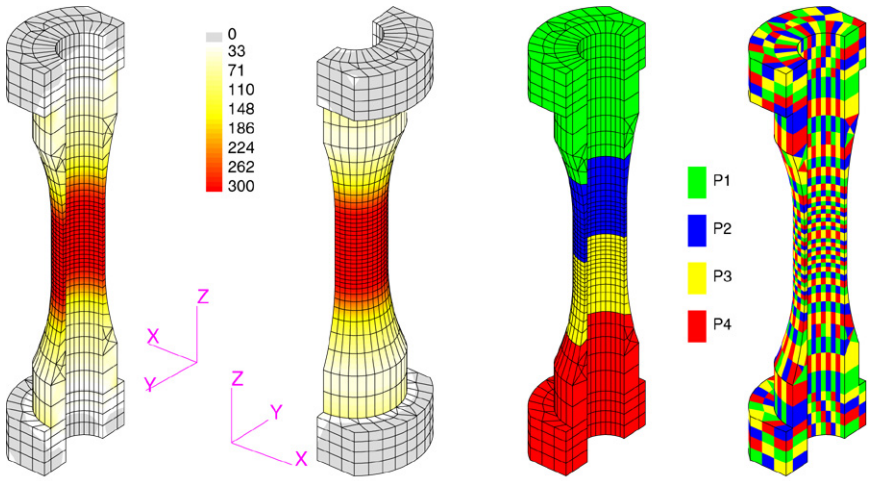

Figure 3: Geometry and model of the specimen – mises equivalent stress

The implementation of the parallel strategy for non-linear simulations is carried out starting from the parallel user language of CAST3M. We present the behaviour of this parallel algorithm on a traction-torsion specimen (figure 3) subjected to a combined loading of traction-torsion by imposing on the extreme sections an axial displacement $Uz = U_0 \sin(2\omega t)$ and a rotation $\Theta = \Theta_0 \sin(\omega t)$. The behavior of material is modelled by A Chaboche's viscoplastic model (material Z6CNDT17-11, AISI 316) [6]. The most stressed zone of the specimen the central

part. The two decompositions are presented figure 3. Figure 5 represents the evolution of the strain and the stress in a point of the center section, for a cycle of loading.

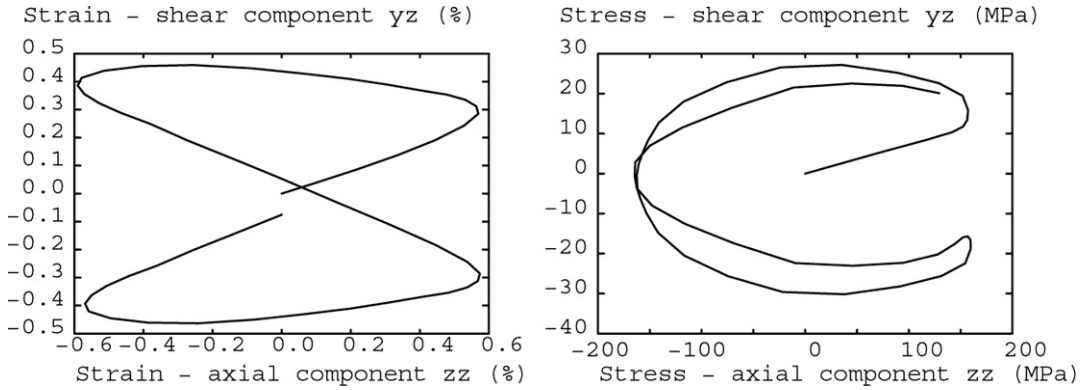

Figure 3: Evolution of the stress et strain in the central part of the specimen

For the resolution of this 3D viscoplastic problem with more than 250 000 d.o.f. a speed-up of more than 3.1 (wall clock time) is reached with 4 processors on an IBM-SP2-WH2 with 4 Gb shared memory. The first tests show possibilities of the proposed parallel approach for non linear simulations: a good load balancing of the computations over the different processors is obtain with out redistributions of the tasks.

REFERENCES

[1] P.R. Amestory, I.S. Duff and J.Y. L'Excellent, Multifrontal parallel distributed symmetric and unsymmetric solvers. *Comput. Methods Appl. Mech. Eng*, **184**, 501-520, (2000).

[2] J.Y. Cognard, F. Thomas and P. Verpeaux. An integrated approach to solving mechanical problems on parallel computers. *Advances in Engineering Software*, **31**, 885-899, (2000).

[3] J.Y. Cognard, A. Poulhalec, F. Thomas and P. Verpeaux. Parallel approach by task distributions using two domain decompositions suited to non-linear simulations. *Developments in Engineering Computationnal Technology*, Civil-Comp, 229-240, (2000).

[4] C. Farhat and F. X. Roux. Implicit parallel processing in structural mechanics. *Computational Mechanics Advances*, Oden J. Tinsley (ed), North Holland, (1994).

[5] M.T. Heath and P. Raghavan. A cartesian parallel nested dissection algorithm. SIAM J. Matrix Anal. Appl., **16**, 235-253, (1995).

[6] J. Lemaitre and J. L. Chaboche. Mécanique des matériaux solides, Dunod Paris, (1985).

[7] A. K. Noor. New computing systems and future high performance computing environments and their impact on structural analysis and design. *Comp. & Struct.*, **64**, 1-30, (1997).

Dynamics of Multilink Transformable Structures with a Shape Memory Wire Actuator

Mark M. Frenkel* **and Vladimir G. Bykov**
Faculty of Mathematics and Mechanics
St. Petersburg State University, St. Petersburg, Russia
e–mail: info@robotics.ru

ABSTRACT

Summary Dynamics of disclosure of a multilink cell of a parallelogram type used in transformable trusses is considered. Existence of four various states (phases of disclosure) under cell transformation by means of shape memory wire actuator is shown. The effect of the heating velocity of the wire and of the resistance force moments in hinges on the number and sequence of alternation of the various phases of disclosure is studied.

The multilink transformable structures find more and more broad application in various areas of engineering. Among various types of drives used in similar constructions, the wire actuators with a shape memory effect (SME) have a good perspective. Due to high reliability, noiselessness, the capability for working in vacuum and in weightless, SME-drives have been using in space industry.

Let's consider dynamics of disclosure of one cell of a parallelogram type used in transformable truss. The cell consists of four rigid links forming hinged tetragon $ABCD$ (Fig.1) and of lever drive mechanism DEB (Fig.2).

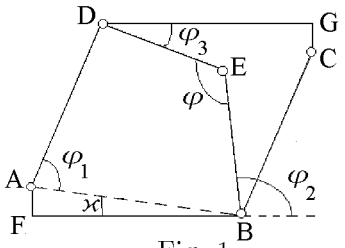

Fig. 1.

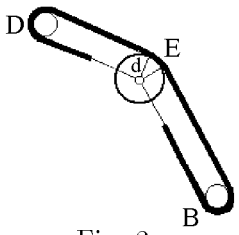

Fig. 2.

The hinges A, B, C and D are tops of the parallelogram. The lever mechanism consists of two rigid links BE and DE and wire SME-drive bending around the hinge E on a directing arc with the radius d [2]. The disclosure of a cell is provided by contraction of length of a wire through heating it by an electric current.

Let's denote through l_1, l_2, l_3, and l_4 the lengths of links AD, BE, DE, and BC correspondingly ($l_1 = l_4$); l_5 and l_6 are the lengths of sections AB and AF; φ_1 is the angle between links AD and FB, φ_2 is the angle between links FB and BE, φ_3 is the angle between links DE and DG.

We can consider element AFB as fixed and write the expression for kinetic energy as follow:

$$T = \frac{1}{2}\left[(J_1^A + J_4^B + m_5 l_1^2)\dot{\varphi}_1^2 + J_2^B\dot{\varphi}_2^2 + J_3^*\dot{\varphi}_3^2 + m_3(V_3^*)^2\right], \qquad (1)$$

where J_1^A is the moment of inertia of link AD concerning the point A, J_2^B and J_4^B are the moments of inertia of links BE and BC concerning the point B, J_3^* is the moment of inertia of a link DE concerning its centre of inertia, m_3 is mass of link DE, m_5 is mass of the element DGC, V_3^* is the velocity of the centre of inertia of the link DE.

Substituting expression for a velocity of centre of inertia of the link DE in (1) we get

$$V_3^{*2} = l_2^2\dot{\varphi}_2^2 + l_3^{*2}\dot{\varphi}_3^2 + 2l_2l_3^*\cos(\varphi_2+\varphi_3)\dot{\varphi}_2\dot{\varphi}_1,$$

where l_3^* is the distance from the point E up to the centre of inertia of the link DE, and taking into account, that $\varphi_2+\varphi_3=\varphi$, we obtain

$$\begin{aligned} T = \frac{1}{2}\Big\{ &\left(J_3^* + m_3 l_3^{*2}\right)\dot{\varphi}^2 + \left(J_1^A + J_4^B + m_5 l_1^2\right)\dot{\varphi}_1^2 + \\ &+ \left[J_2^B + J_3^* + m_3\left(l_2^2 + l_3^{*2} - l_2 l_3^*\cos\varphi\right)\right]\dot{\varphi}_2^2 + \\ &+ 2\left(J_3^* + m_3 l_3^{*2} - m_3 l_2 l_3^*\cos\varphi\right)\dot{\varphi}\dot{\varphi}_2\Big\}. \end{aligned} \tag{2}$$

The cell has one degree of freedom. We select the angle φ as a generalized coordinate, then the other angles φ_1 and φ_2 can be expressed in the generalized coordinate through the geometric relations

$$\begin{aligned} \varphi_1 &= -\kappa + \arccos\frac{l_1^2 + l_5^2 - x(\varphi)^2}{2l_1l_5} \\ \varphi_2 &= \pi - \kappa - \arccos\frac{l_2^2 - l_3^2 + x(\varphi)^2}{2l_2x(\varphi)} - \arccos\frac{l_5^2 - l_1^2 + x(\varphi)^2}{2\,l\,x(\varphi)}, \end{aligned} \tag{3}$$

where κ - angle ABF, $x(\varphi)^2 = l_2^2 + l_3^2 - 2l_2l_3\cos\varphi$.

Substituting (3) in expression for kinetic energy (2) and supposing, that the disclosure of a cell occurs under weightless, the equation of motion of a cell may be written as

$$\frac{d}{dt}\frac{\partial T}{\partial\dot{\varphi}}\frac{\partial T}{\partial\varphi} = Fd - M_S, \tag{4}$$

where F is the force of a tension in the wire drive, M_S is the total moment of the resistance forces set to the hinge E.

We suppose that the resistance forces acting at the hinges A, B, C, and D are identical and designate appropriate moments as M_1. We denote the resistance moments in hinges B and D of the lever mechanism as M_2, and in the hinge E as M_3. Then the total moment of resistance forces may be written as [2]

$$M_S = \frac{4M_1l_2l_3\sin\varphi}{\sqrt{l_1^2l_5^2 - [l_2l_3(1+\cos\varphi) - l_1l_6]^2}} + M_2 + M_3. \tag{5}$$

As shown in [3], for some conditions of heating of the drive the lever mechanism may "kept ahead of the drive" when it moves due to inertia, i.e. the length of a wire has no time to shorten with the disclosing of the mechanism. With an excess of the length there occurs "a slack from a wire" and from this moment the drive becomes non active. Therefore

the transforming cell can be in four various condition, which we call later the phases of disclosure:

phase 1 - static tension of the drive - on heating of the wire the force of a tension is growing but it's insufficient for overcoming the resistance forces in hinges;

phase 2 - active motion - cell is being uncovered by the force of a tension in the drive;

phase 3 - motion on inertia - the drive has "a slack from a wire", but the cell is being uncovered on inertia;

phase 4 - removing of the slack - the cell is motionless and the excess of the length of a wire is reducing by heating of the drive.

Let's consider the phases of disclosure in more details. We assume a linear dependence of a drive length modification L on the temperature T during return martensitic transformation [3]

$$L = L_1 - u(T - A_H), \text{ at } A_H < T < A_K$$

where $u = (L_1 - L_0)/(A_K - A_H)$; L_0 and L_1 are the lengths of a wire with SME in it initial (not tension) and in a tension state; A_H and A_K are the temperatures of the beginning and ending of the return martensitic transformation.

Let's assume that the dependence of temperature on time $T(t)$ during heating of the drive to be monotonically growing function. Then, within the limits of the theory of elasticity, the tension force of the drive in the phase 1 will also monotonically increase

$$F(t) = \frac{SE_a}{L_0} u[T(t) - A_H],$$

where S is the cross-section area of a wire, E_a is the austenite module of an elasticity. When the rotation moment created by the drive of the tension force exceeds a maximum moment of the resistance forces the lever mechanism of a cell will begin to be uncovered. Therefore, the time of the beginning of the second phase is determined from the equation $F(t) = M_s/d$.

In the phase 2 links of a cell is moved under the drive of the tension force, which now depends also on the disclosure angle φ magnitude

$$F(t) = \frac{SE_a}{L_0} u[T(t) - A_H - d\varphi]. \tag{6}$$

The phase of active motion will be completed either with full disclosure of a cell, or with its stop and transition to the phase 1, or with a slack of the drive — transition to the phase 3.

In the phase 3 which can occur only after a phase of active motion when an excess of the length of the drive takes place, i.e. under condition

$$\Delta L = \varphi(t)d - u[T(t) - A_H] > 0,$$

the drive tension force is equal to zero. The phase of the inertial motion is completed either with tension of a wire (transition to phase 2), or with stop of a cell (transition to phase 4), or with its full disclosure.

In the phase 4 the length of a wire due to heating decreases monotonically. Thus the slack formed during the inertial motion is removed. When condition $\Delta L(t) \leq 0$ is satisfied the phase 4 is completed with transition to the phase 1

Thus, during disclosure, the cell is either motionless (phase 1 and 4), or its motion is described by equation (4), where the tension force F is calculated using by formula (6) for the phase 2 and $F = 0$ for the phase 3, and the sequence of alternation of phases is not initially known. On Fig. 3 the scheme of numerical calculation algorithm of disclosure of a cell is presented.

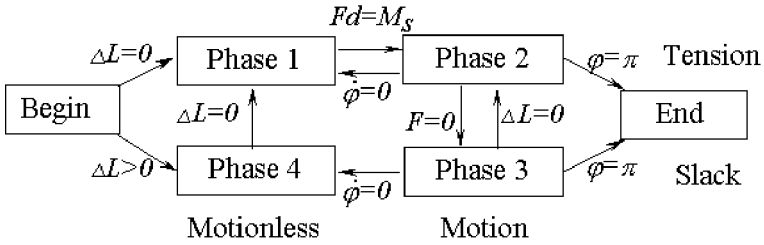

Fig. 3.

As an example we analyzed numerically the cell disclosure of the truss "Rapana" [2]. The change of the length of the drive due to martensitic transformation was supposed to be equal to 5%, i.e. $L_1 = 1.05L_0$. The dependence of the temperature on time was assumed to be linear $T(t) = A_{_H} + vt$.

The obtained results can form the basis for the development of control methods for the processes of disclosure of transformable structures. One should take into account the following effects:

The changing of moments of the resistance forces in the hinges at constant heating velocity results in the changing of the number and sequence of the alternation of various phases of disclosure;

The changing of the heating velocity of the drive effects on the character of dependence of the angle φ and tension force on time. With the increasing of the heating velocity the total number of phases decreases and the duration of the inertial motion (phase 3) increases. It is possible to achieve a full elimination of this phase from the process of disclosure by reducing the heating velocity .

REFERENCES

[1] Razov A.I., Chernyavskij A.G. *Application of Alloys with Shape Memory Effect in Space Technology: Last and Future.* Mechanisms of a strain and destruction of perspective materials. Proc. XXXV Workshop on Actual Problems of Strength. Pskov, 1999. Part I. PP. 254 - 258 (in Russian).

[2] Bykov V.G., Razov A.I. Frenkel M.M. *Static Account of the Wire SME-drive of Transformable Construction.* Vestnik TGU. 1998. Vol. 3, Issue 3. PP. 291 - 292 (in Russian).

[3] Frenkel M.M. *Dynamics of the Lever Mechanism with a Shape Memory Wire Drive.* Mechanisms of a strain and destruction of perspective materials. Proc. XXXV workshop on Actual problems of strength. Pskov, 1999. Part I. PP. 51 - 56 (in Russian).

Formulation of a flat three node shell elasto-plastic element

Aleksandar Filipovski and Costin Pacoste
Department for Mechanics
Royal Institute of Technology, Stockholm, Sweden
e–mail: aleksandar.filipovski@mech.kth.se

ABSTRACT

Summary A shell element based on a flat facet three node element, previously formulated in [4] for investigation of the elastic stability problems of shells is investigated here in the elasto-plastic domain. The element is based on the natural formulation of TRIC element, [5], but modifications of the membrane and drilling stiffness were done using interpolation scheme from [1]. The element is subjected to extension and flexure. Total number of eighteen Cartesian degrees of freedom are included. Isotropic hardening of the material is assumed during numerical tests.

Introduction

Two sets of local coordinates are used to define kinematics of the element: the local Cartesian coordinate system, $X_1^e X_2^e X_3^e$, with the origin at the triangle's centroid, and natural coordinate system $\alpha\,\beta\,\gamma$, with three axes parallel to the sides of the triangle. Following the main idea of free formulation theory, [7], that displacement

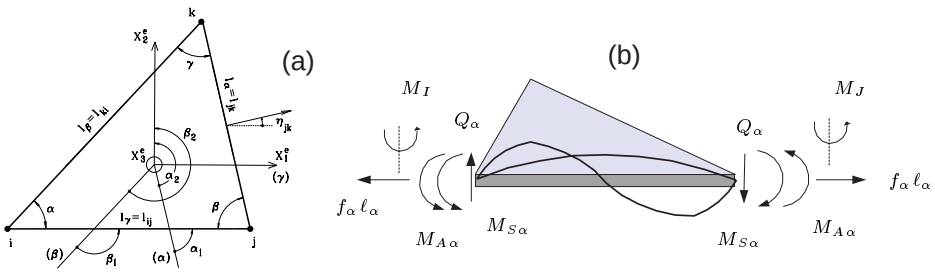

Figure 1: (a) The Cartesian and natural coordinates. (b) Generalized forces and moments in the natural coordinate system for the side (α).

field can be expressed as combination of rigid-body and constant-strains modes (rc-modes) and higher-order modes (h-modes), but, starting from a different point of view, trough *the natural mode method*, developed by Argyris and co-workers[1] the state of displacement in the element is described with: $\boldsymbol{\rho} = [\boldsymbol{\rho}_0\ \ \boldsymbol{\rho}_N]$, where $\boldsymbol{\rho}_0$ is the vector of six rigid-body motion while $\boldsymbol{\rho}_N$ contains the twelve amplitudes of the pure deformational modes, called *natural modes*. These modes are related to the nodal displacements and rotations on the triangular edges. For the TRIC element, four natural straining modes are defined for each side. These modes are: axial stretching, $\boldsymbol{\rho}_{cm} = [\varepsilon^o_{t\alpha}\ \varepsilon^o_{t\beta}\ \varepsilon^o_{t\gamma}]^T$, symmetric bending, $\boldsymbol{\rho}_{cs} = [\psi_{S\alpha}\ \psi_{S\beta}\ \psi_{S\gamma}]^T$, and antisymmetric rotation, $\boldsymbol{\rho}_{ha} = [\psi_{A\alpha}\ \psi_{A\beta}\ \psi_{A\gamma}]^T$, that can be split into two components: antisymmetric bending, $\boldsymbol{\rho}^b_{ha} = [\psi^b_{A\alpha}\ \psi^b_{A\beta}\ \psi^b_{A\gamma}]^T$, together with a transverse shear mode, $\boldsymbol{\rho}^s_{ha} = [\psi^s_{A\alpha}\ \psi^s_{A\beta}\ \psi^s_{A\gamma}]^T$. In addition, three azimuth rotational modes, $\boldsymbol{\rho}_{hm} = [\psi_i\ \psi_j\ \psi_k]^T$, are included. The natural modes vector, $\boldsymbol{\rho}_N$, has the form:

$$\boldsymbol{\rho}_N = [\varepsilon^o_{t\alpha}\ \varepsilon^o_{t\beta}\ \varepsilon^o_{t\gamma}\ \psi_{S\alpha}\ \psi_{S\beta}\ \psi_{S\gamma}\ \psi_{A\alpha}\ \psi_{A\beta}\ \psi_{A\gamma}\ \psi_i\ \psi_j\ \psi_k] \tag{1}$$

and can be divided on constant strain modes, $\boldsymbol{\rho}_c = [\boldsymbol{\rho}_{cm}\ \boldsymbol{\rho}_{cs}]^T = [\varepsilon^o_{t\alpha}\ \varepsilon^o_{t\beta}\ \varepsilon^o_{t\gamma}\ \psi_{S\alpha}\ \psi_{S\beta}\ \psi_{S\gamma}]^T$ and higher order modes, $\boldsymbol{\rho}_h = [\boldsymbol{\rho}_{ha}\ \boldsymbol{\rho}_{hm}]^T = [\psi_{A\alpha}\ \psi_{A\beta}\ \psi_{A\gamma}\ \psi_i\ \psi_j\ \psi_k]^T$.

[1] [5] references all basic papers of Argyris and co-workers on natural mode method.

Natural strains, stresses and internal forces

Total natural axial strain and transverse shear strains can be derived as:

$$\boldsymbol{\varepsilon}_t = \boldsymbol{B}_{tc}\boldsymbol{\rho}_c + \boldsymbol{B}_{th}\boldsymbol{\rho}_{ha} \ , \ \boldsymbol{\gamma}_t = \boldsymbol{B}_{sh}\,\boldsymbol{\rho}^s_{ha} \tag{2}$$

where, $\boldsymbol{B}_{tc}$ and $\boldsymbol{B}_{th}$ depend on coordinates, and $\boldsymbol{B}_{sh}$ is diagonal matrix containing 0.5, [2]. Energy orthogonality is in Ref. [4] enforced by replacing $\boldsymbol{B}_{th}$ by: $\bar{\boldsymbol{B}}_{th} = \boldsymbol{B}_{th} - \frac{1}{V}\int_V \boldsymbol{B}_{th}\,dV$.

In the natural coordinate system the constitutive relations between stress and strain rates reads

$$\dot{\boldsymbol{\sigma}}_t = \left[\begin{array}{ccc} \dot{\sigma}_\alpha & \dot{\sigma}_\beta & \dot{\sigma}_\gamma \end{array}\right]^T = \boldsymbol{\kappa}_t\dot{\boldsymbol{\varepsilon}}_t \ , \quad \dot{\boldsymbol{\tau}}_t = \left[\begin{array}{cc} \dot{\tau}_\alpha & \dot{\tau}_\beta \quad \dot{\tau}_\gamma \end{array}\right]^T = \boldsymbol{\chi}_t\boldsymbol{\gamma}_t \tag{3}$$

Natural axial stresses and transverse shear stresses are uncoupled. Coefficients κ_{ij}, and χ_{ij} are related to the counterpart coefficient in the local Cartesian coordinate system.

Axial load and symmetric bending moments which are the components natural internal forces vector (Fig. 1 b), $\boldsymbol{f}_N$, are respectively,

$$\left[\begin{array}{ccccc} f_\alpha l_\alpha & f_\beta l_\beta & f_\gamma l_\gamma & M_{S\alpha} & M_{S\beta} \quad M_{S\gamma} \end{array}\right]^T = \int_v \boldsymbol{B}^T_{tc}\boldsymbol{\sigma}_t\,dv \tag{4}$$

while antisymmetric bending and azimuth moments related to asymmetric bending drilling rotations, respectively, can be obtained as: $\boldsymbol{M}_A = \boldsymbol{k}_A\boldsymbol{\rho}_{ha}$, and $\boldsymbol{M}_I = \boldsymbol{k}_z\boldsymbol{\rho}_{hm}$, considering related deformations as elastic.

Relation between Cartesian and natural stress and strain states can be written as

$$\left(\begin{array}{c} \boldsymbol{\varepsilon}_t \\ \boldsymbol{\gamma}_s \end{array}\right) = \left[\begin{array}{cc} \boldsymbol{T}^T_B & \cdot \\ \cdot & \boldsymbol{T}_s \end{array}\right]\left(\begin{array}{c} \boldsymbol{\varepsilon}' \\ \boldsymbol{\gamma}' \end{array}\right) \quad \wedge \quad \left(\begin{array}{c} \boldsymbol{\sigma}_t \\ \boldsymbol{\tau}_s \end{array}\right) = \left[\begin{array}{cc} \boldsymbol{T}^{-1}_B & \cdot \\ \cdot & \boldsymbol{T}_s \end{array}\right]\left(\begin{array}{c} \boldsymbol{\sigma}' \\ \boldsymbol{\tau}' \end{array}\right) \tag{5}$$

where $\boldsymbol{\sigma}' = \left(\begin{array}{ccc} \sigma_x & \sigma_y & \sqrt{2}\tau_{xy} \end{array}\right)^T$, and $\boldsymbol{\tau}' = \left(\begin{array}{cc} \tau_{xz} & \tau_{yz} \end{array}\right)^T$, represent Cartesian stress vectors, and transformation matrices depend on the orientation of the local Cartesian system.

Natural stiffness matrix $\boldsymbol{k}_N$

Natural stiffness matrix will be:

$$\underset{12\times 12}{\boldsymbol{k}_N} = \left[\begin{array}{ccc} \underset{6\times 6}{\boldsymbol{k}_{\rho\,c}} & \cdot & \cdot \\ \cdot & \underset{3\times 3}{\boldsymbol{k}_{\rho\,h}} & \cdot \\ \cdot & \cdot & \underset{3\times 3}{\boldsymbol{k}_z} \end{array}\right] \tag{6}$$

where $\boldsymbol{k}_{\rho\,c}$ is the tangent constant strain stiffness matrix that refers to the constant strain modes $\boldsymbol{\rho}_c$, $\boldsymbol{k}_{\rho\,h}$ is the higher order stiffness matrix that refers to the higher order modes $\boldsymbol{\rho}_{ha}$, and, $\boldsymbol{k}_z$, is the azimuth stiffness matrix which refers to drilling modes $\boldsymbol{\rho}_{hm}$. In this paper approach given in [3] is investigated so, the influence of the shearing stresses on the elasto-plastic behaviour of the element is ignored and stiffness matrices $\boldsymbol{k}_{\rho\,h}$, and $\boldsymbol{k}_z$ remain elastic and can be found in [5] and [4], respectively.

Constant strain stiffness matrix can be obtained from the following expression: $\boldsymbol{k}_{\rho\,c} = \int_v \boldsymbol{B}^T_{tc}\,\boldsymbol{\kappa}_t\boldsymbol{B}_{tc}\,dv$, so the natural tangential material stiffness $\boldsymbol{\kappa}_t$ determines element's elasto-plastic behaviour. This matrix is obtained from its Cartesian counterpart, $\boldsymbol{c}_t$ that is related to consistent tangential operator $\boldsymbol{c}_T$,

$$\boldsymbol{\kappa}_t = \boldsymbol{T}^{-1}_B\boldsymbol{c}_t\boldsymbol{T}^{-T}_B \tag{7}$$

In order to incorporate the natural force vector and stiffness matrix, into the Cartesian framework the transformation from natural coordinates is necessary. The required transformation matrix [2] can be constructed as: $\boldsymbol{a}_N = [\partial\boldsymbol{\rho}_N/\partial\bar{\boldsymbol{q}}^e_n]$, $l = 1,12\ n = 1,18$, where the vector: $\bar{\boldsymbol{q}}^e = [\,\bar{\boldsymbol{u}}^e_i\ \bar{\boldsymbol{\vartheta}}^e_i\ \bar{\boldsymbol{u}}^e_j\ \bar{\boldsymbol{\vartheta}}^e_j\ \bar{\boldsymbol{u}}^e_k\ \bar{\boldsymbol{\vartheta}}^e_k\,]$, contains the local displacements at the three nodes of the element. Relations between natural and local Cartesian coordinates for the original TRIC element are defined using strictly geometrical arguments. The membrane formulation from [4] using the third order interpolation scheme introduced by Allman, [1] is adopted. This have direct influence on transformation matrix $\boldsymbol{a}_N$ and azimuth stiffness matrix.

Consistent tangent operator

Cartesian coordinate system is used for the elasto-plastic analysis. The transformation between natural and Cartesian measures is easy with the help of the transformation (5). Strain increments (in Cartesian coordinates) are re-computed as a change in strains from the last converged equilibrium (the end of the last increment). The stresses are also updated from the stresses at the end of the last converged increment. With this procedure (strongly recommended in [6]) a spurious unloading is avoided. An implicit integration algorithm for elasto-plastic constitutive equations in plane stress analysis presented in [8] is adopted. This algorithm produces error of the same order as the one obtained in three dimensional analysis with the radial return algorithm, [6].

A bilinear strain- stress law with an isotropic hardening rule is adopted. Parameters which define relation are: yield stress, σ_Y, elasticity modulus, E, shear modulus, G, Poison coefficient, ν, and hardening parameter H.

The consistent tangent elastoplastic stress-strain matrix which maintains the quadratic convergence of the Newton-Raphson method used at the structural level is so,

$$\boldsymbol{c}_T = \boldsymbol{R}\left(\boldsymbol{I} - \frac{\boldsymbol{a}^T\,\boldsymbol{R}\boldsymbol{a}}{\boldsymbol{a}\,\boldsymbol{a}^T\,\boldsymbol{R} + \dfrac{H}{1-\Delta\lambda_1\,H}}\right) \tag{8}$$

where,

$$\boldsymbol{R} = \begin{bmatrix} \frac{E}{2(1-\nu)A_1} + \frac{G}{A_2} & \frac{E}{2(1-\nu)A_1} - \frac{G}{A_2} & 0 \\ \frac{E}{2(1-\nu)A_1} - \frac{G}{A_2} & \frac{E}{2(1-\nu)A_1} + \frac{G}{A_2} & 0 \\ 0 & 0 & \frac{G}{A_2} \end{bmatrix}, \quad \boldsymbol{a}^T = \frac{1}{\sigma_e}\begin{pmatrix} 2\sigma_x - \sigma_y & 2\sigma_y - \sigma_x & 6\tau_{xy} \end{pmatrix} \tag{9}$$

and A_1, A_2 and $\Delta\lambda_1$ are parameters depending on plastic strain-rate multiplier, $\Delta\lambda$, and effective stress, σ_e. Numerical integration is performed along z direction using Newton-Cotes closed quadratures (rules). The stress

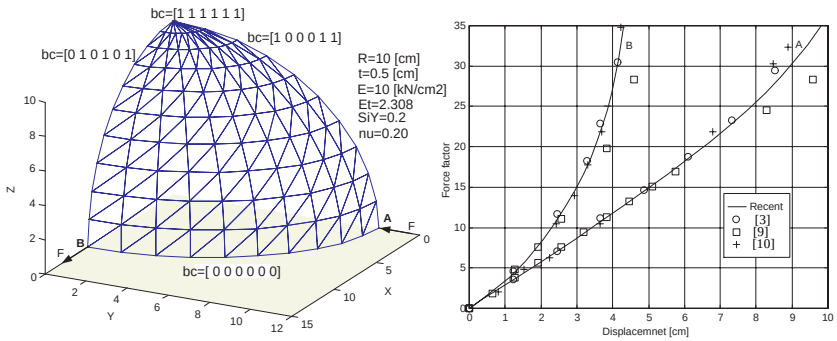

Figure 2: Pinched hemispherical shell.

and strain values are calculated for material points (only one point per layer) through thickness of the triangle i.e. along z-axis which pass the centre of the triangle.

Examples

Figure 2 shows one quarter of the hemispherical shell with a free edge pinched by two concentrated reference forces $F_x = -F_y = 0.001[kN]$. The total number of 190 elements is employed trough co-rotational formulation. The load displacement diagram for two loading points A and B is given. The results are compared with [3], [9] and [10].

Figure 3 shows one octant of the short thin cylinder pinched by two radial reference forces $F_o = F_z = 100[N]$, in the middle of the structure. The boundary conditions were given on the figure. The total number of 392 elements is used. The results are compared with [3], [9], [10] and [11].

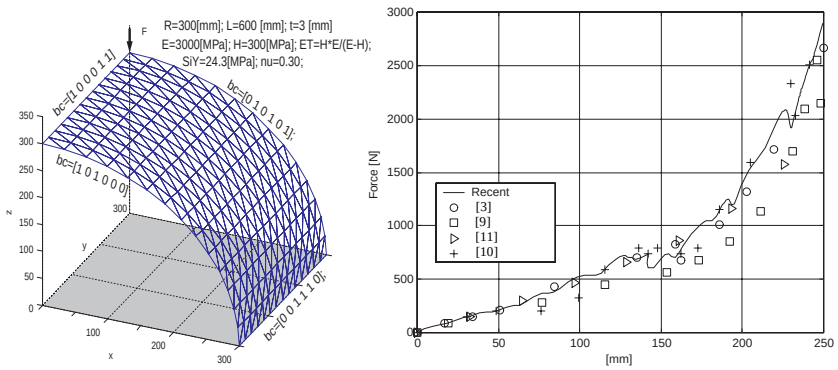

Figure 3: Pinched short cylinder.

REFERENCES

[1] Allman, D. J. Evaluation of the constant strain triangle with drilling rotations. *Inter. J. Num. Meth. Eng.*, **26**, 2645–2655, (1988).

[2] Argyris, J.H. and Papadrakis, M. and Apostolopoulou, C. and Koutsourelakis,S. The TRIC shell element: theorethical and numerical investigation. *Comp. Meth. Appl. Mech. Eng.*, **182**, 217–245, (2000).

[3] Argyris,J. and Papadrakakis,M. and Karapitta,L. Elastoplastic analysis of shells with the triangular element TRIC. In M. Papadrakakis and E. Onate , editors, *Comp. Meth. for Shells and Spatial Struct., IASS-IACM* , pages 1–30, Athens, (2000).

[4] Pacoste,C. and Eriksson, A. Element formulation and numerical techniques for stability problems in shells. *Comp. Meth. Appl. Mech. Eng., preprint*, (2001).

[5] Tenek, L. T. and Argyris,J. H. *Finite element analysis for composite structrures*. Kluwer Academic Publishers, Dordrecht, (1998).

[6] Crisfield, M. A. . *Non-linear finite elemnet analysis of solids and structures*. John Wiley and Sons, Chichester, (1991).

[7] Bergan, P. G. and Nygård, M. K. Nonlinear shell analysis using free formulation finite elements. In P. G. Bergan et al., editors, *Finite element methods for nonlinear problems*, pages 317–338, Berlin. Springer-Verlag, (1985).

[8] Jetteur, P. H. and Cescotto, S. A mixed finite element for the analysis of large inelastic strains. *Inter. J. Num. Meth. Eng.*,**31**, 229–239, (1991).

[9] Simo, J.C. and Kennedy, J.G. On a stress resultant geometrically exact shell model. Part V, Nonlinear plasticity: formulation and integration algorithms. *Comp. Meth. Appl. Mech. Eng.*, **96**, pages 133–171, (1992).

[10] Sorić, J. and Montag, U. and Krätzig,W.B. On the increase of computational algorithm efficiency for elasto-plastic shell analysis. *Eng.Comp.*, **14**, pages 75–97, (1997).

[11] Wriggers, P. and Eberlein, E. and Reese, S. A comparison of three dimensional continuum and shell elements for finite plasticity. *Int. J.Solids Struct.*, **33**, pages 3309–3326, (1996).

Efficient collapse analysis of stiffened panels

B.Skallerud*, **A.K.Mohammed and J.Amdahl**

* Department of Applied Mechanics
Norwegian University of Science and Technology, Norway
e–mail: bjorn.skallerud@mtf.ntnu.no
Department of Marine Structures
Norwegian University of Science and Technology, Norway

ABSTRACT

Summary The present study addresses the merits of a nonlinear Morley thin shell finite element employed in inelastic, large or moderate rotation problems. Cylindrical shells and stiffened plates are employed as examples. Efficiency in terms of cpu consumption is commented.

INTRODUCTION

During accidental conditions ships and offshore structures are subjected to extreme loads. Local collapse is accepted provided that global integrity is not put into jeopardy. If such situations are to be considered in a nonlinear finite element analysis, efficient computational algorithms are required. The objective of the present work is to find simple formulations that can be applied to predict the ultimate strength of stiffened panels. In this context, non–linear shell finite elements and plasticity will be the main focus for the collapse analyses. The formulation used in this paper is based on a triangular constant stress–resultants shell finite element belonging to the family of Morley elements [1],[2],[3]. The element has twelve degrees–of–freedom including three displacement at each of the corner nodes and one rotation at each of the mid–side nodes. The material formulation is based on stress–resultants plasticity with one integration point in the element plane.

THEORY

The middle surface strain tensor and the tensor for curvature changes is expressed in terms of displacement components as,

$$\gamma_{\alpha\beta} = \frac{1}{2}\left(u_{\alpha,\beta} + u_{\beta,\alpha} + u_{\lambda,\alpha}u_{\lambda,\beta} + w_{,\alpha}w_{,\beta}\right) \quad (1)$$

$$\chi_{\alpha\beta} = w_{,\alpha\beta} \quad (2)$$

where u_α ($u_1 = u$, $u_2 = v$) and w are the in–plane and out–of–plane displacement components, respectively. While Equation (1) is valid for arbitrary rotations, Equation (2) is valid only when the rotations remain moderate and the deformations are small. The changes of curvatures will be modified so that the expressions are extended to accommodate arbitrary large rotations.

In terms of stress resultants, the constitutive equation is defined as $d\mathbf{s} = \mathbf{C}_t d\mathbf{e}$ where $\mathbf{s}$ is the stress resultants tensor, $\mathbf{e}$ is the conjugate strain and curvature tensor, and $\mathbf{C}_t$ is the tangent modulus. Let the local element degree of freedom vector, $\mathbf{r}$, be represented as $\mathbf{r}^T = \begin{bmatrix}\mathbf{a}^T & \boldsymbol{\varphi}^T\end{bmatrix} = \begin{bmatrix}\mathbf{u}^T & \mathbf{v}^T & \mathbf{w}^T & \boldsymbol{\varphi}^T\end{bmatrix}$, where $\mathbf{u}$, $\mathbf{v}$, $\mathbf{w}$, and $\boldsymbol{\varphi}$ denote the membrane displacements along the x and y–axes, out–of–plane displacements, and mid–side rotations. From the displacement interpolation the membrane strains reads

$$\boldsymbol{\gamma} = \left(\mathbf{B}_{a1} + \frac{1}{2}\mathbf{B}_{a2}\right)\mathbf{a} \quad (3)$$

The curvature changes reads

$$\boldsymbol{\chi} = \mathbf{B}_{\mathbf{w}}\mathbf{w} + \mathbf{B}_{\varphi}\boldsymbol{\varphi} \tag{4}$$

Equation (2) and hence (4) are only valid within moderate rotations. Since the membrane Equation (1) is applicable within large rotations, it may serve the purpose to employ an updating technique to the changes of curvature so that the curvature changes may accommodate large rotations. Considering only the facet geometry of the triangle, the reference vectors in the current configuration are related to the initial configuration by the expression $[\mathbf{t}_1^n \quad \mathbf{t}_2^n \quad \mathbf{t}_3^n]^T = [\mathbf{R}]\,[\mathbf{t}_1 \quad \mathbf{t}_2 \quad \mathbf{t}_3]^T$, where $\mathbf{R}$ is the rotation tensor. Since we need to update only the unit–normal vector, the following transformation equation serves the purpose $\mathbf{t}_3^n = [R_{31} \quad R_{32} \quad R_{33}]\,[\mathbf{t}_1 \quad \mathbf{t}_2 \quad \mathbf{t}_3]^T$.

With respect to the instantaneously co–rotated configuration, relative displacements and rotations are introduced as a difference between the deformed and co–rotated reference states. As a result, an expression similar to Equation (4) can be found as,

$$\hat{\boldsymbol{\chi}} = \mathbf{B}_w\hat{\mathbf{w}} + \mathbf{B}_{\varphi}\hat{\boldsymbol{\varphi}} \tag{5}$$

where $\hat{\mathbf{w}}$ and $\hat{\boldsymbol{\varphi}}$ denote the relative transverse displacements and relative rotations. This expression may be extended into the regime of finite rotation while strains remain small. In this case, the rate equation for the discrete curvature changes may be expressed as

$$\dot{\boldsymbol{\chi}} = \mathbf{B}_{\mathbf{w}}\dot{\mathbf{w}}_{\mathbf{v}} + \mathbf{B}_{\varphi}\dot{\boldsymbol{\varphi}} \tag{6}$$

where the superposed dot indicates derivative with respect to a time–like parameter. The component vector $\dot{\mathbf{w}}_v$ contains the nodal velocities perpendicular to the instantaneously fixed co–rotating configuration. With reference to rotation of the normal vector for the shell element, (6) may be expressed as,

$$\dot{\boldsymbol{\chi}} = \mathbf{B}_w\left(R_{31}\dot{\mathbf{u}} + R_{32}\dot{\mathbf{v}} + R_{33}\dot{\mathbf{w}}\right) + \mathbf{B}_{\varphi}\dot{\boldsymbol{\varphi}} \tag{7}$$

The discrete equations of equilibrium can now be derived. A t the end of each increment $n+1$, the following expressions apply,

$$\boldsymbol{\psi}^{n+1} = \boldsymbol{\psi}^n + \mathbf{E}_w\left[R_{31}^n\Delta\mathbf{u}^{n+1} + R_{32}^n\Delta\mathbf{v}^{n+1} + R_{33}^n\Delta\mathbf{w}^{n+1}\right] + \mathbf{E}_{\varphi}\Delta\boldsymbol{\varphi}^{n+1} \tag{8}$$

$$\boldsymbol{\gamma}^{n+1} = \left(\mathbf{B}_{a1} + \frac{1}{2}\mathbf{B}_{a2}^{n+1}\right)\mathbf{a}^{n+1} + \frac{1}{2}\mathbf{B}_{\psi_d}^{n+1}\boldsymbol{\psi}^{n+1} \tag{9}$$

$$\boldsymbol{\chi}^{n+1} = \boldsymbol{\chi}^n + \mathbf{B}_w\left[R_{31}^n\Delta\mathbf{u}^{n+1} + R_{32}^n\Delta\mathbf{v}^{n+1} + R_{33}^n\Delta\mathbf{w}^{n+1}\right] + \mathbf{B}_{\varphi}\Delta\boldsymbol{\varphi}^{n+1} \tag{10}$$

Then, for an arbitrary incremental step, the first variation of the strain and curvature tensors are given by $\delta\boldsymbol{\gamma} = \left(\mathbf{B}_{\mathbf{a1}} + \mathbf{B}_{\mathbf{a2}} + \mathbf{B}_{\psi_{\mathbf{d}}}\mathbf{E}_{\bar{\mathbf{w}}}\right)\delta\mathbf{a} + \mathbf{B}_{\psi_{\mathbf{d}}}\mathbf{E}_{\varphi}\delta\boldsymbol{\varphi} = \left(\mathbf{B}_{\mathbf{a}} + \mathbf{B}_{\bar{\psi}}\mathbf{E}_{\bar{\mathbf{w}}}\right)\delta\mathbf{a} + \mathbf{B}_{\bar{\psi}}\mathbf{E}_{\varphi}\delta\boldsymbol{\varphi}$ and $\delta\boldsymbol{\chi} = \mathbf{B}_{\bar{\mathbf{w}}}\delta\mathbf{a} + \mathbf{B}_{\varphi}\delta\boldsymbol{\varphi}$

The equations of equilibrium are derived from the principle of virtual work. For constant stresses and strains the internal virtual work reads $\delta W^i = A\;\delta\mathbf{e}^T\mathbf{s}$. The variation of the internal virtual work, providing the tangent stiffness, is given by $\delta^2 W^i = A\left(\delta\mathbf{e}^T\delta\mathbf{s} + \delta^2\mathbf{e}^T\mathbf{s}\right)$. When isotropic hardening is considered, the original Ilyushin yield surface may be expressed in a general quadratic form as $f(\mathbf{s}, \mathbf{e}^p, \epsilon^p) = \mathbf{s}^T\mathbf{A}\mathbf{s} - \left(1 + \frac{H\epsilon^p}{\sigma_Y}\right)^2 = 0$. The backward

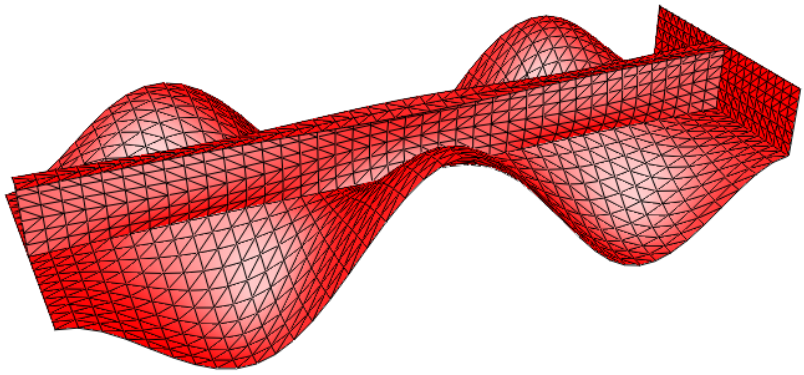

Figure 1: Stiffened panel: finite element mesh and imperfection(exagerated)

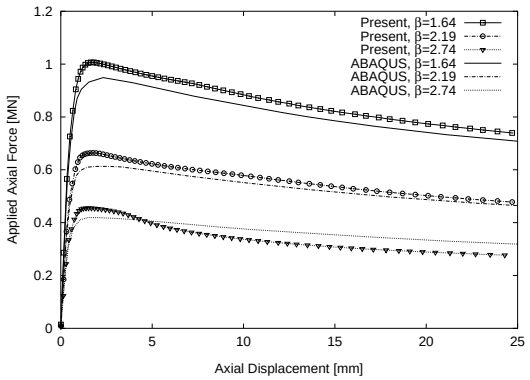

Figure 2: Response of stiffened panel with different transverse pressure levels

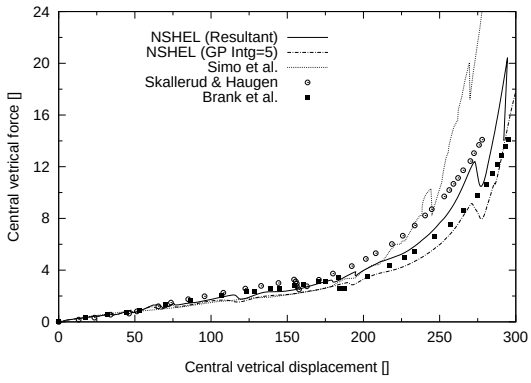

Figure 3: Elasto–plastic response of a pinched cylinder

Euler stress resultant update can be written $\mathbf{s}_{n+1} = \left(\mathbf{Q}\left[\mathbf{I} + 2\lambda\mathbf{\Lambda}\right]^{-1}\mathbf{Q}^{-1}\right)\mathbf{s}_{n+1}^{trial} = \mathbf{V}\mathbf{s}_{n+1}^{trial}$, where at this stage λ remains the sole unknown. The matrices of eigenvalues $\mathbf{\Lambda}$ and eigenvectors $\mathbf{Q}$ represents $\mathbf{C_e A}$. The consistent elasto-plastic tangent modulus $\mathbf{C_t}$ for building the material tangent stiffness matrix and for use in the Newton–Raphson iterations reads $\mathbf{C}_t = \mathbf{H} - \frac{\mathbf{H}\mathbf{g}\mathbf{g}^T\mathbf{H}}{\mathbf{g}\mathbf{H}\mathbf{g}+\beta}$. Details may be found in [3].

CONCLUDING REMARKS

Fig.1 illustrates the finite element mesh and imperfection pattern for the simulations presented in Fig. 2. Some overprediction compared to the results with ABAQUS is observed, this is due to the small nonconservatism inherent in the plasticity formulation and may easily be accounted for. Fig.3 Shows the predicted response with the present formulation, both using stress resultant modeling and 5 integration points through thickness. Comparing with other published results, the agreement is good. Considering cpu time consumption, using 5 integration points over shell thickness increases cpu about 50% compared to the stress resultant approach. Furthermore, alternative moderate rotation formulations ([3]) use approximately 1/4 of cpu compared to the large rotation formulation presented herein. Hence, if a moderate rotation formulation suffices, it should be preferred in the analysis. A complete presentation of the efficiency issues will given in a separate publication.

REFERENCES

[1] L.S.D.Morley. Geometrically nonlinear constant moment triangle which passes the von-Karman patch test. *Int J Numerical Meth Engng*, **31**, 241–263, (1991).

[2] E.Providas and M.A.Kattis. A simple finite element for the geometrically nonlinear analysis of thin shells. *Comp. Mechanics*, **24**, 127–137, (1999).

[3] A.K.Mohammed, B.Skallerud, and J.Amdahl. Simplified stress resultant plasticity on a geometrically nonlinear constant stress shell element. *Int.J. Comp. and Struct.*, **79**, 1723–1734, (2001).

[4] A.Bout. A displacement based geometrically nonlinear constant stress element. *Int.J. Numerical Meth Engng*, **36**, 1161–1188, (1993).

[5] B.Skallerud and B.Haugen. Collapse of thin shell structures - stress resultant plasticity modelling within a co-rotated ANDES finite element formulation. *Int.J. Numerical Meth Engng*, **46**, 1961–1986, (1999).

A symmetric time-stepping scheme for coupled problems

P.A. Wernberg* **G. Sandberg**
Division of Structural Mechanics
Lund University, Lund, Sweden
e–mail: wernberg@byggmek.lth.se

ABSTRACT

Summary In a particular class of coupled problems, the resulting set of equations is unsymmetrical. This paper proposes a simple procedure for introducing a symmetric effective stiffness matrix, used in the implicit stepping scheme for fluid-structure problems. As long as the time step is kept constant, the factorization of the effective stiffness matrix only needs to be performed once.

There is a class of coupled problems that result in an unsymmetrical system of equations. The reason for this, although the complete system is conservative, is how the information is passed between the two domains. The unsymmetrical representation is the most compact representation of the coupled system possible. However, the unsymmetrical system doubles the demand for storing the system matrices and also double the number of operations to be performed for a specific analysis. Hence, there is a benefit in reformulating the system creating a symmetric representation. In a previous work, see [1], this has been done for the coupled eigenvalue problem.

The interacting fluid-structure problem can be written

$$\begin{bmatrix} \mathbf{M}_s & 0 \\ \rho c^2\, \mathbf{H}^T & \mathbf{M}_f \end{bmatrix} \begin{bmatrix} \ddot{\mathbf{d}} \\ \ddot{\mathbf{p}} \end{bmatrix} + \begin{bmatrix} \mathbf{K}_s & -\mathbf{H} \\ 0 & \mathbf{K}_f \end{bmatrix} \begin{bmatrix} \mathbf{d} \\ \mathbf{p} \end{bmatrix} = \begin{bmatrix} \mathbf{f}_b \\ \mathbf{f}_q \end{bmatrix} \tag{1}$$

where $\mathbf{M}_s$ is the structural mass matrix, $\mathbf{K}_s$ is the structural stiffness matrix, $\mathbf{M}_f$ is the fluid mass matrix and $\mathbf{K}_f$ is the fluid stiffness matrix. The coupling matrix can be expressed as

$$\mathbf{H} = \int_s \mathbf{N}_s^T \cdot \mathbf{n}\mathbf{N}_f \mathrm{d}S \tag{2}$$

Introducing the multiplication factor α into the second line of equations in Eq. 1 yields

$$\begin{bmatrix} \mathbf{M}_s & 0 \\ \alpha\rho c^2\, \mathbf{H}^T & \alpha\mathbf{M}_f \end{bmatrix} \begin{bmatrix} \ddot{\mathbf{d}} \\ \ddot{\mathbf{p}} \end{bmatrix} + \begin{bmatrix} \mathbf{K}_s & -\mathbf{H} \\ 0 & \alpha\mathbf{K}_f \end{bmatrix} \begin{bmatrix} \mathbf{d} \\ \mathbf{p} \end{bmatrix} = \begin{bmatrix} \mathbf{f}_b \\ \alpha\mathbf{f}_q \end{bmatrix} \tag{3}$$

Now consider a standard implicit time integration scheme

1. Initialize, $\mathbf{u}_0$, $\dot{\mathbf{u}}_0$, $\ddot{\mathbf{u}}_0$
2. Form the effective stiffness matrix, $\mathbf{K}_{eff} = \mathbf{M}/\beta\left(\Delta t\right)^2 + \gamma\mathbf{C}/\beta\Delta t + \mathbf{K}$
3. Factorize $\mathbf{K}_{eff} = \mathbf{L}\mathbf{D}\mathbf{L}^T$.

   For each time step perform the following steps

(a) Evaluate the effective forces
$\mathbf{f}_{eff} = \mathbf{f}_{n+1} - \mathbf{M}\left(\mathbf{u}_n/\beta\left(\Delta t\right)^2 + \dot{\mathbf{u}}_n/\beta\Delta t + \ddot{\mathbf{u}}_n\left(1-2\beta\right)/2\beta\right)$

(b) Solve $\mathbf{LDL}^T\mathbf{a} = \mathbf{f}_{eff}$.

(c) Calculate the accelerations and velocities at the new timestep.

The crucial part of the scheme is the factorization of the effective stiffness matrix In this case the effective stiffness matrix according to Eq. 3 and step (2) is

$$\mathbf{K}_{eff} = \begin{bmatrix} \mathbf{K}_s + \frac{1}{\beta(\Delta t)^2}\mathbf{M}_s & -\mathbf{H} \\ \frac{\alpha\rho c^2}{\beta(\Delta t)^2}\mathbf{H}^T & \alpha\mathbf{K}_f + \frac{\alpha}{\beta(\Delta t)^2}\mathbf{M}_f \end{bmatrix} \tag{4}$$

Based on the original system , $\alpha = 1$, the effective stiffness matrix is not symmetric and hence symmric solvers can not be utilized. The matrix can be made symmetric, however , if

$$\alpha = -\frac{\beta\left(\Delta t\right)^2}{\rho c^2} \tag{5}$$

For this choice of α the system matrix becomes

$$\mathbf{K}_{eff} = \begin{bmatrix} \mathbf{K}_s + \frac{1}{\beta(\Delta t)^2}\mathbf{M}_s & -\mathbf{H} \\ -\mathbf{H}^T & -\frac{\beta(\Delta t)^2}{\rho c^2}\mathbf{K}_f - \frac{1}{\rho c^2}\mathbf{M}_f \end{bmatrix} \tag{6}$$

The time step enters into the efficient stiffness matrix, hance as long as the time step is kept constant, the same factorization can be used.

Preliminary results shows the anticipated speedup, going from unsymmetric to symmetric representation, is acquired.

REFERENCES

[1] G. Sandberg. A new strategy for solving fluid-structure problems. *Int J Numer Methods Eng.*,**38**, 357–370, (1995).

[2] Calfem. A finite element toolbox to MATLAB Division of Structural Mechanics and Division of Solid Mechanics, Lund Institute of Technology, Lund, Sweden, 1999

Simulation of a drop impact on cold and hot rigid surfaces

Anton V.Chizhov[1,2] * and Kazuyoshi Takayama[1]

[1)] Shock Wave Research Center, Institute of Fluid Science,
Tohoku University, Sendai, Japan
[2)] Ioffe Physical-Technical Institute, Russian Academy of Sciences,
St.Petersburg, Russia

ABSTRACT

Summary Mathematical model of a high-speed drop impact on cold and hot rigid surfaces has been formulated. Numerical approach based on a lagrangian description, a FE method and an adaptive unstructured mesh has been developed. Main physical effects of the phenomenon simulated are briefly described in the present paper, which are a cumulative jet origination, a cavitation and a vaporisation in the thin layer near the hot wall, able to evoke a drop bouncing.

While the interaction between liquid sprays and solid objects occurs in a wide variety of industrial, domestic and environmental applications, our understanding of the mechanisms involved in the process are far from complete. Of fundamental importance to such processes is the hydrodynamic and thermodynamic behaviour of individual droplets which impact a solid surface. Comprehensive reviews on impacts of drops on obstacles can be found in [1-4]. However, phenomenon of high velocity has not been adequately studied even qualitatively.

We consider drops of water or nitrogen, impacting with initial velocities more than some tens of meters per second, a compressibility of the liquid being essential. Let's describe firstly a scheme of such impact on a cold wall [5]. At the initial stage, the free surface, which does not contact the wall, does not deform. The compression region of the drop is bounded by a shock wave adjacent to the contact domain boundary (see Fig. 1A). This is because the velocity of motion of the contact boundary is infinitely large at the contact instant, and the disturbances propagating from the wall do not interact with the free surface. The compression of the liquid is maximal at the contact periphery and continues to increase.

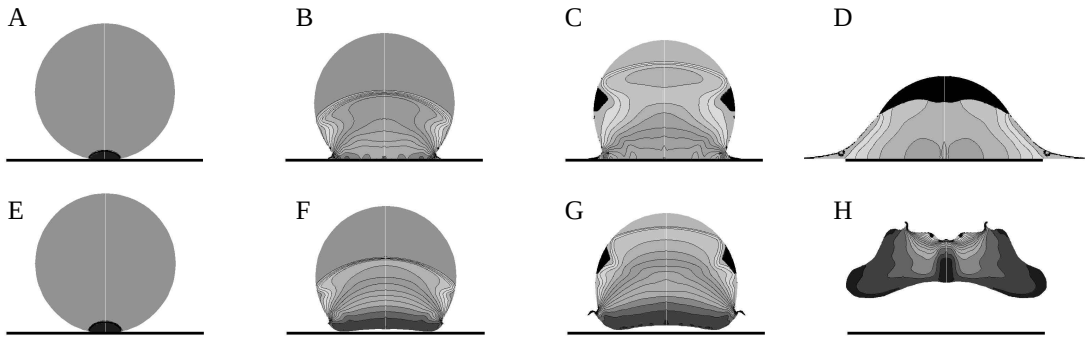

Fig.4. Top row: impact of a nitrogen drop on a cold wall with initial velocity $V_0 = 186\, m/s$; Bottom: impact on a hot wall. Pressure isolines are presented at the time moments 0.01, 0.2, 0.3, 0.9 R_0 / V_0.

At the critical instant, the shock wave leaves the contact boundary and interacts with the free surface to form a shock wave in the ambient gas and an expansion wave propagating inside the

drop. The free surface starts to deform and a near-wall high-velocity cumulative jet is formed (Fig. 1B). The time of jet formation depends on viscous and surface effects in the liquid near the wall, and the jet velocity far exceeds the impact one. When the shock wave in the drop approaches its top, the expansion wave, following the shock wave, causes the formation of a toroidal cavitation area whose cross section is shown in Fig. 1C. At the final stage of interaction, the expansion wave collapses at the symmetry axis, and a vast cavitation area with the greatest rarefaction near the axis is formed (Fig. 1D). The estimations of the time moments of splashing, the jet velocity and maximum pressures can be found in [5].

When impacting on hot wall, the liquid near the contact spot is getting warm and transfers to vapor. Due to short time of impact and comparatively low heat conductivity the layer of the vapor is in some orders smaller than the drop. Getting warm and rarefying, the vapor can push the liquid away. Such influence is negligible if the energy transferred from the wall to fluid during impact is much less than a kinetic energy of the bulk mass of the drop. The influence is valuable in case of the high wall temperature and the small radius of the drop. The smallness of the radius is needed, because the thickness of the heated layer changes approximately as a square root of the time of heating, and this time is proportional to the drop size. That is why the smaller the drop size the bigger is the ratio of layer and drop sizes, and consequently the more compatible are the energies. Under these conditions the shock wave propagating in liquid is forced by the layer and after reflection from the top free surface can evoke an acceleration of the liquid in opposite direction. In the other case of high temperature and big drop size the shock wave is not under the influence of the layer, but large time of interaction leads to dominant role of heat transfer due to convection. The transferred energy evokes the second wave of compression, able to accelerate in back direction the fraction of liquid near the top of the drop.

To simulate these processes occurring in liquid and in incomparably small layer of liquid transferring to vapor two different mathematical models have been formulated, both in the lagrangian approach. Liquid in the drop, excepting the layer, is considered as barotropic fluid governed by the Euler's equations and the Tait's equation of state. Numerical method is based on synthesis of the Finite-Element approach and the TVD-scheme, applied on an adaptive lagrangian unstructured triangular computational mesh [6].

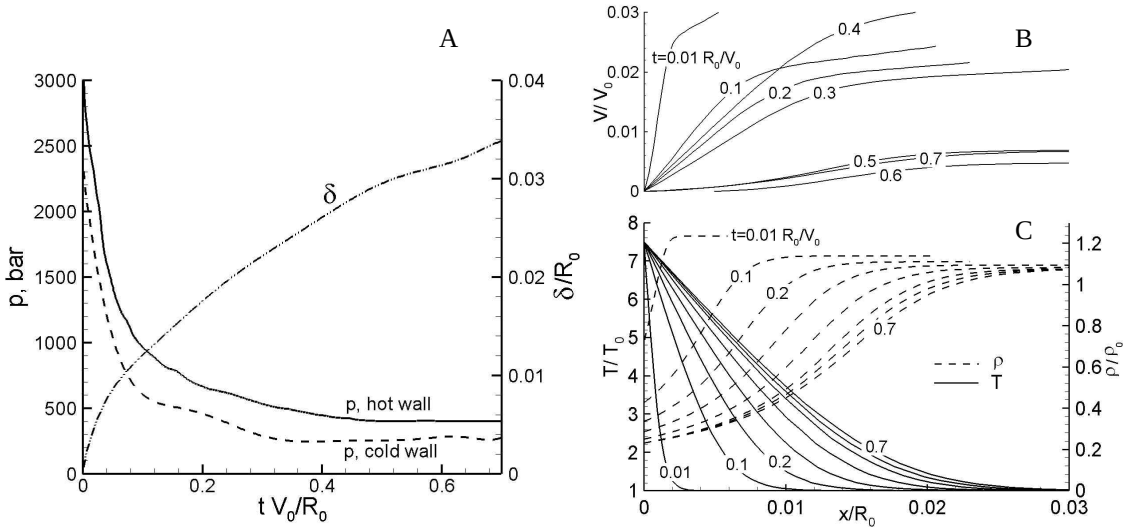

Fig.2 A, Time dependence of pressure near the wall at the axis of symmetry for impacts on cold and hot walls and of the thickness of the vapour layer. **B, C,** The profiles of velocity, pressure and temperature across the layer at different time moments. V_0 , R_0 are the initial velocity and drop radius.

1-D mathematical model of the layer is based on the heat transfer equation, the pressure constancy across the layer, the mass conservation law and the equation of state for both phases of given fluid. These equations give the relation of the fluid velocity on the layer boundary and the pressure. This relation is the boundary condition for the equations, governing the liquid in the domain of the bulk mass of the drop. Final mathematical model for the layer in 2D-case is under construction, the presented results have been obtained for a 1D-problem and in 2-D case by means of a simple approach. The modification of pressure near the wall at the axis of symmetry for the impact (shown on the Fig.1A-D) of nitrogen drop with initial velocity 186 m/s on a cold wall had been calculated. Applying this dependence for the model of the layer and supposing the radius of the drop to be equal to 1mkm, the pressure during the impact on a wall with temperature 600 K was obtained, shown on Fig. 2A along with the thickness of the vapour layer. (The profiles of velocity, pressure and temperature across the layer at different time moments are presented on Fig. 2B,C.) The difference of the pressure values for these cold and hot impacts characterises the influence of the vapour layer on the liquid. For oversimplified consideration of this influence we have carried out another 2-D simulation, supposing to be constant the pressure near the wall (1000 bar) if the influence of gas on liquid exceeds the pressure of liquid on the wall. The results of the simulation are shown on Fig.2E-H, which due to oversimplification should be considered as illustrative results.

Conclusion

In the present paper the main physical effects taking place during impacts of a liquid drop on a cold or heated solid surface were outlined. The mathematical and numerical models of the phenomena were given. Some illustrative results were presented for these two impacts. For the details and estimations on the impact on cold surface the readers are referred to the paper [5].

This study was supported by the Japan Society for the Promotion of Sciences.

REFERENCES

[1] C. Preece, editor, *Erosion.* Academic press, New York, 1979; Mir, Moscow, 1982.

[2] M. Rein. Phenomena of liquid drop impact on solid and liquid surfaces. *Fluid Dynamics Research*, **12**, 61-93, (1993).

[3] M.Lesser, J.Field. The impact of compressible liquids. *Ann. Rev. Fluid Mech.*, **15**, 97-122, (1983).

[4] D.J.E. Harvie, D.F. Fletcher. A hydrodynamic simulation of droplet impacts on hot surfaces, Part I: theoretical model, *Int. J. of Heat and Mass Transfer*, **44**, 2633-2642, (2001).

[5] A.V. Chizhov, A.A. Schmidt. Impact of a High-Velocity Drop on an Obstacle. *Technical Physics*, **45(12)**, 1529–1537, (2000).

[6] Yu.P. Golovachev, E.A. Notkina, A.V. Chizhov, A.A. Schmidt. Simulation of Free-Surface Flows Involving Shock Waves Comput. *Mathematics and Math. Physics,* **41(1)**, 151-162, (2001).

Computer Simulation of the Short Wavelength Transient Elastic Vibration in Solids

R. Barauskas and V. Daniulaitis*
Department of Mechanical Engineering
Kaunas University of Technology, Kaunas, Lithuania
e–mail: rimantas.barauskas@mf.ktu.lt, vytautas.daniulaitis@mf.ktu.lt

ABSTRACT

Summary This document provides information on specially developed and adopted finite element technique for Non-destructive Testing (NDT) problems. Proposed technique is nearly 10 times faster than commercial code ANSYS, and, on the other hand, enables to create and analyse models, solution of which is practically impossible by most commercially available finite element codes due to limitations on model size.

Introduction Short wavelength transient elastic vibrations could be treated as the dynamic processes in regions, dimensions of which 100 to 1000 times exceed length of the propagating wave. In engineering practice the short wave propagation phenomenon is encountered as ultrasonic or impact wave propagation. At the time being, ultrasonic technologies play a prominent role in non-destructive testing (NDT) and monitoring techniques. They afford useful and versatile methods for evaluating microstructures and mechanical properties, as well as detecting microscopic and macroscopic discontinuities in solid materials. A virtual feature of ultrasonic NDT is that each new type of the test has to be analysed theoretically in order to position piezoelectric transducers on the surface of the body under investigation. A great advantage is to have a mathematical model enabling to simulate the testing process and to verify the results. Variety of the finite element codes (ANSYS, ALGOR, etc, however, commercial codes appear to be of little value when modelling NDT processes. Simulation of elastic wave propagation in bodies of complicated geometrical shape requires huge computational resources, which often exceed available capacities of computers.
The motivation of this work is to demonstrate the advantage and efficiency of specially adopted Finite Element procedure in alliances of the regular quadrilateral and free triangular finite element meshes in order to save computational time for the short wavelength wave propagation modelling in NDT processes. The essence of the method lies in the composition of the comparatively small free meshed and large mapped meshed regions, in which explicit recursive formulae for displacements are implemented. This technique permits do not assemble global matrices of the whole structure what leads to high computational speed and small storage.
Application of the finite element method Short wavelength elastic wave propagation analysis is performed by solving the structural dynamic equation

$$[M]\{\ddot{U}\}+[C]\{\dot{U}\}+[K]\{U\}=\{F(t)\}; \tag{1}$$

where $[M],[K],[C]=\alpha[M]$ - the mass, stiffness and proportional damping matrices; $\{F\}$- the external load vector, $\{U\},\{\dot{U}\},\{\ddot{U}\}$ - are the nodal displacement, velocity and acceleration vectors of the structure.
The time integration is being performed by means of the central difference integration scheme:

$$\{\mathbf{U}_{t+\Delta t}\} = [\hat{\mathbf{M}}]^{-1}\left[\{\mathbf{F}_t\} - \left([\mathbf{K}] - \frac{2}{\Delta t^2}[\mathbf{M}]\right)\{\mathbf{U}_t\} - [\tilde{\mathbf{M}}]\{\mathbf{U}_{t-\Delta t}\}\right] \tag{2}$$

where $[\hat{\mathbf{M}}] = \frac{1}{\Delta t^2}[\mathbf{M}] + \frac{1}{2\Delta t}[\mathbf{C}]$, $[\tilde{\mathbf{M}}] = \frac{1}{\Delta t^2}[\mathbf{M}] - \frac{1}{2\Delta t}[\mathbf{C}]$.

Here Δt corresponds to the time discretization step. Generally, the upper limits of discretization steps in space and time can be evaluated by means of the inequality

$$\frac{c \cdot \Delta t}{\Delta x} < 1; \tag{3}$$

where c - velocity of the wave in the media, Δt, Δx - discretization step in time and space respectively.

For elastic solid regions containing several materials we use the discretization steps based on the inequalities

$$\Delta x < \frac{c_{\min}}{5\omega_{exc}} \quad , \quad \Delta t < \frac{\Delta x}{2c_{\max}} \quad , \tag{4}$$

where $c = \sqrt{\frac{E}{\rho}}$ is velocity of propagation of the longitudinal wave , E - Young's modulus of the solid region and ρ - density of the material. Values $c_{\min}$, $c_{\max}$ correspond to minimum and maximum wave propagation velocity if the structure contains several different materials. This leads to huge computational amounts even in 2D case. In steel regions with $c \approx 5200\frac{m}{s}$ and excitation frequency $\omega_{exc} \geq 3MHz$ we obtain $\Delta x < 5 \cdot 10^{-5} m$ and the necessary number of elements of the square plate of dimension $0.1m \times 0.1m$ is about 4 million.

Once concerning the NDT problems, the efficiency of the algorithms could be improved by taking in to account the specifics of the certain problem. As the approach should be oriented to very large models, the computational algorithm is being economised as follows.

a)Large domains under investigation are subdivided into rectangular areas of uniform quadrilateral finite element meshes and small number of areas of arbitrary geometrical shape presented by free meshes, Fig. 1. The recursive formulae for nodes displacement could be derived by proper time integration scheme modification.

The product $[K]\{U_t\}$ for the regular domains is being obtained on the element level and then assembled to nodal vector. As all the matrices of the elements in this domain are identical, the calculation of the product corresponding to node ij , see Fig. 2, can be presented by the simple recursive formula as

$$\begin{aligned}\left([\mathbf{K}]\{\mathbf{U}\}\right)_{\mathbf{i,j}} = &\left([\mathbf{K}^{\mathbf{e}}_{\mathbf{11}}] + [\mathbf{K}^{\mathbf{e}}_{\mathbf{22}}] + [\mathbf{K}^{\mathbf{e}}_{\mathbf{33}}] + [\mathbf{K}^{\mathbf{e}}_{\mathbf{44}}]\right)\{\mathbf{U}\}_{\mathbf{i,j}} + \left([\mathbf{K}^{\mathbf{e}}_{\mathbf{21}}] + [\mathbf{K}^{\mathbf{e}}_{\mathbf{34}}]\right)\{\mathbf{U}\}_{\mathbf{i\text{-}1,j}} + \left([\mathbf{K}^{\mathbf{e}}_{\mathbf{23}}] + [\mathbf{K}^{\mathbf{e}}_{\mathbf{14}}]\right)\{\mathbf{U}\}_{\mathbf{i,j+1}} + \left([\mathbf{K}^{\mathbf{e}}_{\mathbf{12}}] + [\mathbf{K}^{\mathbf{e}}_{\mathbf{43}}]\right)\{\mathbf{U}\}_{\mathbf{i+1,j}} + \\ &+ \left([\mathbf{K}^{\mathbf{e}}_{\mathbf{41}}] + [\mathbf{K}^{\mathbf{e}}_{\mathbf{32}}]\right)\{\mathbf{U}\}_{\mathbf{i,j\text{-}1}} + [\mathbf{K}^{\mathbf{e}}_{\mathbf{24}}]\{\mathbf{U}\}_{\mathbf{i\text{-}1,j+1}} + [\mathbf{K}^{\mathbf{e}}_{\mathbf{13}}]\{\mathbf{U}\}_{\mathbf{i+1,j+1}} + [\mathbf{K}^{\mathbf{e}}_{\mathbf{42}}]\{\mathbf{U}\}_{\mathbf{i+1,j\text{-}1}} + [\mathbf{K}^{\mathbf{e}}_{\mathbf{31}}]\{\mathbf{U}\}_{\mathbf{i\text{-}1,j\text{-}1}} \quad ;\end{aligned} \tag{5}$$

where $\left[K^e_{st}\right] s,t = 1,2,3,4$ are blocks of dimension 2x2 of the stiffness matrix of the quadrilateral element the local nodal numbers of which are being assigned from the bottom left corner in counterclockwise direction.

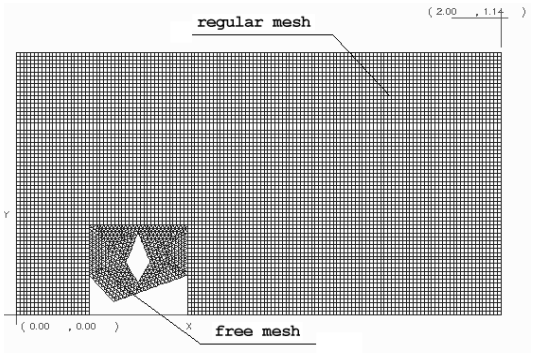

Fig. 1 Finite element model of a plate

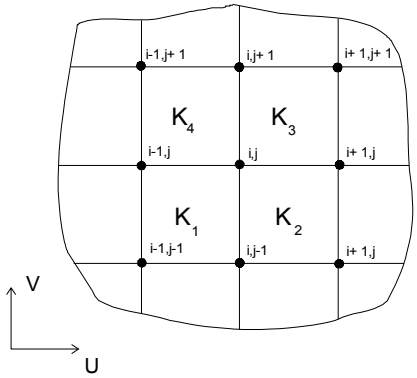

Fig. 2 Fragment of the finite element model

Formula (5) recalls the relations of the finite difference method described in [3] invoking similar number of arithmetic operations to be performed during each time integration step. However, the finite element approach avoids algorithmic difficulties encountered when the finite difference model has to be connected with adjacent regions of arbitrary shape modelled by free finite element meshes. The calculation of the product $[K]\{U_t\}$ for free meshed domains requires considerably greater computational time pro node, however usually the number of nodes in such domains is very small in comparison with the total number of nodes of the model.

b) Diagonal (lumped) mass and damping matrices are being used, therefore no matrix inverse is necessary in (4).

c) The domain regularly meshed by quadrilateral elements is subdivided into rectangular subdomains displacements of which are stored as files on hard disc. For each subdomain the activity index is supplied indicating if the wave has reached the subdomain. Inactive subdomains are excluded from computation of $[K]\{U_t\}$ and considerable time saving is achieved during first stages of the wave propagation. Similarly, the subdomains passed by the wave and containing only very small residual vibration are indicated as inactive and excluded from computation until they are reached by the next wavefront. Proposed technique by means of filtrating allows eliminate noise signal, which propagates more rapidly than longitudinal. Displacements of the nodes are being set to zero value if they do not exceed defined threshold. Actually it is sufficient to nullify all the values below the $10^{-4} \times u_{\max}$, where $u_{\max}$ corresponds to the maximum value of the displacement since the start of program. Displacement's control is being performed after every integration step.

d) Products $[K]\{U_t\}$ could be evaluated for every individual rectangular area by using displacements of certain and adjacent areas. If matrices $[\hat{M}]$ of the areas are diagonal, formula (2) is used for every area separately. That allows permanently to store in the computer memory only products

$[K]\{U_t\}$ corresponding to the nodes shared by adjacent areas while products $[K]\{U_t\}$ corresponding to the internal nodes of the area are stored on computer hard disc.

e) Since computation time may take dozens of hours, created computer program has an option that allows to restart computation from predefined point if process was terminated due to computer failure.

Conclusions Developed computer software was applied to NDT models of the dimension up to 100,000 finite elements. Solution of problems of such dimension is practically impossible by most commercially available finite element codes. By comparing computational time for solution by conventional finite element method and by technique discussed above, it was found that the latter technique is nearly 10 times faster. The improvement of the effectiveness of the numerical simulation was achieved due to use of the explicit time integration schemes in uniform finite element meshes.

REFERENCES

[1] J.H. Argyris, J.St. Doltsinis, W.C. Knudson, L.E. Vaz, K.J. Willam. Numerical Solution of Transient Nonlinear Problems, Comp. Meths. Appl. Mech. Engng., 17/18 (1979), pp 341-409;

[2] K.J. Bathe, E.L. Wilson. Numerical methods in finite element analysis. - Prentice-Hall, Inc., Englewood Cliffs, New Jersey;

[3] K. Harumi. Computer simulation of ultrasonics in a solid, NDT International,vol.19,N5 , October 1986.-pp.315-331;

[4] I. Komura, H. Nakamura. Numerical Analysis of Elastic Wave Propagation in Simulation of Ultrasonic Examination, Proceedings of 7th Eropean Conference of Non-Destructive Testing. Copenhagen, 26-29 May 1998;

[5] O.C. Zienkiewicz, D.W. Kellv and P. Bettess. Marriage a la mode - the best of both worlds (finite elements and boundary integrals). Engineering Computations. 1994.

Stability Judgement of Periodically Excited Rotors Supported by Short Squeeze Film Dampers Taking into Account Inertia Effects and Rupture of the Oil Film

Jaroslav Zapoměl
Department of Mechanics
VSB-Technical University of Ostrava, Ostrava, Czech republic
e–mail: jaroslav.zapomel@vsb.cz

ABSTRACT

Summary A pressure function of short squeeze film dampers is determined by averaging inertia terms in the Navier-Stokes equation related to the axial direction of flow across the width of the damper gap. Velocity components are obtained from a Reynolds' equation. Cavitation areas are characterized by constant value of the pressure. Because of damping forces the equation of motion of a rotor is nonlinear. A series of manipulations (calculation of the steady-state response on periodic excitation by a trigonometric collocation method, calculation of Jacobi matrices of partial derivatives, etc.) result in setting up a transition matrix over the span of time of one period. Magnitudes of its eigenvalues determine stability of the steady-state response.

Inertia effects and cavitation of the oil film

The observations show that squeeze film dampers can cause undesirable operating conditions of rotors. If one or more parameters of the system are close to a stability limit, a bifurcation can occur and the motion tends to jump between different attractors.

Squeeze film dampers are usually incorporated into computational models by means of nonlinear force couplings. To calculate components of the damping force it is necessary to know a pressure function that describes the pressure distribution in the layer of lubricant. If design and geometry parameters of the damper make possible to consider it as short then the pressure gradient is significant only in axial direction. The oil inertia is taken into account by averaging the terms in the corresponding Navier-Stokes equation that are proportional to the oil density across the width of the damper gap.

$$\frac{\rho}{h}\int_0^h\left(\frac{\partial w}{\partial t}+\frac{u}{R}.\frac{\partial w}{\partial \varphi}+v.\frac{\partial w}{\partial Y}+w.\frac{\partial w}{\partial Z}\right)dY=-\frac{\partial p}{\partial Z}+\eta.\frac{\partial^2 w}{\partial Y^2} \qquad (1)$$

p, η, ρ - pressure (pressure function), oil dynamical viscosity, density,
φ, Y, Z - circumferential, radial, axial coordinates,
u, v, w - circumferential, radial, axial velocity components of the oil flow,
h, R, t - width of the gap, radius of the inner ring of the damper, time.

Referring to results of measurements [1] the velocities can be determined from a Reynolds' equation. Their substitution into (1) and consequent integration give the pressure function

$$p=p_a+\frac{1}{2}.\left(\frac{L^2}{4}-Z^2\right)A \qquad (2)$$

$$A = \frac{12.\eta}{h^3}.\left[e.\dot{\gamma}.\sin(\varphi-\gamma)+\dot{e}\cos(\varphi-\gamma)\right]+\frac{\rho}{h}.\left[(\ddot{e}-e\dot{\gamma}^2).\cos(\varphi-\gamma)+(e\ddot{\gamma}+2.\dot{e}\dot{\gamma}).\sin(\varphi-\gamma)\right]$$
$$+\frac{\rho}{10.h^2}.\left[24.e^2.\dot{\gamma}^2.\sin^2(\varphi-\gamma)+24.\dot{e}^2.\cos^2(\varphi-\gamma)+48.e.\dot{e}.\dot{\gamma}.\sin(\varphi-\gamma).\cos(\varphi-\gamma)\right] \qquad (3)$$

e - eccentricity of the journal centre, (dots - derivations with respect to time),
γ - position angle of the line of centres (centers of the outer and inner rings),
p_a - pressure at both ends (faces) of the damper.

The simplest way how to incorporate cavitation into computational models is based on knowledge that pressure of the medium in cavitated regions is approximately constant (p_{cav}). The mean value of the pressure profile in axial direction is then given

$$p_m(\varphi)=\frac{1}{12}A.L^2+p_a \qquad \text{for} \quad \frac{1}{8}A.L^2+p_a \geq p_{cav} \qquad (4)$$

$$p_m(\varphi)=\frac{A}{12.L}.(L^3-3.L^2Z_{cav}+4.Z_{cav}^3)+\frac{2.(p_{cav}-p_a)Z_{cav}}{L}+p_a \quad \text{for} \quad \frac{1}{8}A.L^2+p_a < p_{cav} \qquad (5)$$

$$Z_{cav}=\sqrt{\frac{L^2}{4}-\frac{2.(p_{cav}-p_a)}{A}} \qquad (6)$$

L - length of the damper.

Components of the damping force (F_{HZ} , F_{HY}) are calculated by integration of p_m

$$F_{HY}=-R.L\int_0^{2\pi}p_m(\varphi).\cos\varphi d\varphi \qquad F_{HZ}=-R.L\int_0^{2\pi}p_m(\varphi).\sin\varphi d\varphi \qquad (7)$$

Stability judgement of the periodic response

The model systems are assumed to possess the following properties : (i) the shaft is represented by a beam like body that is discretized into finite elements, (ii) the stationary part is rigid and motionless, (iii) the discs are absolutely rigid, (iv) inertia and gyroscopic effects of the shaft and of the discs are taken into account, (v) material damping of the shaft is viscous, other kinds of damping are linear, (vi) the rotor is supported by rolling-element bearings and squeeze film dapmers, (vii) the rotor rotates at constant angular speed and (viii) is loaded by concentrated and distributed forces of periodical time history. Lateral vibration of such rotors is described by a nonlinear equation of motion

$$\mathbf{M}.\ddot{\mathbf{x}}+(\mathbf{B}+\eta_V.\mathbf{K}_{SH}+\Omega.\mathbf{G}).\dot{\mathbf{x}}+(\mathbf{K}+\Omega.\mathbf{K}_C).\mathbf{x}=\mathbf{f}_A+\mathbf{f}_V+\mathbf{f}_H(\mathbf{x},\dot{\mathbf{x}},\ddot{\mathbf{x}}) \qquad (8)$$

$\mathbf{M}$, $\mathbf{B}$, $\mathbf{K}$, $\mathbf{K}_C$ - mass, damping (external), stiffness, circulation matrices,
$\mathbf{K}_{SH}$ - stiffness matrix of the shaft,
$\mathbf{f}_A, \mathbf{f}_V, \mathbf{f}_H$ - vectors of generalized forces (applied, constraint, damping),
$\mathbf{x}, \dot{\mathbf{x}}, \ddot{\mathbf{x}}$ - vectors of generalized displacements, velocities, accelerations,
η_V, Ω - coefficient of viscous damping, angular speed of the rotor rotation

and by relationships for boundary conditions given by vector $\mathbf{x}_{BC}$ that represents static misaligments of the bearing housings. To be satisfied the boundary conditions the equation of motion (8) is transformed to the form

$$\mathbf{A}_2.\ddot{\mathbf{y}}+\mathbf{A}_1.\dot{\mathbf{y}}+\mathbf{A}_0.\mathbf{y}=\mathbf{b} \qquad (9)$$

Matrices $\mathbf{A}_2$, $\mathbf{A}_1$, $\mathbf{A}_0$ and vectors $\mathbf{y}, \dot{\mathbf{y}}, \ddot{\mathbf{y}}$ and $\mathbf{b}$ are obtained from $\mathbf{A}_2^*, \mathbf{A}_1^*, \mathbf{A}_0^*$ and $\mathbf{x}, \dot{\mathbf{x}}, \ddot{\mathbf{x}}, \mathbf{b}$ by omitting their rows and columns corresponding to the degrees of freedom to which the boundary conditions are assigned.

$$\mathbf{A}_2^* = \mathbf{M} \qquad \mathbf{A}_1^* = \mathbf{B} + \eta_V . \mathbf{K}_{SH} + \Omega . \mathbf{G} \qquad \mathbf{A}_0^* = \mathbf{K} + \Omega . \mathbf{K}_C \tag{10}$$

$$\mathbf{f}^* = \mathbf{f}_A + \mathbf{f}_H - \mathbf{A}_0^* . \mathbf{x}_{BC} \tag{11}$$

Steady-state response of the system on periodic excitation can be determineded for a certain class of problems by means of a trigonometric collocation method [2], [4]. Then

$$\mathbf{y} = \mathbf{a}_0 + \sum_{j=1}^{L} \mathbf{a}_j . \cos\left(j \frac{2\pi}{T} t \right) + \mathbf{b}_j . \sin\left(j \frac{2\pi}{T} t \right) \tag{12}$$

$\mathbf{a}_0$, $\mathbf{a}_j$, $\mathbf{b}_j$ - vectors of Fourier coefficients (j = 1, 2, ... L).

Period of the response T is derived from the period of excitation. Substitution of the assumed solution (12) into (9) for specified collocation points of time results into a set of nonlinear algebraic equations. The unknowns are the Fourier coefficients.

To judge stability of the steady-state vibration of a rotor system its motion is slightly disturbed at the beginning of the investigated period [2], [3]. Damping forces corresponding to the disturbed vibration are determined by means of their expansion into a Taylor series

$$\mathbf{f}_H(\mathbf{x} + \Delta\mathbf{x}, \dot{\mathbf{x}} + \Delta\dot{\mathbf{x}}, \ddot{\mathbf{x}} + \Delta\ddot{\mathbf{x}}) = \mathbf{f}_H(\mathbf{x}, \dot{\mathbf{x}}, \ddot{\mathbf{x}}) + \mathbf{D}_M \Delta\ddot{\mathbf{x}} + \mathbf{D}_B \Delta\dot{\mathbf{x}} + \mathbf{D}_K \Delta\mathbf{x} + \ldots \tag{13}$$

$\Delta\mathbf{x}, \Delta\dot{\mathbf{x}}, \Delta\ddot{\mathbf{x}}$ - vectors of deviations of generalized displacements, velocities, accelerations,

$\mathbf{D}_M$, $\mathbf{D}_B$, $\mathbf{D}_K$ - square matrices of partial derivatives.

A number of manipulations (taking into account only the linear part of (13) and the boundary conditions) result into a differential equation of the first order describing time history of deviations of displacements of the disturbed motion. Because of $\mathbf{D}_M$, $\mathbf{D}_B$ and $\mathbf{D}_K$ its coefficient matrix is a periodic function of time. That's why for stability judgement of the rotor system a Floquet theory can be utilized. After dividing the period of T into N time subintervals Δt, the transtion matrix $\mathbf{H}(T,0)$ is expressed as a product of N partial transition matrices $\mathbf{H}(t+\Delta t,t)$

$$\mathbf{H}(T,0) = \mathbf{H}(T, T-\Delta t).\mathbf{H}(T-\Delta t, t-2\Delta t).....\mathbf{H}(\Delta t,0) \tag{14}$$

Employing kinematic relationships of a Newmark method a relation between kinematic quantities corresponding to times t and $t+\Delta t$ can be derived. The square matrix in it represents a partial transition matrix ($\mathbf{I}$ - identity matrix)

$$\mathbf{H}(t+\Delta t, t) = \begin{bmatrix} \frac{2}{\Delta t}\mathbf{Q}_t - \mathbf{I} & \frac{2}{\Delta t}(\mathbf{P}_t - \mathbf{I}) \\ \mathbf{Q}_t & \mathbf{P}_t \end{bmatrix} \tag{15}$$

$$\mathbf{P}_t = \left(\frac{4}{\Delta t^2}\mathbf{A}_{2,t+\Delta t} + \frac{2}{\Delta t}\mathbf{A}_{1,t+\Delta t} + \mathbf{A}_{0,t+\Delta t} \right)^{-1} . \left(\frac{4}{\Delta t^2}\mathbf{A}_{2,t+\Delta t} + \frac{2}{\Delta t}\mathbf{A}_{1,t+\Delta t} - \mathbf{A}_{2,t+\Delta t}\mathbf{A}_{2,t}^{-1}\mathbf{A}_{0,t} \right) \tag{16}$$

$$\mathbf{Q}_t = \left(\frac{4}{\Delta t^2}\mathbf{A}_{2,t+\Delta t} + \frac{2}{\Delta t}\mathbf{A}_{1,t+\Delta t} + \mathbf{A}_{0,t+\Delta t} \right)^{-1} . \left(\frac{4}{\Delta t}\mathbf{A}_{2,t+\Delta t} + \mathbf{A}_{1,t+\Delta t} - \mathbf{A}_{2,t+\Delta t}\mathbf{A}_{2,t}^{-1}\mathbf{A}_{1,t} \right) \tag{17}$$

Matrices $\mathbf{A}_2$, $\mathbf{A}_1$, $\mathbf{A}_0$ are obtained from $\mathbf{A}_2^*, \mathbf{A}_1^*, \mathbf{A}_0^*$ by omitting their rows and columns corresponding to the degrees of freedom to which the boundary conditions are imposed

$$\mathbf{A}_2^* = \mathbf{M} - \mathbf{D}_M \qquad \mathbf{A}_1^* = \mathbf{B} + \eta_V.\mathbf{K}_{SH} + \Omega.\mathbf{G} - \mathbf{D}_B \qquad \mathbf{A}_0^* = \mathbf{K} + \Omega.\mathbf{K}_C - \mathbf{D}_K \qquad (18)$$

Example

Shaft of the analyzed rotor system (Fig.1) was loaded by two concentrated forces of harmonical time history acting on it at the discs locations in radial directions (300 rad/s - D1, 200 rad/s - D2). Orbit of the rotor journal centre in damper SD1 is drawn in Fig.2. Distribution of eigenvalues of the transition matrix in a Gauss plane is evident from Fig.3. Magnitudes of all of them are less than 1 and it means that the investigated vibration is stable.

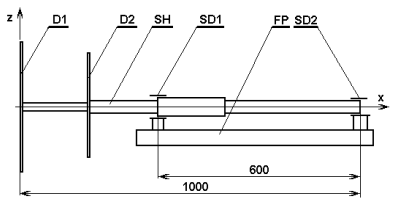

Fig.1

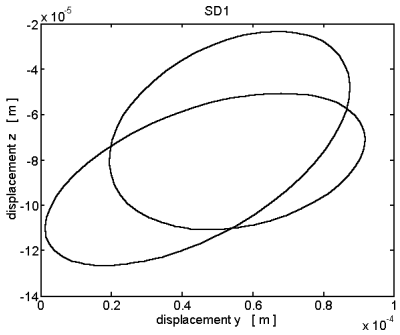

Fig.2

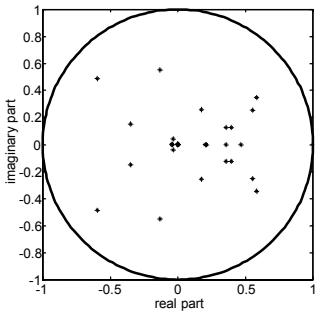

Fig.3

Conclusions

Among the significant advantages of the presented method there are (i) it makes possible to express solution of the Navier-Stokes equation in a closed form and (ii) enables to take into account the influence of inertia and rupture of the oil film on stability of lateral vibration of rotors supported by squeeze film dampers. The carried out computer simulations brought some experience : (i) a trigonometric collocation method is able to find both stable and unstable periodic solutions of the equation of motion, (ii) the most difficult step of the procedure is solving a set of nonlinear algebraic equations and (iii) the described approach to setting up the transition matrix does not require repeated calculations of exponential matrices.

REFERENCES

[1] D. M. Smith. Journal Bearing Dynamic Characteristics-Effect of Inertia of Lubricant. *Proc. I.Mech.E.*, **179**, 37-44, (1964-1965)

[2] J. Zapoměl, E. Malenovský. Approaches to numerical investigation of the character and stability of forced and and self-excited vibration of flexible rotors with non-linear supports. *IMechE Proc. 7th Int. Conf. on Rotating Machinery*, Nottingham, pp.691-699, (2000)

[3] J. Dupal. Stability of non-symetrical rotating 1D continuum with non-isotropic supports. *Proc. of UWB,* **2**, 39-48, (1998)

[4] E. Malenovský. Výpočtové modelování dynamických vlastností nelineárních rotorových soustav. *Inženýrská mechanika*, **6**, 411-426, (1999)

Modal expansion of the perturbation velocity potential for a cantilevered flid-conveying cylindrical shell

Mikael A. Langthjem and Niels Olhoff*
Institute of Mechanical Engineering
Aalborg University, Alborg, Denmark
e–mail: ml@ime.auc.dk and no@ime.auc.dk

ABSTRACT

Summary The subject of this paper is the application of the method of separation of variables and the Galerkin method for discretization of the equations of motion for a cantilevered cylindrical fluid-conveying shell. The perturbation velocity potential is expressed in terms of a series of orthonormal beam modal functions. Comparisons with results obtained from the more precise but also more difficult Fourier transform method are made. Critical flow speeds predicted by the two methods generally agree well.

1 Introduction

Fluid-conveying cylindrical shells are found in numerous industrical applications, in particular in connection with power generation. There are also numerous physiological applications, e.g. in connection with respiratory systems and blood flow. The dynamics of fluid-conveying shells have thus been studied rather extensively. In practical applications clamped-clamped boundary conditions are probably the most common. But cantilevered (clamped-free) shells are also found. For example, ref. [1] mentions a cantilever-type 'intermediate' heat exchanger in the reactor vessel of a fast breeder reactor. No direct support is added at one end because of large thermal expansion. But the main interest in cantilevered shells is probably as a model problem to study flow-induced dynamic instabilities due to the non-conservative character of the fluid forces.

Analyses of complicated systems are commonly being based on the finite element method. In contrast, fundamental studies of simpler systems are often based on 'semi-analytical' discretization methods, such as power series expansion [2, 3], or the Galerkin method [4, 5]. Four boundary conditions are specified at each end and accordingly, a power series expansion is limited to eight wave numbers. The Galerkin method is not subject to this restriction and may therefore give more accurate solutions.

Through the fundamental studies referred to up to this point, potential flow theory has proved to be adequate in yielding correct stability characteristics. The variables in the perturbation velocity potential Φ, expressed with respect to cylindrical polar coordinates (x, θ, r), can be separated by assuming solutions of the form

$$\Phi = \Phi(x, \theta, r, t) = R(r)X(x)\Theta(\theta)T(t) \tag{1}$$

where $R(r)$, $X(x)$, $\Theta(\theta)$, and $T(t)$ are functions of one variable only, and t is the time. The potential function Φ must satisfy the Laplace equation

$$\Delta\Phi = 0, \tag{2}$$

where Δ is the Laplacian. By virtue of the solution assumption (1) and simple assumptions regarding $\Theta(\theta)$ and $T(t)$, the partial differential equation (2) is split up into two ordinary differential equations, a modified Bessel equation in $R(r)$ (also including the circumferential mode number n) and a one-dimensional wave equation in $X(x)$,

$$X''(x) + k^2 X(x) = 0, \tag{3}$$

where k is a discrete wave number and a prime means differentiation with respect to the argument. By the power series expansion method, the assumption $X(x) = C\exp(\mathrm{i}kx)$ is applied, C being a constant, and each term satisfies (3) for all possible sets of boundary conditions.

Modal expansion of $X(x)$ and the structural deflections is straightforward in the pinned-pinned case and works well in connection with the Galerkin method, as the fluid and structural modes are orthogonal, see e.g. ref. [6]. The situation is more complicated when clamped ends are involved. In such cases the potential has previously been discretized by application of Fourier transform [4, 5]. A less restrictive variable separation is then used in the Laplace equation, namely

$$\Phi(x, \theta, r, t) = \mathcal{R}(r, x)\Theta(\theta)T(t) \tag{4}$$

and the r and x variables are separated in the Fourier domain by applying the Fourier transform couple

$$\mathcal{R}^*(r, k) = \int_{-\infty}^{\infty} \mathcal{R}(r, x)\mathrm{e}^{\mathrm{i}kx}dx, \quad \mathcal{R}(r, x) = \frac{1}{2\pi}\int_{-\infty}^{\infty} \mathcal{R}^*(r, k)\mathrm{e}^{-\mathrm{i}kx}dk, \tag{5}$$

where k here is a continuously varying wave number. A drawback of this approach is that the integrals most often only can be evaluated numerically. And for the case of a cantilevered shell, a model of the jet issuing from the free end also needs to be included. This is unnecessary when the problem is posed as a boundary value problem, as the behavior of the jet then is related to the structure through boundary conditions.

The primary goal of the present paper is to derive simple, approximate expressions for the generalized fluid forces, based on a Galerkin discretization of the coupled fluid-structure problem where both the structural deflections and the fluid perturbation pressure are expanded in the same set of orthonormal beam modal functions, $f_m(x)$ say. Rather than using Fourier transform, the problem is posed as a boundary value problem. To carry this through, it will be accepted that (3) is not satisfied exactly, but only approximately, in the averaged, 'weak' form of the Galerkin method. This is because the fulfillment of the (structural) natural boundary conditions ($\partial^2 f_m/\partial x^2 = 0$ and $\partial^3 f_m/\partial x^3 = 0$) at the free end is given higher priority than satisfying the Laplace equation (2) exactly.

2 Theory

Let U be the uniform entrance velocity of an incompressible inviscid fluid of density ρ, flowing steadily in the axial direction within a flexible cylindrical shell of radius a. The fluid is entering at the clamped end $x = 0$ and discharging at the free end $x = L$. The eigenfunctions $X_m(x)$ of (3) are, at the outset, expanded in terms of

$$H_m f_m(x), \tag{6}$$

where $f_m(x)$ are the eigenfunctions for a vibrating beam and H_m are constants. The eigenvalues k_m are obtained from the Galerkin equations

$$\sum_{m=1}^{\infty} H_m \int_0^L \left\{ f'_m f'_j - k_m^2 f_m f_j \right\} dx = 0, \quad j = 1, 2, \ldots, \tag{7}$$

which are obtained as the weak form of (3) with (6) inserted, and with imposition of boundary conditions. [Again, a prime indicates differentiation with respect to the argument x.] As the to (7) corresponding matrix is symmetric and positive definite, all eigenvalues are positive. The equation system is basically the Rayleigh-Ritz method by Kamke's quotient (rather than Rayleigh's quotient) as the boundary conditions are not satisfied by the expansion functions $f_m(x)$, but incorporated through integration by parts.

The generalized fluid dynamics forces Q_{msn} can be written as

$$Q_{msn} = -\omega^2 \mu Q^{(1)}_{msn} + 2\mathrm{i}\omega U \mu Q^{(2)}_{msn} + U^2 \mu Q^{(3)}_{msn}, \tag{8}$$

$$Q^{(1)}_{msn} = \mathcal{I}_{mn}\delta_{ms}, \quad Q^{(2)}_{msn} = \tfrac{1}{2}(\mathcal{I}_{mn} + \mathcal{I}_{sn}) b_{ms}, \quad Q^{(3)}_{msn} = \textstyle\sum_j \mathcal{I}_{jn} b_{mj} b_{js}, \tag{9}$$

where ω is a frequency parameter, μ is a structural mass parameter, δ_{ms} is Kronecker's delta, $b_{ms} = \frac{1}{L}\int_0^L f'_m f_s dx$, and $\mathcal{I}_{mn} = I_n(k_m a)/k_m a I'_n(k_m a)$, I_n being the modified Bessel function of first kind and order n. The three terms $Q^{(j)}_{msn}$, $j = 1, 2, 3$, in (9) correspond to: (1) added mass; (2) fluid damping; and (3) follower-type centrifugal force, respectively.

To validate the main results (9), they will be compared with those obtained by the Fourier transform method. Following [4, 5, 7], the Fourier representation of $Q^{(j)}_{msn}$, $j = 1, 2, 3$, is given by

$$Q^{(j*)}_{msn} = \frac{\zeta_j}{2\pi} \int_{-\infty}^{\infty} \mathcal{I}_n \left\{ \int_0^1 f_m \mathrm{e}^{\mathrm{i}\bar{k}\bar{x}} d\bar{x} + \int_1^{\infty} g_m \mathrm{e}^{\mathrm{i}\bar{k}\bar{x}} d\bar{x} \right\} \left\{ \int_0^1 f_s \mathrm{e}^{-\mathrm{i}\bar{k}\bar{x}} d\bar{x} \right\} d\bar{k}, \tag{10}$$

where $\zeta_j = 1, -\mathrm{i}\bar{k}, -\bar{k}^2$ for $j = 1, 2, 3$, respectively. $g_m(\bar{x})$ is a so-called 'outflow model' [8], and $\mathcal{I}_n = I_n(ka)/kaI'_n(ka)$. An overbar indicates a non-dimensionalized quantity.

3 Numerical examples

In order to check the present method some dynamic stability calculations will be made for the beam mode oscillations, i.e., for $n = 1$. This means that only deflections in radial direction will be considered. As the focus point of this paper is on the fluid-dynamical modeling, the influence of shear deformation on the tube dynamics will be ignored, although this may be of significance in cases of short, 'stubby' tubes. Two non-dimensional parameters will be introduced, namely

$$\bar{U} = UL\sqrt{\frac{\text{fluid mass per unit length}}{\text{bending stiffness}}}, \quad \beta = \frac{\text{fluid mass per unit length}}{\text{total mass per unit length}}. \tag{11}$$

Stability curves depicting critical flow speed $\bar{U}_{cr}$ as function of the slenderness ratio a/L are shown in Figure 1 for (a) $\beta = 0.2$, (b) $\beta = 0.5$, and (c) $\beta = 0.8$. Ten modal functions were applied in all calculations. The solid curves depict the results of the modal expansion method, while the dots are the results of the Fourier transform method. The agreement between the critical flow speed predictions appear to be good in any case.

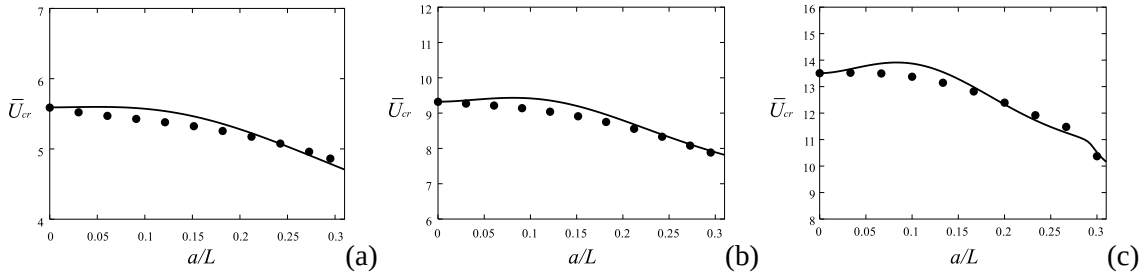

Figure 1. Non-dimensional critical flow speed $\bar{U}_{cr}$, at which dynamic instability is initiated, as function of the slenderness ratio a/L: —, the present method; ●, the Fourier transform method. (a) For the mass ratio $\beta = 0.2$; (b) for $\beta = 0.5$; (c) for $\beta = 0.8$.

4 Conclusion

The paper has proposed a modal expansion of the fluid velocity potential through application of the method of separation of variables and the Galerkin method. The method is a useful, simple alternative to the Fourier transform method in the analysis of dynamics and stability of cantilevered fluid-conveying shells and short beams.

REFERENCES

[1] K. Fujita, T. Itoh, and S. Kajii. Studies on seismic response analysis, including fluid-structure interaction in a fast breeder reactor. In *Proceedings of ICONE-1*, pages 197–202, Tokyo. JSME, (1991).

[2] F.I. Niordson. Vibrations of a cylindrical tube containing flowing fluid. *Trans. Roy. Inst. of Tech. Stockholm, Sweden*, **73**, 1–27, (1953).

[3] M.P. Païdoussis and J.-P. Denise. Flutter of thin cylindrical shells conveying fluid. *J. Sound Vibr.*, **20**, 9–26, (1972).

[4] L.K. Shayo and C.H. Ellen. Theoretical studies of internal flow-induced instabilities of cantilevered pipes. *J. Sound Vibr.*, **56**, 463–474, (1972).

[5] M.P. Païdoussis, T.P. Luu, and B.E. Laitier. Dynamics of finite-length tubular beams conveying fluid. *J. Sound Vibr.*, **106**, 311–331, (1986).

[6] S.-S. Chen. Free vibrations of a coupled fluid/structure system. *J. Sound Vibr.*, **21**, 387–398, (1972).

[7] M.P. Païdoussis *Fluid-Structure Interactions. Slender structures and axial flow. Volume 1*. Academic Press, London, (1998).

[8] V.B. Nguyen, M.P. Païdoussis, and A.K. Misra. A new outflow model for cylindrical shells conveying fluid. *J. Fluids Struct.*, **7**, 417–419, (1993).

A virtual vehicle laboratory for computational simulation and design

P. Davidsson* **and G. Sandberg**
Department of Structural Mechanics
Lund University, Lund, Sweden
e–mail: peter.davidsson@byggmek.lth.se

G. Björkman and J. Svenningstorp
Volvo Technological Development Corporation
Göteborg, Sweden

ABSTRACT

Summary A virtual laboratory for analyzing vehicle structures is described with focus on the prediction of the interior noise level in a vehicle compartment. The presentation points out the advantages and possibilities of this modeling environment where research results can be implemented on realistic models. Cooperation between different research projects is simplified as well as the interaction with industrial groups.

The Swedish research programme Integral Vehicle Structure (IVS) deals with future generations of vehicles. The programme includes four subprogrammes:

- Structural Design
- Vehicle Acoustics
- Drag Prediction and Flow
- Design and Materials and Manufacturing.

Each subprogramme consists of several research projects. In connection with this programme a Virtual Integral Vehicle Structure Laboratory (VIVS-lab) is developed. This virtual laboratory aims to be a common base where results from the different research projects can be implemented. Having this base collaboration between research projects and communication between researchers and industrial groups are simplified.

VIVS-lab is developed within the modeling framework AML (Adaptive Modeling Language). AML has an underlying object-oriented architecture and enables integration of all steps in a product development cycle by interfaces to different programs. The program to be used depends on the task, which may involve design (CAD) or analysis (FEA), for example. In VIVS-lab generic geometry models of different vehicle structures are created. This allows research results to be tested on realistic models.

The implementation in VIVS-lab of the coupled structure-acoustic fluid interaction problem using the finite element method is described. The aim is to determine the vehicle interior noise produced by a given excitation force. The analysis is based on substructuring and modal reduction where the uncoupled modes of the two domains are used to reduce the problem.

To study this problem a simple geometry model is generated in VIVS-lab. The geometry is automatically meshed by use of MSC/Patran. The complexity of the geometry model is thereby unimportant to the effort to achieve the finite element model.

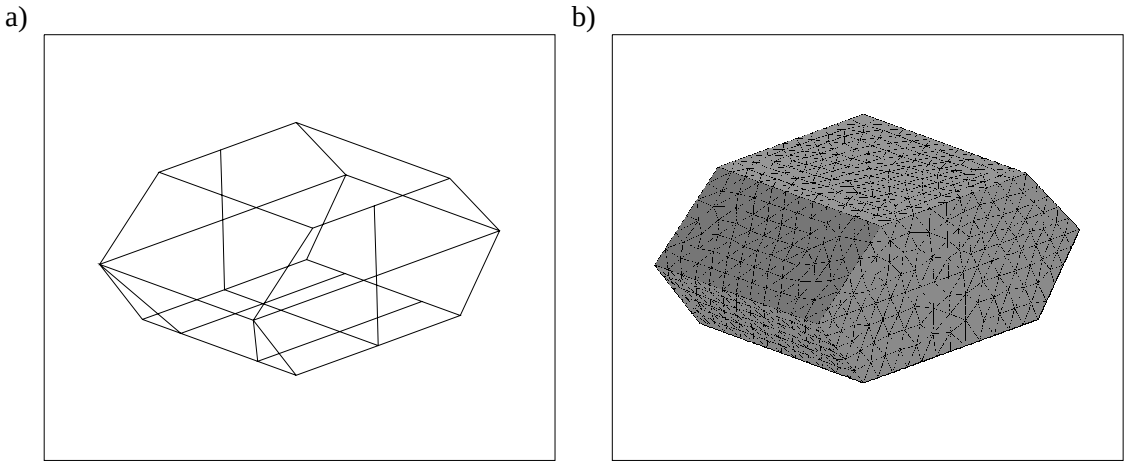

Figure 1: a) Simple geometry model, b) Finite element mesh.

The coupled analysis is divided into two parts. In the first step the coupled problem is analyzed in MSC/Nastran. VIVS-lab generates the input data files on the basis of material properties, loads, boundary conditions and the mesh that MSC/Patran provides. The coupling between the structural and fluid domain is accomplished in MSC/Nastran.

In the second part an in-house code will be used to determine the response of the system. The uncoupled eigenvalue problems, i.e. the structural domain and fluid domain separately, are solved using MSC/Nastran. These results are then employed when analyzing the coupled problem with the developed code. This shows the strength of this modeling environment where different analyzes can be easily connected and research and computational results can be displayed in a readily fashion.

REFERENCES

[1] G. Sandberg, A New Strategy for Solving Fluid-Structure Problems, International Journal for Numerical Methods in Engineering, 38 (1995) 357-370.

[2] G. Sandberg, Acoustic and Interface Elements for Structure-Acoustic Analysis in CALFEM, Report TVSM-7113, Lund Institute of Technology, Division of Structural Mechanics, Lund (1996).

[3] The MacNeal-Schwendler Corporation, MSC/NASTRAN ENCYCLOPEDIA - V70.5, (1998).

[4] Technosoft Inc, Adaptive Modeling Language - Version 3.2.0, (2000).

[5] K.-G. Olsson, P.-E. Austrell, M. Ristinmaa, and G. Sandberg, CALFEM — a finite element toolbox to Matlab, Version 3.2, Report TVSM–9001, Lund Institute of Technology, Division of Structural Mechanics and and Department of Solid Mechanics, Lund, Sweden (1999).

High-speed induced ground vibrations
- an application of the scaled boundary finite element method

Torbjörn Ekevid* and Nils-Erik Wiberg
Department of Structural Mechanics.
Chalmers university of Technology, Göteborg, Sweden
e–mail: torek@sm.chalmers.se

Summary The paper presents a hybrid method based on the combination of conventional finite element- and the scaled boundary finite element methods suitable for wave propagation problems in unbounded domains. Solution procedures for the coupled time-dependent non-linear system involving both ordinary differential equations and algebraic constraint equations are discussed. Furthermore, an example of high-speed train induced ground vibrations is presented.

1. INTRODUCTION

In Sweden[1] and other countries in Western Europe[2], propagating shock waves induced by high-speed trains have been observed on actual lines where the railroad superstructure is built on soft soils possessing a very low natural wave propagation velocity. As the speed of trains approaches or even exceeds the Rayleigh wave velocity in the ground material, high-level vibrations may be generated in the track structure and the surrounding ground material. In extreme cases, potential risk for damage to the track structure and the power supply equipment may exist. The phenomenon has been recognised to have many similarities to supersonic booms in the field of fluid dynamics.
In the present paper we concentrate on potential difficulties regarding finite element simulations of wave propagation in unbounded domains. Concerning simulations of railway induced wave propagation, no natural and distinct boundary conditions exist and special considerations regarding the boundaries of the domain are necessary in order to prevent unphysical reflections.
Based on a combination of conventional finite elements and the scaled boundary finite element[3]-[5] method, we propose an efficient hybrid method for analysing wave propagation phenomena involving non-reflecting boundaries. Since ordinary finite elements are used in the interior of the domain, detailed geometrical modelling of the railway components also including non-linear material properties may be used. The approach also makes it possible to study how efficient different proposals of reinforcements reduce the amplitudes of the propagating waves.

2. SCALED BOUNDARY FINITE ELEMENT METHOD

In the current section we give a very short description of the basic concepts of the scaled boundary finite element method. A more complete description and derivation of the method can be found in Song and Wolf[5] or Ekevid and Wiberg[6].

2.1 Basic ideas

The main objective of the scaled boundary finite element method is to establish a relation between deformations of the interface region and the corresponding reaction forces for the unbounded domain. If such relation, the unit impulse response matrix, is known at all times i.e. the response for a unit deformation for each one of the nodes, the total reaction forces can be obtained from a convolution integral according to (1).
The method is based on four major concepts; the concept of similarity mapping, limit analysis for dynamic equilibrium as the thickness approaches zero for one layer of elements, introduction of

approximations in the continuous consistent infinitesimal finite-element cell equation and finally solution of the resulting matrix equations.

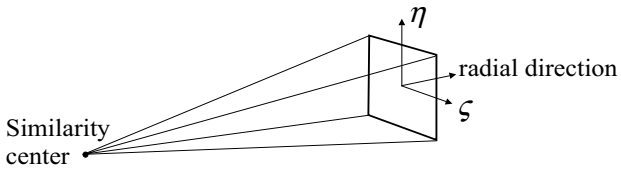

Figure 1. One element for the scaled boundary finite element method.
Local coordinate directions

In contrast to Boundary Elements or similar methods, no fundamental solution is required and free surfaces do not need to be discretized. The method is exact in the radial direction and any finite element approximation can be used in the other two local coordinate direction η and ς, see Figure 1.

$$\boldsymbol{R}(t) = \int_0^t \boldsymbol{M}^{\infty}(t-\tau)\,\boldsymbol{a}(\tau)\,d\tau \tag{1}$$

From a computational aspect, the most expensive operation is the solution of the matrix equations, involving Schur factorisation of relatively large dense matrices to obtain the unit impulse response matrix.

3. THE HYBRID METHOD

The coupling between the conventional finite element and the scaled boundary discretization approximating the unbounded domain is based on dynamic equilibrium for the finite element domain. Since non-conforming grids are used in the interface region, a systematic approach based on Lagrange multipliers for handling general constraint equations has been adopted. For the finite element domain the dynamic equilibrium equation at t_{n+1} according to (2) and the additional constraint equation (3) have to be satisfied.

$$\boldsymbol{F}^{ext}_{n+1} - \left(\boldsymbol{F}^{a}_{n+1} + \boldsymbol{F}^{v}_{n+1} + \boldsymbol{F}^{d}_{n+1} + \boldsymbol{F}^{\lambda}_{n+1} + \boldsymbol{R}^{i}_{n+1}\right) = \boldsymbol{0} \tag{2}$$

$$\boldsymbol{\Phi}_{n+1} = \boldsymbol{0} \tag{3}$$

Here, $\boldsymbol{F}^{ext}_{n+1}$ are the external forces and $\boldsymbol{F}^{a}_{n+1}$, $\boldsymbol{F}^{v}_{n+1}$, $\boldsymbol{F}^{d}_{n+1}$, $\boldsymbol{F}^{\lambda}_{n+1}$ represents inertia forces, damping forces, internal forces and forces from constraint equations, respectively. Furthermore, $\boldsymbol{R}^{i}_{n+1}$ denotes the interaction forces from the unbounded domain, see Figure 2, and $\boldsymbol{\Phi}_{n+1}$ the set of algebraic equations relating the displacements in the interface region.

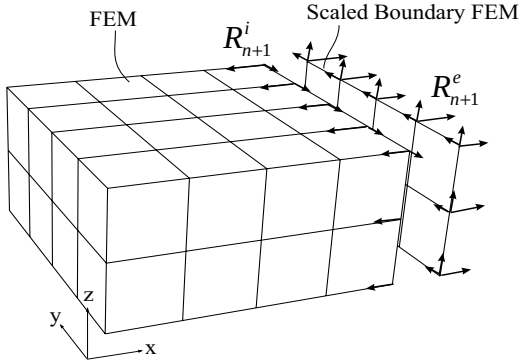

Figure 2. Illustration of coupling in the interface region between the finite element domain and the unbounded domain represented by scaled boundary finite elements.

3.1 Solution procedure for DAE-system

In the present stage we have adopted the ordinary Newmark procedure for the solution process of the non-linear DEA system (2)-(3) above. The evolution of the displacements $\boldsymbol{d}_{n+1}$ and velocities $\boldsymbol{v}_{n+1}$ at time t_{n+1} are assumed to follow (4) and by the choice $\alpha = 0.5,\ \beta = 0.5$ we obtain the well-documented constant average acceleration scheme which is energy conserving and unconditional stable.

$$\begin{aligned} \boldsymbol{v}_{n+1} &= \boldsymbol{v}_n + \Delta t_n \left((1-\alpha)\boldsymbol{a}_n + \alpha \boldsymbol{a}_{n+1} \right) \\ \boldsymbol{d}_{n+1} &= \boldsymbol{d}_n + \Delta t_n \boldsymbol{v}_n + \frac{\Delta t_n{}^2}{2} \left((1-\beta)\boldsymbol{a}_n + \beta \boldsymbol{a}_{n+1} \right) \end{aligned} \tag{4}$$

In order to compute the first set of residual forces we make a prediction according to (5).

$$\begin{aligned} \boldsymbol{a}_{n+1}^0 &= \boldsymbol{a}_n \\ \boldsymbol{v}_{n+1}^0 &= \boldsymbol{v}_n + \Delta t_n \left((1-\alpha)\boldsymbol{a}_n + \alpha \boldsymbol{a}_{n+1}^0 \right) \\ \boldsymbol{d}_{n+1}^0 &= \boldsymbol{d}_n + \Delta t_n \boldsymbol{v}_n + \frac{\Delta t_n{}^2}{2} \left((1-\beta)\boldsymbol{a}_n + \beta \boldsymbol{a}_{n+1}^0 \right) \\ \boldsymbol{\lambda}_{n+1}^0 &= \boldsymbol{\lambda}_n \end{aligned} \tag{5}$$

Corrections of accelerations $\delta \boldsymbol{a}^i$ and Lagrange multipliers $\delta \boldsymbol{\lambda}^i$ are obtained from linearisation of (2)-(3) applying an ordinary Newton iteration scheme until a prescribed tolerance criterion is fulfilled.

$$\begin{bmatrix} \left(\boldsymbol{M}^*\right)^i & \left(\boldsymbol{\Phi}^d\right)^T \\ \boldsymbol{\Phi}^d & \boldsymbol{0} \end{bmatrix} \begin{pmatrix} \delta \boldsymbol{a}^i \\ \delta \boldsymbol{\lambda}^i \end{pmatrix} = \begin{pmatrix} \left(\boldsymbol{R}_a\right)^i \\ \left(\boldsymbol{R}_\lambda\right)^i \end{pmatrix} \tag{6}$$

Here, $\left(\boldsymbol{M}^*\right)^i$ is the efficient stiffness matrix according to (7), where $\boldsymbol{M}$, $\left(\boldsymbol{C}\right)^i$ and $\left(\boldsymbol{K}^t\right)^i$ are the conventional mass, damping and tangent stiffness matrix, respectively and $\boldsymbol{M}_1^\infty$ is the first unitimpulse response matrix from the convolution sum (10) associated to velocities $\boldsymbol{v}_{n+1}$.

$$\left(\boldsymbol{M}^*\right)^i = \boldsymbol{M} + \alpha \Delta t_n \left(\boldsymbol{C}\right)^i + \beta \Delta t_n{}^2 \left(\boldsymbol{K}^t\right)^i + \alpha \Delta t_n \boldsymbol{M}_1^\infty \tag{7}$$

Furthermore, $\boldsymbol{\Phi}^d$ is the Jacobian of the constraint equations containing the partial derivatives with respect to the displacement components. The right-hand side in (6) represents the residual forces and the violation of the constraint equations as:

$$\left(\boldsymbol{R}_a\right)^i = \boldsymbol{F}_{n+1}^{ext} - \left(\boldsymbol{F}_{n+1}^a + \boldsymbol{F}_{n+1}^v + \boldsymbol{F}_{n+1}^d + \boldsymbol{F}_{n+1}^\lambda + \boldsymbol{R}_{n+1}^i \right)^i \tag{8}$$

$$\left(\boldsymbol{R}_\lambda\right)^i = -\frac{\boldsymbol{\Phi}_{n+1}^i}{\beta \Delta t_n{}^2} \tag{9}$$

For each iteration cycle, accelerations, velocities and displacements and Lagrangie multipliers have to be updated accordingly before a successive iteration in the Newmark procedure is done. In the numerical procedure all unit response matrices are assumed to be constant in each time step and hence the convolution integral in (1) for the interface forces can be approximated by a corresponding convolution sum according to (10).

$$\boldsymbol{R}_{n+1}^i = \sum_{i=1}^{n+1} \boldsymbol{M}_{n+1-i+1}^\infty \int_{t_{i-1}}^{t_i} \boldsymbol{a}(\tau)\, d\tau = \boldsymbol{M}_1^\infty \boldsymbol{v}_{n+1} - \boldsymbol{M}_1^\infty \boldsymbol{v}_n + \sum_{i=1}^{n} \boldsymbol{M}_{n+1-i+1}^\infty \left(\boldsymbol{v}_i - \boldsymbol{v}_{i-1} \right) \tag{10}$$

4. HIGH-SPEED EFFECTS, RESPONSE OF A RAILROAD SECTION

In this example, we study the influence of different train velocities to the dynamic response of the railroad section in Figure 3 consisting of rails, sleepers, ballast and subground material. In this case the material is elastic but in the formulation described above any non-linearities can easily be included. Two different velocities of the train; 40 and 60 m/s are considered and the train is modelled as a collection of moving concentrated forces.

The results in Figure 3b indicates presence of propagating shock waves as the velocity of the moving loads exceeds the surface velocity in the ground material. The displacement for points at the railhead and 6m from the centre-line of the rail have also been compared to in-situ measurements conducted in spring 2000 and the results show good agreement. For velocity 60 m/s, the displacement amplitude of the railhead exceeds 15 mm.

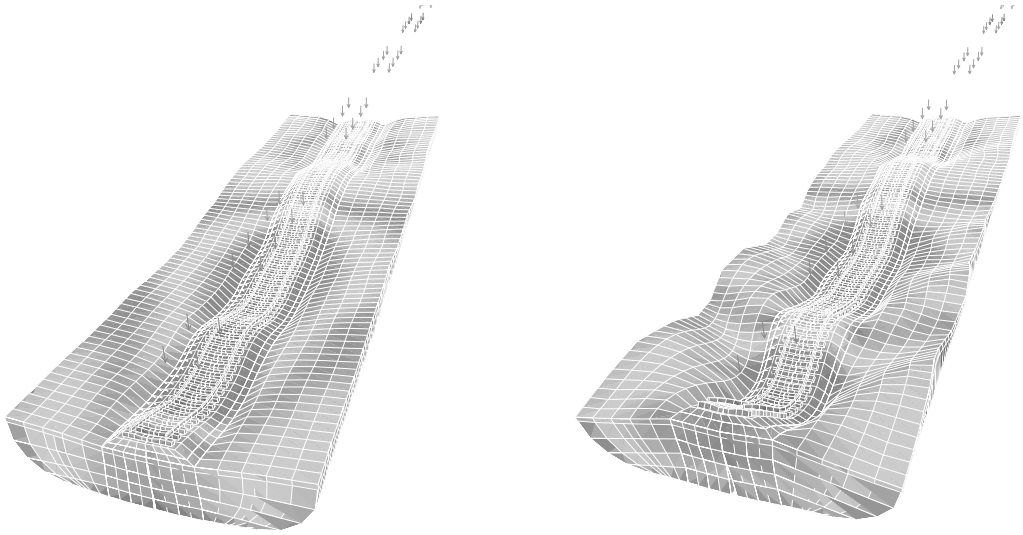

a) b)

Figure 3. Global response of the railroad section. Two different train-speeds are considered a) v= 40 m/s and b) v = 60 m/s. Displacements magnified by a factor 200.

5. REFERENCES

[1] Banverket, *High speed lines on soft ground: evaluation and analyses of measurements from the West Coast line*, Swedish National Rail Administration, Borlänge, Sweden, (1999).

[2] W. Gardien, H. Stuit and F. de Boer, Finite element wave propagation model. *Proc. Second European LS-DYNA Users Conference*, Gothenburg, (Sweden), 33-42, (1999).

[3] J. P. Wolf and C. Song. The scaled boundary finite-element method-a primer: derivations. Computers & Structures, **78**, 191-210 (2000)

[4] J. P. Wolf and C. Song. The scaled boundary finite-element method-a primer: solution procedures. Computers & Structures, **78**, 211-225 (2000)

[5] C. Song and J. P. Wolf. Consistent infinitesimal finite-element cell method: three-dimensional vector wave equation. *Int. j. numer. methods eng.*, **39**, 2189-2208 (1996)

[6] T. Ekevid, N.-E. Wiberg and M. X.D. Li. On Wave Propagation Problems Associated to High-speed Trains. *European Conference on Computational Mechanics, ECCM 01*, Cracow (Polen), June 2001.